Coronal Heating and Solar Wind Acceleration by Alfvén Wave Turbulence: a Global Computational Model and Observations

by

Rona Oran

A dissertation submitted in partial fulfillment
of the requirements for the degree of
Doctor of Philosophy
(Atmospheric, Oceanic and Space Sciences and Scientific Computing)
in The University of Michigan
2014

Doctoral Committee:

Professor Tamas I. Gombosi, Co-Chair
Associate Research Scientist Bartholomeus van der Holst, Co-Chair
Associate Research Scientist Enrico Landi, Co-Chair
Professor Susan T. Lepri
Professor Ken Powell
Research Scientist Igor Sokolov

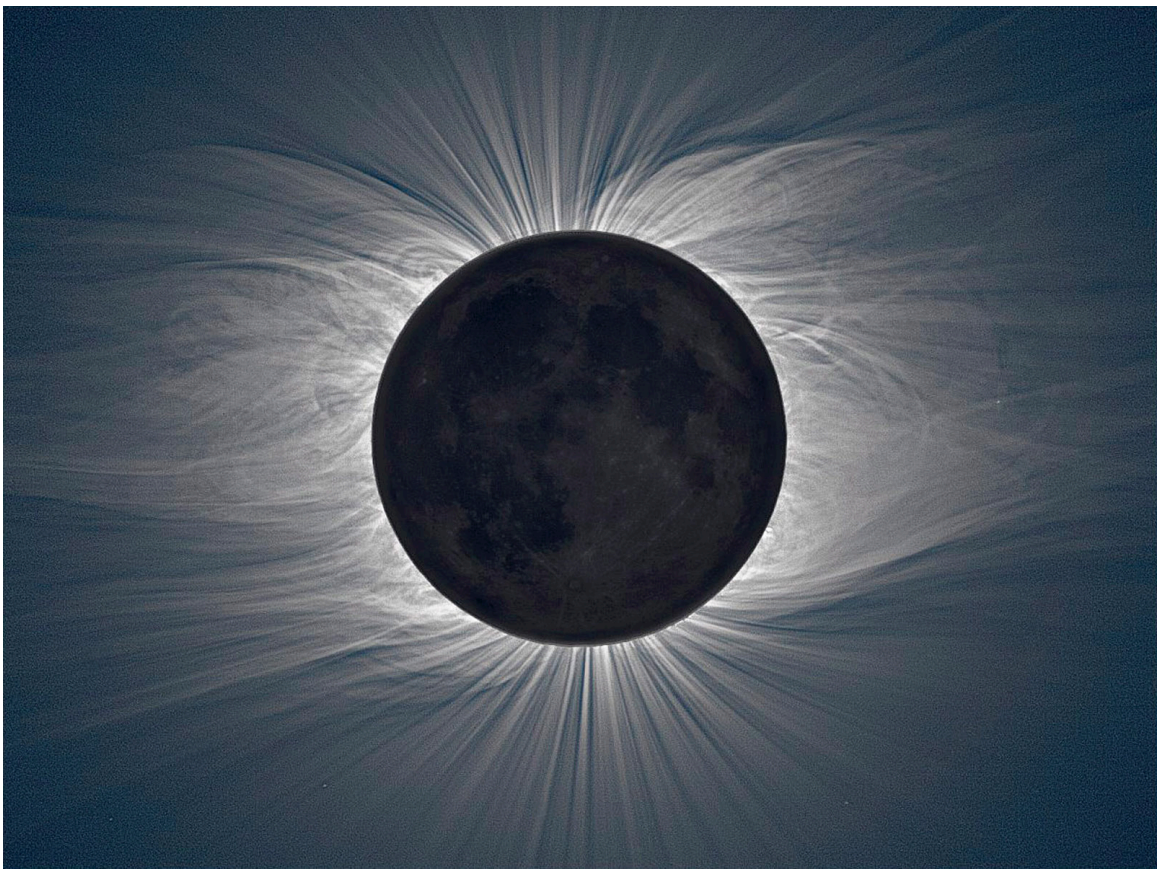

The Moon comes between humans and their Sun; the Corona is shining.

For My Constant and the Little Hamster

ACKNOWLEDGEMENTS

As this journey of completing my PhD studies is reaching its end, I would like to thank all those who have made this work possible. To my adviser, Professor Tamas Gombosi, I would like to express my gratitude for believing in me, supporting me throughout my graduate studies, and guiding me through the process of becoming a scientist. His encouragement and constructive feedback have taught me the importance of being focused on the task at hand, while broadening my horizons and keeping track of the big picture. His knowledge and deep understanding of the field of space physics has inspired me and provided me with an invaluable resource for professional development. His creativity and innovativeness were crucial for building this body of work, and I am truly fortunate to have had him as an adviser.

I wish to express my gratitude to Dr. Bart van der Holst, co-chair of my dissertation committee. His breadth of knowledge and expertise in computational science and solar physics were pivotal for acquiring the skills I needed to perform this research. His consistent willingness to help, teach, and share his expertise have always encouraged me to push on and set new goals for myself. His support throughout my graduate studies has allowed me to face difficult challenges and have made this journey stimulating and enjoyable.

I wish to thank Dr. Enrico Landi, co-chair of my dissertation committee, who exposed me to the fascinating field of solar spectroscopy. He has patiently taught me how to use this important tool, and I am fortunate to have had the opportunity to explore the observational aspects of solar physics under his guidance. I learned a lot

from his resourcefulness and meticulousness, and I have greatly benefited from his support and encouragement. I believe the knowledge he provided me with will serve me for many years to come.

I also wish to thank the other members of my dissertation committee. From my work with Dr. Igor Sokolov I learned the importance of rigorous thinking and analytical understanding. He has always set high standards, and has often led me to gain a better and more profound understanding of my work. I am thankful for his support during my dissertation work.

I wish to thank Professor Sue Lepri, who has always been willing to engage in open discussion about solar physics. Her observational expertise and helpful suggestions have often opened a door to further exploration, and led me to step outside of the beaten path. Professor Lepri is an inspiring role model due to her high level of professionalism, dedication, and persistence.

I would like to thank Professor Ken Powell, for his guidance and advice during my participation in the Scientific Computing program, for his service on my dissertation committee and for making helpful suggestions.

I am thankful for many other faculty in AOSS, and especially the CSEM team. Dr. Gabor Toth has been instrumental in my professional training, as he has guided me through several computational projects, from which I have learned a great deal. He has always set high standards for code development, and taught me the importance of using caution when interpreting simulation results. He was always willing to offer advice and constructive criticism, and I have no doubt that the lessons I learned from working with him will serve me well in the future.

I would like to thank the members of the CSEM solar group, Dr. Chip Manchester and Dr. Rich Frazin. I am grateful for their willingness to review my work and offer their perspective. Their feedback has often led to me to improve the methods I was using and significantly enhance and refine the results. I would like to express my

gratitude to Dr. Darren De Zeeuw, for always willing to lend a helping hand in computation and visualization.

I would like to thank my family for their constant support and encouragement during my time in Michigan. Being away from them was a difficult decision to make and live by, both for them and for me, and I am grateful for their patience and for maintaining such a warm connection with me despite the distance. I am extremely thankful for my dear friends Raluca Ilie, Erika Roesler, Martin Rubin, Lars Daldorff and Valeriy Tenishev, whose friendship and infinite support is precious to me. We shared many fun and happy times in and outside of the academic setting, and they made my life in Michigan so much more enjoyable. I am grateful for my friendship with Liora Shani, who has been a constant source of encouragement and comfort throughout the many challenges of graduate school.

To my wonderful office mates - past and present - getting to know you was one of the best features of graduate school. Ofer Cohen, Dan Welling, Alex Glocer, Xing Meng, Meng Jin, Zhenguang Huang, Dmirty Borovikov, Judit Szente, Lizzy Sparks and Stav Ofer - your friendship and the time we shared together will always be close to my heart. We had a lot of fun, and we ate a lot of interesting food! To my step office mates: Jonathan Nickerson, Chuanfei Dong, Weiye Yao, John Haiducek, Lois Kepler and Doga Ozturk - I love you all as well!

Last but not least, I would like to thank the administrative and IT staff of the AOSS department, for their patience and dedication, which helped make my time in Michigan a pleasant experience.

TABLE OF CONTENTS

LIST OF FIGURES

Figure

ABSTRACT

Coronal Heating and Solar Wind Acceleration by Alfvén Wave Turbulence: Models and Observations

by

Rona Oran

Chair: Prof. Tamas Gombosi

Alfvén waves emanating from the chromosphere have been suggested as a possible driver of coronal heating and solar wind acceleration. Here, we explore whether Alfvén waves can simultaneously predict the observed extreme ultraviolet (EUV) emission from the lower corona and the in-situ measurements of the solar wind.

For the first time, a global magnetohydrodynamics (MHD) model driven by wave turbulence was developed. This model, the Alfvén Wave Solar Model (AWSoM), extends from the top of the chromosphere up to 2 AU. It solves the two-temperature MHD equations coupled to wave transport equations. Wave pressure gradients accelerate the wind, while wave dissipation due to a turbulent cascade is the only heating mechanism. The strength of this new model is in the unified approach for describing wave dissipation in both open and closed field lines. The three-dimensional distribution of heating and acceleration rates that can explain both EUV and in-situ observations emerges naturally and self-consistently from this approach.

We explored the transport of wave energy in the corona by producing synthetic emission lines from the model results. The line profiles, whose widths depend on

the wave amplitude, were compared to spectral observations. We demonstrated that turbulent dissipation can simultaneously explain the observed heating rates and wave amplitudes in the lower corona.

Wind acceleration was studied by simulating the ionization of heavy elements as they flow along open field lines. The emission due to the predicted charge states was calculated and compared to spectral observations up to a height of 1.16Rs above the limb. We found that the model cannot explain all the spectral observations at these heights; however, it can qualitatively reproduce and explain the large-scale variations in charge state composition observed in the slow and fast wind. Finally, the possible presence of supra-thermal electrons was shown to improve the agreement with both remote and in-situ observations.

This work shows that turbulent Alfvén waves can explain the large-scale structure of the corona, solar wind, and charge-state composition. The AWSoM model constitutes a major step toward a physics-based global solar model, and can improve our ability to predict space weather.

CHAPTER I

Introduction

The "empty" space in the solar system is filled by a rarefied ionized gas, or plasma, which originates in the solar atmosphere. The plasma is carried from the Sun in all directions in an ever-present flow called the solar wind. The solar wind is embedded with a magnetic field, originally generated by the Sun, and carried away by the wind flow. The solar wind can interact with the space environment of other solar system bodies. Solar storms and other disturbances in the solar atmosphere release matter and energy into the solar wind, which propagate into interplanetary space and interact with the ambient solar wind. If these disturbances reach the near-Earth space environment, they may trigger various phenomena such as distortions of the geomagnetic field, enhancement of electrical currents in the magnetosphere and ionosphere, auroral activity, precipitation of energetic particles and so forth. These phenomena may cause disruptions to electrical systems both in space and on the ground, and pose a hazard to astronaut safety. The conditions of the plasma and the magnetic field in interplanetary space are collectively referred to as Space Weather. As society becomes increasingly dependent on space technology, there is a greater need to better understand and predict space weather. Understanding the processes dominating the solar atmosphere and the solar wind is thus a crucial part of the study of space weather.

The solar environment allows us to study how plasmas behave under conditions that cannot be recreated in the laboratory, and to explore plasma processes over a large range of spatial and temporal scales. Many naturally occurring phenomena in the solar environment present us with challenging scientific problems.

In the last few decades, considerable effort was made to better understand this system, with an increasing availability of observations and the development of complex computational models. This allowed for significant progress to be made, but a number of questions still remain unanswered. Two of the main outstanding problems in solar physics concern the heating of the solar corona and the formation and acceleration of the solar wind. This work aims to build on previous efforts, and explore these questions using large-scale sophisticated numerical simulations, complemented by observations of the solar corona and solar wind.

1.1 The Solar Corona

The solar corona is the hot extension of the Sun's atmosphere, filled with solar material that has been fully-ionized due to high temperatures of 1-2 million degrees. The corona cannot be seen by the naked eye, since the much larger brightness of the solar disk prevents the emission from the corona to be discerned. Solar eclipses, during which the solar disk is occulted by the moon, have provided humankind with spectacular views of the corona. Contrary to planetary atmospheres, which are simple spherical shells around the body, the solar corona exhibits significant structure, with bright, petal-like features extending outward up to 2-4 times the solar radius, interspersed by darker regions. The corona, which stands for "crown" in Latin, owes its name to this formation.

The solar corona can be imaged by an instrument called a coronagraph - which imitates a solar eclipse by occulting the solar disk from the imager. Figure 1.1 shows composite white-light images of the corona taken during two solar eclipses, from 1998

and 2001. The outer part of each composite was taken by the LASCO C-2 coronagraph on board the Solar and Heliospheric Observatory (SoHO) satellite, which has been monitoring the solar environment since 1995.

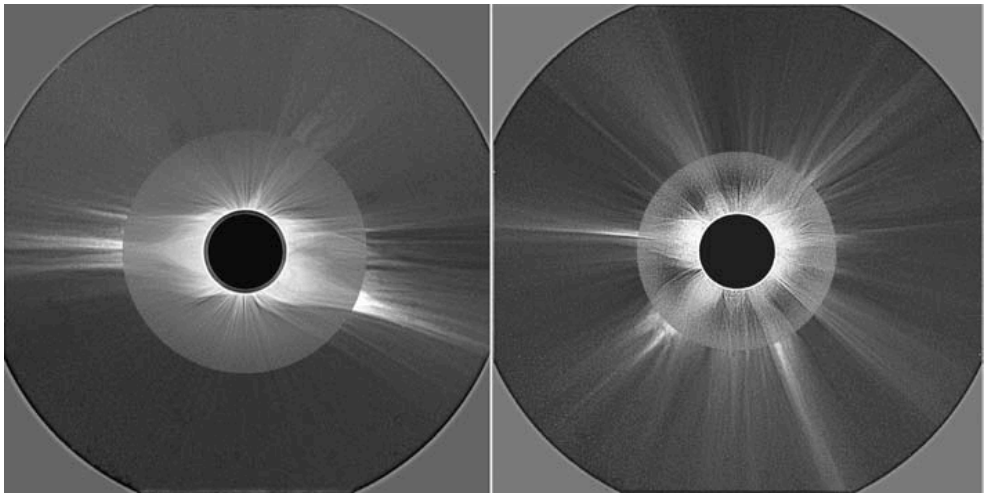

Figure 1.1: *Eclipse and SOHO/LASCO C-2 composite of the solar corona, credit: S. Koutchmy. The left images were taken during a solar eclipse in 1998 (during solar minimum). The right images were taken during a solar eclipse in 2001 (during solar maximum). .*

The coronal plasma is organized into observed structures by the solar magnetic field, which is generated by a magnetic dynamo process in the solar interior. The magnetic field lines penetrate through the solar surface and extend into the corona. The coronal magnetic field lines can be either "closed", i.e. both ends of the field lines connect back to the surface, or "open" i.e. they are attached to the Sun at only one end, while the other end is stretched into interplanetary space (theoretically, these field lines close at infinity). The corona is made up of ionized plasma and the charged particles move along magnetic field lines while gyrating around them. This causes the plasma to be "trapped" along closed magnetic field lines, known as coronal loops, which appear in X-ray images of the lower corona (e.g. *Orrall*, 1981). The largest closed-field structures appear as the bright regions in white-light coronagraph images, where the increased brightness is due to their higher densities. These structures are

commonly called helmet streamers. Along open magnetic field lines, the hot coronal plasma can escape into interplanetary space. This causes open field regions to have lower densities, and to appear darker in images of the corona (e.g. *Zirker*, 1977). Because of this, open field regions are often called coronal holes.

The large scale topology of the corona slowly changes throughout the 11-year long solar activity cycle, due to changes in the intrinsic solar magnetic field. During solar minimum, the solar magnetic field is close to a dipole configuration; the helmet streamers are centered in a belt around the solar magnetic equator, while coronal holes are mostly confined to the magnetic poles (see left panel of Figure 1.1). During solar maximum the corona is much less organized, with a patchier streamer belt and coronal holes appearing at all latitudes (see right panel of Figure 1.1).

1.2 The Solar Wind

Away from the Sun, coronal plasma is accelerated radially outward, eventually forming the solar wind, which becomes supersonic beyond about 10 solar radii. Since the solar wind is invisible due its low density, its existence was only revealed in the 20^{th} century. Before the advent of the space-age, when spacecraft first detected the solar wind particles, it was only through indirect deduction that the concept of a solar wind was developed. Carrington was the first to relate a solar flare event to a geomagnetic storm occurring a day later, as early as 1859. However, it was only in 1916 that Birkeland suggested that continual auroral activity could be explained by a continuous flow of both negative and positive charged particles. A continuous flow of particle was also suggested by Biermann in 1951 from his study of the direction of comet tails.

Nowadays, the solar wind is routinely detected and analyzed by spacecraft, which has supplied us with a wealth of information about the wind speed, density, temperature, magnetic field and composition. Figure 1.2 shows Ulysses observations of the

solar wind speed during solar minimum (left) and maximum (right). The sunspot number is shown in the bottom panel, which indicates the variation of solar activity during the cycle. Ulysses's orbit around the Sun was close to polar and provided measurements from almost all latitudes. The plots reveal that the solar wind consists of two distinct types: the fast ($\sim 700 km/s$) and slow ($\sim 400 km/s$) solar wind. During solar minimum, the slow wind is concentrated around the equator, more or less aligned with the streamer belt in the corona. During solar maximum fast and slow wind flows are mixed together at all latitudes. These two wind types differ not only in their speed but also in their temperature, density and heavy element and ion composition. Furthermore, the slow wind shows high temporal variability in all these quantities, while the fast wind is more steady in nature, as will be discussed further below.

1.3 Early Theoretical Models of the Corona and Solar Wind

The idea of a continuous flow from the solar atmosphere was not easily accepted since it was believed that the solar atmosphere has to be in hydrostatic equilibrium due to the large gravitational force of the Sun. As pointed out in *Parker* (1958), the thermal speed of hydrogen ions in a coronal plasma of ∼3MK will be $\sim$ 260 km/s, while escape from the solar gravitational field would require a minimum speed of 500 km/s.

However, motivated by Biermann's observations of comet tails mentioned above, Parker was the first to show that a hydrostatic corona cannot exist, and established the first theoretical picture of the solar wind. Using the Euler equations for a spherical atmosphere, he showed that a static solution will lead to a finite plasma pressure at infinity. He concluded that the solar atmosphere must expand into interplanetary space, and that the plasma flow becomes super-sonic away from the Sun. The Parker hydrodynamic solution is a corner-stone of solar physics; however, the wind speeds it

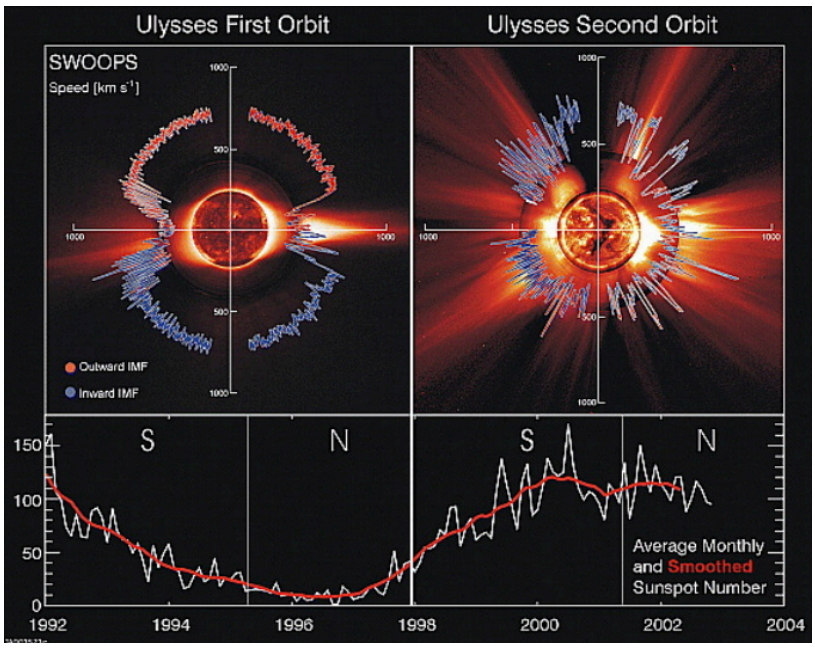

Figure 1.2: *Ulysses measurements of the solar wind speed as a function of heliolatitude for solar minimum (left) and for solar maximum (right). The curve is colored by the radial polarity of the magnetic field: red and blue indicate an outward and inward pointing magnetic field vectors, respectively. The bottom panel shows the sunspot number variation with time, which indicates the level of solar activity. The white vertical line marks the periods over which the wind speed data was gathered. The wind speed plots are overlaid on top of composite images of the solar disk and the corona typical of each period. Each composite is made of three images: the innermost is an EUV image taken by the Extreme-ultraviolet Imaging Telescope (EIT) on board SoHO, blended into the Mauna Loa K coronameter image, and the outermost taken by the LASCO-C2 white light coronagraph on board SoHO. The left composite was taken on 8/17/1996 and the right composite was taken on 12/07/2000.(Taken from: McComas et al., 2003).*

predicts are too low, suggesting there is an additional energy source missing from the description.

The Parker solution is purely hydrodynamic, and the magnetic field does not play a part in determining the wind flow properties. Since the solar atmosphere is made of an ionized quasi-neutral plasma, its evolution will be coupled to the magnetic field evolution. The simplest approximation for describing this system is the equations of ideal Magnetohydrodynamics (MHD). The MHD equations are obtained from coupling the Euler equations to the Maxwell equations for electromagnetic fields, resulting in a self-consistent description of both the plasma and the magnetic field. In ideal MHD the plasma is assumed to be fully ionized and to have infinite electric conductivity; in addition, the plasma is assumed to behave as a single fluid, i.e the negatively and positively charged particles are moving with the same velocity.

One of the interesting features stemming from ideal MHD, is the concept of frozen-in magnetic flux - the magnetic flux in a volume of plasma must be conserved as the plasma is convected. This means that as the wind is accelerated away from the Sun, it continuously carries away the magnetic field embedded within it. This explains the open field lines stretching from the corona into interplanetary space. As the Sun rotates, consecutive parcels of plasma that flow radially outward are released from different azimuthal angles. As a result, the field lines frozen into the flow will develop spiral shapes in the heliopshere. This is the well-known Parker Spiral, depicted schematically in Figure 1.3.

The solar corona and solar wind are both highly structured, with a bi-modal (fast and slow) wind, and open and closed field line regions in the corona. The first ideal MHD model of the solar corona that takes these structures into acount was presented by *Pneuman and Kopp* (1971). They assumed the corona is axi-symmetric, and that the intrinsic magnetic field can be described by an ideal dipole. This configuration is an idealization of a solar minimum corona. Their work demonstrated the effects the

outward flow has on the magnetic field, and vice versa. By advancing the solution iteratively, they were able to solve for the steady-state configuration of the magnetic field and the wind flow. Figure 1.4 shows the results, where dashed curves represent the initial dipole magnetic field, while solid curves represent the final steady state configuration. Several important effects can be learned from this result. First, magnetic field lines from higher latitudes are stretched outward by the flow and become "open", thus forming the coronal holes. The closed field lines around the equator remain closed, but their shape is stretched compared to the dipole field. The material along these lines is trapped by the magnetic loops and remains in static equilibrium. This closed field region can be identified as the streamer belt. Further, one can note that open field lines expand super-radially, with the largest expansion occurring for field lines coming from mid-latitude regions. The first open field lines just outside the streamer legs reach the magnetic equator at a heliocentric distance of $\sim 2.5 R_{\odot}$. This leads to the formation of a current layer at the equatorial plane, since the field lines lying on each side of the equator are coming different hemispheres and have opposite magnetic polarities. This layer is known as the Heliospheric Current Sheet, and is observed in the solar wind throughout the heliosphere.

1.4 The Coronal Heating Problem

The solar corona has provided us with one of the most fascinating mysteries of space research. Although it is much dimmer than the Sun in the visible light range, the solar corona is actually about 200 times hotter than the solar surface. This means that thermal energy transport from the solar surface into the corona due to either radiation, convection or conduction, cannot supply the required heating. In particular, thermal conduction will cause heat from the corona to flow back down toward the Sun, and not the other way around. Thus heating the corona requires non-thermal energy to be transported from the solar surface into the corona. The challenge of identifying

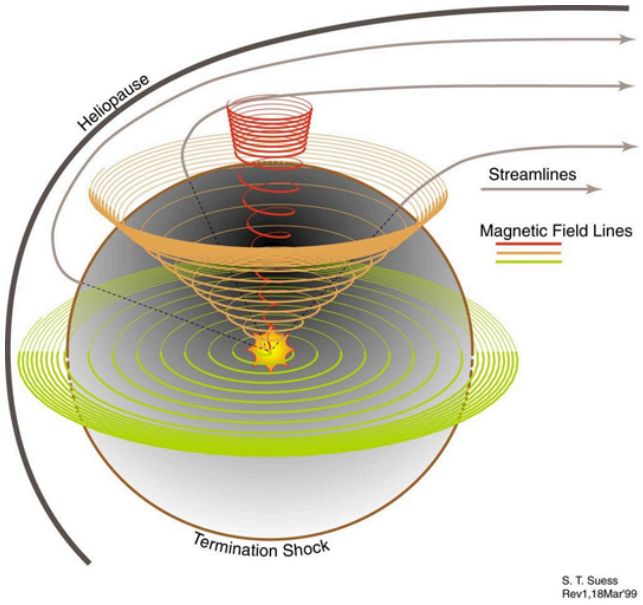

Figure 1.3: *The Parker Spiral shown for open field lines rooted in different latitudes on the solar surface.*

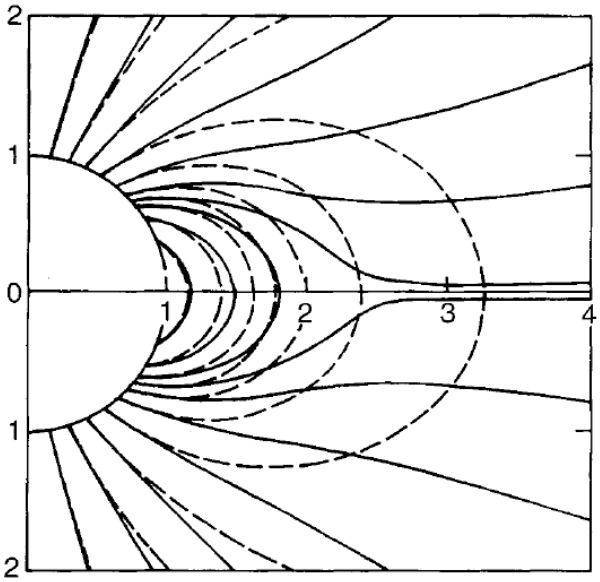

Figure 1.4: *MHD solution for an axi-symmetric corona with an ideal dipole magnetic field. The dashed lines denote an initial dipole magnetic field lines, while the solid curves show the magnetic field due to the interaction with a steady outward flow of the solar wind. (Taken from Pneuman and Kopp, 1971).*

the non-thermal heating mechanism is referred to as the "coronal heating problem", and has been the focus of numerous theoretical and observational studies over the last few decades. Despite this considerable effort, a conclusive theoretical model of coronal heating has not yet been achieved.

The thermal structure of the different layers of the solar atmosphere are depicted in Figure 1.5, which also lists their respective temperatures. The innermost layer is called the photosphere. This is the solar surface as viewed in the visible range. The solar radiation reaching Earth mainly originates in this layer, which has a temperature of ~ 5000 K. The layer just above it is the chromosphere, named after its red color (which can only be seen with the naked eye during total eclipses). The chromosphere contains dynamic features such as filaments and spicules. It is separated from the corona by a thin layer called the transition region. Across this region, the density sharply drops, and the temperature rises by two orders of magnitude. The density and temperature profiles from the photosphere and up to the corona are shown in Figure 1.6.

Necessary Ingredients of a Coronal Heating Theory

The main requirements of any coronal heating theory are that it must identify and describe:

1. the energy source for the heating.
2. the mechanism by which this energy is transported into the corona.
3. how this energy is converted into thermal energy.
4. quantitative predictions that can be directly compared to observations.

Several theories have been developed which satisfy these requirements, usually invoking either wave phenomena or magnetic reconnection as the driver of coronal heating (c.f. *Karachik and Pevtsov*, 2011). However a further complication of the coronal heating problem is that different parts of the corona have very different temperatures. The challenge of explaining the observed global distribution of coronal heating rates

is still not fully addressed.

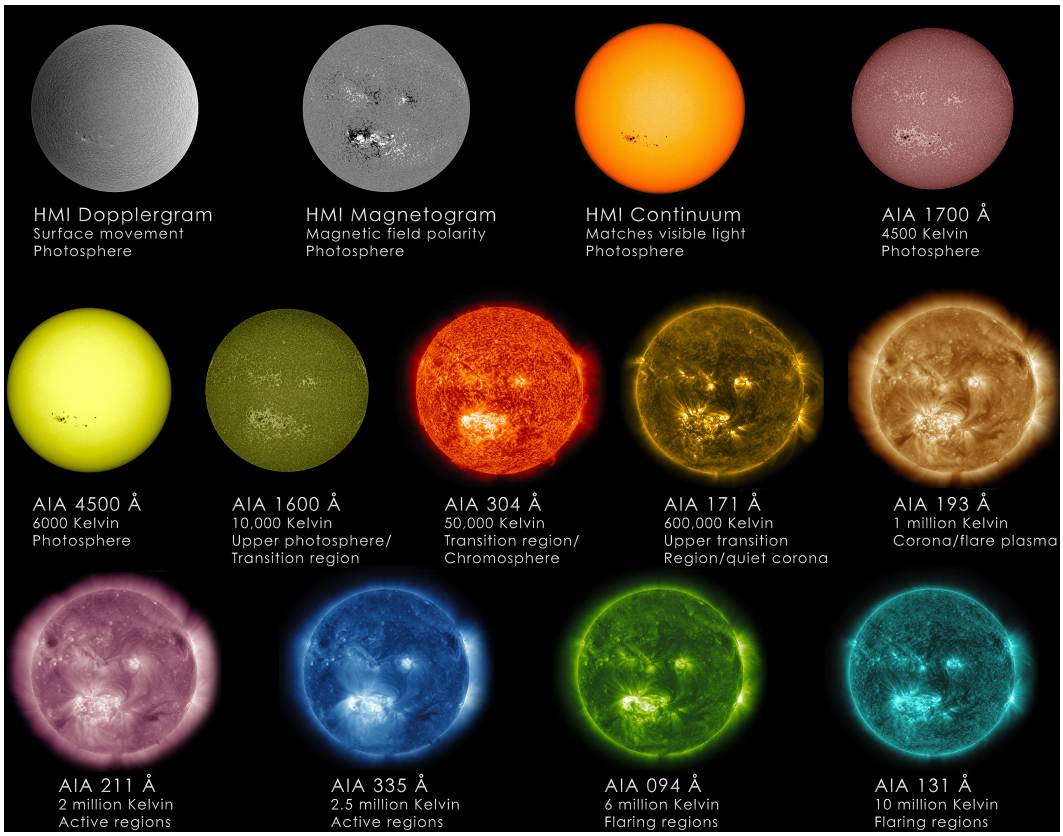

Figure 1.5: *The different layers of the solar atmosphere, visible at different wavelength due to their different temperatures, as observed by SDO. Image credit: NASA/SDO.*

1.5 The Basic Wind Acceleration Problem

The processes responsible for the formation and acceleration of the fast and slow solar wind are still not well understood. The first question to arise regards the magnitude of the wind speed in the heliosphere (as observed e.g. by Ulysses, see Figure 1.2). The thermal energy of coronal plasmas is much smaller than the energy required for the wind to overcome the gravitational pull of the Sun and reach the kinetic energy found in the other end of the wind trajectory, both for slow and fast wind flows (see, e.g., *Parker* (1958)). This suggest that there are additional sources

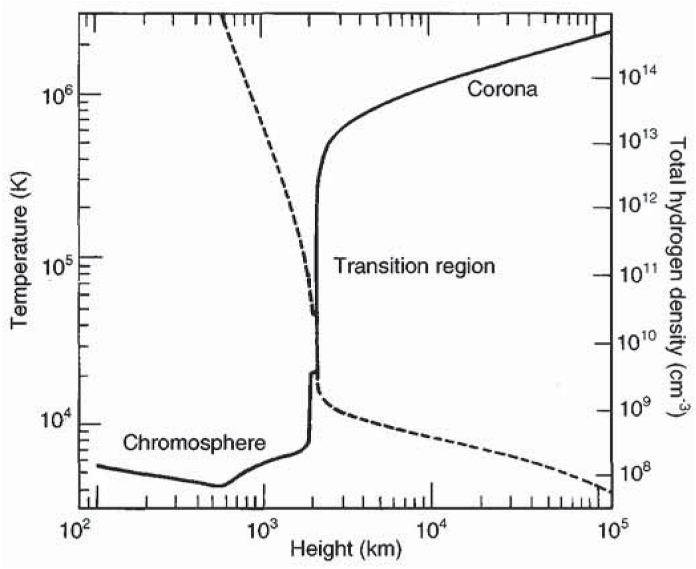

Figure 1.6: *Density and temperature as function of distance, from inside the photosphere up to the corona.*

of momentum and energy that need to be identified and taken into account.

Since the introduction of these first models, considerable effort has been made to improve our understanding of the processes responsible for solar wind acceleration. A robust theory of the solar wind formation must not only explain the wind speeds, but also their three-dimensional distribution, and how this distribution varies during the solar cycle. Since the wind is organized by the solar magnetic field, models that aim to describe the global structure of the solar atmosphere often rely on the observed photospheric magnetic field as an inner boundary condition. The efforts to develop such global models, and their successes and shortcomings are described below.

1.6 Global Models of the Solar Environment

Whatever the mechanisms responsible for coronal heating and wind acceleration are, it is clear that both problems are closely related, as the dynamical processes in the corona are feeding and driving the solar wind. Thus any first-principles model should attempt to self-consistently describe the entire system, and be able to reproduce

observed properties in the corona, as well as in the inner heliosphere, where the solar wind reaches its final speed and the fast and slow solar wind flows should be clearly identified.

Current state of the art models of the solar environment can be divided into two major types:

1. Idealized models which prescribe the magnetic field topology (usually that of an ideal polar coronal hole) - this allows a detailed description of the small-scale physical processes involved in coronal heating or wind acceleration.

2. Realistic global (3D) models which use the measured photospheric magnetic field as input. These usually use a more simplified approach, often invoking empirically-motivated heating functions.

Although models of the first type can be used to gain a deeper physical insight into the dynamics of ideal structures, global models allow us to test our theories against specific observations of realistic configurations of the system. For example, the shape, location and plasma properties of coronal holes and streamers change over time; with a global model driven by the measured photospheric magnetic field, we can compare the model predictions to remote and in-situ observations taken at the same time. Furthermore, the study of space weather prediction relies on the development of robust and validated models, which are capable of reproducing as large a range of observables as possible. These include the density and temperature distributions in the solar corona, as well as the flow properties of the solar wind. As these are organized by the magnetic field, such models should be able to treat any magnetic topology self-consistently. Models with idealized and prescribed magnetic fields are therefore less suited for space weather prediction efforts.

Early 3D models of the corona were based on a potential field extrapolation of the measured photospheric magnetic field (e.g. *Altschuler and Newkirk*, 1969). In this picture, the magnetic potential, Φ_M, is assumed to obey the Laplace Equation,

$\nabla^2\Phi_M = 0$, which holds only when no currents are present. These models were successful in predicting the location of major topological features of the corona, such as helmet streamers and coronal holes, but their assumptions were restrictive and known to be physically invalid in the corona, where a variety of current systems occur. In addition, potential field models are inherently not self-consistent, as they do not take into account the effect of the plasma on the magnetic field.

First attempts at a self-consistent 3D model were based on ideal magnetohydrodynamics (MHD). The first global numerical model that solved the MHD equations using the photospheric magnetic field as an inner boundary condition was presented in *Usmanov* (1993). This model included a self-consistent description based on first principles, and solved the MHD equations from the bottom of the corona up to 1AU. Although it was successful in qualitatively reproducing the observed wind properties at 1AU close to the ecliptic plane, it did not fully capture the bi-modal distribution of wind speeds, as speeds higher than 600km/s were not obtained.

Later models (*Linker et al.*, 1999; *Mikić et al.*, 1999; *Riley et al.*, 2006) have employed a modified energy equation, in which the polytropic index of the plasma was reduced, in order to reproduce the observed density and temperature profiles in the corona. This suggests that thermodynamic processes, probably related to coronal heating, are missing from the standard MHD equations. These models were able to reproduce the large-scale morphology of coronal holes and helmet streamers, and showed good agreement with full disk and coronagraph images. However, they extended only to $30R_\odot$ and therefore could not predict the wind speeds at 1AU.

The first global models that were able to reproduce the large scale bi-modal structure of wind speeds were presented by *Roussev et al.* (2003); *Cohen et al.* (2007). These models extend from the base of the corona up to 1-2AU, and the polytropic index was varied everywhere in the domain in order to account for the different heating and acceleration rates. In addition, the inner boundary conditions at the base

of the corona were determined empirically, so that the 1MK corona already exhibits a three-dimensional structure. Although they capture the overall solar wind structure, the modified polytropic index may produce unphysical results in the presence of CMEs and shocks.

The main limitation of the models discussed above is that the inner boundary is set at the bottom of the corona with temperatures in the 1MK range, thus avoiding the problem of the formation of the hot corona from the much cooler chromosphere. Other models have addressed coronal heating more directly by setting the lower boundary at the top of the chromosphere (*Lionello et al.*, 2009; *Downs et al.*, 2010), and employing a more sophisticated physical description of the system by including thermodynamic processes such as coronal heating, heat conduction and radiative cooling in the MHD equations. These models were the first to include the transition region in a global 3D model and produce simulated EUV images of the lower corona. By comparing the simulated EUV emission to observations one could test the temperature and density distributions predicted by the model. Although successful in reproducing key features in the observations, they were restricted by the use of geometric heating functions in order to describe coronal heating. Thus the heating mechanism was not described self-consistently, as it did not evolve with the plasma. Furthermore, different geometric heating functions had to be introduced in order to account for the different heating rates observed in coronal holes, streamer belts and active regions. It should also be noted that these efforts were focused on reproducing the observed emission from the lower corona, and did not attempt to predict the distribution of solar wind properties in the heliosphere.

The discussion above points to two main issues that need to be addressed in order to develop a self-consistent global model which is capable of addressing both coronal heating and wind acceleration. First, in order to gain a meaningful physical understanding of the processes dominating the corona and solar wind, the use of

geometric heating functions and empirical boundary conditions must be avoided as much as possible. Second, the model must explain both the formation of the 1MK corona from the cooler underlying chromosphere, as well as the bi-modal distribution of wind speeds. In order to achieve this, the computational domain must extend from the top of the chromosphere out to the solar wind at 1AU. This will enable us to test whether the model can describe and reproduce observations of both remote observations of the lower corona, and in-situ observations in the solar wind. The aim of the work presented in this thesis is to develop such a global model, and compare its predictions to as wide a range of observations as possible. For this purpose, we need to not only explain the global distribution of densities, temperatures and speeds of the plasma, but also address the well-known variations in chemical composition observed in the corona and the solar wind. These are described in the next Section.

1.7 Distinct Properties of the Fast and Slow Wind

The solar wind has been measured and analyzed extensively over the last few decades, and considerable amounts of data have been gathered. This has led to the identification of several properties that are distinctly different when measured either in the fast or slow wind. The main differences are summarized in Table 1.1, and described below.

The first three rows of Table 1.1 show typical values of wind speed, proton density and temperature measured by Ulysses (*Ebert et al.*, 2009). The flow properties of the fast wind are relatively steady (e.g. *McComas et al.*, 2008), while those measured in the slow wind are highly variable (*Schwenn and Marsch*, 1990; *Gosling*, 1997; *McComas et al.*, 2000). The two wind types differ in their heavy element and ion composition. The abundances of elements heavier than helium in the solar atmosphere are low. The photospheric abundances of the most abundant elements are listed in the second column of Table 1.2, based on *Feldman et al.* (1992). For each of the

heavy elements, the photospheric abundance is less than 0.001 relative to the hydrogen abundance. Although the abundances obtained using different observations and diagnostic techniques may vary (see, for example, *Asplund et al.*, 2009; *Caffau et al.*, 2011), these variations amount to less than 4% of the values reported in Table 1.2. In the corona, the abundances of certain elements are higher than the photospheric values, but these are usually enhanced by only a factor of 3-4 (as discussed in more detail in Section 1.7.1). Thus, heavy element abundances are very low compared to the main components of the plasma, and therefore their contribution to the overall dynamics of the solar atmosphere is negligible.

The importance of the heavy elements in the solar atmosphere lies in their response to the state of the plasma in which they are embedded, making them important tracers of the evolution of the corona and solar wind. Indeed, both the elemental abundances and the ionization states of the heavy ions vary between different coronal structures, such as coronal holes, closed-field structures, and active regions, as discussed in Sections 1.7.1 and 1.7.2. These differences are reflected in the fast and slow solar wind, as summarized in Table 1.1. The fast wind exhibits abundances characteristic of the photosphere and coronal holes (*von Steiger et al.*, 2001; *Zurbuchen et al.*, 1999, 2002), while the slow wind exhibits abundances similar to that of the closed-field corona (*Feldman and Widing*, 2003).

In addition, the charge state composition of the fast and slow wind are markedly different. The ionization status of different ions measured in-situ in the solar wind can supply us with information about the electron temperature and density in the region at which these ions were formed. This process is described at length in Section 1.7.2. Here we briefly mention that the charge states measured in the fast wind are compatible with a coronal electron temperature of $\sim$1.0MK, similar to that occurring in coronal holes (e.g. *Gloeckler et al.*, 2003; *Zurbuchen*, 2007), while the charge states in the slow wind are compatible with coronal electron temperatures of $\sim$1.5MK, sim-

Value at 1AU	Slow Wind	Fast Wind
Speed [km/s] [a]	392 (variable)	745 (steady)
Proton Density [cm^{-3}] [a]	5.55	2.12
Proton Temperature [10^5 K] [a]	0.80	2.46
Charge States [b]	Consistent with coronal $T_e \approx 1 \times 10^6 K$	Consistent with coronal $T_e \approx 1.5 \times 10^6 K$
Elemental Abundances	Coronal (FIP Bias)	Photospheric

a as reported in *Ebert et al.* (2009) based on Ulysses measurements.
b based on estimations by *Gloeckler et al.* (2003), who used the O^{7+}/O^{6+} ratios measured by Ulysses to calculate the coronal electron temperature using the equilibrium model of *Ko et al.* (1997).

Table 1.1: *Summary of fast and slow solar wind properties. Details are in the text.*

ilar to the temperature of closed-field regions (e.g. *Gloeckler et al.*, 2003; *Zurbuchen et al.*, 2002).

Finally, we note that similar to the flow properties, the chemical composition of the fast wind is relatively steady (*Geiss et al.*, 1995; *von Steiger et al.*, 1995; *Zurbuchen*, 2007), while that of the slow wind is highly variable (*Zurbuchen and von Steiger*, 2006; *Zurbuchen*, 2007).

1.7.1 Elemental Abundances

Abundances in the quiet Sun and in active regions are modified compared to their abundances in the photosphere depending on their First Ionization Potential (FIP) The FIP of the most abundant elements in the solar atmosphere are listed in the third column of Table 1.2. *Meyer* (1985) reviewed the abundances data available at the time, which included both in-situ observations in the solar wind as well as spectroscopic observations in the solar corona, and demonstrated that all abundances showed the same pattern: elements with FIP larger than 11eV ("high-FIP") were about 4 times more abundant in the corona and wind compared to photospheric abundances, while those with FIP lower than 9eV ("low-FIP") maintained their photospheric abundances. This effect is referred to as the FIP bias.

Element	$\log_{10}$ Abundances	FIP [eV]
1 H	12.00	13.6
2 He	10.99	24.6
6 C	8.604	11.3
7 N	8.0O5	14.5
8 0	8.93	13.6
10 Ne	8.11	21.6
11 Na	6.33	5.1
12 Mg	7.58	7.6
13 Al	6.47	6.0
14 Si	7.55	8.2
16 S	7.21	10.4
18 Ar	6.65	15.8
20 Ca	6.36	6.1
26 Fe	7.51	7.9
28 Ni	6.25	7.6

Table 1.2: *Summary of the most abundant elements in the photosphere, and their First Ionization Potential. The abundances are shown on a log_{10} scale, relative to a hydrogen abundance set arbitrarily at 12 (adapted from Feldman et al. (1992)).*

Feldman and Widing (2003) showed that the observed abundances above coronal holes are close to photospheric abundances, while those found above closed field regions exhibit a FIP bias of about 4 (see Figure 1.7). The FIP bias increases the longer the plasma is confined in a closed magnetic structure. The largest FIP bias ($\sim$15) is observed in old active regions (*Feldman and Widing*, 2003; *Phillips et al.*, 2008).

The dependence of elemental abundances on the ionization potential has led *Geiss* (1982) to suggest that some electric or magnetic mechanism is responsible for separating the ions from the neutrals at the base of the atmosphere . If such a mechanism exist, then the high-FIP elements, which are not yet ionized in the cooler photosphere, will not be affected by it, leading to a relative enhancement in low-FIP elements reaching the corona. To date, there is still no clear and conclusive picture that explains the observed FIP bias in the corona, but several promising theories are being developed (see *Laming* (2009, 2012) for a review of this active research area). As mentioned above, the elemental abundances found in the slow wind exhibit a FIP bias similar

to that of the closed-field corona, while those found in the fast wind are similar to that of the photosphere. Thus the elemental abundances measured in the solar wind, together with their high variability in the slow wind, impose an important constraint of theories aiming to explain the formation and acceleration of the fast and slow solar wind, as we will discuss in Section 1.7.3.

1.7.2 Heavy Ion Charge States

1.7.2.1 Observed Properties

Heavy ion charge state distributions measured in-situ at 1AU and beyond are known to be significantly different when measured in either the fast or slow solar wind. The most commonly used charge state indicators of wind type are the average charge state of iron ($< Q >_{Fe}$) and the charge state ratios for carbon C^{6+}/C^{5+} and oxygen O^{7+}/O^{6+} (where X^{m+} stands for the element X that has lost m of its electrons). Figure 1.8 shows the variation of these quantities as measured by the Solar Wind Ion Composition Spectrometer (SWICS, *Gloeckler et al.*, 1992) on board Ulysses from 1990 to 2010. This period covers two solar minima (centered around the years 1996 and 2007), separated by a solar maximum, where solar activity peaked around 2001. The figure shows, from top to bottom: the solar wind speed, the average charge state of iron, the charge state ratios C^{6+}/C^{5+} and oxygen O^{7+}/O^{6+} (overlaid), and the bottom panel shows the heliocentric distance (black curve) and latitude (red curve) of the spacecraft. The data reveal two important properties of the charge state indicators. First, both the C^{6+}/C^{5+} and oxygen O^{7+}/O^{6+} ratios are about 1-2 orders of magnitude higher when measured in the slow wind. Differences in the mean value of $< Q >_{Fe}$ between the slow and fast wind are more subtle. The mean value of $< Q >_{Fe}$ in the fast wind is very close to that in the slow wind, although the range of observed values is wider in the slow wind (this behavior is also reported in *Lepri et al.*, 2001). Second, all three charge state indicators exhibit high levels of

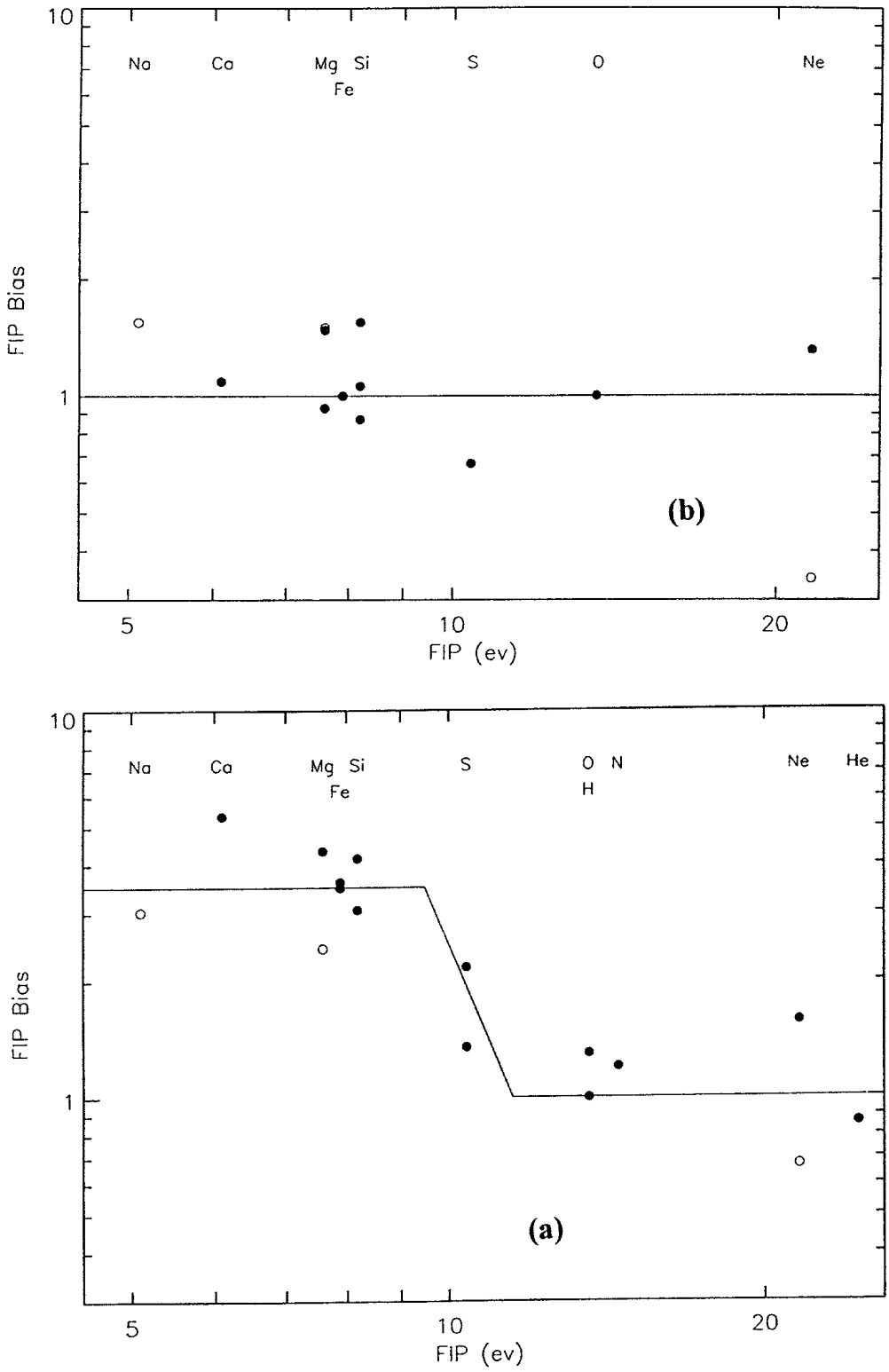

Figure 1.7: *Elemental abundances vs. First Ionization Potential above polar coronal holes (top) and above equitorial quiet regions (bottom). Taken from Feldman and Widing (2003).*

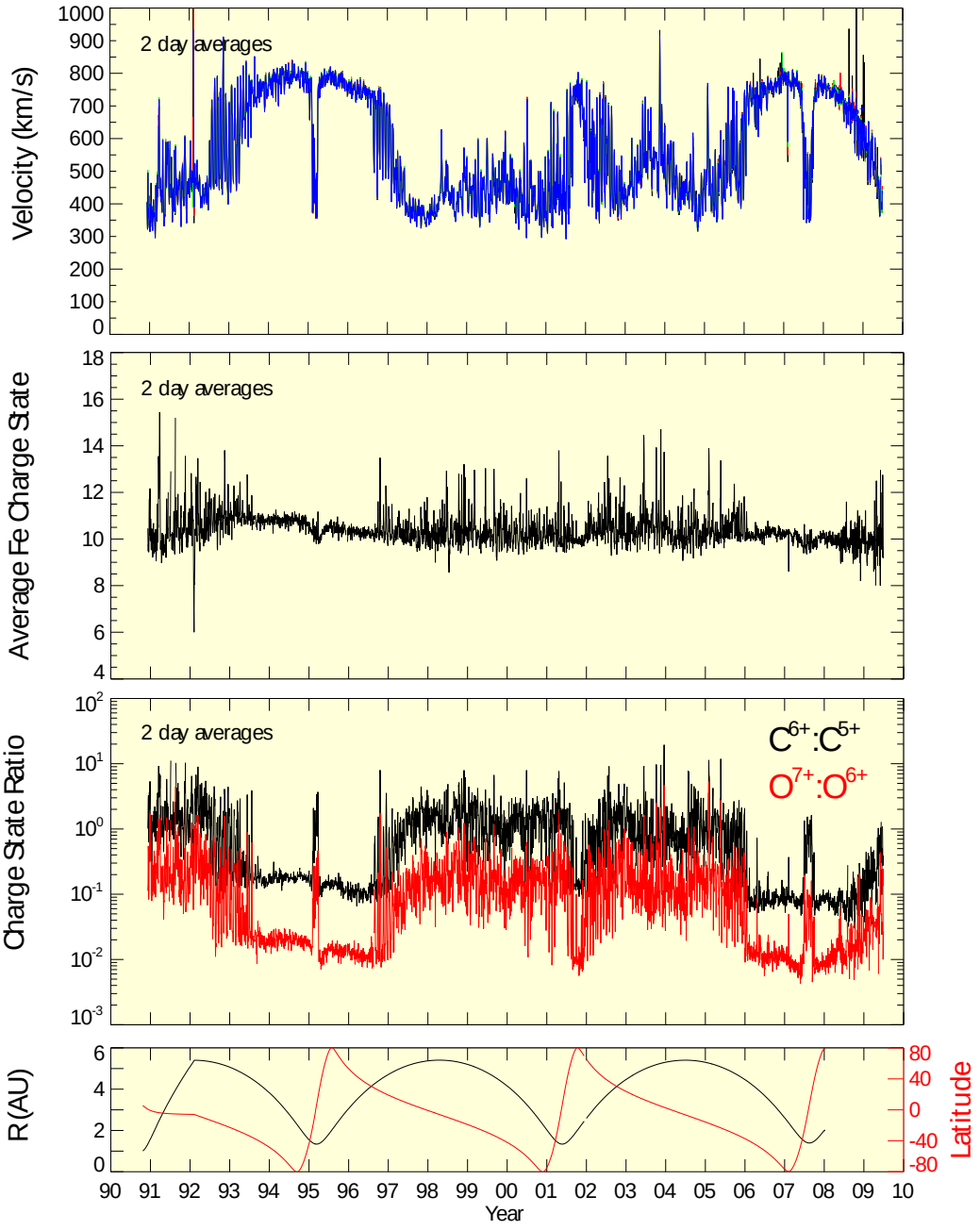

Figure 1.8: *Changes in charge state composition in the fast and slow solar wind. From top to bottom: the solar wind speed, the average charge state of iron, the charge state ratios C^{6+}/C^{5+} and oxygen O^{7+}/O^{6+} (overlaid). The bottom panel shows the heliocentric distance (black curve) and latitude (red curve) of the spacecraft. Data courtesy of the ESA/Ulysses Data Service.*

variability in the slow wind, and are steady in the fast wind. This behavior is easily seen during the solar minima, but the pattern is less clear during solar maximum, when the wind speed is not organized into a clear bi-modal distribution over latitude as it does during solar minimum.

1.7.2.2 Charge State Evolution

In contrast to elemental abundances, the charge state evolution along a flow line can be fully described as long as the flow properties (electron density, temperature, the ion speed) are known. As the ions propagate away from the Sun, they undergo ionization and recombination due to collisions with electrons. This leads to an evolution of the charge state distribution, i.e. the fraction of the ions of an element X at charge state m changes with time depending on the local plasma conditions. A change in electron density will effectively change the rate at which collisions occur, while the electron temperature will affect the ionization and recombination rate coefficients (which can be determined from atomic physics). Finally, the speed at which the ions travel will determine the length of time they spend at a given plasma volume with given electron density and temperature.

At a certain distance from the Sun the plasma becomes colisionless due to the decrease in density. At this point the charge state evolution is said to "freeze-in", which occurs at distances between 1.5 to 4 $R_{\odot}$, depending on the element (*Hundhausen et al.*, 1968). The charge state distribution measured in the solar wind therefore supplies information about the conditions in the wind source regions in the corona. As such, heavy ion charge states have played an important role in testing the various theories concerning the mechanisms responsible for the acceleration of the fast and slow wind, and in determining the source regions of the slow solar wind.

1.7.3 The Source Region of the Slow Wind

While it is generally accepted that the fast wind originates from coronal holes, the markedly different heavy element and ion composition of the slow and fast wind has led to an on-going and vigorous debate regarding the source region of the slow wind (*Kohl et al.*, 2006; *Suess et al.*, 2009; *Abbo et al.*, 2010; *Antiochos et al.*, 2011; *Antonucci et al.*, 2012; *Antiochos et al.*, 2012).

Several models explain the distribution of wind speeds by relating the wind acceleration rate to the expansion of flux tubes (*Suess*, 1979; *Kovalenko*, 1981; *Withbroe*, 1988; *Wang and Sheeley*, 1990; *Cranmer and van Ballegooijen*, 2005; *Cranmer et al.*, 2007). In this picture, the slow wind originates from the boundary region between coronal holes and closed field lines. As the flux tubes rooted in these regions undergo a larger expansion compared to deeper inside the coronal holes, they lead to smaller acceleration rates and thus to a slower wind. However, these models do not directly address the observed differences in heavy element and ion composition observed in the fast and slow wind (c.f. *Antiochos et al.*, 2012, and references therein.).

The similarities between the heavy element abundances in the closed-field corona and the slow wind, as well as the higher freeze-in temperatures of the slow wind charge states (see Section 1.7), has led several authors to hypothesize that the slow wind material originates in the hotter and denser closed field region in the corona. Such theoretical models invoke some kind of dynamic release of this material due to reconnection between open and closed field lines, although the details of the release process and the location where it occurs vary (e.g. the Interchange Reconnection Model, (*Fisk et al.*, 1998; *Fisk*, 2003; *Fisk and Zhao*, 2009); the Streamer-Top Model, (*Wang et al.*, 2000); the S-web Model, (*Antiochos et al.*, 2007, 2011, 2012)). The idea of dynamic release is also related to the observed variability in the slow wind, in which not only the wind speed, but also the composition can vary rapidly (*Zurbuchen and von Steiger*, 2006; *Zurbuchen*, 2007), compared to the more steady nature of the

fast wind.

1.8 Coronal Heating and Wind Acceleration by Alfvén Waves

1.8.1 Motivation: Why Alfvén Waves?

Existing theoretical models of coronal heating can be broadly classified into AC and DC models (named after AC and DC electric currents). In AC models, the heating and acceleration mechanism is due to some type of continuous wave field interacting with the plasma. DC models invoke a series of reconnection events or nano-flares that impulsively release energy into the plasma. In both cases, the energy source can be linked back to the mechanical energy of turbulent motions of the field lines in the photosphere and chromosphere (although the connection is not always explicitly described). It is important to note that AC and DC models do not fundamentally contradict each other. The processes they invoke as the source of heating can co-exist, although their relative contribution to coronal heating has not been conclusively determined.

DC models are based on the observation that turbulent convective motions cause flux tubes to twist and bend around each other. When a critical tilt angle between adjacent flux tubes is reached, magnetic reconnection will release thermal energy into the system (e.g. *Yeates et al.*, 2014). From the point of view of global modeling, this approach presents several important difficulties. First, the magnetic energy of the braided field lines has to build-up until the structure becomes unstable. As pointed out in *Klimchuk* (2006), if this happens too early or too late, the amount of energy that can be released will be too small or too large, considerably affecting the resulting heating rate. Second, magnetic reconnection releases the energy impulsively into thin flux tubes called strands which make up the larger structure (e.g. a magnetic loop), with different strands being heated at different times even for the same reconnection

event. For a global model of the entire 3D corona, resolving this evolution in both space and time presents a significant computational challenge. Furthermore, information about the convective motions of individual structures is not known. Thus the basic picture presented here has to be adapted in order to describe the energy build-up and release process in a more approximate way, while still capturing the physics.

AC models are based on the fact that the turbulent convective motions at the solar surface will generate waves that will propagate upward. Their energy can then heat the corona through wave dissipation. A variety of wave modes exist in the photosphere and chromosphere, for example: acoustic waves, Alfvén waves, and fast and slow magnetosonic plane waves. However, the sharp density and temperature gradient in the transition region acts as a filter to most wave modes, limiting the energy flux that makes it through to the corona. Alfvén waves, including the so-called Alfvén-like torsional and kink tube waves, are the most likely to pass through the transition region with sufficient flux.

The advantage of incorporating Alfvén waves in a model of the solar atmosphere is that they can also accelerate the plasma and thus can address the problem of solar wind acceleration. Turbulent Alfvén waves emanating from the chromosphere were first suggested as a possible mechanism to both accelerate the solar wind and heat the plasma in the solar corona by *Alazraki and Couturier* (1971) and *Belcher* (1971). In this picture, the waves exchange energy and momentum with the fluid, providing both the heating and the acceleration necessary to sustain both the corona and the solar wind. This idea is an attractive choice for global modeling in particular. Since the waves follow magnetic field lines, the flux of waves reaching different parts of the corona will be different. Thus, in a 3D configuration of the magnetic field, with open and closed field lines, Alfvén waves will automatically produce different heating and acceleration rates in different regions.

1.8.2 Basic Properties of Alfvén Waves

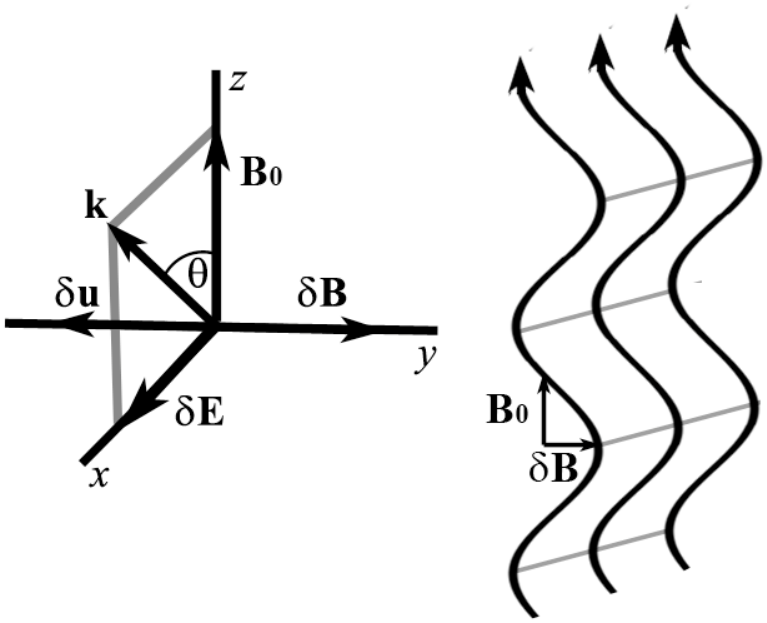

Figure 1.9: *Schematic view of Alfén waves. Left: direction of the perturbations carried by the Alfvén wave. The background magnetic field ($\mathbf{B}_0$) is in the z directions. The perturbation in the magnetic field and velocity are perpendicular to $\mathbf{B}_0$, and have opposite directions along the y direction. An electric field perturbation is in the x direction. Right: illustration of the total magnetic field due to the propagating wave.*

In 1942, Hannes Alfvén hypothesized the existence of "electrodynamic-hydrodynamic waves" (now simply called MHD waves). Alfvén realized that any motion of a conducting fluid in the presence of a magnetic field will result in the magnetic field acting back on the fluid, through the Lorentz force (*Alfvén*, 1942). In the context of MHD, this interaction is referred to as magnetic tension, by which a magnetized fluid will resist any bending of the magnetic field lines. If a fluid element is displaced perpendicular to the background magnetic field, $\mathbf{B}_0$, it will drag the magnetic field line with it, creating a magnetic field component $\delta\mathbf{B}$ in the perpendicular direction, causing a bending of the field line. Magnetic tension will act to straighten the magnetic field lines, and move the fluid element in the opposite direction with velocity $\delta\mathbf{u}$. Thus

magnetic tension acts as a restoring force, and will cause the disturbance to propagate along the magnetic field line, much like a wave on a string. This behavior is illustrated in Figure 1.9. The waves will propagate at the Alfvén speed, V_A, given by:

$$V_A = \frac{B_0}{\sqrt{\mu_0 \rho}} \tag{1.1}$$

where ρ is the mass density of the fluid and μ_0 is the magnetic permeability of free space. The perturbations $\delta\mathbf{B}$ and $\delta\mathbf{u}$ describe the wave amplitudes, and are related by:

$$\delta\mathbf{B} = \pm\frac{B_0\delta\mathbf{u}}{V_A}. \tag{1.2}$$

where the plus or minus sign depends on the wave polarity, i.e. whether the wave propagates parallel or anti-parallel to the magnetic field. It is easy to show that this relation is equivalent to equipartition of energy, i.e. the magnetic energy and kinetic energy of the wave are equal at any given moment. The total wave energy density, which is just the sum of the magnetic energy density and kinetic energy density is therefore:

$$w = \frac{1}{2\mu_0}\langle\delta\mathbf{B}^2\rangle + \frac{1}{2}\rho\langle\delta\mathbf{u}^2\rangle = \frac{1}{\mu_0}\langle\delta\mathbf{B}^2\rangle = \rho\langle\delta\mathbf{u}^2\rangle \tag{1.3}$$

where $< \cdot >$ denotes an average over the wave period.

1.8.3 Deriving the Wave Energy Flux

The energy flux of Alfvén waves emanating from the chromosphere determines the energy available for coronal heating and wind acceleration by these waves. Since Alfvén waves carry an electromagnetic field, the energy flux of is given by the Poynting vector $\mathbf{S}$:

$$\mathbf{S} = \frac{1}{\mu_0}\mathbf{E} \times \mathbf{B}, \tag{1.4}$$

where $\mathbf{E}$ and $\mathbf{B}$ are the total electric field and magnetic field vectors, respectively. For a frozen-in plasma with bulk velocity $\mathbf{u}$, we have $\mathbf{E} = -\mathbf{u} \times \mathbf{B}$ and $\mathbf{S}$ becomes:

$$\mathbf{S} = -\frac{1}{\mu_0}\mathbf{B} \times (\mathbf{B} \times \mathbf{u}). \tag{1.5}$$

We can express the magnetic field and velocity vectors as a sum of a background state and an oscillating part: $\mathbf{B} = \mathbf{B}_0 + \delta\mathbf{B}$ and $\mathbf{u} = \mathbf{u}_0 + \delta\mathbf{u}$. The oscillatory component means that in order to get a physically meaningful energy flux we must average the expression above over a full period. Thus we get:

$$\mathbf{S} = -\frac{1}{\mu_0}\langle(\mathbf{B}_0 + \delta\mathbf{B}) \times [(\mathbf{B}_0 + \delta\mathbf{B}) \times (\mathbf{u}_0 + \delta\mathbf{u})]\rangle. \tag{1.6}$$

This expression can be simplified by expanding it and considering the individual terms. Note that by definition $\langle\delta\mathbf{B}\rangle = \langle\delta\mathbf{u}\rangle = 0$ and $\langle\mathbf{B}_0\rangle = \mathbf{B}_0$, $\langle\mathbf{u}_0\rangle = \mathbf{u}_0$. As a result, all the terms that are first-order in the perturbation will drop out. Since $\delta\mathbf{B}||\delta\mathbf{u}$, the term involving $\delta\mathbf{B} \times \delta\mathbf{u}$ will drop out as well. We recall that for Alfvén waves we have:

$$\delta\mathbf{B}, \delta\mathbf{u} \perp \mathbf{B}_0, \tag{1.7}$$

and:

$$\delta\mathbf{B} = \pm\frac{B_0\delta\mathbf{u}}{V_A}. \tag{1.8}$$

Using the last relation we can eliminate $\delta\mathbf{u}$ and after some manipulations we get:

$$\mathbf{S} = -\frac{1}{\mu_0}[\mathbf{B_0} \times (\mathbf{B}_0 \times \mathbf{u}_0)] + \frac{1}{\mu_0}(\mathbf{u}_0 \pm V_A\mathbf{b})\langle\delta\mathbf{B}^2\rangle, \tag{1.9}$$

where $\mathbf{b}$ is a unit vector in the magnetic field direction. The first term on the RHS is the flux of electromagnetic energy solely due to the convection of the background magnetic field with the plasma flow due to the frozen-in regime, while the second term

is a purely Alfvén waves energy flux. The sign in front of the Alfvén speed depends on whether we consider waves propagating parallel or anti-parallel to the magnetic field direction **b**. We can relate the Poynting flux to the wave energy density w, defined in Eq. 1.3, to finally get:

$$\mathbf{S}_w = (\mathbf{u}_0 \pm V_A \mathbf{b}) w \tag{1.10}$$

where $\mathbf{S}_w$ denotes the Poynting vector arising from the waves alone. This result can be interpreted as an energy density w propagating at speed $\mathbf{u}_0 \pm V_A \mathbf{b}$; i.e. the energy is carried at a speed which is the sum of the wave phase speed in the rest frame, and the bulk motion of the magnetized fluid. In the chromosphere and very low in the corona, the wind speed along field lines is still very low, and the contribution from the bulk velocity is often neglected.

1.8.4 Estimating the Energy Flux of Alfvén Waves in the Solar Atmosphere

The source of Alfvén waves in the solar atmosphere is assumed to be the turbulent fluid motions in the photosphere and the constant reconfiguration of the magnetic field in the chromosphere. Regardless of the exact formation mechanism, these rapid and small scale events create perturbations at the base of the magnetic flux tubes, which are then propagated outward in the form of Alfvén waves. This scenario is depicted schematically in Figure 1.10. The black arrows show the main magnetic field (in the z direction), while the red curves show the magnetic field due to the wave. The perturbations due to the wave (which are exaggerated in size for clarity) are in the y direction, perpendicular to the main field. The waves propagate along the main magnetic field in the z direction.

In a ground breaking paper, *De Pontieu et al.* (2007) reported on observations of Alfvén waves in the chromosphere and estimated their energy flux. This was made possible by analyzing the motions of spicules, which are short-lived finger-like jets of

chromospheric material extending into the corona. Figure 1.11 shows an image of chromospheric spicules (left panel) and a schematic illustration (right). The effect of Alfvén waves on spicules and other chromospheric plasmas is illustrated in Figure 1.10. The thick orange curve at the bottom of the field line at the front of the figure represents the density enhancement due to the spicule. The spicule material (as well as other chromospheric plasma) will move in a direction transverse to the magnetic field due to the Alfvén wave propagating through it. *De Pontieu et al.* (2007) analyzed Hinode observations of spicule motions and estimated the frequencies and the amplitudes of the waves traveling through them. This important work was the first to quantify the Poynting flux of Alfvén waves emitted by the chromosphere, which can then be carried into the transition region and the corona. With wave amplitudes ranging between $\delta\mathbf{u} = 12 - 15$ km/s, the Poynting flux can supply the energy required for coronal heating and wind acceleration.

Once they reach the corona, Alfvén waves propagate along the magnetic field lines with velocity $\mathbf{V}_A = \pm V_A \mathbf{b}$. In the complex magnetic topology of the corona, some of the waves will propagate away into the solar wind along open magnetic field lines while those emitted at the foot points of closed field lines, or loops, are confined to the corona. This situation is depicted schematically in the top panel of Figure 1.12. The bottom panel shows an image of a collection of coronal loops, taken by NASA's Transition Region And Coronal Explorer (TRACE). Two magnetic flux concentrations (appearing as brownish circles on the solar surface) have opposite magnetic polarity; the loop is formed by magnetic field lines (thick blue curves) connecting these two regions. The thin wavy blue lines represent the magnetic field due to Alfén waves propagating along both open and closed field lines (in a direction indicated by blue arrows). Along open magnetic field lines both the plasma and the waves can escape upward into the solar wind. On coronal loops, waves from the two foot points will propagate in opposite directions along the loop axis (only a single

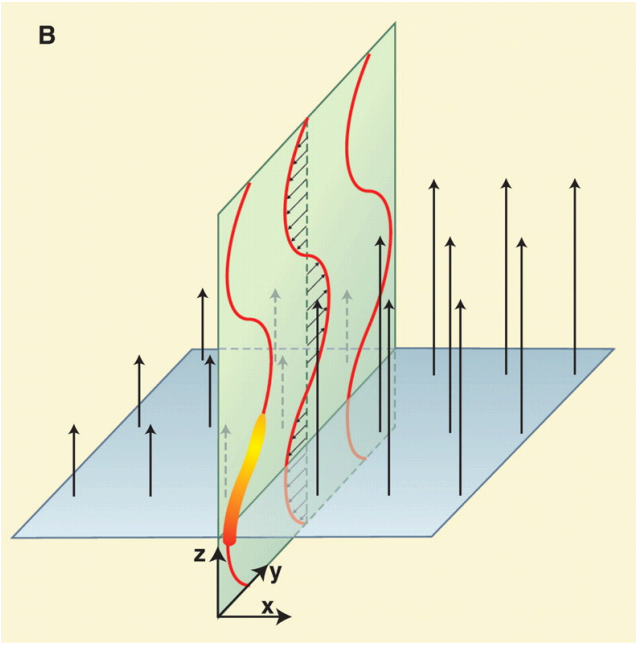

Figure 1.10: *Alfvénic perturbations along magnetic field lines in the chromosphere. The background magnetic field is depicted by the black vertical arrows (z direction). The perturbations associated with the wave are in the y direction, i.e. perpendicular to the background field. The waves propagate along the field lines (z direction). The orange coloring at the bottom represents a chromospheric feature with enhanced density (such as a spicule or a prominence) that follows the field lines as the wave propagates through it. (Taken from Erdélyi and Fedun, 2007).*

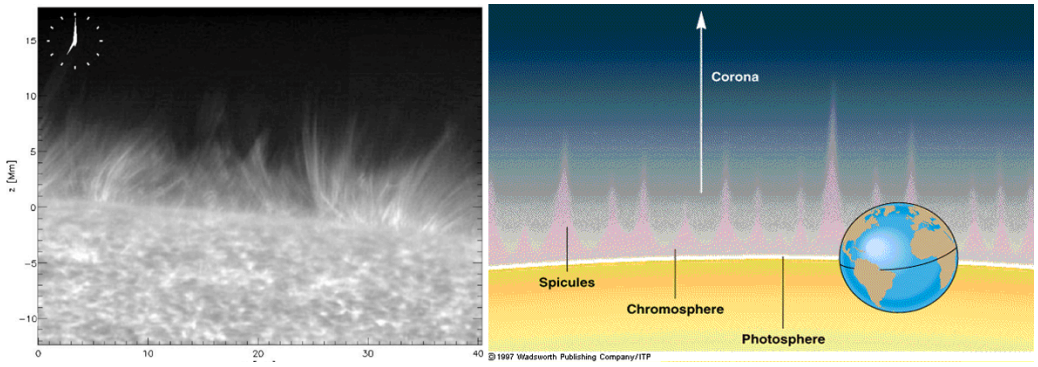

Figure 1.11: *Left: Ca II image of spicules obtained with the SOT instrument ob board Hinode (taken from Judge and Carlsson (2010). Right: artist conception of spicules, seen as protrusion of the chromosphere into the corona. The Earth's size is shown for comparison (taken from: www.ualberta.ca/ ∼ pogosyan/teaching/ASTRO*$_1$*22/lect9/lecture9.html).*

polarity is shown in the Figure). The shading around the loop represent the density of the plasma trapped along the loop. The oscillating transverse displacements of the loop material is represented by the red lines and arrows.

The transverse displacement of the loop material allowed *McIntosh et al.* (2011) to identify Alfvén waves in coronal loop and estimate their amplitude as $\delta\mathbf{u} \approx 20$ km/s, which leads to a Poynting flux sufficient to drive coronal heating and wind acceleration.

1.8.5 Heating and Acceleration by Alfvén Waves

1.8.5.1 Heating

The concept of wave-driven coronal heating satisfies the requirements for a coronal heating theory as outlined in Section 1.4:

1. **Energy Source:** Alfvén waves are created in the photosphere and chromosphere due to the constant small-scale reconfiguration of the magnetic field; as seen in Section 1.8.4, the observed wave Poynting flux in the chromosphere and lower corona is sufficient to supply the required energy.

2. **Energy Transport:** Alfvén waves can transport energy from the chromosphere into the solar corona and wind, i.e. in the direction opposite to that of heat conduction. The waves will undergo damping in the partially ionized chromosphere due to the finite resistivity (*De Pontieu et al.*, 2001), while the steep density gradient in the transition region will cause a significant amount of the wave energy to be reflected. However, radiative-MHD simulations by *De Pontieu et al.* (2007) have shown that between 3% to 15% of the chromospheric wave energy will be transmitted into the corona, with a resulting energy flux that is sufficient to sustain the corona and solar wind. Indeed, Alfvénic perturbations are ubiquitous in the solar environment, and have been observed in the photosphere, chromosphere, in coronal structures, and

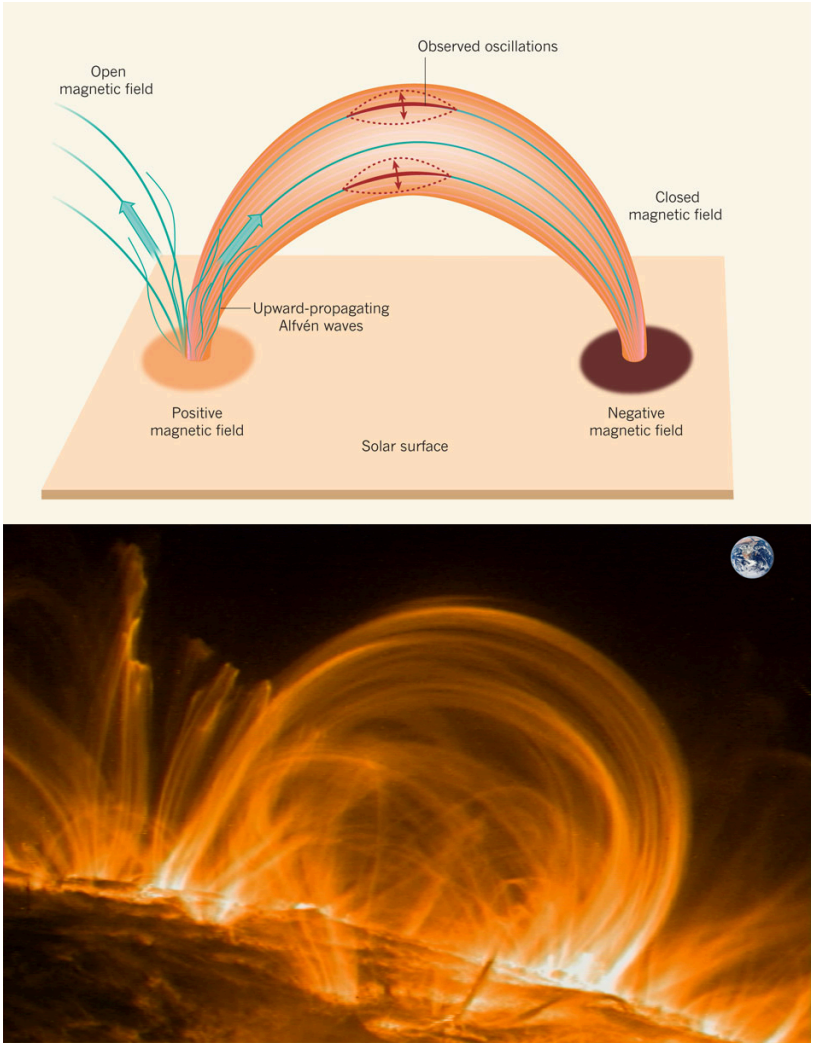

Figure 1.12: *Top: Alfvén wave propagation in the corona along open field lines and a coronal loop. The solid lines blue curves represent magnetic field lines. The wavy blue lines show the magnetic field line due to an upward-propagating Alfvén waves. The solid arrows indicate direction of propagation. The shaded orange region represents the plasma density along the loop. Red lines and arrows illustrate the transverse displacements of the plasma due to the waves (taken from Cargill and de Moortel, 2011). Bottom: An image of coronal loops in an active region, oriented in different directions. The Earth is shown for size comparison (image courtesy of NASA/TRACE).*

in the solar wind at Earth's orbit (c.f. *Banerjee et al.*, 2011; *McIntosh et al.*, 2011).

3. **Energy Conversion:** In order to account for coronal heating, these waves must undergo some sort of dissipation, which will convert the wave energy into thermal energy of the plasma. Several theoretical models of Alfvén wave dissipation have been suggested. These include phase mixing (*Heyvaerts and Priest*, 1983), turbulent cascade (*Matthaeus et al.*, 1999), and resonant absorption (*Goossens et al.*, 2011).

4. **Observable Predictions:** EUV spectroscopy of the lower corona can be used to:

- test the heating rate by comparing predicted and observed emission rates (which depend on the electron density and temperature).
- find evidence of Alfvénic velocity perturbations and estimate their amplitude using the Doppler-broadening of emission lines.

From all of the above, it is the energy conversion mechanism that is still not well defined. Although several wave dissipation mechanisms stand on sound theoretical arguments, it is not clear whether and by how much they contribute to the actual heating processes in the corona. Direct and conclusive observational evidence to support these theories is hard to obtain, due in part to the inherent uncertainty in remote sensing measurements. In this work, we aim to explore whether the turbulent cascade is a viable candidate to explain coronal heating, and therefore we will discuss this mechanism in more detail in Section 1.9.

1.8.5.2 Acceleration due to Alfvén Waves

Acceleration of the plasma due to Alfén waves is created by gradients in the wave amplitude. To understand this process we start with the concept of magnetic pressure,

which is related to the magnetic field magnitude by $p_M = B^2/2\mu_0$. Similar to thermal pressure, magnetic pressure can be best visualized as the force per unit area that a magnetic field exerts on charged particles impinging on the boundary between regions with and without a magnetic field (e.g. in the Earth's magnetopause). This force acts in a direction perpendicular to the discontinuity and the magnetic field direction. If we consider a continuous medium filled by a magnetized plasma, any gradients in the magnetic field will cause a bulk motion of the fluid along the gradient direction, unless the magnetic field gradient is exactly balanced by a gradient in thermal pressure (this can be readily obtained from the MHD momentum equation, presented in Eq. (2.2)). In Alfvén waves, the oscillating magnetic field component will give rise to an average magnetic pressure given by:

$$p_w = \frac{< \delta \mathbf{B}^2 >}{2\mu_0} \tag{1.11}$$

where p_w is commonly referred to as wave pressure. A gradient in $< \delta \mathbf{B}^2 >$ will act on the fluid just like a gradient in the static magnetic field as discussed above; that is, a bulk motion will develop along the gradient direction. This is equivalent to saying that gradients in the wave pressure will accelerate the plasma.

1.9 Wave Dissipation due to the Turbulent Cascade

1.9.1 Turbulent Wave Spectrum

The concept of turbulence is closely related to the theory of unstable flows. Instability occurs in hydrodynamic flows having a Reynolds number (R_e) which is larger than some critical value R_{cr}. This value is problem-specific. Above the critical value, the flow becomes unstable - an initial perturbation introduced to the system will grow, depending on its frequency and the Reynolds number of the flow. As the instabilities grow with time, their contribution to the background state in no longer negligible and non-linear effects will become important. In such a flow non-linear

wave-wave interactions will create waves at new frequencies, which themselves may become unstable. If this process is allowed to continue, it will ultimately result in a continuous spectrum of perturbations, often referred to as a turbulent spectrum.

A fully developed turbulence means that the system exhibits perturbations in a wide range of temporal and spatial scales. Locally, all quantities will fluctuate in an unpredictable manner. That is, the solution is not fully determined by the boundary conditions, but rather has many degrees of freedom (each degree of freedom is associated with a degree of instability, i.e, for a secondary instability only, we have 2 degrees of freedom etc.).

1.9.2 Energy Cascade and Wave Dissipation

In a turbulent regime, the energy of the system is associated with eddies of variable scale. The distribution of turbulent energy over the different scales is often represented in Fourier space, which describes the energy of the fluctuations as a function of wave number, k. A turbulent energy spectrum is depicted schematically in Figure 1.13. The turbulent energy is injected into the system on the large eddies scale (also called the integral scale, which is associated with small wave numbers). On the other edge of the spectrum, the eddies with scales comparable to the thermal motions of the fluid will dissipate and their energy will be converted into heat. The corresponding wave number range is called the dissipation scale; at this scale energy is removed from the turbulent field and the wave spectrum will show a cut-off at the corresponding wave number.

In quasi steady-state, the energy injected into the large eddies must be removed at the same rate at the dissipation scale. As proposed by *Kolmogorov* (1941), it follows that the turbulent energy must be passed from the large eddies to successively smaller eddies, until the eddies are small enough such that the dissipation scale is reached and the eddies are dispersed. From Kolmogorov's *second assumption of similarity,* the

statistical behavior of the turbulence is uniquely determined by the energy dissipation rate.

The energy cascade from the large eddies to the smaller eddies occurs at a range of wave numbers called the inertial range, shown in Figure 1.13. The energy spectrum of the inertial range can be found from dimensional arguments (and some phenomenological assumptions). The Kolmogorov spectrum was derived in such a way and agrees very well with observed hydrodynamic turbulence. The energy E of a wave is related to the wave number k and to the dissipation rate of small eddies ϵ by:

$$E(k) \propto \epsilon^{2/3} k^{-5/3} \tag{1.12}$$

Several analytical models for the turbulent wave spectrum were developed, and different powers of k were found (*Iroshnikov*, 1964; *Kraichnan*, 1965; *Marsch and Tu*, 1990). The differences stem from different assumptions regarding the energy cascade time scale. However, solar wind observations and numerical simulations favor the Kolmogorov spectrum for the solar environment.

1.9.3 Turbulent Dissipation in the Corona

Inhomogeneities in the magnetic field and plasma parameters can cause Alfvén waves to undergo reflections, giving rise to counter-propagating waves. Counter-propagating waves will also naturally occur independently of reflections along closed-field lines, where outgoing waves of opposite polarities are launched from the two foot points. Regardless of their formation mechanism, counter-propagating waves will undergo non-linear wave-wave interactions and subsequent evolution of the wave spectrum. In a turbulent regime, this scenario will lead to an energy cascade into smaller and smaller wave lengths, a process that must eventually result in the conversion of wave energy into plasma thermal energy. The cut-off in the spectrum is

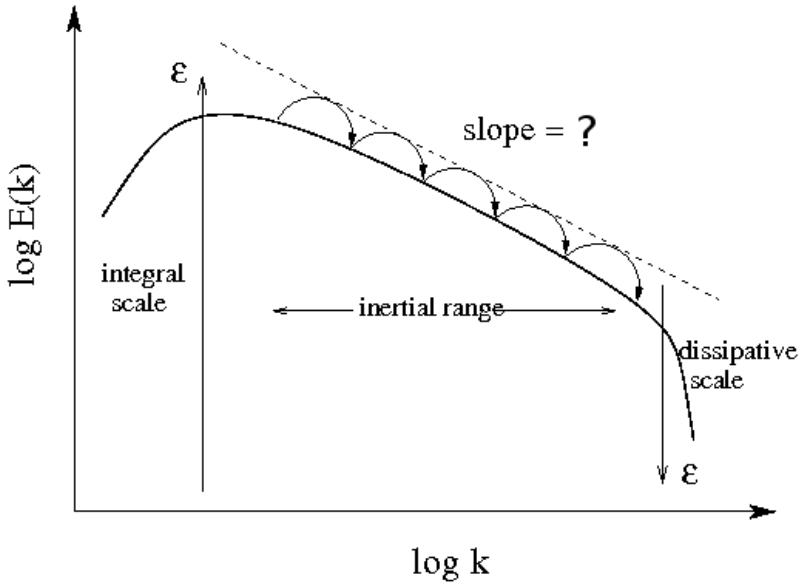

Figure 1.13: *Turbulent wave spectrum, showing the distribution of wave energies as a function of wave number. Energy is injected into the system at the integral rage, associated with the largest eddies. The energy cascades through the inertial range, and is converted into heat at the dissipation scale, corresponding to eddies with dscales comparable to the thermal scale. Figure taken from Jonathan Pietarila Graham's itVery brief primer on turbulence* (http://www.ams.jhu.edu/ jgraha39/Primer.html).

assumed to occur at scales near the ion cyclotron radius.

1.10 Wave-Driven Solar Models

The key element of any wave driven model is the exchange of momentum and energy between the plasma and the Alfvén wave field. This interaction can be described self-consistently by the coupled system of the MHD and a wave kinetic equation for Alfvén waves. The latter can be derived under the Wentzel-Kramers-Brillouin (WKB) approximation (*Jacques*, 1977), which is valid for wave-lengths shorter than the length scale of variations in the background. This description is justified if one wishes to describe the large scale dynamics of the system, rather than the detailed conversion of wave energy into thermal energy.

The coupled system of MHD equations and a wave kinetic equation were first solved for an axisymmetric solar wind model in *Usmanov et al.* (2000), and later in *Usmanov and Goldstein* (2003), assuming an ideal dipole magnetic field. The model results were in general good agreement with Ulysses observations of the fast and slow solar wind. However, this model did not address the problem of coronal heating, since the inner boundary was already at the 1MK range. In addition, the description only accounted for Alfvén waves of a single polarity, and their dissipation was described by a simple linear loss term.

Previous works have simulated this process directly by describing wave reflections and frequency-dependent wave-wave interactions in idealized open flux tubes (e.g. *Cranmer and van Ballegooijen* (2005), *Cranmer et al.* (2007), *Verdini and Velli* (2007)). While this approach is instructive for prescribed magnetic fields, its application to a 3D model with a realistic and self-consistent magnetic field is quite involved.

An alternative to this approach was proposed in *Hollweg* (1986), who calculated a

Kolmogorov-type energy dissipation rate. In this approach, the cascade process due to the presence of counter-propagating waves was assumed to be fast enough, such that the reflected wave energy is totally dissipated before it can propagate away. Under this assumption one can relate the dissipation rate to the macroscopic properties of the system. This property of the Kolmogorov-type treatment makes it especially attractive for global MHD modeling, since it does not require directly describing wave reflections and spectral evolution. However, it does require us to make some assumptions about the efficiency of the cascade process, as we will discuss in Section 2.2.2.

The dissipation rate proposed in *Hollweg* (1986) was applied to a magnetogram-driven coronal model in *van der Holst et al.* (2010), which also included separate electron and proton temperatures. The model results were validated against observations at 1AU in *Jin et al.* (2012). In *Evans et al.* (2012), this model was extended to include the contribution of surface Alfvén waves to the dissipated energy. However, Hollweg's approach was developed for the case where outgoing waves of a single polarity are injected into the base an expending flux tube. Thus it could not be applied to closed field lines, and consequently no wave energy was injected at the foot points of coronal loops. It should be noted that the *van der Holst et al.* (2010); *Evans et al.* (2012) model did not aim to create the global structure of the corona starting from the rather uniform underlying chromosphere. Instead, it derived the temperature and density distribution at the inner boundary from tomographic data of the 1MK coronal plasma.

1.11 The Purpose of this Work

In our efforts to develop a self-consistent and physics-based description of the solar atmosphere, we must be able to reproduce at least the large scale distribution of the various solar wind properties. As our understanding of this system develops,

increasingly sophisticated models are being created, and their results can be compared to a widening range of observations.

Previous observational and theoretical efforts have suggested the turbulent Alfvén waves can supply the energy required to heat the corona and accelerate the solar wind. However, a single unified model that explains these processes at all locations in the corona and the solar wind simultaneously was not developed prior to this work. We therefore develop a global numerical model which describes Alfvén wave propagation and dissipation throughout the solar corona and wind. The coronal heating problem will be addressed by starting the model from the top of the chromosphere, with the expectation that the waves will create the required heating to form the 1 million degrees observed in the corona.

The model will then be used to analyze the large scale structure and the details of the wave dissipation mechanism in idealized conditions. This will lead the way to simulating the corona and wind using the magnetic field measured in the photosphere, which will enable us to compare model results to a wide range of observations. This step is crucial in benchmarking any global model.

The viability of the wave dissipation mechanism proposed in this model will be tested against independent estimations of both the heating profiles and the wave amplitudes from spectroscopic observations of the lower corona. This will allow us to gain insight into the strengths and weaknesses of our description.

The model predictions will be used to predict the charge state composition in the fast and slow solar wind. Comparison of the predicted composition to observations will enable us to make a step forward in understanding the acceleration and source regions of the fast and slow wind.

CHAPTER II

Global Model of the Solar Corona and Solar Wind

2.1 Introduction

In this Chapter, the computational model developed for this work is described, and the wave dissipation mechanism assumed in the model is presented and analyzed in detail. The goal of this chapter is to demonstrate that the model is capable of reproducing the large-scale distributions of density and temperature in the corona, and the wind speeds in the heliosphere. The results are validated against remote and in-situ observations.

The Alfvén Wave driven Solar Model (AWSoM) is a first-principles global model extending from the top of the chromosphere out to the solar wind, based on a wave kinetic / extended MHD framework. The model is driven by a Poynting flux of Alfvén waves that is injected at all magnetic field foot points, and its magnitude is related to the local radial magnetic field. The wave energy is then transported along magnetic field lines into the corona and the solar wind.

In order to reproduce the observed three-dimensional distributions of temperature and density in the corona without invoking geometric heating function, we require a heating mechanism that depends on the magnetic field topology. At the same time, the open and closed field line regions should emerge naturally and self-consistently, without the need to a-priori determine their locations. In *Sokolov et al.* (2013),

the Kolmogorov-type approach presented in *Hollweg* (1986) for calculating the wave dissipation in open flux tubes was generalized such that it can also be applied to closed magnetic field lines, where counter propagating waves naturally arise from the topology.

In order to complete the description of a wave driven model, one must also specify the Poynting flux injected into the system. *Suzuki* (2006) showed that the required flux can be determined by considering energy conservation along expanding flux tubes in the solar wind, i.e. by relating the energy flux at the foot-point of a field line to the final wind speed along the same field line. One clear limitation of this approach is that it can only be applied to open field lines. Furthermore, complete information about the final wind speed even for all open field lines is not available, and the terminal wind speed at a spherical surface at 1AU has to be taken from some semi-empirical model, e.g. the Wang-Sheeley-Arge (WSA) model (*Arge and Pizzo*, 2000). In this work, we wish to take a different approach, and specify a wave Poynting flux that is independent of conditions at 1AU and only constrained by observations of chromospheric Alfvén waves.

This Chapter is organized as follows. The AWSoM model equations and the physical processes included in the model, as well as the constraints on the adjustable input parameters, are described in Section 2.2. The numerical model is described in Section 2.3, where we discuss the choice of computational grid and the inner boundary conditions. We then present results from idealized simulations in Section 2.4, where we focus on analyzing the validity and implications of our choice of wave dissipation. Model validation for a real magnetogram field for a solar minimum case is presented in Section 2.5. We compare our model prediction to remote observations of the solar corona (line-of-sight EUV and X ray images) and in situ observations made by the Ulysses spacecraft. This enables us to test how well the model reproduces both coronal structures and the fast and slow solar wind distribution. Conclusions and

discussion of the results and future work are given in Section 2.6.

2.2 Model Description

2.2.1 Governing Equations

The macroscopic evolution of the coronal and the solar wind plasma can be adequately described by the equations of non-resistive MHD. Although this approximation breaks down in the partially ionized chromosphere, by setting the inner boundary of the model at the top of the chromosphere, resistive effects can be neglected. To account for the different thermodynamic processes acting on electrons and protons, we start from the two-temperature MHD equations derived in *Braginskii* (1965). We assume that the Hall effect can be neglected, and that the electrons and protons flow with the same velocity. Together with the assumption of quasi-neutrality this leads to single-fluid continuity and momentum equations. The electrons and protons obey separate energy equations. Non ideal-MHD processes such as heating, electron heat conduction and radiative cooling become important at certain regions and should be included as source terms in the energy equations. Finally, the modified MHD equations are coupled to wave kinetic equations for parallel and anti-parallel waves, as described in *Sokolov et al.* (2009), *van der Holst et al.* (2010) and *Sokolov et al.* (2013). The governing equations then become:

$$\frac{\partial \rho}{\partial t} + \nabla\cdot(\rho \mathbf{u}) = 0, \tag{2.1}$$

$$\rho\frac{\partial \mathbf{u}}{\partial t} + \rho\mathbf{u}\cdot\nabla\mathbf{u} = -\rho\frac{GM_\odot}{r^3}\mathbf{r} - \nabla(p_e + p_p + p_w) + \frac{1}{\mu_0}(\nabla\times\mathbf{B})\times\mathbf{B}, \tag{2.2}$$

$$\frac{\partial \mathbf{B}}{\partial t} + \nabla\cdot(\mathbf{uB} - \mathbf{Bu}) = 0, \tag{2.3}$$

$$\frac{\partial w^{\pm}}{\partial t} + \nabla\cdot[(\mathbf{u} \pm \mathbf{V_A})w^{\pm}] = -\frac{1}{2}(\nabla\cdot\mathbf{u})w^{\pm} - Q_w^{\pm}, \tag{2.4}$$

$$\frac{\partial p_p}{\partial t} + \nabla\cdot(p_p\mathbf{u}) = (\gamma-1)[-p_p\nabla\cdot\mathbf{u} + \frac{1}{\tau_{pe}}(p_e - p_p) + f_p Q_w], \tag{2.5}$$

$$\frac{\partial p_e}{\partial t} + \nabla\cdot(p_e\mathbf{u}) = (\gamma-1)[-p_e\nabla\cdot\mathbf{u} + \frac{1}{\tau_{pe}}(p_p - p_e) - Q_{rad} + (1-f_p)Q_w - \nabla\cdot\mathbf{q}_e]. \tag{2.6}$$

The basic state variables are the mass density, ρ, the bulk flow velocity, $\mathbf{u}$, the magnetic field, $\mathbf{B}$, and the proton and electron thermal pressures, p_p and p_e, respectively. $w^{\pm}$ is the energy density of Alfvén waves propagating parallel(+) or anti parallel(-) to the magnetic field. Next, G is the gravitational constant, $M_{\odot}$ is the solar mass, μ_0 is the magnetic permeability, and γ the polytropic index set to be constant at 5/3. The Alfvén velocity is given by $\mathbf{V}_A = \mathbf{B}/\sqrt{\mu_0\rho}$. For the wave pressure tensor, we use the derivation by *Jacques* (1977), who found it to be isotropic and given by $p_w = (w^+ + w^-)/2$.

Eqs. (2.1)-(2.2) describe the conservation of mass and momentum. Eq. (2.2) includes acceleration due to solar gravity, gradients in the electron, proton and wave pressures and the Lorentz force. Eq. (2.3) is the induction equation for the magnetic field in the non-resistive limit. The wave kinetic equations are given in Eq. (2.4), which represents two separate equations, for waves traveling parallel (+) and anti-parallel (-) to the magnetic field. The wave energy density dissipation rate for each wave polarity is denoted by $Q_w^{\pm}$. The total wave energy density dissipation rate is given by $Q_w = Q_w^+ + Q_w^-$. The explicit form of the dissipation term will be discussed in Section 2.2.2.

The pressure equations for protons and electrons are given in Eqs. (2.5) and (2.6). Both equations include electrons-protons heat exchange and the total wave dissipation

rate, Q_w. The radiative cooling rate, Q_{rad}, is calculated from the CHIANTI 7.1 atomic database (*Dere et al.*, 1997; *Landi et al.*, 2013), assuming coronal elemental abundances (taken from *Feldman et al.* (1992)) and each ion's radiative emission is calculated by solving the equations for statistical equilibrium and obtaining the ion's level populations assuming ionization equilibrium (obtained from the local electron density and temperature and the ionization and recombination rates appearing in *Landi et al.* (2013)).

The total dissipated wave energy heats both protons and electrons, with the fraction of heating going into the protons denoted by the constant $f_p = 0.6$ (see *Breech et al.* (2009), *Cranmer et al.* (2009) for more details). Heat exchange due to Coulomb collisions between electrons and protons enters the energy equations through the second term on the right hand side of both equations. The collisional heat exchange results in temperature equilibration on a time scale τ_{pe}, which is given by (*Goedbloed and Poedts*, 2004):

$$\tau_{pe} = 3\pi\sqrt{2\pi}\epsilon_0 \frac{m_p}{\sqrt{m_e}} \frac{(kT_e)^{3/2}}{ln\Lambda e^4 n}, \tag{2.7}$$

where m_p and m_e are the proton and electron masses, respectively, e is the elementary charge, k is the Boltzmann constant, T_e is the electron temperature, ϵ_0 is the permittivity of free space, n is the plasma number density (under the assumption of quasi-neutrality) and $\ln\Lambda$ is the Coulomb logarithm, taken to be uniform with $\ln\Lambda = 20$. Since the heat exchange between the protons and the electrons is proportional to the plasma number density, n (where the plasma is assumed to be quasi-neutral), the thermal coupling between the two species is only important close to the Sun, and becomes negligible at larger distances as the density drops off and the plasma becomes collisionless. The electron energy equation, Eq. (2.6), also includes field-aligned electron heat conduction term, which depends on the electron heat conduction tensor $\mathbf{q}_e$, given by the Spitzer form:

$$\mathbf{q_e} = -\kappa T_e^{5/2} \frac{\mathbf{BB}}{B^2} \cdot \nabla T_e, \tag{2.8}$$

with $\kappa = 9.2 \times 10^{-12} Wm^{-1}K^{-7/2}$ (calculated by assuming a uniform $ln\Lambda = 20$, as before).

2.2.2 Turbulent Wave Dissipation

The coupling of the wave field to the background MHD plasma, as described by equations (2.2) and (2.4) - (2.6), allows us to account for the conversion of wave energy into plasma thermal energy. However, these equations do not explicitly describe the dissipation mechanism itself. In order to complete our description and close the set of equations, we must specify the total wave energy density dissipation rate, Q_w.

The nature of the wave dissipation mechanism depends on the local conditions of the plasma in which the waves propagate. In the chromosphere, the plasma is partially ionized and Alfvén waves are damped due to finite resistivity / magnetic diffusion effects (c.f. *De Pontieu et al.*, 2001). By setting the model's inner boundary at the top of the chromosphere, we can reasonably avoid treating these effects, and only describe the dissipation due to turbulent cascade of Alfvén wave energy in the fully ionized corona, where most of the heating takes place. In order to calculate the dissipation rate for any arbitrary magnetic field topology, we apply the unified approach we presented in *Sokolov et al.* (2013), where open and closed field regions are treated on the same footing. The generalized dissipation term will be discussed below.

2.2.2.1 Dissipation due to Counter-Propagating Waves

The non-linear interaction of Alfvénic perturbations can be directly derived from the MHD equations, by separating the magnetic field and velocity vectors into a background component and a turbulent perturbation component, $\mathbf{B} = \tilde{\mathbf{B}} + \delta\mathbf{B}$ and $\mathbf{u} = \tilde{\mathbf{u}} + \delta\mathbf{u}$. The wave energy densities, $w^{\pm}$, are related to these perturbations by $w^{\pm} = \rho|\delta\mathbf{u}|^2 = |\delta\mathbf{B}|^2/\mu_0$ (which follows from the equipartition of kinetic and

thermal energies of Alfvén waves). Substituting these into Eqs. (2.1) - (2.3) results in several terms which are second order in the perturbation, essentially describing the evolution of the turbulent energy field due to non-linear wave-wave interactions. The basic derivation can be found in *Sokolov et al.* (2013). Here we only briefly mention that the dissipation rate due to turbulent cascade will be proportional to the term $\nabla\cdot(\mathbf{z}_{\mp}w^{\pm})$, where $\mathbf{z}_{\pm}$ are the Elsässer variables, defined as $\mathbf{z}_{\pm} = \delta\mathbf{u} \pm \delta\mathbf{B}/\sqrt{\mu_0\rho}$. The Elsässer variables are related to the wave energy densities $w^{\pm} = \rho z_{\pm}^2/4$. We can approximate the energy density dissipation rate due to a turbulent cascade as:

$$Q_w^{\pm} = \frac{1}{L_\perp} z_{\mp} w^{\pm} = \frac{2}{L_\perp}\sqrt{\frac{w^{\mp}}{\rho}}\, w^{\pm}. \tag{2.9}$$

Here $L_\perp$ is a length scale associated with the transverse correlation length of the turbulent field. Following *Hollweg* (1986), $L_\perp$ is assumed to be proportional to the width of the magnetic flux tube, which implies that $L_\perp \propto 1/\sqrt{B}$. The total dissipation rate (and therefore the heating rate) can be found by summing the contributions from both waves, $Q_w = Q_w^+ + Q_w^-$. Thus the total dissipation rate for counter-propagating waves is given by:

$$Q_w = \frac{1}{L_\perp\sqrt{\rho}}(w^+\sqrt{w^-} + w^-\sqrt{w^+}), \tag{2.10}$$

where the factor of 2 was absorbed into $L_\perp$ for simplicity. The value of $L_\perp$ is not well-known, but can be constrained by comparison to observations (see Section (2.2.3) for more details).

It is useful to compare Eq. (2.10) to the phenomenological dissipation term appearing in previous works developed in the framework of Elsässer variables (c.f. *Hossain et al.* (1995), *Zhou and Matthaeus* (1990), *Matthaeus et al.* (1999), *Dmitruk et al.* (2001, 2002), *Cranmer et al.* (2007), *Chandran and Hollweg* (2009)), wherein the total

energy density dissipation rate is given by:

$$Q_w^* = \rho\epsilon_{turb}\frac{z_+^2 z_- + z_-^2 z_+}{4L_\perp} = \frac{\epsilon_{turb}}{L_\perp\sqrt{\rho}}(w^+\sqrt{w^-} + w^-\sqrt{w^+}), \tag{2.11}$$

where ϵ_{turb} is a constant specifying the efficiency of the turbulent dissipation (i.e. the ratio of dissipated energy to the injected energy). In the last step we have written this expression in terms of the wave energy densities and absorbed a factor of 2 into $L_\perp$ for consistency with Eq. (2.10). It can be easily seen that Eq. (2.11) is almost identical to the total dissipation rate given by Eq. (2.10), differing only by the additional factor of ϵ_{turb}. In *Dmitruk and Matthaeus* (2003), it was shown that ϵ_{turb} will in general depend on the relative magnitude of the Alfvén travel time, τ_A, and the reflection time scale, τ_R (as well as on the time scales associated with the driving wave field). Simply stated, the efficiency of turbulent heating depends on whether the cascade process has sufficient time to develop and heat the plasma before the wave energy is propagated away. *Dmitruk and Matthaeus* (2003) found that ϵ_{turb} can take values between $13 - 60\%$ for a set of numerical simulations, where the efficiency increases as the reflections become stronger. In the limit of a fully developed cascade where $\tau_R << \tau_A$, the efficiency, ϵ_{turb}, will approach unity, and therefore $Q_w \approx Q_w^*$. Thus the dissipation rate presented in Eq. (2.10) is consistent with that derived in previous works, if a fully-developed turbulent cascade is assumed. Even if this assumption is relaxed, Eq. (2.10) will only differ by a factor of order unity from Eq. (2.11).

2.2.2.2 Dissipation due to Wave Reflections in Open Flux Tubes

On closed-field lines, waves of opposite polarities are launched from the two footpoints, and Eq. (2.10) gives an adequate description. On the other hand, if only one wave polarity is present, Q_w will reduce to zero. In the real solar atmosphere both wave polarities will also be present on open field lines, to some degree, due to

reflections. If the local reflection coefficient is given by C_{refl}, then the energy density of the reflected wave, w^{refl}, is related to the energy density of the outgoing wave, w^{out}, by $w^{refl} = C_{refl}^2 w^{out}$. However, since our model does not explicitly describes reflections, an important distinction has to be made between the theoretical wave energies w^{out}, w^{refl} and the model variables $w^{\pm}$. For a flux tube with $B_r > 0$, for example, the variable w^+ can be associated with the energy density of the outgoing wave, and we can set $w^+ = w^{out}$. However, we cannot associate the variable w^- with w^{refl}, since the actual wave reflection was not calculated. In fact, the variable w^- will be equal to zero in this region (up to a round-off error). The opposite will be true in regions where $B_r < 0$. In order to properly calculate the dissipation rate in open flux tubes, we must consider a "virtual" reflected wave. This wave will have an energy density equal to $w_*^{\pm} = C_{refl}^2 w^{\mp}$, and the energy density dissipation rate of the outgoing wave will then become:

$$Q_w^{\pm} = \frac{1}{L_{\perp}\sqrt{\rho}} \sqrt{w_*^{\mp}} w^{\pm} = \frac{1}{L_{\perp}\sqrt{\rho}} C_{refl} \left(w^{\pm}\right)^{\frac{3}{2}} . \tag{2.12}$$

This expression gives the correct energy dissipation rate along open field lines, by taking into account local reflections, without directly simulating the reflections themselves. Note that the above dissipation rate has a similar form as the one derived in *Hollweg* (1986) for open flux tubes, namely $Q_w = (1/L_{\perp}\sqrt{\rho}) w^{3/2}$, where w was defined there as the wave energy density of a single polarity. However, the two forms differ by the factor C_{refl}, which in the solar corona is estimated to have values between 0.01 and 0.1 (see Section 2.2.3 for more details).

2.2.2.3 Generalized Wave Dissipation Rate

The next step is to combine the counter-propagating wave dissipation with the reflected wave dissipation into a single dissipation term that can be applied everywhere.

To do so, we note that at any given location either of these mechanisms will be the dominant one, depending on the level of imbalance between the two wave polarities. Thus, we can write:

$$Q_w^{\pm} = \frac{1}{L_\perp \sqrt{\rho}} \sqrt{max(w^{\mp}, C_{refl}^2 w^{\pm})} w^{\pm}. \tag{2.13}$$

This form ensures that in regions where both wave polarities have energies within the same order of magnitude (which will occur in closed field line regions), the counter-propagating wave dissipation as it appears in Eq. (2.10) will be taken into account, while in open field regions or very close to the inner boundary, Eq. (2.13) will reduce to Eq. (2.12). The advantage of this form is both practical and conceptual. First, the magnetic topology does not have to be determined a-priori in order to "select" a dissipation mechanism (thus making the computational implementation more efficient). More importantly, our form of wave dissipation will cause the distribution of coronal temperatures and wind speeds to emerge naturally and self-consistently with the magnetic topology. This can be understood as follows. The dissipation rate in closed field lines will be larger than that in coronal holes, due to the presence of two wave polarities. This will result in higher heating rates in helmet streamers compared to coronal holes. At the same time, the lower heating rates within coronal holes will lead to more wave energy being available to accelerate the plasma, resulting in a faster solar wind. Any excess of thermal energy will be transported by electron heat conduction down to the chromosphere, where is can be efficiently removed from the system through radiative cooling. The combination of wave dissipation, heat conduction and radiative cooling will then allow the system to reach a steady-state. This process is depicted schematically in Figure 2.1. Another consequence of Eq. (2.13) is that the heating rate in active regions will be higher than in the quiet Sun. To see this, we recall that the transverse correlation length, $L_\perp$, is inversely proportional to

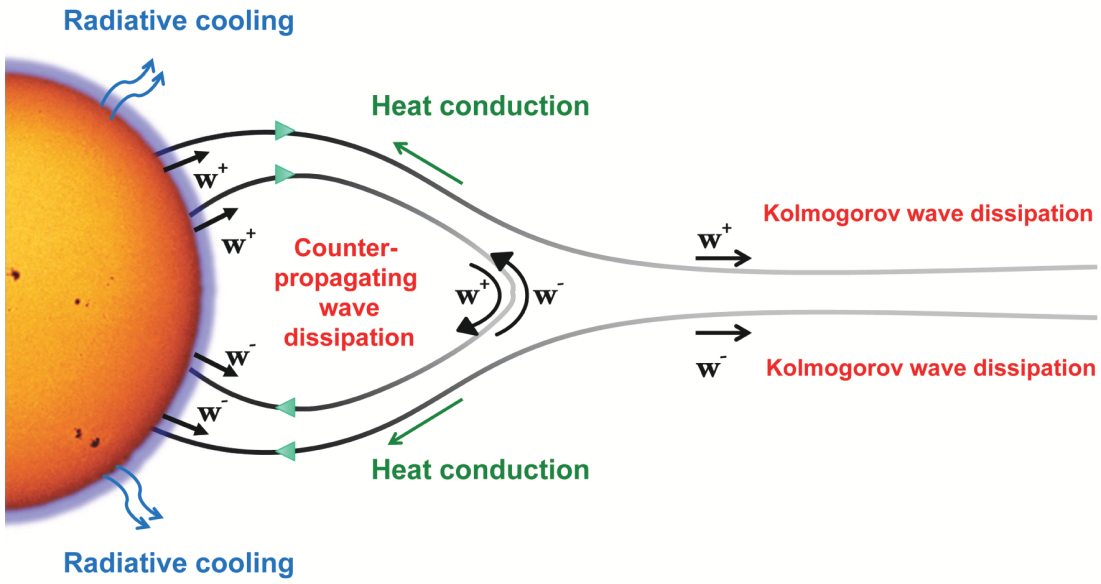

Figure 2.1: *A schematic picture of the physical processes included in the AWSoM model. Black curves represent magnetic field lines. The chromosphere is represented by the light red region above the photosphere.*

$\sqrt{B}$. Consequently, regions with higher magnetic field will have a shorter dissipation length scale, and larger dissipation rates. All in all, our choice of the wave dissipation term is capable of self-consistently reproducing the large scale properties of the solar corona and solar wind without invoking geometric heating functions. The only free parameters in this description are the transverse correlation length, $L_{\perp}$,and the reflection coefficient, C_{refl}. We will discuss how we can constrain their numerical values in Section (2.2.3).

2.2.3 Constraints on Adjustable Input Parameters

The adjustable input parameters used in this model are:

- The transverse correlation length at the inner boundary, $L_{\perp,0}$.
- The pseudo-reflection coefficient, C_{refl}, which is assumed to be uniform everywhere.
- The Alfvén waves Poynting flux at the inner boundary.

2.2.3.1 Transverse Correlation Length, $L_{\perp,0}$

This parameter is used to determine the local correlation length, $L_\perp$, everywhere in the computational domain. Following *Hollweg* (1986), we assume that $L_\perp$ is proportional to the width of the magnetic flux tube. Due to the conservation of magnetic flux the local correlation length will scale with the magnetic field as $L_\perp = L_{\perp,0}/\sqrt{B[T]}$ (where $B[T]$ stands for B measured in units of Tesla). In the present work we found that a value of $L_{\perp,0} = 25\ km$ gives the proper heating and acceleration rates for solar minimum, by comparing model results to observations. We next compare this value with that employed in other models, and give a general constraint on the choice of $L_{\perp,0}$ for future applications. *Hollweg* (1986), which solved the problem for idealized coronal hole flux tubes, has estimated $L_{\perp,0}$ to be 75 km. Note, however, that in this latter work, the reflection coefficient was in effect absorbed into the dissipation length. Thus in comparing our formulation (as in Eq. (2.13)) to the Hollweg one, we have $C_{refl}/L_{\perp,0} = 1/75\ km$. With a choice of a reflection coefficient between 0.4-0.6 used in this work, we get $L_{\perp,0}$ between 40km to 62.5km, so the discrepancy with the *Hollweg* (1986) value is not significant. Other models which incorporated a more sophisticated description of the turbulent field were found to be in good agreement with observations using values such as 28.76 km (*Cranmer et al.*, 2007) and 115.5 km (*Cranmer and van Ballegooijen*, 2005). More recently, *Cranmer* (2010) has determined $L_{\perp,0}$ to be around 60 km, while *Sokolov et al.* (2013) estimated that the correlation length should be in the range $20 - 100\ km$, which more or less overlaps the values of previous works. Thus we conclude that our choice of the dissipation length is within the range of previous works. A smaller dissipation length will lead to excessive heating close to the inner boundary, and less wave energy will be available for solar wind acceleration farther away.

2.2.3.2 Pseudo-Reflection Coefficient

The reflection coefficient of Alfvén waves traveling in an inhomogeneous medium will depend both on the wave frequency, as well as on the gradients in the density and magnetic field. In the present work, we consider, as a first approximation, a uniform reflection coefficient, which can be thought of as an average over the spectrum and over the spatial variance of the plasma. In order to be consistent with previous estimations of the reflection coefficient (c.f. *Velli* (1993)), we restrict C_{refl} to take values between 0.01 and 0.1. The actual value chosen for specific simulations will appear in the relevant sections. A more realistic description of the corona should be based on a self-consistent and therefore a spatially-varying reflection coefficient. The assumption of a uniform reflection coefficient can be justified for a global model if one compares the predicted and observed of Alfvén wave amplitude in the heliosphere (see 2.4.3), as well as compare the resultant solution to that obtained from a more rigorous treatment of wave reflections. Such a comparison will be presented in Landi et al. (2014, in preparation).

2.2.3.3 Poynting Flux

The Poynting flux from the chromosphere to the corona determines the energy input to the model. Detailed observation of perturbations in the chromosphere have suggested that they are likely Alfvénic in nature, and their power spectrum was estimated (*De Pontieu et al.*, 2007; *McIntosh and De Pontieu*, 2012). The Poynting flux associated with Alfvén waves is given by:

$$\mathbf{S} = (\mathbf{u} \pm \mathbf{V}_A)\rho\overline{\delta u}, \tag{2.14}$$

where we define the time averaged velocity amplitude as $\overline{\delta u} = \sqrt{< \delta \mathbf{u}^2 >}$. At an inner boundary at the top of the chromosphere, the flow speed is negligible and we may set

$\mathbf{u} = 0$. The absolute value of the Poynting flux along the magnetic field is then:

$$S_{||} = \sqrt{\frac{\rho}{\mu_0}} B \overline{\delta u}, \tag{2.15}$$

where $B = |\mathbf{B}|$. The numerical value of $S_{||}$ at each point on the inner boundary is therefore completely specified if the plasma density, wave amplitude and magnetic field magnitude are known. The local magnetic field at the inner boundary is derived from either a synoptic magnetic map or an imposed dipole field. For lack of similar global observations of chromospheric Alfvén waves, we set $\overline{\delta u}$ to be uniform at the inner boundary, and constrain its value using the observations reported in *De Pontieu et al.* (2007), which found $\overline{\delta u}$ to be in the range of $12 - 15\ km\ s^{-1}$ at the altitude where the number density is $n = 2 \times 10^{16}\ m^{-3}$.

We wish to examine the validity of our approximation by comparing the resulting Poynting flux to other models and observational constraints. Inserting the values given above into Eq. (2.15), we get: $S_{||} \approx (0.74 - 1.16) \times 10^2 B\ Wm^{-2}$. Note that the lower limit agrees well with the Poynting flux assumed in the *Suzuki* (2006) model ($0.7 \times 10^2 B\ Wm^{-2}$), while the upper limit is comparable to that employed by the unsigned flux heating model (*Abbett*, 2007), estimated at $S = 1.1 \times 10^2 B\ Wm^{-2}$.

2.3 Numerical Model

The model is implemented within the Space Weather Modeling Framework (SWMF), and is based on the BATS-R-US code, a versatile, massively parallel MHD code developed at the University of Michigan. Detailed description of the BATS-R-US code and the SWMF can be found in *Tóth et al.* (2012) and references therein. BATS-R-US provides a variety of schemes and solvers designed for finite-volume cell-centered numerical methods. In the present implementation, the model equations are solved by a second-order numerical scheme. We found that best results are achieved for this

specific model by using an explicit scheme. However, the heat conduction term in Eq. (2.6) requires the calculation of second-order derivatives in space, and may constitute a stiff source term, especially in regions of sharp temperature gradients (which will occur near the inner boundary). This may lead to a significant slowing down of the calculation when solved explicitly. In order to overcome this difficulty, we use operator splitting to first solve the hyperbolic operators and non-stiff source terms using an explicit time step, followed by a step which updates the heat conduction term implicitly.

Stability is guaranteed by setting the Courant number at 0.8 (*Courant et al.*, 1928). Although this ensures stability for the hyperbolic terms in the model equations, the inclusion of source/loss terms such as wave dissipation, radiative cooling and heat conduction, may lead to negative thermal and/or wave energies. We therefore must further limit the time step by requiring that the loss accrued during a time-step due to any of these processes, and at any given cell, will not exceed the available energy. This is done automatically at runtime, and separately for each of the thermal and wave energy variables.

2.3.1 Computational Grid

The use of the SWMF allows us to separate the solar wind model into two coupled physical components - the Solar Corona (SC) component, and the Inner Heliosphere (IH) component. This allows us to optimize our choice of physics, grid geometry and numerical scheme in each domain. The inner boundary of the SC component is located at the top of the chromosphere (which we set at $r = 1R_s$), and the outer boundary can be anywhere in the heliosphere, provided that the flow speed at that distance exceeds the fast magnetosonic speed, in order to allow for outflow boundary conditions. Nominally, we set the outer boundary at $r = 24R_s$. The inner boundary of the IH components is set at $r = 16R_s$, while the outer boundary is set at a distance

of a few AU, depending on the application. The coupling between the two components is performed such that the IH component derives its inner boundary conditions from the overlapping cells in the SC domain. The coupling is performed such that second order accuracy in space is maintained.

The model equations are solved on a three dimensional logically Cartesian spatial grid. The computational cells are organized in a block tree, such that each block is composed of the same cell structure. The SC component uses a spherical grid with a block structure of 6x4x4 cells, corresponding to the number of cells in the (r, ϕ, θ) direction. The IH component uses a Cartesian grid with a block stricture of 4x4x4, corresponding to the number of cells in the (x, y, z) directions. The capabilities of the BATS-R-US code also include a solution adaptive mesh refinement (AMR), in which blocks are refined by dividing each block into 8 daughter blocks with the same cell structure. The refinement level of neighboring blocks can differ by up to one level of refinement, such that resolution jumps are limited to a factor of 2 in each direction. For the steady-state solutions presented in this work, AMR is used to automatically resolve current sheets, as we describe in Section (2.3.1.2). The resulting grid typically has 3 million cells in the SC domain and 10 million cells in the IH domain.

2.3.1.1 Resolving the Transition Region

In order to allocate sufficient resolution to the transition region and lower corona, while minimizing the number of cells at larger heliocentric distances, we use non-uniform grid spacings in the radial direction. Building on the work presented in *Downs et al.* (2010), we construct the radial spacings such that more grid points are concentrated close to the Sun. The magnitude of the radial spacings Δr is a smooth function of $\ln(r)$, becoming uniform in $\ln(r)$ beyond $r = 1.7R_s$. The resulting grid is depicted in the left panel of Figure 2.2.

The smallest radial spacing, occurring near the inner boundary and inside the

transition region, is $\Delta r = 0.001 R_s \approx 700\ km$. However, the typical length scales of the dynamic processes in the transition region can be as small as a few kilometers. Resolving the transition region to these scales is impractical in the framework of a global model extending to the solar wind. We therefore use the method presented in *Lionello et al.* (2009), in which the following transformation is applied to the model equations:

$$Q_w \rightarrow Q_w/f \qquad Q_{rad} = Q_{rad}/f \qquad \kappa_0 \rightarrow f\kappa_0 \qquad ds \rightarrow f ds, \tag{2.16}$$

where ds is the path length along a field line and f is a scalar factor given by:

$$f = \left(\frac{T_m}{T_e}\right)^{\frac{5}{2}}, \tag{2.17}$$

where T_m is some constant reference temperature, and T_e is the local electron temperature. This transformation essentially rescales the energy equation. For $T_e < T_m$ we will have $f > 1$, effectively increasing the characteristic length scale of the processes participating in the energy balance, thus widening the temperature profile in the transition region. We must choose T_m such that the length scale in the transition region will be increased so as to accommodate several grid points. As estimated in *Sokolov et al.* (2013), this condition will be satisfied for $T_m = 220,000K$. We must also require that this transformation will not affect the coronal solution, which is sufficiently resolved, and so the transformation is only applied in the range $T_0 < T_e < T_m$ where T_0 is the temperature at the inner boundary, $T_0 = 50,000K$. Note that f smoothly approaches unity at $T_e = T_m$, thus ensuring the widened temperature profile at the transition region will smoothly connect to the coronal temperature profile. In the simulations presented in this work, a value of $T_m = 220,000K$ was chosen, which allows for a minimal grid spacing of 0.001 $R_\odot$ at the inner boundary.

Although this transformation will not affect the solution in the corona and solar

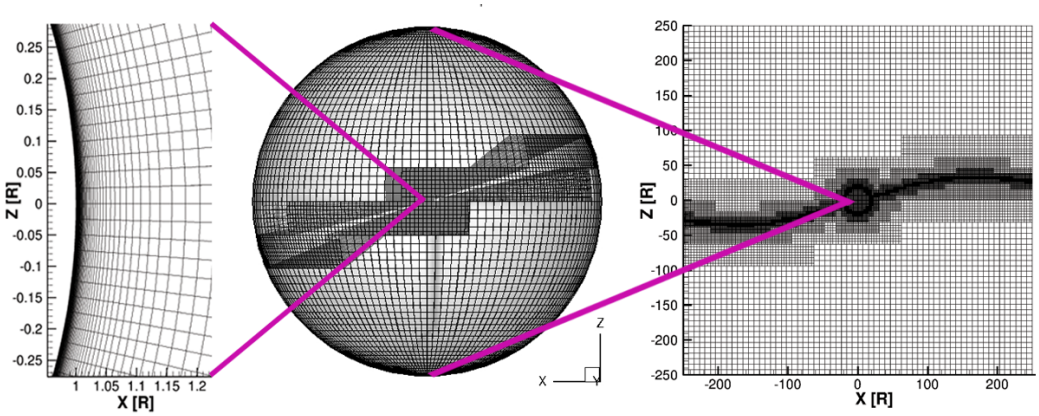

Figure 2.2: *The computational grid structure for a pure dipole simulation, with the dipole axis tilted at 15 degrees from the Z axis. Left: The SC (Solar Corona) component grid, near the inner boundary, where the transition region refinement is applied. Center: The entire SC grid, extending up to 24 R_s. Right: The IH (Inner Heliosphere) component grid. In both the SC and IH components, a finer grid is automatically created by AMR due to the presence of the heliospheric current sheet (in blocks where the radial magnetic field changes sign).*

wind, care has to be taken when comparing our model results to observations in the lower corona. In this case we must map modeled profiles back into realistic scales, by applying the inverse transformation. An example of this procedure is given in Figure 2.3, showing the temperature profile along a streamer belt field line in an ideal dipole simulation. The blue curve shows the model result, and the red curve shows the remapped profile. One can see how the modeled temperature profile is gradually compressed by the mapping, restoring the sharp temperature gradient in the transition region. This procedure should be repeated when calculating line-of-sight integrals as well (as is done, for example, when creating synthesized images). In what follows, we will show original model results, without the remapping, unless otherwise specified.

2.3.1.2 Other Geometric Considerations

The spherical nature of the problem makes a spherical grid a natural choice for the SC component. However, the simple spherical grid introduced here will give rise

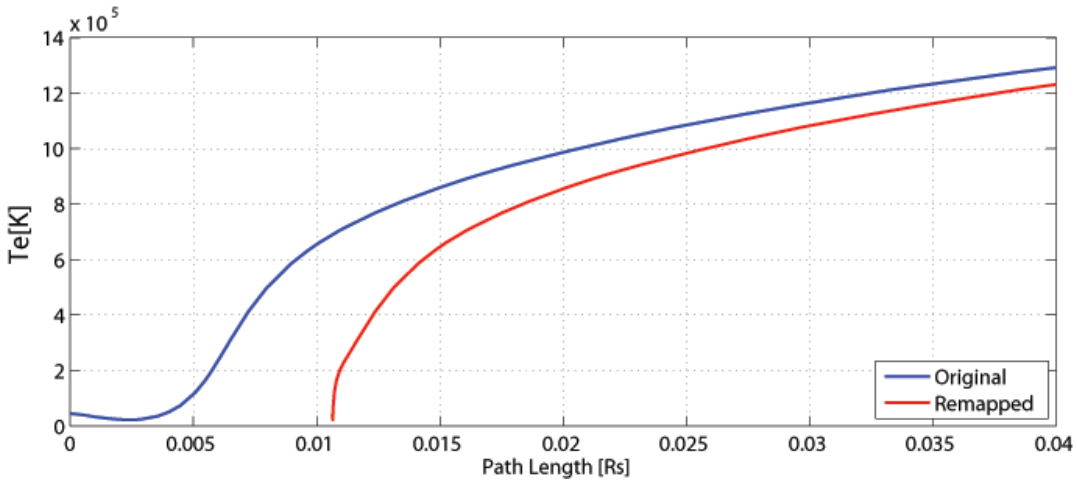

Figure 2.3: *Temperature profile taken along a closed field line in the streamer belt, from an ideal dipole simulation. The blue curve shows the modeled profile. The red curve shows the temperature profile after remapping it using the inverse scale transformation.*

to a singularity along the polar axis, where cell faces touching the pole will have a zero area. This means that fluxes cannot move across the pole. In order to overcome this, we use the super-cell algorithm described in *Tóth et al.* (2012). We apply the super-cell algorithm to a single layer of cells surrounding the pole, from the inner boundary and up to the edge of the SC domain.

In both SC and IH components, we use adaptive mesh refinement in order to resolve current sheets. The criterion for refining a block is whether the radial component of the magnetic field changes sign inside the block. The largest current sheet is the heliospheric current sheet, a thin current layer originating from coronal hole boundaries and extending over the entire heliosphere. Although its topology is wrapped by solar rotation, it remains a rather thin layer throughout the heliosphere. Since cell sizes increase with radial distance in a spherical grid, a Cartesian grid is a more suitable choice for the IH component. The current sheet refinement is excluded from regions with $r < 1.7\ R_s$, so as to avoid over-refinement in the transition region grid. Figure 2.2 shows the resulting refinement for the case of a pure dipole that is tilted by 15 degrees from the Z axis.

2.3.2 Inner Boundary Conditions

Synoptic magnetograms of the photospheric magnetic field are routinely obtained by several solar observatories, and their use in global coronal models is widespread. Here, we use synoptic magnetograms to specify the radial component of the magnetic field at the inner boundary.

The temperature and density are assumed to be uniform at the inner boundary. The proton and electron temperatures are set to $T_e = T_p = 50,000K$. The particle number density can take values in the range $n = n_e = n_p = 2 \times 10^{16} \div 2 \times 10^{17}$ m^{-3}. The mean velocity amplitude of the Alfvén waves, $\overline{\delta u}$, is uniform at the inner boundary as well. Under these assumptions, the Poynting flux defined in Eq. (2.15), will vary with the surface magnetic field according to $S_{||} = C_S B \ Wm^{-2}$ where C_S is a scalar coefficient which is uniform over the solar surface. As discussed in Section 2.2.3, we constrain the wave amplitude to take values in the range $\overline{\delta u} = 12 - 15 \ km \ s^{-1}$ at the altitude where the density is $n = 2 \times 10^{16} \ m^{-3}$, leading to a Poynting flux per unit magnetic field in the range $C_S = 0.74 - 1.16 \times 10^2 \ Wm^{-2}G^{-1}$. If the simulation is to start at a lower altitude with higher number density, the Poynting flux at the inner boundary should be increased such that the desired flux is obtained at the altitude where $n = 2 \times 10^{16} \ m^{-3}$.

Once the Poynting flux at each point on the inner boundary is known, we calculate the wave energy density according to $w^{\pm} = \rho\overline{\delta u}$. At each location on the inner boundary, we use the polarity of the magnetic field to determine which wave mode carries the Poynting flux, such that it is only carried by an outgoing wave. The energy density of the in-going wave is set to zero, so that if any in-going wave reaches the inner boundary (as in closed magnetic loops) then it will be perfectly absorbed.

The radial bulk speed at the solar surface is theoretically zero. However, this implies a null mass flux coming from the inner boundary, and can create unwanted artifacts in the solution. We therefore avoid explicitly specifying the velocity at the

inner boundary. Rather, we require a zero electric field, which in the frozen-in regime implies that $\mathbf{u}||\mathbf{B}$ in the frame rotating with the Sun. We thus simply impose field-aligned flow at the inner boundary. The resulting solutions show that this choice leads to very small bulk speeds close to the surface (up to a few kilometers per second), which are later accelerated as expected.

2.4 Model Results for Idealized Magnetic Fields

Ideal cases with simple magnetic topology will help us test the model and gain physical insight into the resulting steady-state solutions. For this purpose, we assume the Sun's intrinsic magnetic field is an ideal dipole field, with a polar field strength of 5.6 G (which is comparable to the observed polar field during solar minimum). The idealized field is used to define the radial magnetic field at the inner boundary, and the total magnetic field is allowed to evolve self-consistently. In this simulation the adjustable input parameters are set to $C_{refl} = 0.4$, $L_{\perp,0} = 25$km and $\bar{\delta u} = 12$ km/s.

2.4.1 Coronal and Solar Wind Structure

Figure 2.4 shows the distribution of radial speeds in the meridional plane up to $24R_s$, taken from steady-state solutions (in a co-rotating frame) of ideal dipole fields. In the left panel the dipole axis is aligned with the solar rotation axis (Z-axis) while in the right panel the dipole axis is tilted by 15 degrees with respect to the Z-axis. The black curve in each panel shows the location of the Alfvénic surface, where $u_r = V_{A,r}$. As can be seen, the model produces a velocity distribution of fast and slow solar wind flows. The aperture of the slow solar wind in about 20 degrees from the equatorial plane. The location of the Alfvénic surface, at about $8R_s$, is consistent with previous studies.

As mentioned in Section (2.3.1.2), the singularity at the Z axis of the spherical grid may constitute a numerical challenge, since numerical fluxes are inhibited there

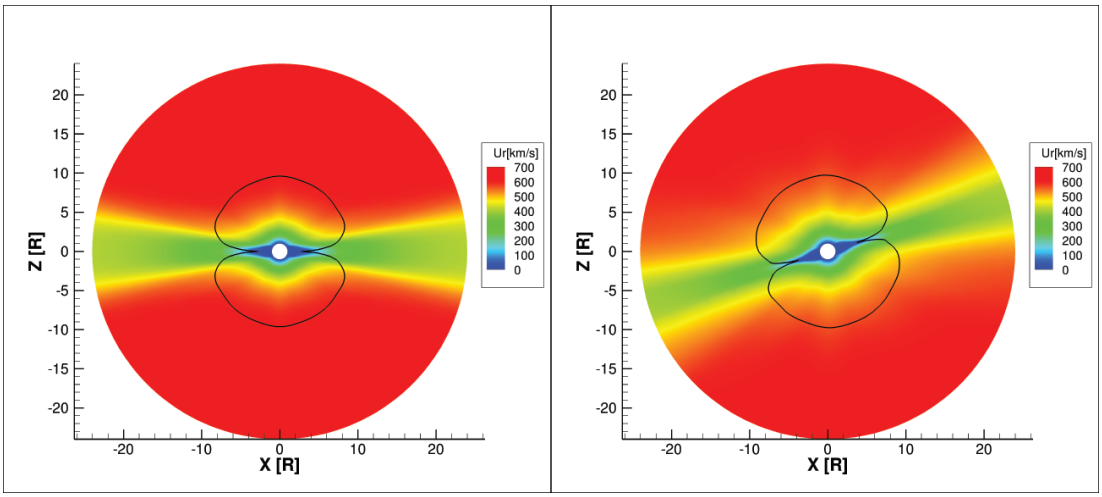

Figure 2.4: *Radial velocity in a meridional plane for a two-temperature, ideal dipole simulation. The black curve shows the location of the Alfvénic surface. Left: dipole axis aligned with solar rotation (Z) axis. Right: dipole axis tilted by 15 degrees with respect to the rotation axis.*

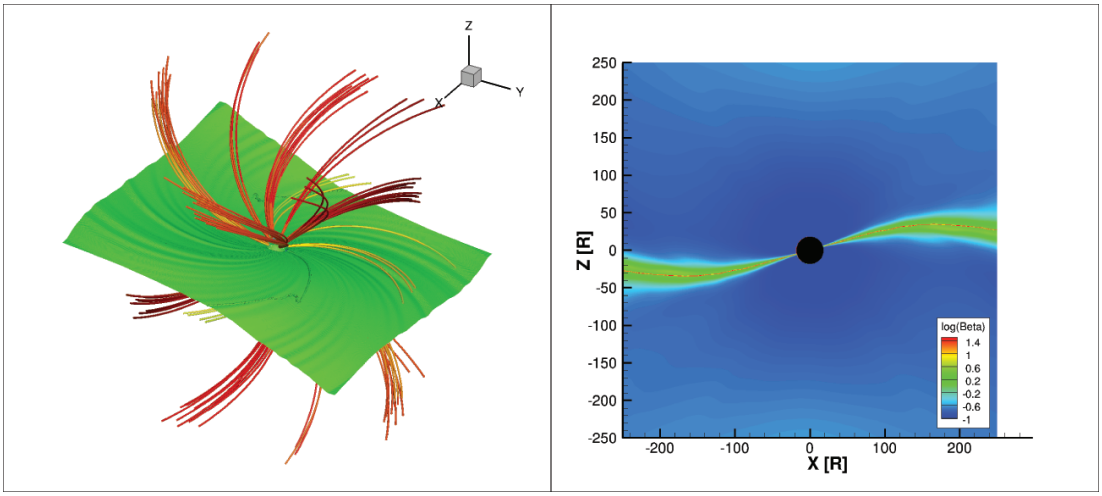

Figure 2.5: *Results of a the tilted dipole simulation in the inner heliosphere, up to* 250 R_s. *Left: 3D structure. Green surface shows the location of the current sheet (where* $B_r = 0$*). Stream lines show the magnetic field, colored by the radial speed (using the same color scale as in Figure 2.4). Right: Plasma beta in the y=0 plane.*

and a special treatment of the pole is required. Comparing the cases of the tilted and non-tilted dipole, we have verified that the model produces the expected results even when the symmetry axis of the problem is not aligned with the symmetry axis of the grid. No numerical artifacts seem to be created by the pole singularity.

In the non-tilted dipole case, the problem is azimuthally symmetric. However, when there is a tilt angle between the rotation axis and magnetic axis, the heliospheric current sheet will warp and bend, producing the well-known "Ballerina skirt" further away from the Sun. Figure 2.5 shows the steady state solution for the tilted dipole case, up to a heliocentric distance of $250R_s$. The left panel shows the three-dimensional structure of the current sheet (green surface), and the magnetic field lines (colored by radial speed). The right panel shows the plasma beta (ratio of thermal to magnetic pressures). The region of high plasma beta (red) signifies a null magnetic field. This figure demonstrates that the heliospheric current sheet remains thin throughout the simulation domain.

2.4.2 Two-Temperature Effects

Figure 2.6 shows the electron (left panel) and proton (right panel) temperature distribution in a meridional plane. This result demonstrates the combined effects of electron heat conduction and electron-proton thermal decoupling. First, the field-aligned electron heat conduction causes the electron temperature to be almost uniform along closed magnetic field lines. For protons, a clear maximum occurs at the tip of the helmet streamer, where wave dissipation due to counter-propagating waves is largest (see below). Due to the low coronal density, the second term on the right hand side of Eqs. (2.5)-(2.6), which gives the electron-proton thermal coupling, becomes negligible at these altitudes. In the absence of a mechanism for the protons to lose their energy, the proton thermal energy remains "trapped" locally. Overall, the protons are about two times hotter than the electrons. This can be understood

as follows. Electrons can efficiently conduct excessive heat from the hot corona down to the much cooler transition region and chromosphere, where the radiative cooling rate is considerably higher due to high plasma densities and low temperatures. Since we assume the radiated energy does not interact with the plasma (which is a reasonable approximation for the corona), the transition region can be viewed as a heat sink for electrons. At lower altitudes this mechanism also cools the protons due to thermal coupling between the two species, but this process becomes inefficient above the transition region.

The importance of a two-temperature description can be further demonstrated if we compare the above result to that obtained in a single temperature simulation. This is achieved by setting $p_p = p_e$ in Eqs. (2.2), (2.5), and (2.6). All other free parameters are kept the same as the two-temperature simulation. Figure 2.7 shows the resulting plasma temperature (left) and velocity field (right) in a meridional plane. This should be compared to the corresponding quantities obtained from the two-temperature simulation shown in Figure 2.4 (velocity) and Figure 2.6 (electron and proton temperature). One can see that in the single-temperature case, the corona is cooler and the solar wind is slower than in the two-temperature case, even though the Poynting flux injected into the system is the same. A single temperature description is equivalent to the assumption that the electrons and protons are in thermodynamic equilibrium, so that wave dissipation and heat conduction affect the plasma as a whole. In the absence of electron-proton decoupling, less thermal energy can be retained by the protons. This causes more thermal energy to be removed from the system by heat conduction and subsequent radiative cooling. The resulting steady state must therefore be less energetic as a whole for a single-temperature case.

We conclude that a two-temperature description is more realistic than a single-temperature one. The effects of decoupled protons may become more important when describing solar eruptions, where the ejecta can be magnetically connected to the Sun,

allowing for thermal energy to flow back to the Sun, thus producing unrealistic shock structures. This is further discussed in *Jin et al.* (2013).

2.4.3 The Role of Wave Dissipation

The AWSoM model is the first global model to unify the treatment of open and closed field lines. This is a direct result of Eq. (2.13), which describes a wave energy dissipation rate that automatically adjusts to the magnetic field topology, allowing either reflected-wave dissipation or counter-propagating wave dissipation to dominate.

The interplay between the two types of dissipation mechanisms can be best studied by examining the evolution of the wave energy and its coupling to the plasma along typical magnetic structures, like helmet streamers and coronal holes. Figure 2.8 shows the electron and proton temperature, as well as the plasma density, extracted along a magnetic loop in the helmet streamer (marked by the blue field line in Figure 2.6). We note that our model reproduces sufficiently well the sharp density and temperature gradients known to exist in the transition region. The temperature profile of the electrons (top panel) is almost flat in the corona, while the protons become hotter at the top of the streamer. In order to study in more detail how this peak is created, we must examine the wave energy density and dissipation rates of both wave polarities. These are shown in Figure 2.9. The top panel shows the energy densities of the parallel and anti-parallel waves along the same field line. The two wave modes have their maximum energy at opposite foot points of the streamer loop, since only a single wave mode is launched from each point on the inner boundary. One can see that the energy density sharply decreases at the middle of the loop, reaching negligible amounts at the other foot point. The energy density dissipation rate (bottom panel), is largest in the transition region. Above the transition region, the dissipation rate of each wave mode smoothly decreases from its maximal value at its respective foot point due to the reflected wave dissipation term in Eq. (2.13). At the top of the loop,

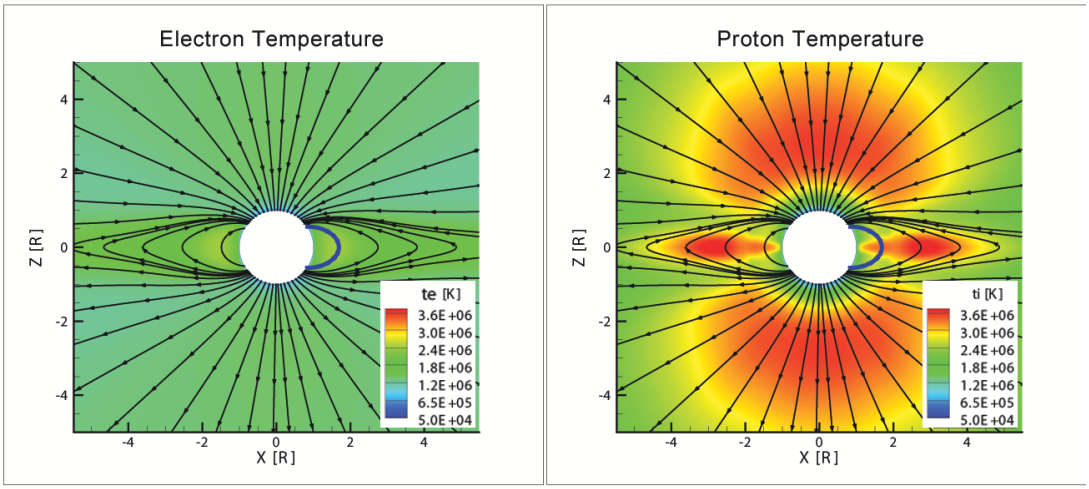

Figure 2.6: *Electron temperature (left) and proton temperature (right) in a meridional plane for an ideal dipole simulation. The black curves show the magnetic field. The blue curve denotes the closed field line used for extracting the data used in figures (2.8) and (2.9).*

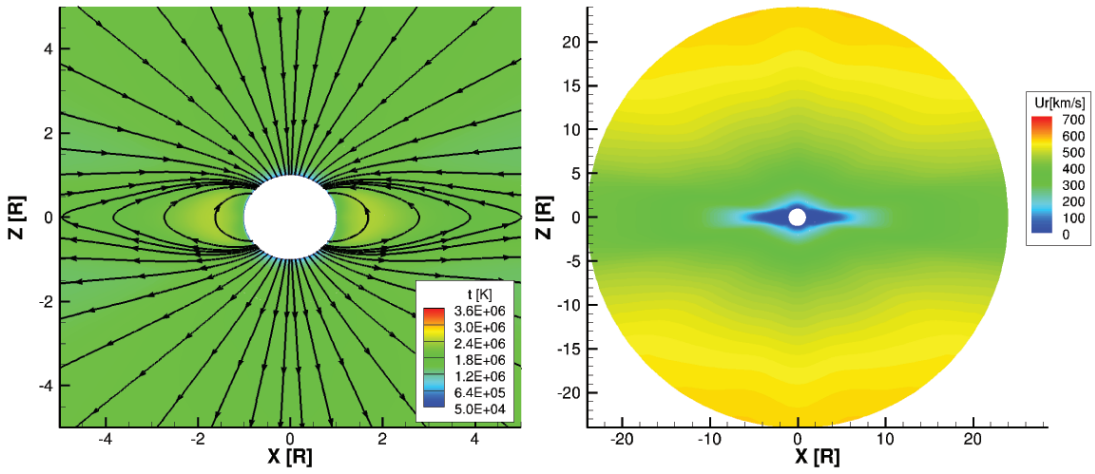

Figure 2.7: *Steady-state solution in a meridional plane for the single-temperature, ideal dipole simulation. Left: plasma temperature. Right: Radial speed and magnetic field lines.*

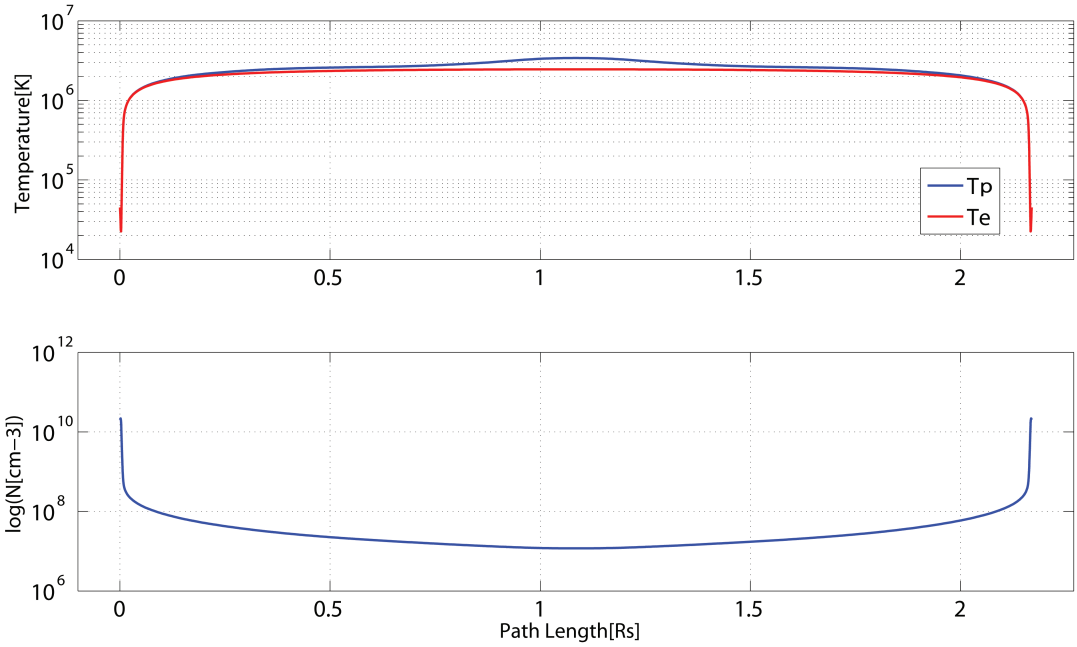

Figure 2.8: *Plasma properties extracted along a loop in the streamer belt of an ideal dipole solution. Top: electron and proton temperatures. Bottom: density. Data was extracted from the loop shown in purple in figure (2.6).*

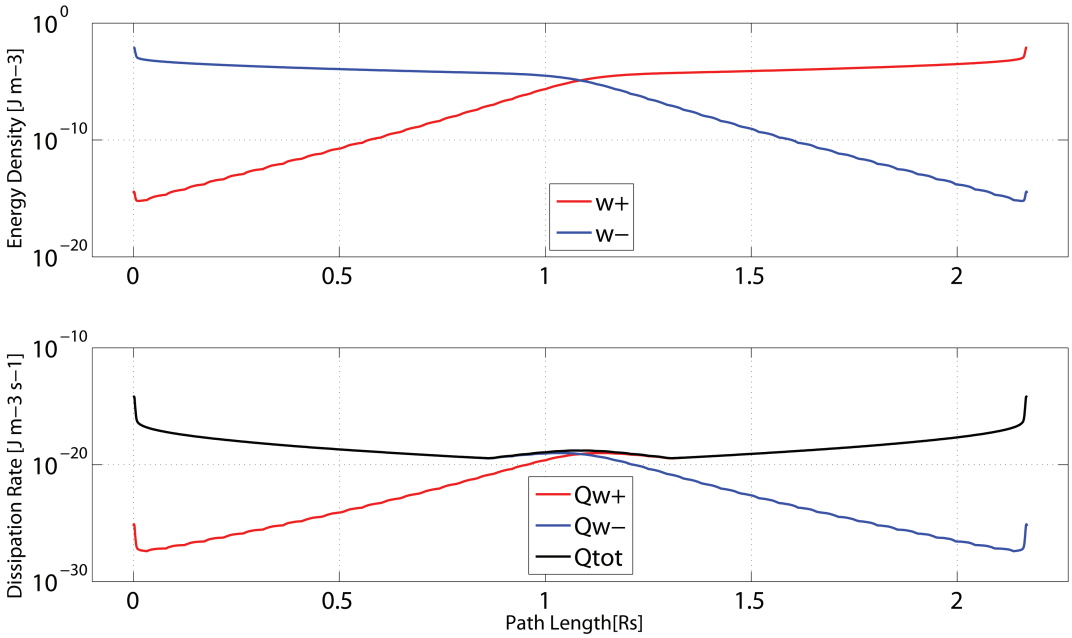

Figure 2.9: *Wave energy densities (top) and energy density dissipation rates (bottom) for both wave polarities, extracted along a loop in the streamer belt of an ideal dipole solution, shown as the purple field line in figure (2.6).*

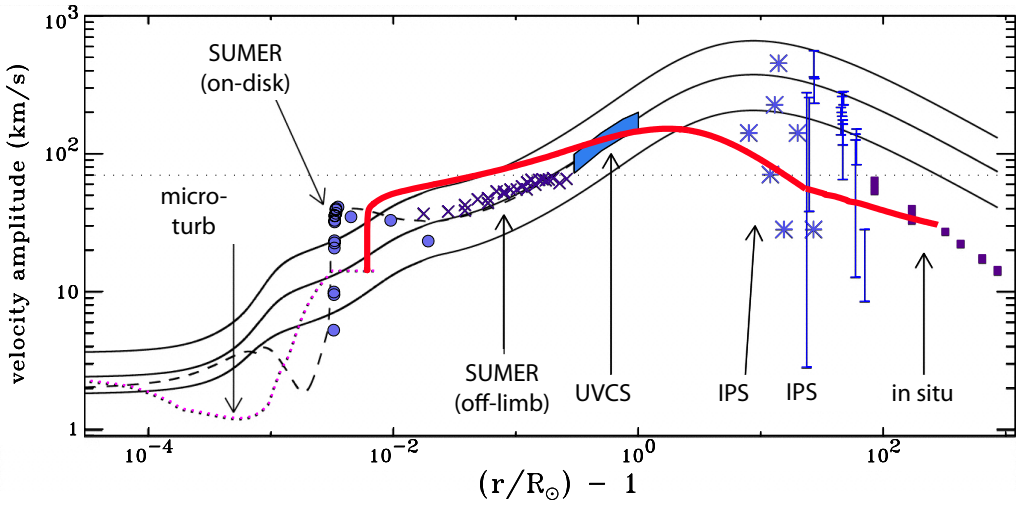

Figure 2.10: *Velocity perturbation vs. heliocentric distance from model results and observations. The figure shows AWSoM model results (red curve) overlaid on a compilation of measurements of the wave amplitude, adapted from Figure 9 from Cranmer and van Ballegooijen (2005). Blue symbols represent observed values, while the black solid curves show the Cranmer and van Ballegooijen (2005) model results. The AWSoM results were extracted along a polar coronal hole field line, for an ideal dipole simulation. The numbers (1) - (7) indicate observation sources, see Cranmer and van Ballegooijen (2005).*

the wave energies of the two modes become comparable, and the counter-propagating term kicks in. This produces a local maximum in the total dissipation rate, and the peak in proton temperature.

The electron temperature in the streamer belt is about 70% higher than that in the coronal holes (see Figure 2.6). This can be understood if we notice that wave dissipation rates will be higher in closed-field regions, where two wave modes are injected into a single field line, while in coronal holes dissipation is only due to reflections. As a result, more wave energy will be available in coronal hole flux tubes, enabling higher acceleration rates due to the action of wave pressure. Thus the temperature distribution is closely related to the velocity field distribution. Examining Figure 2.4, we can immediately recognize that the regions of lower temperatures in the coronal holes correspond to the source region of fast solar wind flows, while the hotter streamer is embedded in a region of slow solar wind. Thus, our choice of wave

mechanism automatically produces the observed large-scale temperature and velocity structure of the solar corona and wind.

In order to complete the discussion of wave dissipation, and to further justify our proposed turbulent wave dissipation mechanism, we must examine whether the resulting wave field is consistent with observations. Figure 2.10 shows the amplitude of the velocity perturbation, $\delta\mathbf{u}$, associated with the outgoing wave, as a function of radial distance, calculated along a polar coronal hole. At lower altitudes, where $Te < 220,000K$, the profile was rescaled in order to compensate for the artificial transition region broadening, as discussed in Section 2.3.1.1. This profile is qualitatively in good agreement with the observations compiled in *Cranmer and van Ballegooijen* (2005) (see Figures 7 and 15 therein). In particular, the sharp gradient in wave amplitude close to the inner boundary occurs at roughly the same altitude ($10^{-2}R_s$), and reaches a similar magnitude (40 $km\ s^{-1}$) in both the model and the observations. The second local maximum occurs around $2R_s$, where the wave amplitude reaches 150 $km\ s^{-1}$. Finally, the wave amplitude at 1 AU is about 30 $km\ s^{-1}$. These fall within the range of observed values. It should be noted that modeled values will be somewhat different in a steady state solution corresponding to a specific Carrington rotation. Since the available observations span several rotations, we regard the steady-state solution of an ideal dipole field as a proxy for a generic solar minimum configuration.

2.5 Model-Data Comparison for Solar Minimum

In order to directly compare our model results with the variety of available observations, we simulate a steady-state solution for Carrington Rotation CR2063 (11/4/2007 - 12/2/2007), which took place during solar minimum. We compare our results to remote observations in the lower corona, as well as in-situ observations in the solar wind. We can thus test whether the model can simultaneously reproduce observations at these highly different environments, while the entire system is driven only by the

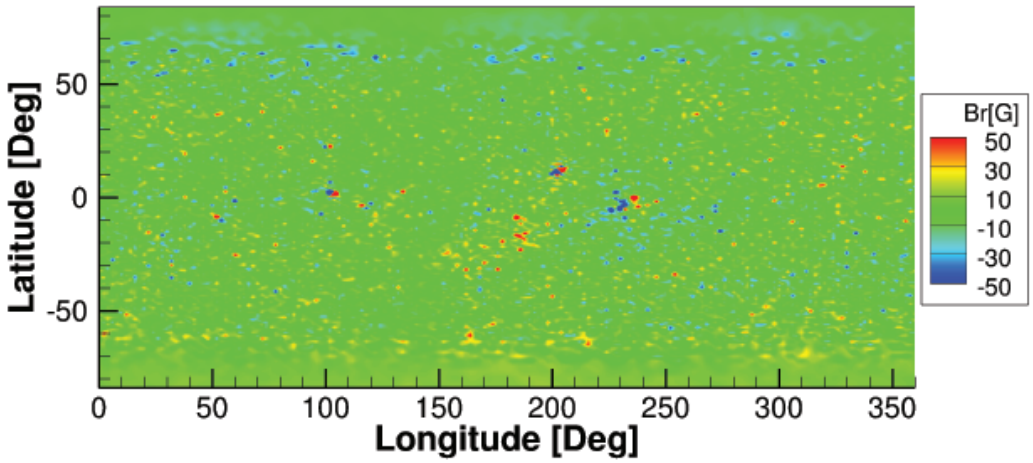

Figure 2.11: *Boundary condition for the radial magnetic field for CR2063, obtained from an MDI magnetogram with polar interpolation. Note that the color scale was modified so that the large scale distribution can be seen. However magnetic field intensity can reach up to 500 G in the small regions in the vicinity of active regions.*

rather simple boundary conditions described in Section 2.3.2.

2.5.1 Model Input and Limitations

As an input to the model, we set $L_{\perp,0} = 25km/\sqrt{T}$, $C_{refl} = 0.06$ and $\overline{\delta u} = 15\ km\ s^{-1}$. For the magnetic field, we use a line-of-sight synoptic magnetogram obtained by the Michelson-Doppler Interferometer (MDI) instrument on board the Solar and Heliospheric Observatory (SOHO) spacecraft (*Scherrer et al.*, 1995). The magnetogram radial field is used to determine the inner boundary condition for the model.

Line-of-sight magnetograms possess an inherent uncertainty at the polar regions, since the line-of-sight to these regions is almost perpendicular to the radial direction. We therefore use a polar-interpolated synoptic magnetogram, provided by the Solar Oscillations Investigation (SOI) team (*Sun et al.*, 2011). Synoptic magnetograms are also known to possess uncertainties in the magnetic field intensity over the entire disk. Several studies have shown that the intensity derived from magnetograms may vary

depending on spatial and temporal resolutions, location on the disk, instrument noise and zero-offset bias, and level of solar activity (c.f. *Pietarila et al.* (2012)). Although some of these difficulties are mitigated by proper calibrations, synoptic magnetograms from different instruments may still give different results. MDI data have been found to scale by a factor of 0.6 - 1.4 compared to other instruments (*Liu et al.*, 2012; *Pietarila et al.*, 2012). Since the "true" magnetic field intensity is not known, we increased the magnetogram field for CR2063 by a factor of 2, which we estimated by comparing modeled and observed coronal hole boundaries. We note that without scaling, the magnetogram leads to unrealistically large coronal holes in the model, suggesting that the input field is too weak to contain the plasma and field lines that should be closed are opened up by the plasma flow. The resulting boundary condition for the radial magnetic field is shown in Figure 2.11.

It should be noted that the use of synoptic magnetograms, which are collected over a period of a full solar rotation (about 27 days), limits our ability to capture short-lived magnetic structures. The steady-state solution we obtain should therefore be considered as simulating the average state of the system over the period covered by the magnetogram.

2.5.2 Coronal Density and Temperatures Profiles

Figure 2.12 shows the three-dimensional steady-state solution. The solar surface is colored by the radial magnetic field. Streamlines denote magnetic field lines, colored by radial speed. Also shown are temperature iso-surfaces for electron and protons (left and right panels, respectively). As expected for a solar minimum configuration, the coronal holes are mostly concentrated around the poles, with some open field lines emerging from lower latitudes. Proton temperatures reach about 3 MK, while the electron reach 1.5 MK, consistent with our previous analysis for the ideal dipole case.

In order to compare the predicted temperature and density profiles in the corona

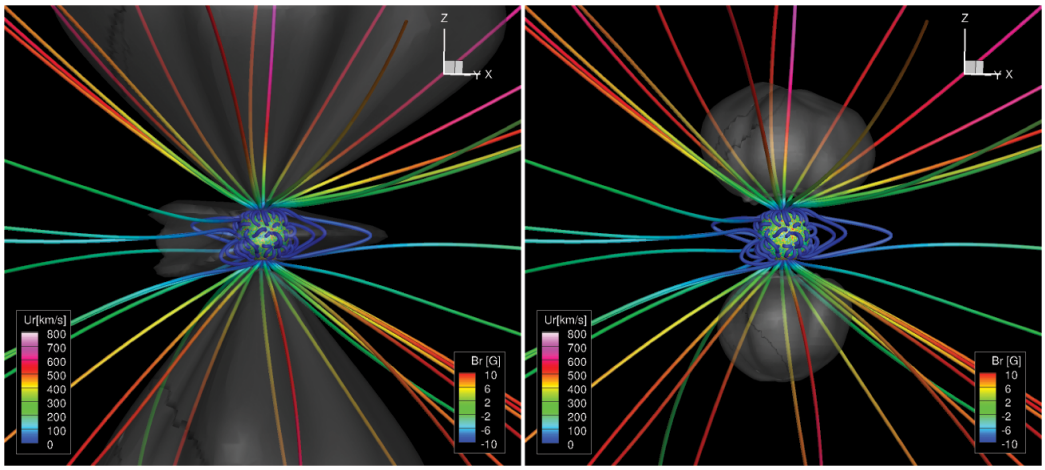

Figure 2.12: *Results for CR2063. Solar surface colored by radial magnetic field strength. Field lines are colored by radial speed. The left panel shows a temperature iso-surfaces for electrons at 1.3MK. The right panel shows a temperature iso-surface for protons at 3MK.*

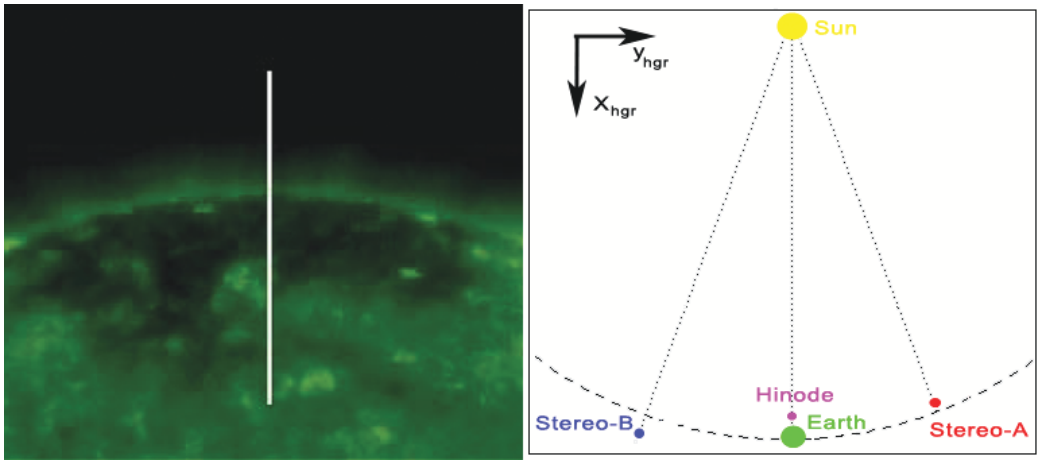

Figure 2.13: *Left panel: Location of the EIS slit used to observe coronal hole spectra for electron temperature and density diagnostics. The slit is overlaid on an EUV image from the Extreme ultraviolet Imaging Telescope (EIT) on board SOHO, taken on November 16, 2007. The SUMER slit was at the same E-W location as the EIS slit, but stretched into higher altitudes, up to 1.3$R_{\odot}$. Right panel: positions of the STEREO-A, STEREO-B and Hinode (Solar-B) spacecraft for November 17, 2007, projected on the x=0 plane of the Heliographic Inertial (HGI) coordintate system.*

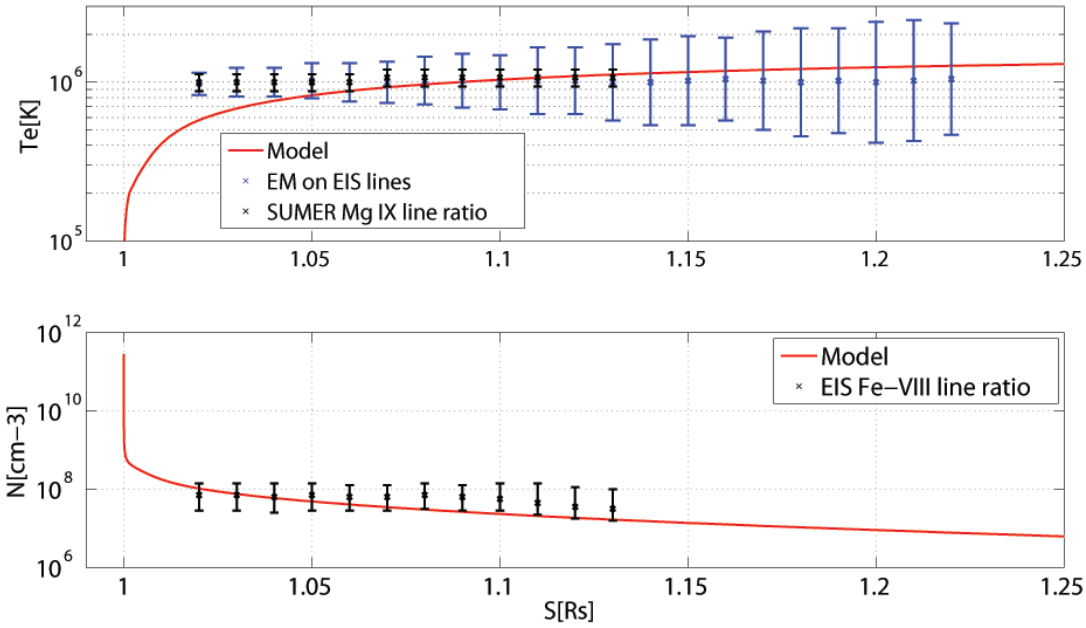

Figure 2.14: *Observed vs. predicted electron temperature (top panel) and density (bottom panel) radial profiles. The electron temperature was calculated using two methods: from the Mg IX line intensity ratio (blue symbols) measured by SUMER, and the EM loci method (black symbols) using EIS spectral lines. The density was calculated from the EIS Fe VIII line intensity ratio.*

to observations, we use spectral line intensities measured by the EUV Imaging Spectrometer (EIS) on-board the Hinode (Solar-B) spacecraft (*Culhane et al.*, 2007) and the Solar Ultraviolet Measurements of Emitted Radiation (SUMER) instrument on board SOHO (*Wilhelm et al.*, 1995). EIS observations were performed with the slit pointed as shown in Figure 2.13 during November 16, 2007. The SUMER slit was placed at the same position as the EIS slit in the east-west directions, but stretched radially from 1.0 to $1.3R_s$. The density was calculated using the EIS Fe VIII line intensity ratio. The electron temperature was calculated using two methods: the line intensity ratio between two Mg IX lines at 694.0Å and 706.0Å observed by SUMER, and the EM loci method applied to EIS lines, as described in *Landi* (2008). It should be noted that the spectral line intensities used in these measurements are integrals along the line-of-sight. In order to recover the density and temperature profiles responsible for the emission it was assumed that the coronal hole plasma is optically thin in these wavelengths. Observational data below $1.02R_s$ was discarded due to the presence of cold spicule plasma, which is not optically thin. The model results were extracted along a magnetic field line passing through the center of the coronal hole and overlapping the slit. The profile was remapped in order to account for the artificial broadening of the transition region, as we described in Section (2.3.1.2). The transition region broadening affected results up to $1.02R_s$. Comparison of the observations to model results is shown in Figure 2.14. The top panel shows the density, while the bottom panel shows the electron temperature. As can be seen, the modeled electron density agrees rather well with the measured density at all heights (and are within the uncertainties of the measured values), while the modeled temperature agrees with the data above a distance of $1.05R_s$. The apparent disagreement between measured and modeled electron temperatures at altitudes lower than $1.05R_s$ can be due to line of sight effects. In fact, the line of sight at those altitudes crosses field lines at very different distances from their footpoints. The field lines closest to the plane of

the sky are crossed at distances where their plasma is still too cold to emit the Mg IX lines; thus the observed Mg IX emission is coming from field lines whose footpoints are located at lower latitudes and are crossed by the line of sight at positions where their plasma is hot. At higher altitudes, this geometrical effect is diminished and the comparison of the modeled temperature at the center of the coronal whole to the observations is more appropriate. In Chapter 3, a more careful comparison of model results to line of sight temperature measurements is performed, by considering the contribution of plasma all along the line of sight (see Section 3.7.5).

2.5.3 Multi-Point EUV and Soft X-Ray Images

Full-disk emission images of the lower corona serve as an important diagnostic tool for global models. The photon flux in a given spectral line will in general depend on the electron density and temperature distribution along the line of sight to the detector, and therefore comparing model results to full-disk images in different spectral bands will allow us to test how well the predicted three-dimensional temperature and density distributions agree with the observations. In order to make the comparison, we must create synthetic line-of-sight images from the model results. In the most general case, this requires solving the full radiative transfer problem, which can be rather complex. For a first-approximation comparison, however, it is sufficient to assume the plasma is optically thin in the wavelengths under consideration. In this limit, the number of photons in a spectral band i, detected in a unit time at a given pixel in the imager, is given by:

$$\Phi_i = \int n_e^2 f_i(n_e, T_e) dl \quad [dN s^{-1}], \tag{2.18}$$

where dl is a path length along the line-of-sight, n_e and T_e are the electron density and temperature, respectively, and $f_i(n_e, T)$ is the instrument response function in that

band. Φ_i is measured in units of number of photons per second, dNs^{-1}. The procedure used to calculate the synthetic full-disk images is identical to that presented in *Downs et al.* (2010). Since our model does not simulate the wind-induced departures from ionization equilibrium for the entire computational domain, the response functions f_i are constructed from the CHIANTI 7.1 atomic database (*Dere et al.*, 1997; *Landi et al.*, 2013), based on coronal elemental abundances (*Feldman et al.*, 1992), and assuming ionization equilibrium obtained from the ionization and recombination rates appearing in *Landi et al.* (2013). The assumption of ionization equilibrium can be relaxed if one can calculate the ionization status of the emission ions, as is done for selected field lines in Chapter 4.

We here compare our model results to both EUV and soft X-ray images. We use EUV images obtained by the Extreme Ultraviolet Imager (EUVI) on board the two STEREO spacecraft (*Howard et al.*, 2008). For soft X-ray images, we use the X-ray Telescope (XRT) on board the Hinode (Solar-B) mission (*Kano et al.*, 2008; *Matsuzaki et al.*, 2007). Both observed and synthesized images were taken around 2007-11-17, 01:00:00 UTC, which is approximately at the middle of the Carrington rotation, making the comparison to a steady-state solution most appropriate. At the time of observation, STEREO-A and STEREO-B were separated by about 40.5 in heliographic longitudes, with Hinode's position roughly in between them, along the Sun-Earth line. This set-up allows for a multi point-of-view model-data comparison. The respective locations of the spacecraft are shown in Figure 2.13. In preparing the observed images from the raw data, including calibration, noise reduction and normalization of the photon flux by the exposure time, we used the SolarSoft (SSW) package written in IDL (*Freeland and Handy*, 1998).

For EUVI-A and EUVI-B comparison, we use the 171Å, 195Å and 284Å wavelengths, which are dominated by the ions Fe IX, Fe XII, and Fe XV, respectively. The corresponding temperature ranges are $1MK$, $1.4MK$, and $2.2MK$. The images

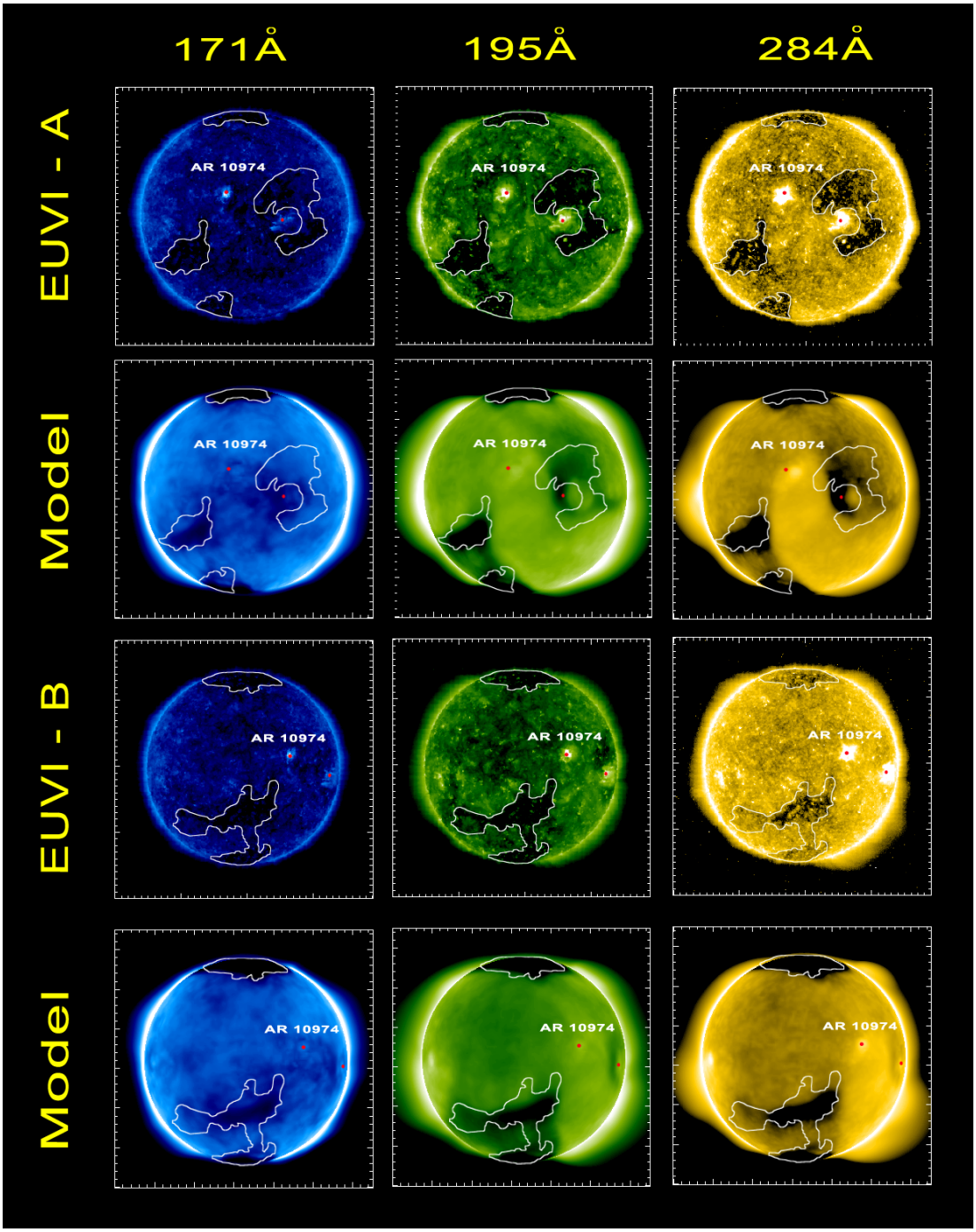

Figure 2.15: *STEREO/EUVI images vs. synthesized images in three different bands using the S1 filter. Top two panels: observations and synthesized images for EUVI-A (STEREO Ahead). Bottom two panels: observation and synthesized images for EUVI-B (STEREO Behind). The spacecraft location at the time of observation is shown in the right panel of figure (2.13).*

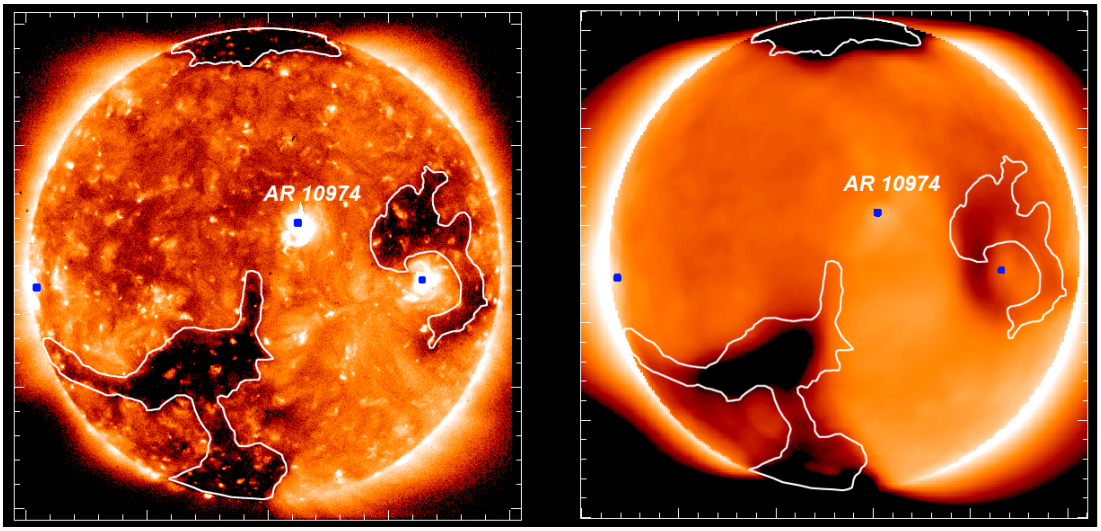

Figure 2.16: *Observed (left panel) and synthesized (right panel) images for the Hinode/XRT instrument, using the Al-Poly filter. The location of the Hinode spacecraft at the time of observation is shown in the right panel of figure (2.13).*

were obtained using the S1 filter, and the response tables for the synthesized images were calculated accordingly. The comparison is shown in Figure 2.15. Each column corresponds to a different spectral band, with temperature increasing from left to right. The top two rows show observed and predicted emission for STEREO-A, while the two bottom rows show a comparison for STEREO-B. Figure 2.16 shows the comparison of model results to the XRT soft X-ray image, taken using the thin Al-poly filter, which is most sensitive to temperatures between $2MK$ and $10MK$ (*Golub et al.*, 2007). The left panel shows the observed image, while the right panel shows the synthesized image.

We marked the location of the active region and other bright features on the solar disk in both observed and synthesized images. Note that there is only a single active region with a NOAA designation for that time period. Although some traces of the active region appear in all synthesized images, the model best captures the intensity of this region in the 284Å band. In all bands, the active region is fainter compared with the observations. This suggests that in the modeled active regions,

the material possessing the corresponding temperatures is not dense enough and/or hot enough to produce sufficient radiative power. This discrepancy between observed and modeled active regions can be attributed to the fixed boundary conditions used in this simulation. First, the magnetic field at the inner boundary was derived from a synoptic magnetic map, constructed from disk-center observations acquired over an entire Carrington rotation. Such a map might not reflect the instantaneous magnetic field strength that exists at the moment of the observations, especially in the highly variable active regions. In addition, in the real corona and chromosphere, the high heating rates in the active region will lead to heat being conducted down to the chromosphere, resulting in chromosphere evaporation, which will cause more plasma to flow up into the active region loops (c.f. *Klimchuk* (2006)). Such a process is completely absent from our model, since we have a fixed density at the inner boundary. A dynamic boundary condition should be considered if one wants to more realistically simulate active regions in a global model.

In order to see how well the model reproduces the overall topology, we manually trace the coronal hole boundaries on the observed images, and overlay the resulting contour on the synthesized images. As can be seen, the model correctly reproduced the location and approximate shape of the coronal holes. Although the overall topology agrees quite well, there are some discrepancies between the predicted coronal hole boundaries and the observed ones. It is important to note all EUV imagers suffer from some degree of stray light scattering into the imaging plane. The stray light contribution to the detected intensity is negligible in the brighter regions of the image, but can contribute significantly in the fainter regions. *Shearer et al.* (2012) found that stray light contamination in EUVI can reach up to 70% for the EUVI instrument, resulting in observed coronal holes that are likely brighter than in reality. The topology is best captured by the soft X-ray case, which reveals the hotter, and therefore higher, layers of the corona. A possible interpretation is that the model

better predicts the temperature structure at these higher altitudes than closer to the inner boundary.

Finally, we note that some of the smaller scale details are not captured by the model, which can be attributed to the following: 1. Magnetogram accuracy and resolution: since the magnetogram field is the only external input to the model, information that is not well captured in the magnetogram will not be passed to the model. 2. A steady-state solution with fixed magnetic field boundary conditions cannot capture transient phenomena. 3. The MHD model cannot resolve small-scale physical processes.

2.5.4 Solar Wind Structure up to 2AU and Comparison to In-situ Measurements

By coupling the solution in the SC component discussed in the previous sections to the IH component, we obtained a steady-state solution for CR2063 up to 2AU. Figure 2.17 shows the 3D structure of the solution, with magnetic field lines and the current sheet surface (where $B_r = 0$) colored by the radial speed. The presence of interaction regions between the fast and slow streams is apparent.

One of the most important features of the solar wind is the latitudinal distribution of fast and slow solar wind streams, most comprehensively observed by the Ulysses spacecraft, orbiting the Sun in a nearly polar orbit. In order to examine how well the model reproduces these structures, we wish to compare our results to Ulysses measurements covering as wide a latitudinal range as possible. This requires an observation period much larger than a single Carrington Rotation, but since CR2063 took place within solar minimum, the latitudinal distribution of fast and slow wind streams does not change considerably from one Carrington Rotation to another. We therefore compare our model results to measurements taken from June 2007 to June 2008 (i.e. during a period of a year centered around the simulation time). Ulysses

covered a latitude range between -55 to +80 degrees and heliocentric distances between 1.4 to 2 AU. Comparison of modeled wind speed, proton density, and dynamic pressure are shown in Figure 2.18. The shaded region shows the period for which the magnetogram used as boundary condition was obtained. Note that this is a comparison between a steady state solution and a year worth of measurements, and therefore we do not expect to capture small scale or transient features. We also expect the agreement between the simulation and the observations to worsen as we move further away from the magnetogram time. What most concerns us here is to obtain the correct average properties of both the fast (high latitude) and slow (low latitude) wind. As can be seen from the top panel, the model has correctly captured the fast (800 $km\ s^{-1}$) and slow (300 $km\ s^{-1}$) wind speeds. The modeled proton density, shown in the middle panel, is only slightly higher than the observed one, and they are in very good agreement by order of magnitude. The bottom panel shows the wind dynamic pressure carried by the protons. At the heliocentric distances under consideration, this is the dominant energy component. As can be seen, here again the model and observations agree quite well.

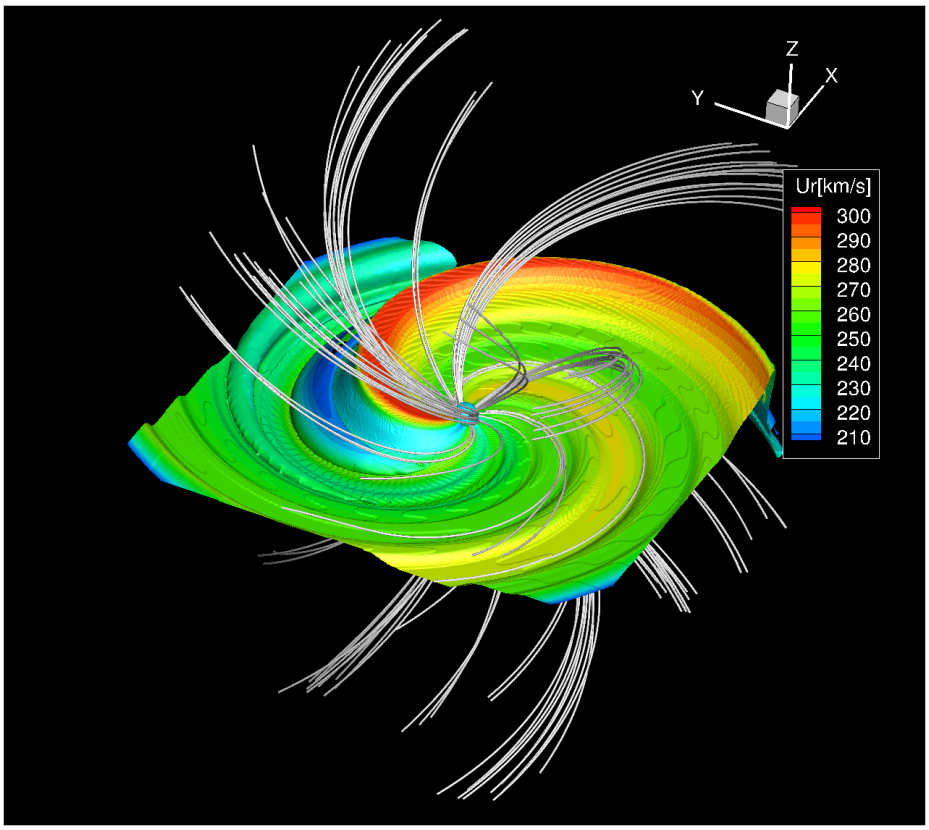

Figure 2.17: *Results for CR2063 up to a heliocentric distance of 2AU. Surface shows the location of the current sheet (where $B_r = 0$), colored by the radial speed. Stream lines show the magnetic field.*

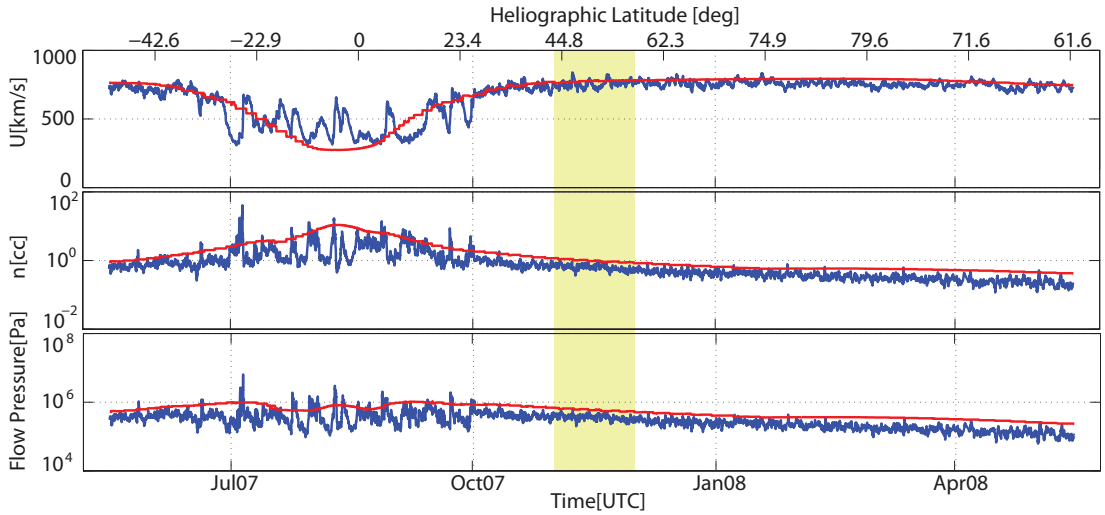

Figure 2.18: *Model-Data Comparison for CR2063 along Ulysses's orbit. Blue curves show Ulysses data and red curves show model data extracted along Ulysses's orbit. The shaded region denotes the period covered by the input magnetogram which was used to obtain the steady-state solution. The top panel shows the solar wind radial speed. The middle panel shows the proton density, while the bottom panel shows the proton dynamic pressure.*

Thus, we have shown that our simulation has correctly predicted the distribution of wind acceleration in the inner heliosphere for CR2063, a solar minimum configuration. To complete this discussion, it would be instructive to examine the energy associated with the Alfvén waves at these distances. We refer back to the results shown in Figure 2.10, which has shown that the wave amplitude obtained for solar minimum (ideal dipole) case is consistent with the results obtained by several observation campaigns.

2.6 Conclusions

In this Chapter, we presented and analyzed the AWSoM model, which is aimed at simulating the solar and heliospheric environment from the upper chromosphere to deep in the heliosphere within the extended-MHD approximation. In this model, a single heating mechanism is assumed: turbulent dissipation of Alfvén waves. This mechanism is controlled by a simple set of three adjustable parameters, namely the chromospheric Poynting flux, the transverse correlation length, and a pseudo-reflection coefficient.

Compared to previous global models, the wave dissipation mechanism assumed here is capable of treating both open and closed field line regions, and we do not need to a-priori determine whether a field line is open or closed. Rather, the open and closed magnetic structures emerge naturally and self-consistently with the distribution of solar wind speeds and coronal heating rates. This eliminates the need for empirical boundary conditions or ad-hoc geometric heating functions.

We analyzed our choice of wave dissipation and adjustable parameters by simulating a steady-state solution for an ideal dipole configuration. We demonstrated that the sharp gradients in temperature and density between the chromosphere and the corona are reproduced, as well as the thermal differences between the polar coronal holes and the streamer belt. As a further validation, we compared the predicted ra-

dial profile of wave energy to a large number of observations, ranging from the solar surface and up to 1AU. We found the predicted and observed profiles to be in good agreement.

Model-data comparison for CR2063 shows that the model simultaneously predicts the thermal structure near the Sun, as well as the flow properties of the solar wind at distances of 1-2 AU. This capability is a major step forward in global modeling of the entire chromosphere-to-wind system. We demonstrated this by comparing: 1. modeled electron density and temperature profiles to EIS and SUMER measurements 2. synthesized EUV and X-ray full disk images to observed ones, and 3. predicted solar wind properties to in-situ measurements obtained by Ulysses.

The two-temperature / extended MHD description better describes the energetics of the system compared to a single-temperature description. For the latter case, a higher Poynting flux would be required in order to sufficiently accelerate the fast wind to observed values. In the two-temperature case, the combined action of electron heat conduction and electron-proton thermal decoupling will modify the spatial distribution of heating and acceleration rates. The two-temperature description has the advantage of allowing us to extend model-data comparisons to a wider set of observables. In the present work, we tested the predicted electron properties against remote observations of the lower corona, and found them to be in good agreement at altitudes above 1.05 R_s. Predicted proton properties were compared to in-situ measurements in the solar wind. These were found to agree reasonably well, although a more complete thermodynamic description, such as the inclusion of collisionless heat conduction, might improve the results.

A robust model of the ambient solar corona and solar wind is a crucial building block in space weather prediction. The AWSoM model can be used to simulate eruptive events such as CMEs (*Jin et al.*, 2013), as well as to predict the location and properties of co-rotational interaction regions (CIR's) in the inner heliosphere.

The small set of adjustable parameters can also provide a testing ground for various coronal heating models based on turbulent dissipation.

Finally, we mention possible ways to improve the present model. First, our model does not directly simulate wave reflections, and we assume a uniform reflection coefficient throughout the system. A more detailed and physics-based description of the wave dynamics is required to self-consistently determine the reflection coefficient from the local state of the plasma. Such a treatment is included in van der Holst et al. (2014). Second, the extended MHD description cannot account for the supra-thermal electron population. These electrons can carry a significant fraction of the thermal energy of the plasma, and affect the dynamics through the action of collisionless heat conduction (which becomes important at distances above 10 R_s).

CHAPTER III

Alfvén Wave Transport and Heating in the Lower Corona

3.1 Introduction

Direct and conclusive observational evidence to support the different mechanisms invoked for Alfvén wave dissipation in the solar corona is hard to obtain, due in part to the inherent uncertainty in remote sensing measurements. In this Chapter, we examine whether heating due to a turbulent cascade of Alfvén waves, as described by the AWSoM model, is a viable candidate for coronal heating by performing independent observational tests. Apart from comparing the predicted electron density and temperature to observations, we must produce from the model an observable that is related to the Alfvén wave amplitude, in order to verify that the wave energy distribution is consistent with observations.

Extreme Ultraviolet (EUV) emission by heavy ions provides us with critical tools to study the physical properties and dynamic processes of coronal plasma. Coronal abundances of ions heavier than Helium are low, and therefore these elements do not affect the overall dynamics, but nevertheless their emission in selected spectral lines is routinely observed by spaceborne observatories. While the total line flux depends mainly on the electron density and temperature, the line width is related to

the dynamical state of the ion responsible for the emission. Specifically, unresolved motions will give rise to Doppler broadening of the spectral line. There are two mechanisms that dominate line broadening in the solar corona: thermal ion motions (due to their finite temperature), and non-thermal ion motions. Non-thermal motions of coronal ions have been suggested to be due to transverse Alfvén waves (e.g *Hassler et al.*, 1990; *Banerjee et al.*, 1998; *Doyle et al.*, 1998; *Moran*, 2001; *Banerjee et al.*, 2009). Recently, *McIntosh and De Pontieu* (2012) have reported on observational evidence that non-thermal line broadenings are correlated with Alfvénic oscillations. Non-thermal line broadening may also be associated with high speed flows taking place in nano-flares (*Patsourakos and Klimchuk*, 2006). In this work we study spectral lines formed in the quiet Sun, and therefore we do not address the contribution of nano-flares to the line width. Measuring non-thermal mass motions is a difficult endeavor, since both ion temperatures and the non-thermal motions contribute to the observed line width and therefore some assumptions need to be made on the former in order to measure the latter (see *Phillips et al.*, 2008, and references therein). *Hahn et al.* (2012); *Hahn and Savin* (2013) studied the observed line broadening in a coronal hole, and found evidence of wave damping. Despite many efforts, direct observational evidence of wave damping in the equatorial corona remain inconclusive. This may be attributed to line-of-sight effects, whereby different spectral lines are actually emitted from different regions.

Several numerical models were aimed at simulating Alfvénic perturbations in the solar corona and predicting the observed non-thermal motions. *Ofman and Davila* (1997) generated Alfvén waves in a 2.5D resistive magnetohydrodynamics (MHD) model of an idealized coronal hole. In *Ofman and Davila* (2001) and *Ofman* (2004) this work was extended to a multi-fluid description in order to directly simulate the motions of the emitting ion species due to a broad band Alfvén wave spectrum injected at the base. They directly calculated the resulting line-broadening and found it to

agree well with observations. Recently, *Dong and Singh* (2013) have presented results from test-particle simulations showing that a Maxwellian distribution of ion speeds will be broadened when subjected to Alfvén waves. They found that the Maxwellian shape is more likely to be preserved during this process when acted on by a wave-spectrum, compared to a monochromatic wave. While these efforts allowed for a detailed description of wave-induced motions, they were restricted to prescribed and idealized magnetic fields. In this work, we wish to extend these efforts to a global model, in which the magnetic field evolves self-consistently with the plasma and wave field, and whose topology can be derived from synoptic maps of the photospheric magnetic field. This allows us to predict EUV line widths and compare them to observations at any location in the lower corona and along any line of sight.

The wave energy in the AWSoM model description represents the time-average of the perturbations due to a turbulent spectrum of Alfvén waves. By relating this energy to the non-thermal line broadening, and combining the 3D model results with a spectroscopic database, we are able to calculate synthetic emission line profiles integrated along the entire line-of-sight. The synthetic spectra are used in two ways. First, we compare the synthetic line widths to observations in order to test the accuracy of the model predictions of the Alfvén wave amplitude and ion temperatures. Second, the synthetic and observed total line fluxes are compared, in order to test the accuracy of the model predictions of electron density and temperature distributions along the line of sight. In addition, we directly compare the model electron density and temperature to remote measurements based on line intensity ratios. For this purpose, we perform a careful analysis of the emission along the SUMER line of sight as predicted by the model, in order to locate the region that is responsible for the relevant line emission.

This series of independent observational tests allows us to examine whether we can simultaneously account for the coronal plasma heating rate, together with the

amount of remaining (non-dissipated) wave energy. Such a comparison provides a vital benchmark for the scenario where coronal heating is due to Alfvén wave dissipation. To the best of our knowledge, this is the first time that observed non-thermal mass motions are used to test the heating mechanism in a three-dimensional global model. In the particular case of the AWSoM model, an agreement between the model results and observations would suggest that both the amount of wave energy injected into the system (i.e. the Poynting flux from the chromosphere) and the rate at which the wave energy dissipates at higher altitudes, are consistent with observations.

In order to make meaningful comparisons to observations, we require high quality, high spatial and high spectral resolution data. We selected a set of observations carried out by the Solar Ultraviolet Measurements of Emitted Radiation (SUMER) instrument on board SoHO (*Wilhelm et al.*, 1995) during 21-22 November, 1996, in which the SUMER slit was oriented along the solar east-west direction and the SUMER field of view stretched radially from 1.04 to 1.34 solar radii outside the west limb. The AWSoM model was used to create a steady-state simulation for Carrington Rotation 1916 (11 Nov. - 9 Dec. 1996), from which we produced synthetic spectra in selected SUMER lines. The radial orientation of the slit allows us to compare predicted and observed quantities as a function of distance from the limb.

3.2 Thermal and Non-thermal Line Broadening

Unresolved thermal and non-thermal motions of ions will cause emission lines associated with these ions to exhibit Doppler broadening. Outside active regions, the resulting line profile can be approximated by a Gaussian, whose width depends on both the thermal and non-thermal speeds. In the most general case where the non-thermal motions are assumed to be random, the observed full width half maximum

(FWHM) of an optically thin emission line will be given by (*Phillips et al.*, 2008):

$$FWHM = \sqrt{\Delta\lambda_{inst}^2 + 4ln(2)\left(\frac{\lambda_0}{c}\right)^2\left(\frac{2k_BT_i}{M_i} + v_{nt}^2\right)}, \tag{3.1}$$

where $\Delta\lambda_{inst}$ is the instrumental broadening, λ_0 is the rest wavelength, c the speed of light, k_B the Boltzmann constant, T_i and M_i are the temperature and atomic mass of ion i, respectively, and v_{nt} is the non-thermal speed along the line-of-sight. It is evident from Eq. (3.1) that one cannot determine the separate contributions of thermal and non-thermal motions from the observed FWHM alone. Instead, one must either make some assumption about the ion temperatures or use some model that describes and predicts the magnitude of v_{nt}. In this work, we take a different approach, in which we predict both the ion temperatures, T_i, and the non-thermal speed, v_{nt} at every location along the line of sight from AWSoM global model of the solar atmosphere, and compare the resulting spectra to observations. For this purpose we assume that the non-thermal motions of coronal ions are due to transverse Alfvén waves, which cause the ions to move with a velocity equal to the waves velocity perturbation, $\delta\mathbf{u}$. In this case the non-thermal speed can be determined according to (*Hassler et al.*, 1990; *Banerjee et al.*, 1998):

$$v_{nt} = \frac{1}{2}\sqrt{<\delta u^2>}|\cos\alpha|, \tag{3.2}$$

where $<\cdot>$ denotes an average over time scales much larger than the wave period, and α is the angle that the plane perpendicular to the magnetic field makes with the line of sight vector. Eq. (3.2) shows that the non-thermal speed is related to the root mean square (rms) of the velocity perturbation rather than to the instantaneous vector. This is due to the fact that line broadening is associated with unresolved motions whose periods are much smaller than the integration time of the detector. The dependence on α reflects the fact that the non-thermal motions due to Alfvén

waves are inherently anisotropic. The vector $\delta\mathbf{u}$ lies in a plane perpendicular to the background magnetic field, and only its component along the line-of-sight contributes to the Doppler broadening of the emission. This dependence on the magnetic field direction is often neglected in works involving coronal holes, which might be a reasonable approximation fro coronal holes, but its effects are far more dramatic in the equatorial solar corona, where the magnetic field is more complex, and the field lines can be anywhere between perpendicular to parallel to the line of sight.

The quantity $< \delta u^2 >$ can be calculated from a wave-driven model of the solar corona which describes the evolution of the wave field coupled to an MHD plasma self-consistently. In order to calculate the ion temperatures in detail, one in principle should use a multi-species / multi-fluid MHD description (e.g. *Ofman and Davila*, 2001; *Ofman*, 2004). Such an approach to a global model of the solar atmosphere is quite involved and is beyond the scope of the present work. However, an extended-MHD description which includes separate electron and proton temperatures might be sufficient, if one assumes that the ions are in thermodynamic equilibrium with the protons. This assumption can be reasonable in the equatorial lower corona due to the high density. Thus, a model that allows the calculation of both the wave amplitude and the proton temperature should be capable of predicting the line broadening under the assumptions we just stated.

3.3 Relating the Non-thermal Speed to the Modeled Wave Energy

In the AWSoM model the wave energy evolves under the WKB approximation. The perturbations due to Alfvén waves propagating parallel and anti-parallel to the background magnetic field can be conveniently described by the Elsässer variables, defined as $\mathbf{z}_{\pm} = \delta\mathbf{u} \mp \delta\mathbf{B}/\sqrt{\mu_0\rho}$, where $\delta\mathbf{u}$ and $\delta\mathbf{B}$ are the velocity and magnetic

field perturbations, respectively, and μ_0 is the permeability of free space. The wave energy densities can be expressed as $w^{\pm} = \rho z_{\pm}^2/4$, while the square of the velocity perturbation can be obtained from:

$$\delta u^2 = \frac{(\mathbf{z}_+ + \mathbf{z}_-)^2}{4} = \frac{z_+^2 + z_-^2 + 2\mathbf{z}_+ \cdot \mathbf{z}_-}{4}. \tag{3.3}$$

On open field lines, only one wave polarity should dominate if the reflection is negligible so that the product $\mathbf{z}_+ \cdot \mathbf{z}_-$ will be zero. On closed field lines, opposite wave polarities are injected at the two foot points of the field line, giving rise to counter-propagating waves. However, in the balanced turbulent regime near the top of the closed field lines these perturbations are presumed to be uncorrelated: $< \mathbf{z}_+ \cdot \mathbf{z}_- >= 0$. Thus the last term on the right hand side of Eq. (3.3) will drop out in any magnetic topology. The square of the velocity perturbation now becomes:

$$\delta u^2 = \frac{z_+^2 + z_-^2}{4} = \frac{w^+ + w^-}{\rho}. \tag{3.4}$$

Combining Eqs. (3.2) and (3.4) we can relate the thermal speed to the wave energies as:

$$v_{nt} = \frac{1}{2}\sqrt{\frac{w^+ + w^-}{\rho}}|\cos\alpha|. \tag{3.5}$$

Note that under the WKB approximation, the wave energy density is already an average over time scales much larger than the wave period and there is no need for averaging.

3.4 Steady-State Simulation for Carrington Rotation 1916

In order to produce a realistic steady-state solution for the period during which the SUMER observations were taken, we derive the inner boundary conditions of the model using a synoptic line-of-sight magnetogram of the photospheric radial magnetic

field, acquired during Carrington Rotation (CR) 1916 (lasting from 11-Nov-1996 to 9-Dec-1996). The magnetogram was obtained by the Michelson-Doppler Interferometer (MDI) instrument on board the Solar and Heliospheric Observatory (SoHO) spacecraft (*Scherrer et al.*, 1995). In order to compensate for the reduced accuracy at polar regions, we use a polar-interpolated synoptic magnetogram, provided by the Solar Oscillations Investigation (SOI) team (*Sun et al.*, 2011). The resulting radial magnetic field is shown in Figure 3.1.

The values used for the model's adjustable parameters and inner boundary conditions for this simulation are in accordance with those used in Chapter 2 for CR2063. The use of the same values for CR1916 is reasonable since both rotations took place during solar minimum. Nonetheless, we verify the validity of the global solution used here by comparing model results to full-disk images in Section 3.7.1.

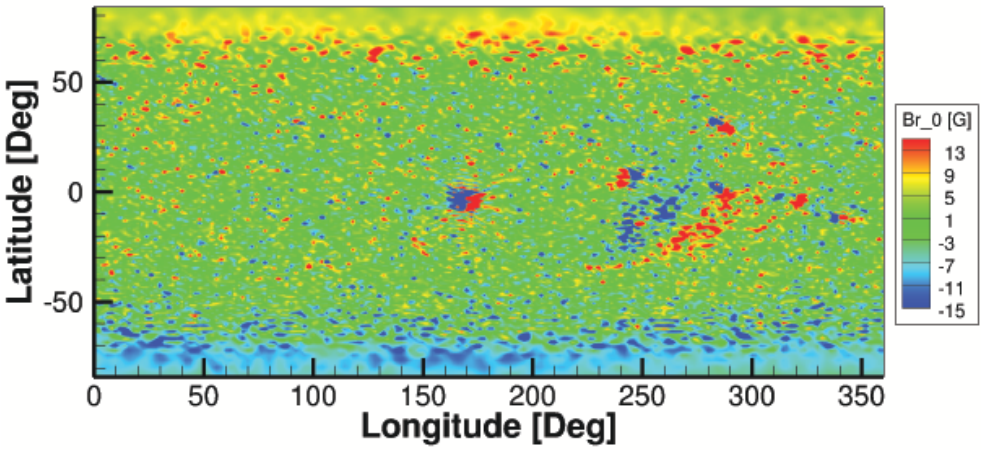

Figure 3.1: *Boundary condition for the radial magnetic field for CR1916, obtained from an MDI magnetogram with polar interpolation. Although the magnetic field magnitude can reach up to 2000 G in the vicinity of active regions, the color scale was modified so that the large scale distribution can be seen.*

3.5 Observations

The observations we used in this work were taken by SUMER instrument on board SoHO on 21–22 November 1996. During this time, SoHO was rolled 90 degrees so that the SUMER slit was oriented along the East-West direction. The center of the SUMER 4"×300" slit was pointed at (0",1160") so that the field of view stretched almost radially from 1.04 to 1.34 R_s lying outside the west solar limb at the solar equator. The entire 660-1500 Å wavelength range of SUMER detector B was telemetered down; given the particular instrumental configuration, this range was divided into 61 sections of 43 Å, each shifted from the previous one by ≈13 Å. Each section was observed for 300 s. More details on these observations can be found in *Landi et al.* (2002).

From the available spectral range, we chose a set of bright and isolated spectral lines (listed in Table 3.1), which allow accurate measurements of both line fluxes and line widths up to high altitudes. We note that the very bright O VI doublet at the 1031-1037 Å range was not selected because these lines are partially formed by instrumental scattering of disk radiation, and thus their theoretical FWHM is more complex than given in Eq. (3.1), making them inadequate for our purposes.

Ion Name	Wavelength [Å]	R_{max} $[R_S]$
Fe XII	1242.0	1.275
S X	1196.2	1.265
Mg IX	706.0	1.245
Na IX	681.7	1.285
Ne VIII	770.4	1.255

Table 3.1: *Selected emission lines used in this study.* $R_{\max}$ *indicates the highest altitude at which the observed flux is at least 2 times larger than the instrument-scattered flux (see Section 3.5.2).*

3.5.1 Data Reduction

The data were reduced using the standard SUMER software made available by the SUMER team through the SolarSoft IDL package (*Freeland and Handy*, 1998); each original frame was flat-fielded, corrected for geometrical distortions, and aligned with all other frames. In order to increase the signal-to-noise ratio, the data were averaged along the slit direction in 30 bins, each 0.01 R_s wide. Spectral line profiles were fitted with a Gaussian curve removing a linear background. The resulting count rates were then calibrated using the standard SUMER calibration also available in SolarSoft. The accuracy of the spectral flux calibration of SUMER detector B before June 1998 is ≈20% (*Wilhelm*, 2006, and references therein).

3.5.2 Scattered Light Evaluation

The micro-roughness of the SUMER optics causes the instrument to scatter the radiation coming from the solar disk into the detector, even when the instrument is pointing outside the limb. The scattered light forms a ghost spectrum of the solar disk at rest wavelength superimposed onto the actual spectrum emitted by the region imaged by the SUMER slit.

This ghost spectrum can provide important, though undesired, contributions to measured line fluxes when the local emission of the Sun is weak; these contributions need to be evaluated and, when necessary, removed. Unfortunately, the strength of the ghost spectrum depends on a number of factors (slit pointing, strength of the disk spectrum etc.) which make it impossible to devise a procedure to automatically remove it from the observations; its estimation needs to be performed on a case-by-case basis.

In the case of the present observations, the almost radial pointing of the SUMER slit allows us to use the rate of decrease of spectral line intensities with distance from the limb in order to determine an upper limit on the contributions of the ghost

spectrum. Since emission line intensities depend on the square of the electron density, the rapid decrease of the latter with height causes the coronal line intensities to decrease by almost two orders of magnitude from the closest to the farthest end of the slit in the present observation; on the contrary, the scattered light intensity, which is not emitted by the plasma in the observed region, is only reduced by a factor $\lesssim 2$ over the same range.

Landi (2007) devised a two-step method to determine an upper limit of the scattered light contribution to any spectral line for off-disk observations stretching over a large range of distances from the limb. First, the rate of decrease of the scattered light intensity with height is determined, based on several lines that are not emitted by the corona and whose off-disk intensity is entirely due to scattering. Second, the rate of decrease of scattered light intensity is used to get an upper limit on its contribution to a specific coronal line as follows. We measure the intensity of the coronal line at the location farthest from the limb in the instrument's field of view, and assume that this intensity is entirely due to scattered light. The radial rate of decrease of the scattered light intensity is then normalized to match that coronal line intensity at the farthest height, giving an upper limit to the scattered light contribution at all other heights. Note that this method actually overestimates the scattered light contribution to coronal lines.

To estimate the radial rate of decrease of scattered light intensity, we have used the intensity of the continuum at 1475 Å, and of the following lines: He I 584 Å, C II 1335 Å, C III 977 Å, O I 1032 Å, 1304 Å and 1306 Å, O III 835 Å, and Si III 1206 Å. These lines and continuum are emitted by the solar chromosphere, so that they are expected to be too weak to be observed at the heights covered by the SUMER field of view: their observed intensity is entirely due to scattered light. The rate of decrease of each of these lines and continuum have been normalized to the value of the intensity at the largest distance from the limb and averaged together to provide the

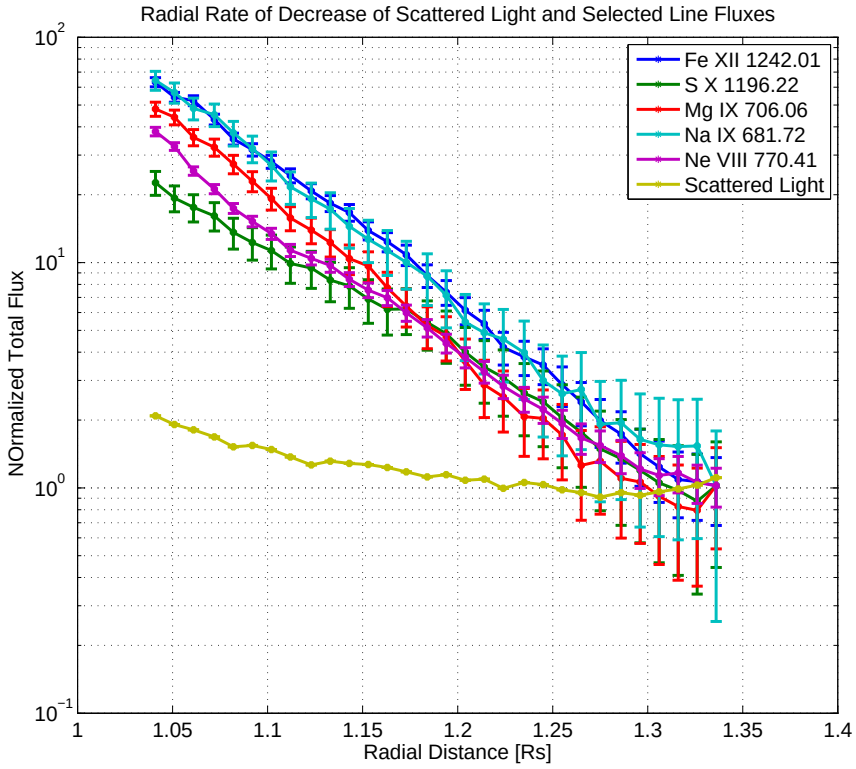

Figure 3.2: *Intensity vs. distance for the spectral lines in Table 3.1, normalized to the scattered light intensity measured at* $r = 1.34\ R_s$ *(the farthest point of the SUMER slit). The orange curve shows the averaged scattered light rate of decrease, while the dashed line indicated an intensity level of two times the scattered light intensity at the farthest edge of the slit.*

final scattered light intensity vs. height curve. This curve appears as the solid black curve in Figure 3.2. The normalized intensity vs. height curve for the coronal lines in Table 3.1 are also shown for comparison. We verified that all of them decreased at a rate much larger than the scattered light intensity: this suggests that the latter is at best a minor contributor to the intensity of each of the lines in Table 3.1 at almost the entire range of heights. We also determined the maximum heliocentric distance R_{max} below which our estimate of the scattered light contribution to the coronal line intensity is less than 50%. We take this arbitrary limit as an indication of the range of heights where we can safely neglect the scattered light. This height is reported in

the third column of Table 3.1. We note that all the emission lines considered here possessed a clear Gaussian line shape that could be separated from the background up to distances larger than R_{max}.

3.6 Synthesizing EUV Emission Line Profiles from 3D Model Results

The synthetic line profiles have been calculated by combining the AWSoM model predictions of the plasma properties and wave energy with the spectral emissivity calculated from the CHIANTI 7.1 atomic database. CHIANTI takes into account known line formation mechanisms and is capable of calculating the total emission of a spectral line, given the electron density and temperature. The calculations included in this work were carried out assuming that the plasma is optically thin and in ionization equilibrium. Photo-excitation was neglected as a line formation mechanism.

3.6.1 Total Flux of Ion Emission Lines

The total line emission in a plasma volume, dV, having electron temperature T_e and density N_e is given by:

$$\epsilon_{ji} = G_{ji}(N_e, T_e) N_e^2 dV, \tag{3.6}$$

where $G_{ji}(N_e, T_e)$ is the contribution function for a spectral line associated with an electronic transition from an upper level j to a lower level i, defined as:

$$G_{ji}(N_e, T_e) = A_{ji} \frac{N_j(X^{+m})}{N(X^{+m})} \frac{N(X^{+m})}{N(X)} \frac{N(X)}{N(H)} \frac{N(H)}{N_e} \frac{1}{N_e}, \tag{3.7}$$

where G_{ji} is measured in units of photons cm^3 s^{-1}. X^{+m} denotes the ion of the element X at ionization state $+m$. The contribution function also depends on the

following quantities:

1. $N_j(X^{+m})/N(X^{+m})$ is the relative level population of X^{+m} ions at level j, and depends on the electron density and temperature ;

2. $N(X^{+m})/N(X)$ is the abundance of the ion X^{+m} relative to the abundance of the element X, and depends on the electron temperature ;

3. $N(X)/N(H)$ is the abundance of the element X relative to hydrogen ;

4. $N(H)/N_e$ is the hydrogen abundance relative to the electron density ($\approx$0.83 for a fully ionized plasmas); and

5. A_{ji} is the Einstein coefficient for spontaneous emission for the transition $j \rightarrow i$.

As T_e and N_e are known from the model solution, the contribution function in any computational volume element can be calculated. In this work we used coronal element abundances as given in *Feldman et al.* (1992), and the latest ionization equilibrium computation available in CHIANTI.

Once the contribution function is calculated at every point along the line-of-sight, the total observed flux in the optically thin limit is given by integrating the emissivity along the line of sight:

$$F_{tot} = \int \frac{1}{4\pi d^2} G_{ji}(N_e, T_e) N_e^2 dV, \tag{3.8}$$

where d is the distance of the instrument from the emitting volume dV. F_{tot} is measured in units of photons cm^{-2} s^{-1}. This volume integral can be replaced by a line integral by observing that $dV = Adl$, where A is the area observed by the instrument and dl is the path length along the line of sight (LOS). In the case of the present observations, the area covered by the instrument is 4"$\times$1". In order to calculate the LOS integral from the 3D model results, we interpolate G_{ji} and N_e from the AWSoM non-uniform spherical computational grid onto a uniformly spaced set of points along each observed LOS. The spacing used for the interpolation was set

to match the finest grid resolution of the model. This procedure ensures that the integration is second-order accurate.

3.6.2 Synthetic LOS-integrated Line Profiles

Knowledge of the magnitude of thermal and non-thermal ion motions allows us to calculate a synthetic spectrum, which explicitly includes their effects on the line profile. Thus instead of merely predicting the total flux of an emission line, we can predict the full spectral line profile, to be compared with the observed spectrum.

For each location along the line of sight, the local spectral flux can be calculated by imposing a Gaussian line profile characterized by the predicted total flux, F_{tot}, the rest wavelength λ_0, and line width, $\Delta\lambda$, determined from the ion temperature and the magnitude of non-thermal motions. The spectral flux, measured in units of photons $\mathrm{cm}^{-2}\ \mathrm{s}^{-1}\ \mathrm{\AA}^{-1}$, can be written as:

$$F(\lambda) = F_{tot}\phi(\lambda), \tag{3.9}$$

where $\phi(\lambda)$ is the normalized line profile. In case of a Gaussian line profile, $\phi(\lambda)$ is given by:

$$\phi(\lambda) = \frac{1}{\sqrt{\pi}\Delta\lambda} exp\left[-\left(\frac{\lambda-\lambda_0}{\Delta\lambda}\right)\right], \tag{3.10}$$

and the line width, in accordance with Eq. (3.1), can be written as:

$$\Delta\lambda = \frac{\lambda_0}{c}\sqrt{\frac{2k_BT_i}{M_i} + v_{nt}^2}. \tag{3.11}$$

The non-thermal speed, v_{nt}, can be calculated from the AWSoM model through Eq. (3.5). The emitting region in our case is a three-dimensional non-uniform plasma, where each plasma element along the line-of-sight gives rise to different values of the total flux and the line width. In order to synthesize the line profile from the model,

we must perform the line-of-sight integration for each wavelength separately, i.e. we must calculate the spectral flux at the instrument, $F(\lambda)$, given by:

$$F(\lambda) = \int \frac{A}{4\pi d^2} \phi(\lambda) G_{ji}(N_e, T_e) N_e^2 dl. \tag{3.12}$$

The spectral flux is calculated over a wavelength grid identical to the SUMER spectral bins. In order to compare the synthetic spectra with observations, we must also take into account the SUMER instrumental broadening. For this purpose, we convolve the LOS-integrated spectral flux with the wavelength-dependent instrumental broadening for SUMER detector-B, as given by the standard SUMER reduction software available through the SolarSoft package.

3.6.3 Uncertainties in Atomic Data and Line Flux Calculations

Atomic data uncertainties directly affect the line fluxes calculated from the AWSoM simulation results. It is therefore necessary to discuss the accuracy of the data available for the emission lines for which we wish to produce synthetic spectra. Table 3.1 lists the five spectral lines that were used for detailed line profile calculations. They were chosen mainly because they are bright and clearly isolated from neighboring lines, so that their profile could be resolved accurately to as large a height as possible.

3.6.3.1 Ne VIII 770.4Å and Na IX 681.7Å

These two lines belong to the Li-like iso-electronic sequence, i.e. they possess one bound electron in their outer shell. Their atomic structure is relatively simple and the theoretical calculation of their collisional and radiative rates is expected to be accurate. *Landi et al.* (2002) verified the accuracy of this calculation for all lines belonging to this sequence by comparing the fluxes calculated from CHIANTI to

those measured in the 1.04 R_s section of the observations used here. The authors used the electron density and temperature measured in that section as input to CHIANTI. They found excellent agreement among all lines of the sequence, indicating that the collisional and radiative rates are indeed accurate. However, they found a systematic factor-2 overestimation of the abundance of all ions of this sequence, which they ascribed to inaccuracies in the ionization and recombination rates used in their work (from *Mazzotta et al.*, 1998). However, more recent assessments of ionization and recombination rates made by *Bryans et al.* (2006, 2009) largely solved this discrepancy, as shown by *Bryans et al.* (2009). Since we are using ion abundances that take into account the new electron impact ionization by *Bryans et al.* (2009), the fluxes of these two lines are expected to be reasonably free of atomic physics problems.

3.6.3.2 Mg IX 706.0Å

The CHIANTI calculation of the flux of this line was found to be in agreement with other lines from the same sequence by *Landi et al.* (2002); however some problems were found with some other Mg IX line observed by SUMER, making this ion a candidate for uncertainties in atomic data. However, the radiative and collisional transition rates used in the present work (from CHIANTI 7.1) have been improved from those used by *Landi et al.* (2002), which used CHIANTI 3 (*Dere et al.*, 2001). The new calculations now available in CHIANTI, from *Del Zanna et al.* (2008), solved the problems so that the atomic data for this ion should be accurate.

3.6.3.3 S X 1196.2Å

The atomic data of the S X 1196.2Å line were also benchmarked by *Landi et al.* (2002), who showed that while all the data in the N-like iso-electronic sequence were in agreement with each other, they all indicated a larger plasma electron temperature

than the other sequences, suggesting that improvements in this sequence were needed. Subsequent releases of CHIANTI adopted larger and more sophisticated calculations for this ion, so that the accuracy of the predicted flux for S X 1196.2Å should be relatively good. However, this line is emitted by metastable levels in the ground configuration, and its flux is strongly density sensitive. Thus, any inaccuracies in the predicted electron density may result in large errors in the calculated line flux.

3.6.3.4 Fe XII 1242Å

The Fe XII has a complex electronic structure and therefore large atomic models are required to fully describe its wave functions. For example, when EUV lines emitted by this ion are used to measure the electron density, they are known to overestimate it relative to the values measured from many other ions (*Binello et al.*, 2001; *Young et al.*, 2009; *Watanabe et al.*, 2009). The atomic data from *Del Zanna et al.* (2012) in CHIANTI 7.1 include improved atomic data for this ion, but inaccuracies in the predicted flux of this line may still be expected; in particular, *Landi et al.* (2002) found that the atomic data in CHIANTI 3 underestimated the predicted flux by $\simeq$30% while the CHIANTI 7.1 predicted fluxes are decreased by a factor 1.5-2 compared to Version 3 levels. Thus we still expect a factor ≈ 2 underestimation of the total flux of the Fe XII 1242Å line.

3.7 Results

3.7.1 Model Validation for CR1916: EUV Full Disk Images

Comparing observed full disk images to those synthesized from model results allows us to test how well the global, three-dimensional solution, and specifically the temperature and density distributions, can reproduce the observations. Such a comparison also tests the model's prediction of the location and shape of the boundaries

between open and closed magnetic field regions, as the coronal holes appear much darker than closed field regions in EUV images.

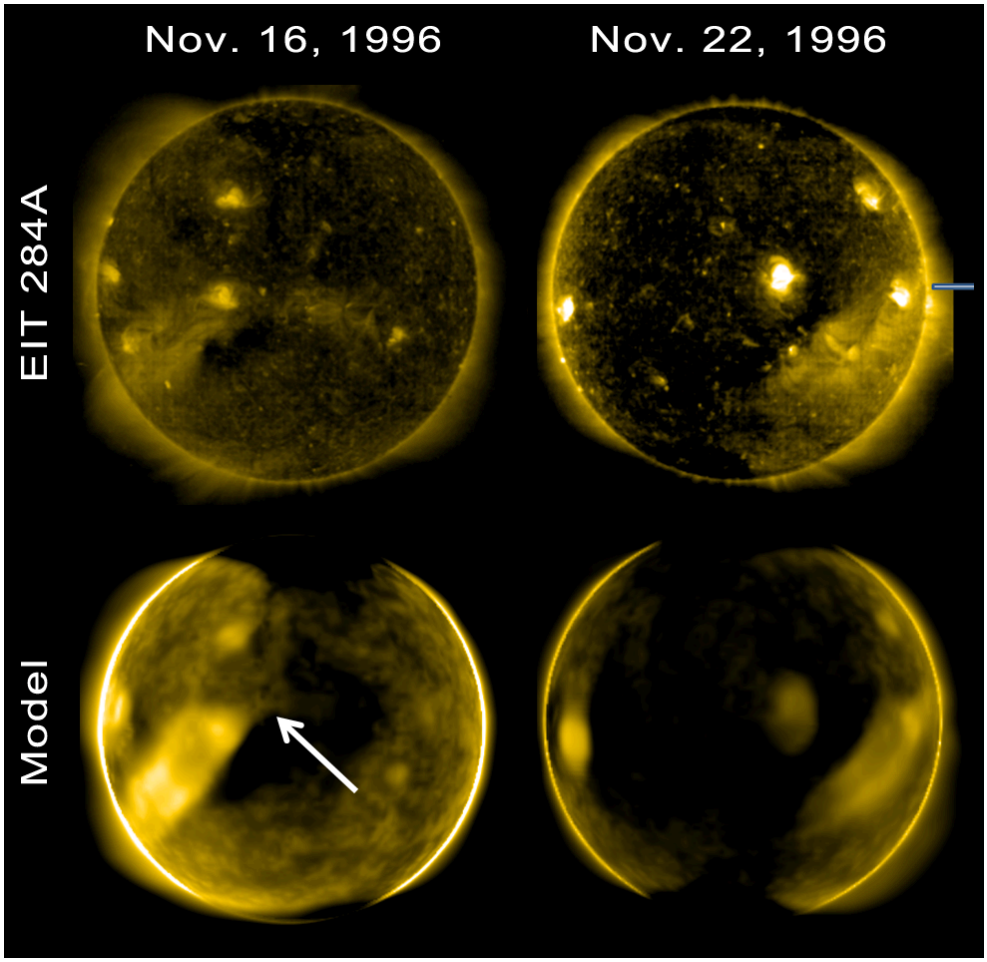

Figure 3.3: *SoHO/EIT images vs. synthesized images in the 284 Å band. Top row shows the observations while the bottom row shows images synthesized from AWSoM. The left column shows images for Nov. 16, 1996 (i.e. a week prior to the observation time), and the white arrow points to the approximate location of the intersection between the SUMER slit and the plane of the sky. The right column shows images for Nov. 22, 1996. The approximate location of the SUMER slit is superimposed on the observed image.*

We compare our model results for CR1916 to images recorded by the EUV Imaging Telescope (EIT; *Delaboudinière et al.*, 1995) on board SoHO. In preparing instrument-specific response tables, as well as observed images from the raw data, including calibration, noise reduction and normalization of the photon flux by the exposure

time, we used the SolarSoft IDL package.

Figure 3.3 shows observed vs. synthesized images of the 284 Å band, which is dominated by the Fe XV ion, corresponding to an electron temperature of ~ 2.2 MK. We present images taken at two different times: the top image shows the solar disk as viewed by SoHO at the time of the SUMER observations, while the bottom figure shows the emission from the solar disk a week earlier, so that the region containing the plane of the sky during the SUMER observation can be viewed close to disk center. As can be seen, the large scale features of the corona, such as coronal hole boundaries and active region locations, are reproduced by the simulation.

3.7.2 Comparison of Synthetic and SUMER Spectra

In order to perform 3D line-of-sight analysis, we begin with extracting model results, such as electron and proton densities and temperatures, as well as the Alfvén waves energy density, along the line of sight to the SUMER slit. The geometry of the problem is illustrated in Figure 3.4, where the SUMER line-of-sight for the entire slit width is traced within the three-dimensional space of the model solution. The figure shows the solar surface, colored by the radial magnetic field magnitude, the horizontal plane containing the SUMER slit, colored by the electron density, and the plane of the sky for the time of SUMER observations.

Using the model results and the CHIANTI database, we calculated the spectral flux LOS integral according to Eq. (3.12) for each of the lines in Table 3.1 at each of the 30 radial sections of the SUMER slit. The resulting spectra are compared to the observed spectra in Figures 3.5 - 3.9. The two panels on the left of each figure show color contour plots of the synthetic and observed line spectra at all heights covered by the SUMER slit. The middle panel compares the line profile in absolute units at two different distances above the limb: 1.04 R_s and 1.14 R_s. The blue symbols and error bars show the observed flux and the associated uncertainty, which takes into

account a calibration error of 20% for SUMER detector-B (*Wilhelm*, 2006), and the statistical error in the photon count. The blue curve shows the fit to a Gaussian of the measured flux. The red curve shows the model result. On the right, we show the normalized line profile in each of these heights, using the same color coding as before. The normalized line profile allows us to examine the accuracy of the model prediction of the line width, independent of the absolute value of the predicted total flux. The first thing to notice is that for all lines the observed and predicted line widths are in good agreement at both heights. These results imply that the combination of thermal and non-thermal motions predicted by the AWSoM model is accurate. The predicted and observed spectral line fluxes are in good agreement for Mg IX and Na IX ions, while the model under predicts their magnitude in the S X, Fe XII and Ne VIII ions. We discuss possible causes of these discrepancies in Section 3.7.3.

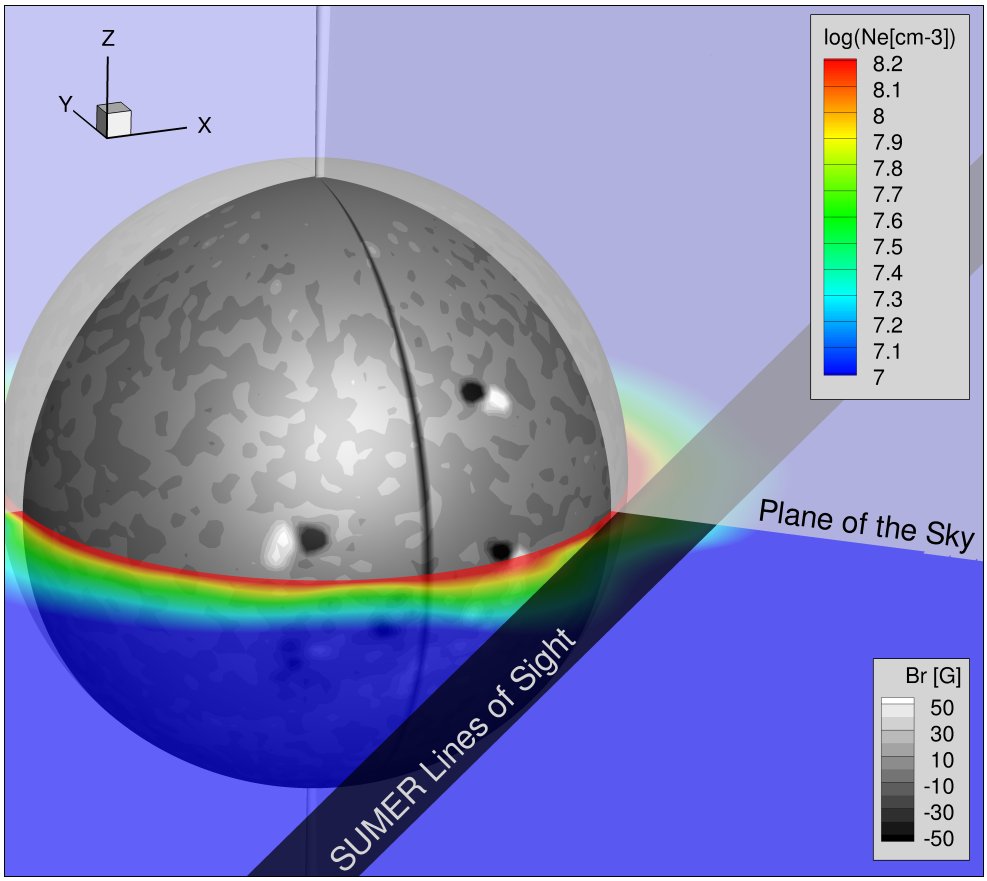

Figure 3.4: *3D model results, location of the plane of the sky, and SUMER line of sight. The plane containing the SUMER slit is colored by the electron density. The solar surface is colored by the radial magnetic field.*

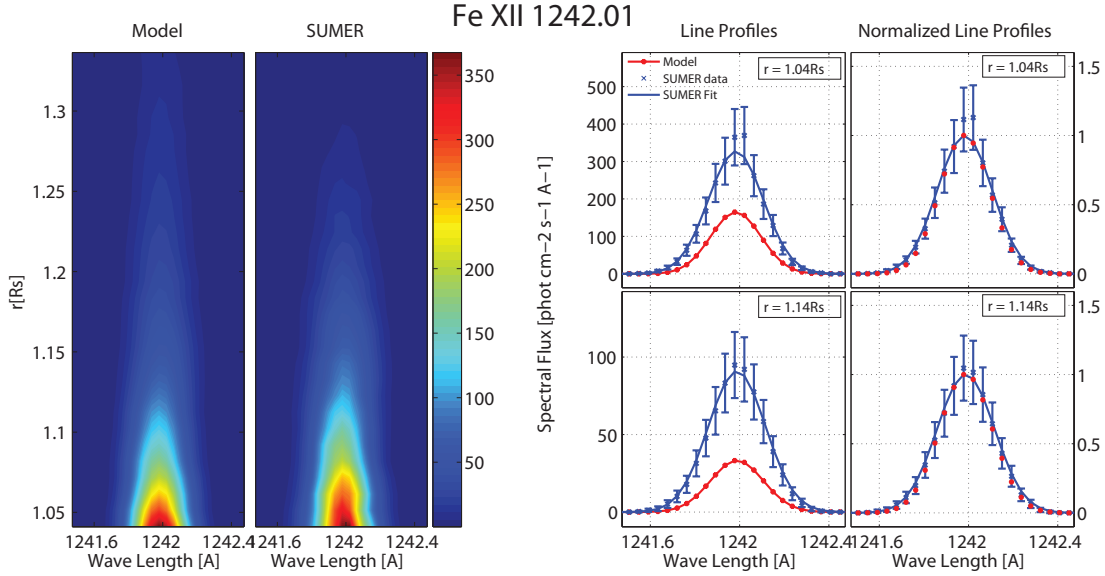

Figure 3.5: *Comparison of synthetic and observed spectra for Fe XII 1242 Å. Left two panels: color plots of synthetic and observed spectra at distances* $r = 1.04 - 1.34R_s$. *Middle: Selected line profiles extracted at* $r = 1.04R_s$ *(top) and at* $r = 1.14R_s$ *(bottom). Blue symbols with error bars show the SUMER data, the blue solid curve shows the fit to a Gaussian, and the red curve shows the line profile synthesized from the model. Right: Normalized line profiles for the same heights. Curves are color coded in the same way as the middle panels.*

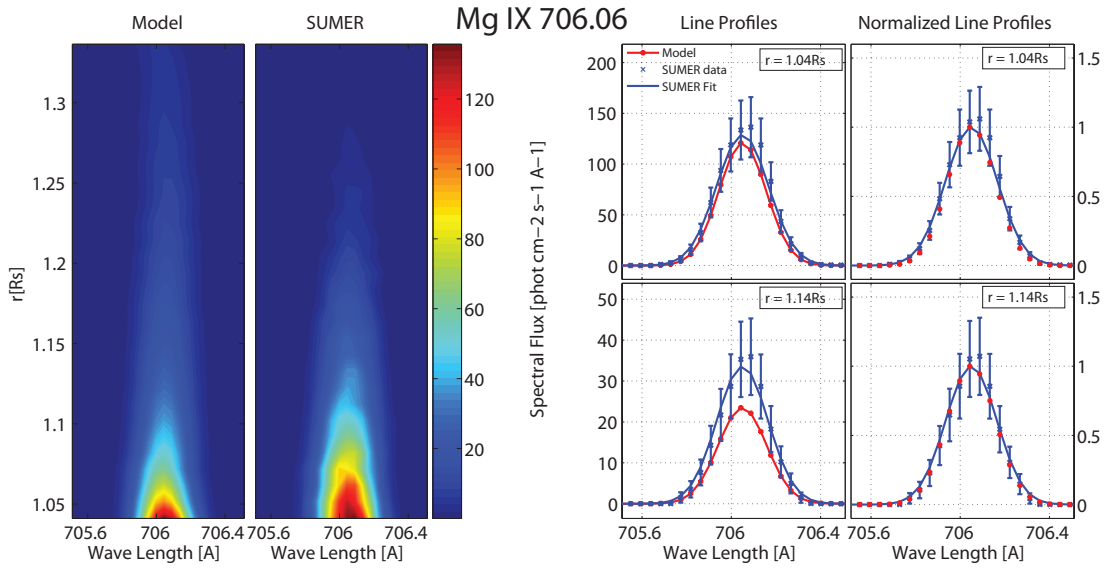

Figure 3.6: *Comparison of synthetic and observed spectra for Mg IX 706 Å. See Figure 3.5 for the full description.*

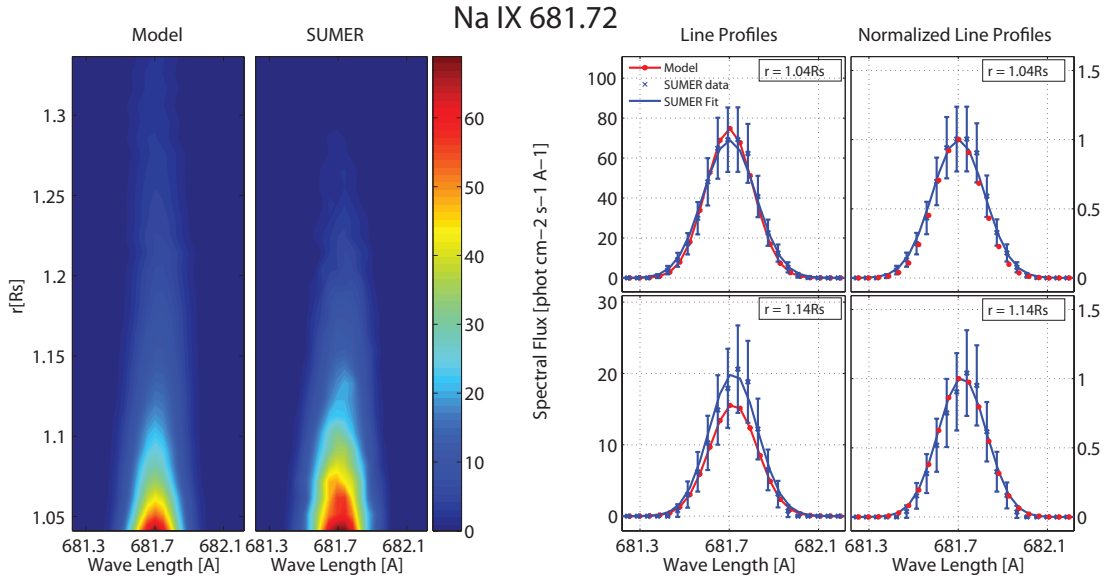

Figure 3.7: *Comparison of synthetic and observed spectra for Na IX 681 Å. See Figure 3.5 for the full description.*

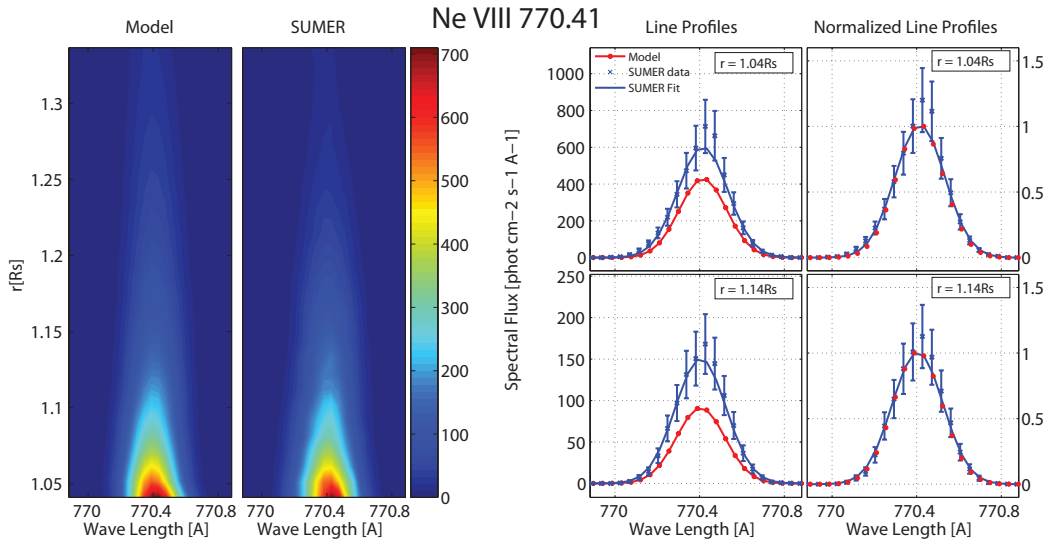

Figure 3.8: *Comparison of synthetic and observed spectra for Ne VIII 770 Å. See Figure 3.5 for the full description.*

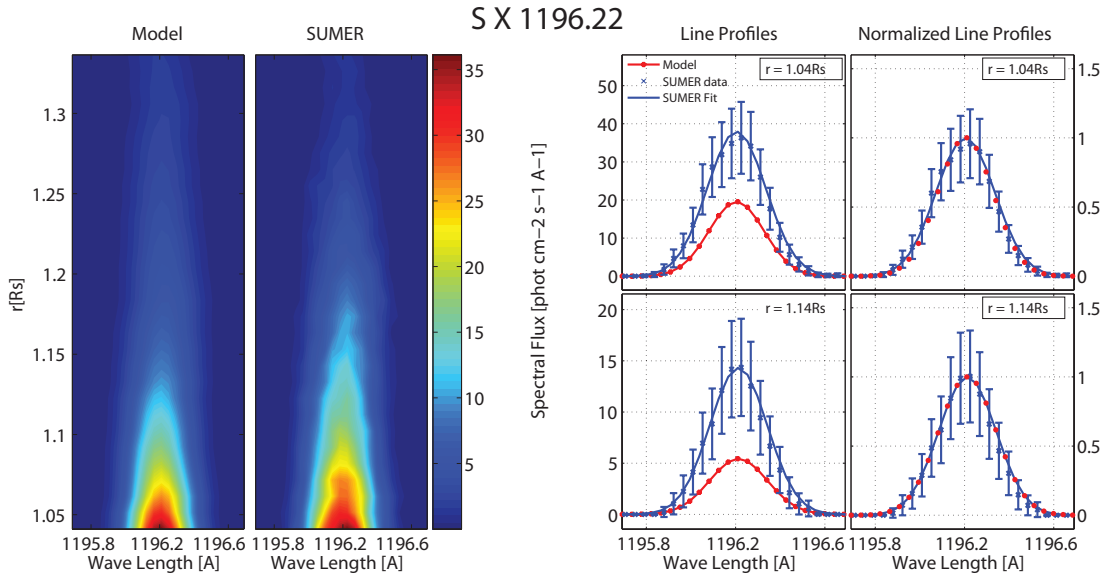

Figure 3.9: *Comparison of synthetic and observed spectra for S X 1196 Å. See Figure 3.5 for the full description.*

3.7.3 Comparison of Total Flux vs. Height

The total flux predicted by the model depends on the distribution of electron density and temperature along the line of sight. In turn, the radial profiles of the electron density and temperature depend on the heating rate, which in our case is a result of turbulent dissipation of Alfvén waves. Thus comparing the radial profiles of the total flux to the observations allows us to verify that the large scale distribution of heating rates predicted by the model give realistic results.

Figure 3.10 shows a comparison of the radial profiles of the total flux for all the lines listed in Table 3.1. The left panels display the predicted and observed total flux, F_{tot}, at all heights covered by the SUMER slit. The panels on the right side of Figure (3.10) display the ratio between observed and predicted total line fluxes, as a measure to determine the agreement or disagreement between model and observations. The discrepancies between the model and the observations seem to decrease with radial distance, as all ions show agreement above 1.2 solar radii. However, this improvement is due in part to the increase with height of the uncertainties of the observed fluxes. The regions shaded by an orange color correspond to heights where the error in the measured flux is larger than the measured value itself. For these cases, the ratio between predicted and observed total flux becomes meaningless, and these points are excluded from the ratio calculation. The regions shaded in blue correspond to the height above the limb where the scattered light contribution may reach up to 50% of the observed line flux, as discussed in Section 3.5.2. These heights are summarized in the third column of Table 3.1. We next discuss the results for the separate lines in more detail.

Mg IX and Na IX - The successful comparison for Mg IX and Na IX is very important. Since no atomic physics problems were expected for these lines (see Section 3.6.2), the agreement indicates that the overall temperature and density distributions predicted by the AWSoM model along the line of sight are realistic, although line of

sight effects might compensate for local inaccuracies.

Fe XII - The total flux of the Fe XII line is underestimated, but it is important to note that the factor of 2 to 3 discrepancy we find is similar to the underestimation we expected from this line (see Section 3.6.2) so that the disagreement could be largely due to atomic data inaccuracies.

Ne VIII and S X - The synthetic fluxes for Ne VIII are underestimated by a factor ≈ 1.5, which is slightly larger than the experimental uncertainties. One possible cause for such a disagreement could be radiation scattering for the Ne VIII line, which we neglected in the present emission calculation. However, *Landi* (2007) showed that radiative scattering is not a significant source of line excitation for Ne VIII below 1.5 R_s. The S X line flux is also underestimated by the AWSoM model by a factor ≈ 2, although the uncertainties on the observed flux are rather large. An overestimation of the electron density along the line of sight might account for part of the disagreement, as the 1196 Å line contribution function, $G(N_e, T_e)$, defined by Eq. (3.7), decreases as the density increases beyond $N_e = 10^8$ cm^{-3}. However, the discrepancy between the predicted and observed fluxes of both Ne VIII and S X could also be due to an inaccurate estimation of their abundances. Coronal element abundances are affected by the fractionation processes active in the corona known as the "FIP effect" (*Feldman and Laming*, 2000, and references therein). It has been observed that the abundances ratio of elements with a low (< 10 eV) First Ionization Potential (FIP) to elements with a high FIP is larger in the corona compared to the photosphere, by a factor known as the "FIP bias". The coronal abundances used in the present calculation (from *Feldman et al.*, 1992) adopt a FIP bias of 4. However, the FIP bias of S is not known with accuracy: *Feldman et al.* (1992) report a FIP bias of 1.15, while, for example, *Feldman et al.* (1998) indicate a FIP bias between 1.2 and 2.0, which is large enough to account for the disagreement we find. The FIP bias of Ne has never been measured, since the photospheric abundance of Ne is

unknown. Theoretical models of the FIP effect suggest that Ne is also affected by this process (*Laming*, 2012, and references therein), so that the absolute abundance of this element in the corona is also subject to uncertainty. These uncertainties might be causing the discrepancies we find in the total fluxes of these two lines.

3.7.4 Comparison of Line Width vs. Height

The comparison of the radial variation of the line width in the synthetic spectra to that found in the observations allows us to determine how well the predicted plasma and wave properties are able to account for the observed line broadening in the inner $(1.04 - 1.34 R_s)$ part of the equatorial solar atmosphere.

Figure 3.11 compares the radial profiles of the synthetic and observed line widths for each of the spectral lines in Table 3.1. The regions where the scattered light flux may contribute up to 50% to the line flux are shaded in blue. These radial distances are reported in Table 3.1. The panels on the left hand side show the model and observed width cast in units of speed using Width(km s^{-1}) = $(\Delta\lambda/\lambda_0)c$, where c is the speed of light in km s^{-1}. This quantity is often referred to as the effective speed. The blue curve with error bars shows the observations, while the red dashed line shows the model results. In order to examine the relative contribution from the thermal and non-thermal speeds, we repeated the calculation of the line widths while ignoring the non-thermal speed as a line broadening mechanism. The results are shown as the green curves on the left panels. The panels on the right hand side show the ratio of the observed to synthetic line width (blue curve). The solid black line denotes a ratio of one, i.e. a perfect agreement. The first thing we note is that the ratios for all lines are all very close to unity, with a discrepancy of less than 10% at most heights. This implies that the combination of ion temperatures and non-thermal speeds predicted by AWSoM can produce synthetic line widths whose magnitudes are very close to the observed ones, at least in the case of the lower equatorial corona. As in the case of the

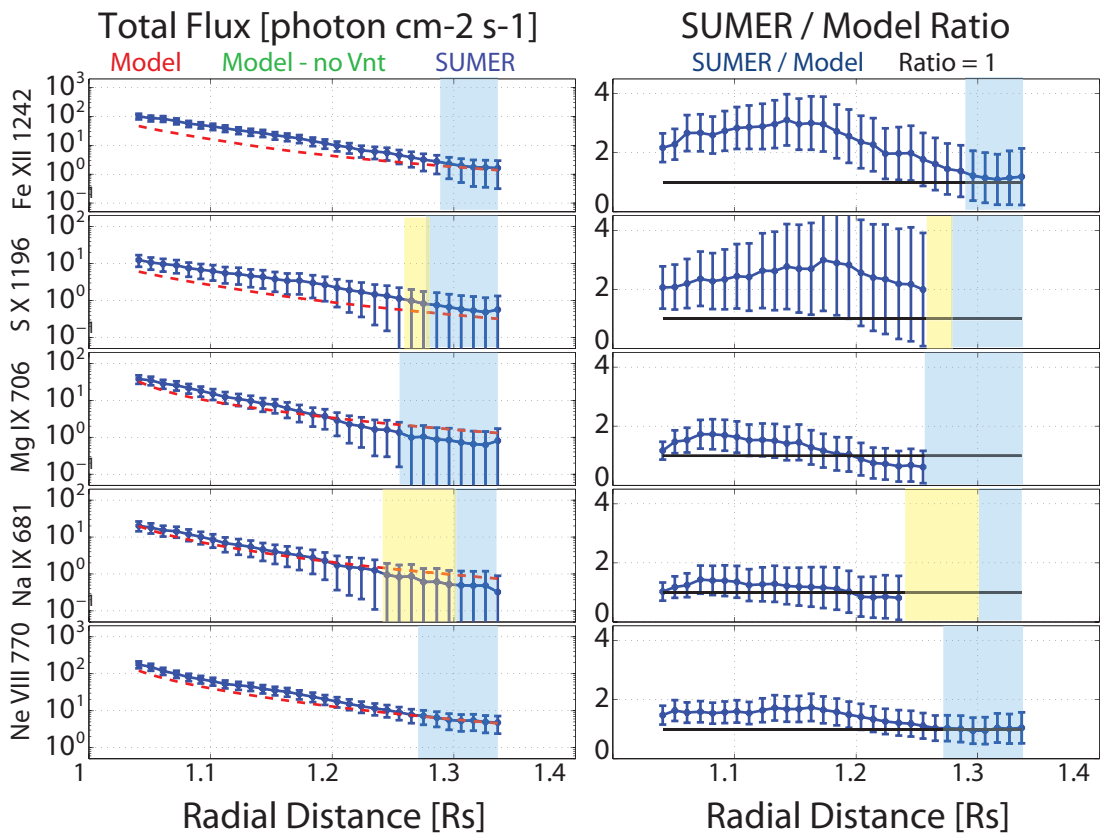

Figure 3.10: *Total flux comparison. Left column: Observed (blue) and predicted (red) total fluxes. Right column: Ratio of observed to modeled total fluxes (blue curve). The black curve shows a ratio of 1, for convenience. The regions shaded in orange correspond to heights where the uncertainty in the observed flux becomes larger than the measured value. In this case the uncertainty in the ratio leads to a lower bound that is negative, and therefore, meaningless. The regions shaded in blue corresponds to heights above which the stray light contribution might reach up to 50% of the observed flux, as reported in Table 2.*

total flux comparisons, we note that line-of-sight effects may compensate for any local inaccuracy in the AWSoM prediction. The removal of the non-thermal speed from the calculation of the synthetic profiles greatly reduces the agreement between the model and the observations. This implies that the non-thermal motions induced by the waves are necessary for predicting line widths which are consistent with observations. While the line width due to thermal motions alone does not change considerably with radial distance, the total line width which includes the wave-induced motions shows a clear radial dependence. This dependence is due in part to the effects of the magnetic topology, as we will discuss in Section 3.7.6.

The comparison also sheds some light on the validity of our assumption that all the ions have the same temperature. Under this assumption, the thermal contribution to the line broadening at a given location (as given in Eq. (3.11)) will be inversely proportional to the ion's mass. On the other hand, the non-thermal contribution to the line width will be the same for all ions. In other words, the synthetic widths of each of the lines in Figure 3.11 are obtained by combining different thermal contributions (since each line is emitted by an ion of a different element) and equal non-thermal contributions. A simultaneous agreement of the synthetic widths of all ions with observations is therefore consistent with our assumptions that all the ions have the same temperature and that they all have the same non-thermal speed.

We note that for Fe XII, the agreement between the synthetic and observed line width decreases with height. This discrepancy may be due to the uncertainty in the observations, but it is also possible that our assumption that this ion, which has the largest mass, has the same temperature as the protons breaks down at higher altitudes.

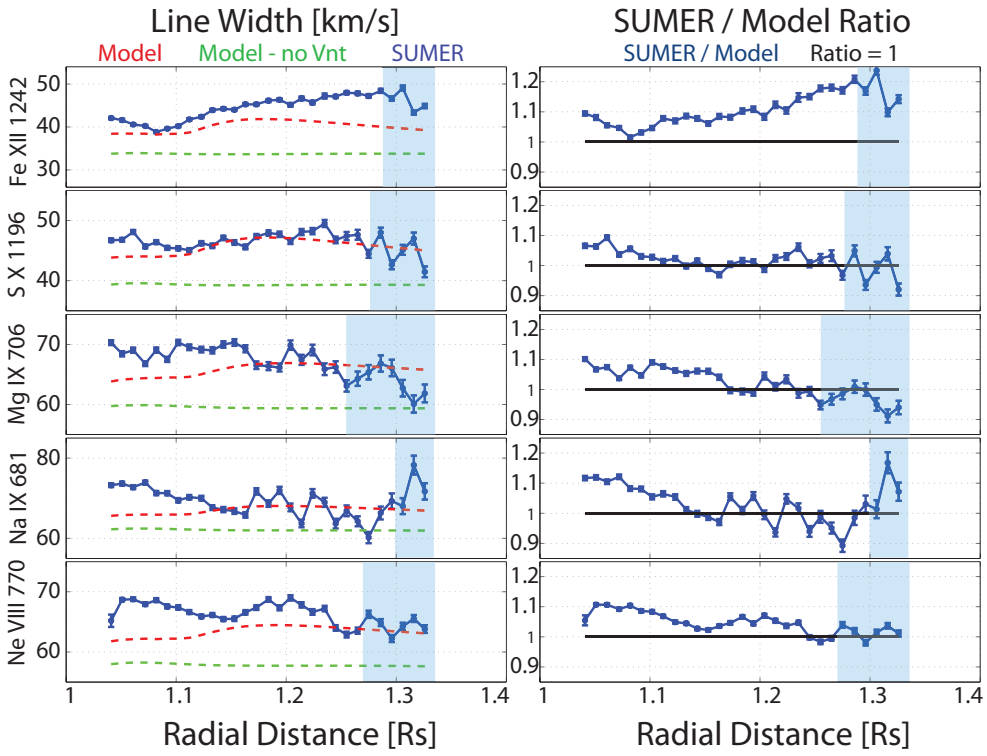

Figure 3.11: *Model - SUMER comparison of FWHM. Blue curves with error bars show the measured FWHM. Red curved show the AWSoM predicted FWHM. Green curves show the AWSoM prediction if the non thermal speed is not be taken into account.*

3.7.5 Comparison of Electron Properties

In the previous sections, we showed that the modeled wave amplitude is consistent with observed line-widths of several different ions, suggesting that the model correctly predicts the amount of wave energy propagating in the corona. To complete this discussion, we wish to verify that the observed coronal heating rate, which depends on the wave dissipation rate, is also reproduced. Since the heating rate impacts the electron density and temperature, comparing the modeled and measured electron properties along the SUMER slit serves as an independent check on the dissipation mechanism assumed in the model. *Oran et al.* (2013) found that the AWSoM model's prediction of electron properties in a polar coronal hole during solar minimum were in good agreement with measurements. The simple geometry of the coronal hole allowed the authors to compare the line-of-sight measurements to model results extracted along the coronal hole axis. However, in the present case of observations of the equatorial quiet corona, which exhibits a more complex magnetic topology, it becomes less clear which region along the line-of-sight should be compared to the measurements. We therefore adopt a more detailed approach, which takes into account the variable emission from different magnetic structures crossing the line-of-sight.

3.7.5.1 Overcoming Line-of-Sight Effects: 3D Emission Analysis

The advantage of a three-dimensional model is that it enables us, when combined with the CHIANTI atomic database, to calculate the relative contribution of each emitting volume along the line-of-sight to the total observed emission using the calculations presented in Section 3.6. This allows us to assess the amount of contamination to a given coronal structure from emission in the background and foreground, as well as guide us in the interpretation of diagnostic results. We here concentrate on electron density and temperature diagnostics; the electron density along the SUMER slit was measured using the line flux ratio of S X 1196Å and S X 1212Å, while the

electron temperature was measured using the line flux ratio of Mg IX 706Å and Mg IX 749Å. If a single, well-defined magnetic structure can be identified as a major source of the emission in these lines, then the corresponding modeled quantity in that structure may be compared to the measurement results. We must also require that the relative contribution of this region to the total emission is the same for each of the lines used in the flux ratio calculation. In this way, the ratio of the line fluxes integrated over the selected region will be equal to the ratio of line fluxes integrated over the entire line-of-sight, making the comparison to the observations appropriate. The procedure is somewhat different in case of electron density and temperature measurements, and we discuss these separately.

3.7.5.2 Region of Maximum Emission for Electron Density Measurements

The electron density along the SUMER slit was obtained from the line flux ratio of the S X 1196Å and S X 1212Å lines. Figure 3.12 shows the relative contribution of each location along the line of sight to the total emission, calculated using the AWSoM results and the CHIANTI database. The top row shows the fractional contribution to the total emission along each of the lines of sight. The bottom panels show the cumulative normalized LOS integral of the emission for these lines, which ranges from 0 to 1 (corresponding to the two edges of the line of sight). It can be seen that for both lines, the strongest emission comes from a narrow region around the plane of the sky (where we set the path length to 0). At lower altitudes, there is a significant contribution coming from an additional region behind the central region. We have found that $\sim 24\%$ of the total emission of both lines comes from a region that is less than $0.2R_s$ wide, marked by the black and purple curves. The black curves show the bounds of the 24% region for S X 1196Å , while the purple curves show the same for S X 1212Å . Since the two regions more or less overlap, the density modeled in this region is suitable for comparison with the density measurement.

We next locate this region in the model's three-dimensional magnetic topology. Figure 3.13 shows the MHD solution in an equatorial plane. Color contours show the radial speed while black curves show the magnetic field. The boundaries of the 24% region for S X 1196Å are marked by the white squares (corresponding to the purple curves in Figure 3.12). Interestingly enough, we see that a large part of the emission is coming from a distinct magnetic structure of a pseudo-streamer, i.e. a loop structure topped by open field lines of a single polarity. The flow speed above the streamer is slower than the surrounding regions.

3.7.5.3 Region of Maximum Emission for Electron Temperature Measurements

The electron temperature along the SUMER slit was obtained from the line flux ratio of Mg IX 706Å and Mg IX 749Å. As for the S X line pair, we wish to verify that both lines give similar relative contribution to the line-of-sight emission in the pseudo-streamer region. The cumulative contribution along the line of sight is shown in Figure 3.14. The overlaid curves represent the region where the relative contributions of the two lines are similar, and account for 36% of the total line-of-sight emission. The black and purple curves correspond to the 706Å and the 749Å lines, respectively. As can be seen, these regions almost entirely overlap. Calculating the temperature from the observed line flux ratio also requires us to know the electron density, which we take from the measurement discussed in the previous section. We therefore wish to compare the location of the region of equal contribution of the Mg IX lines to the region of equal contribution of the S X lines, i.e. the pseudo-streamer region selected in the previous section. The comparison is shown in Figure 3.15. The panels show the fractional contribution for Mg IX 749Å (left) and for S X 1212Å (right). The purple curves represent the region of equal contribution of the S X line pair (as in Figures 3.12 and 3.13), while the black curves represent the region of equal

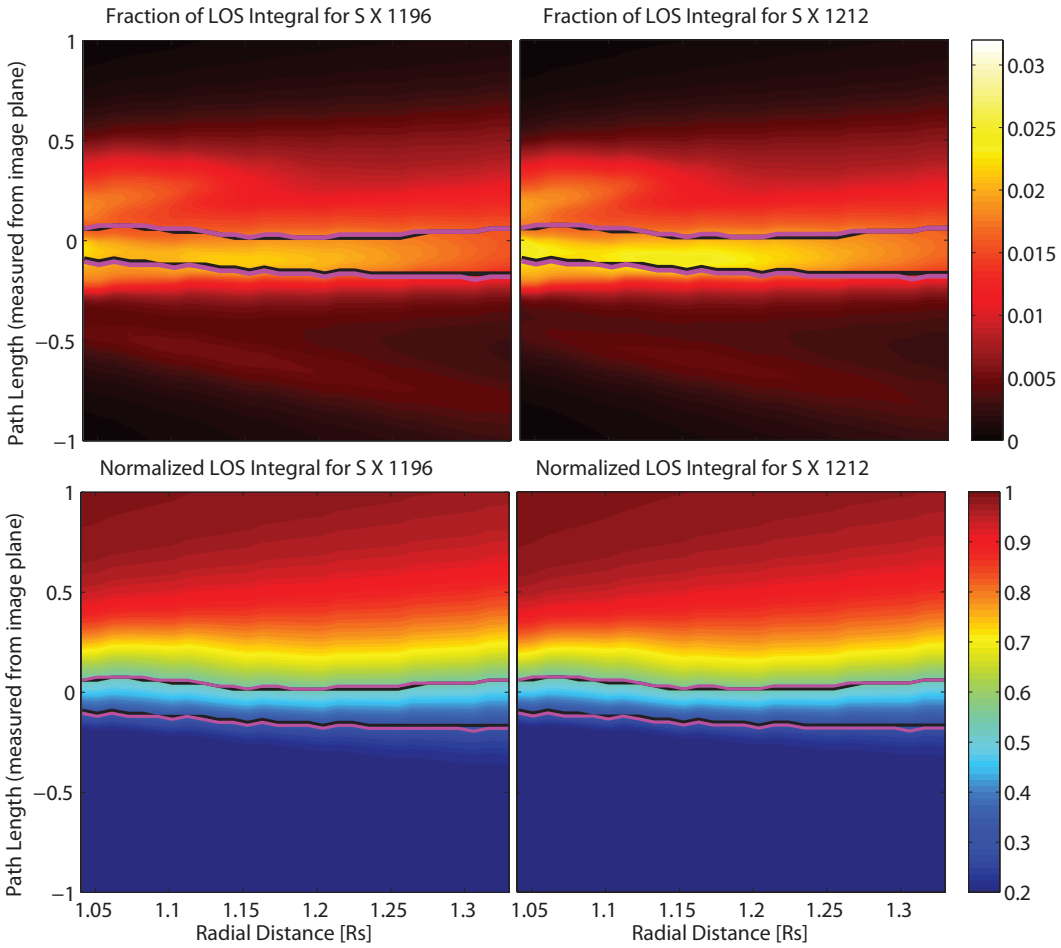

Figure 3.12: *Emissivity line of sight integral for S X 1196Å(left column) and S X 1212Å(right column). The top row shows the fractional contribution to the total line of sight integral, along all 30 SUMER lines of sight used in this study. The bottom row shows the cumulative contribution to the LOS integral. The purple curves represent the ranges along the LOS that account for 24% of the total emission of S X 1196Å , while the black curve represents the region that accounts for 24% of the total emission in the S X 1212Å line.*

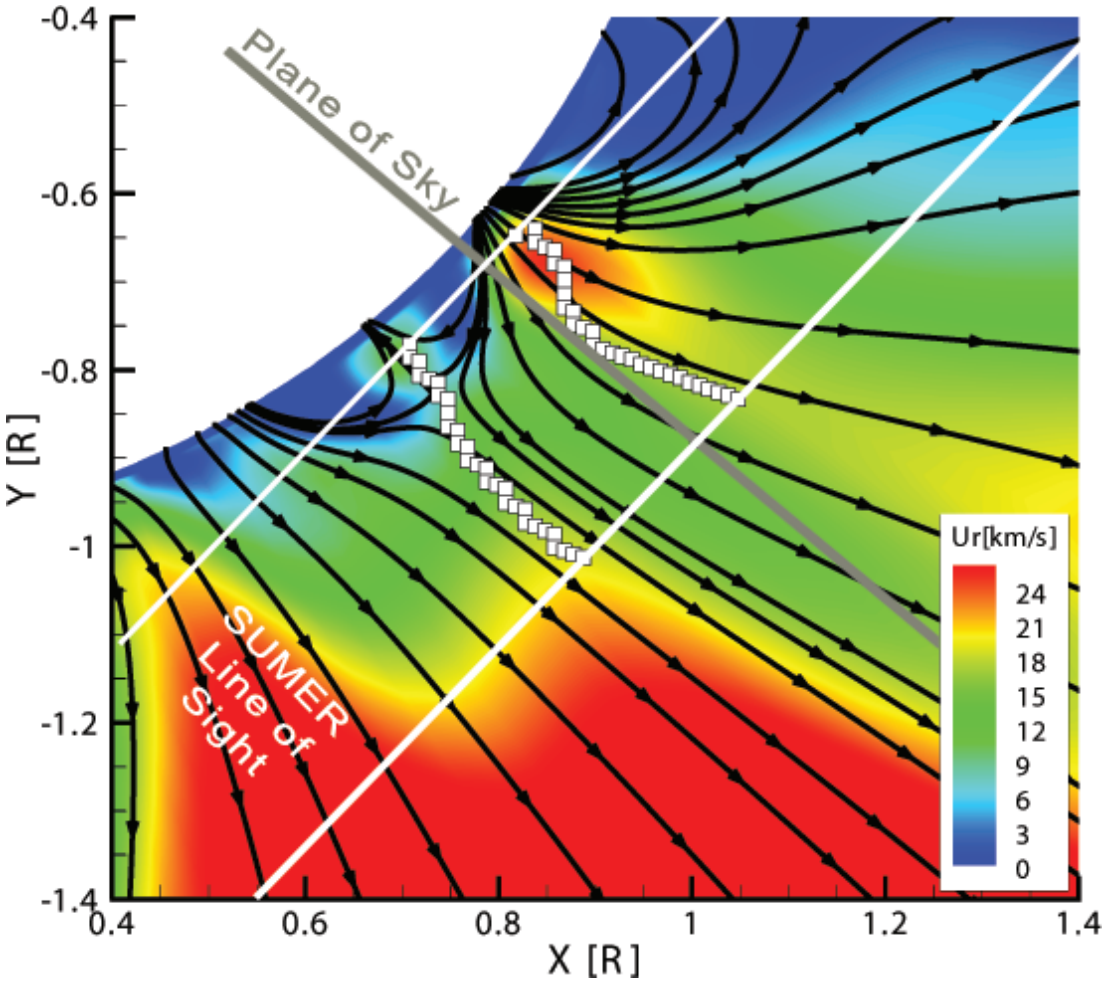

Figure 3.13: *Location of maximum emission for the S X 1196 Å. The color contours show the radial flow speed in the equatorial plane containing the SUMER lines-of-sight (marked by the two white lines). The gray line denotes the plane of the sky for the day the observations. Black stream lines show the magnetic field. White squares show the bounds of line of sight segments corresponding to the purple curves in Figure 3.12.*

contribution of the Mg IX line pair (as in Figure 3.14). As can be seen, the spatial distributions of the emission are quite different, mostly at low altitudes. The regions of equal contribution more or less overlap above an heliocentric distance of 1.15 R_s. We therefore restrict the comparison of measured and predicted electron temperature to these altitudes only, where we can safely assume that the density and temperature measurements apply to the same region. Examining Figure 3.13, we can see that this altitude corresponds to the purely open field line region of the pseudo-streamer, while at lower altitudes the lines of sight intersects both open and closed field line structures.

3.7.5.4 Electron Density and Temperature in a Pseudo-Streamer

We located a distinct and narrow region which accounts for significant and equal parts of the total fluxes used in the electron density and temperature measurements. For each line of sight, we average the predicted quantity over the segment bounded by the white squares in Figure 3.13, to obtain a radial profile along the SUMER slit.

Figure 3.16 shows the comparison of the predicted electron density in the pseudo streamer with the SUMER measurement. The blue curve with error bars shows the measured electron density while the dashed red line shows the model results. The error bars in the model indicate the minimum and maximum electron density found along the line of sight segments over which we take the average. The shaded region represent the altitude where the observed flux of the lines used for this measurement has decreased to below twice the scattered light flux, making the measurement less reliable at these heights. As can be seen, the model and measurements are in very good agreement, although the uncertainty in the electron density measurement is quite large.

The predicted electron temperature along the SUMER slit and its comparison to observations is shown in Figure 3.17. The color coding, as well as the role of the error

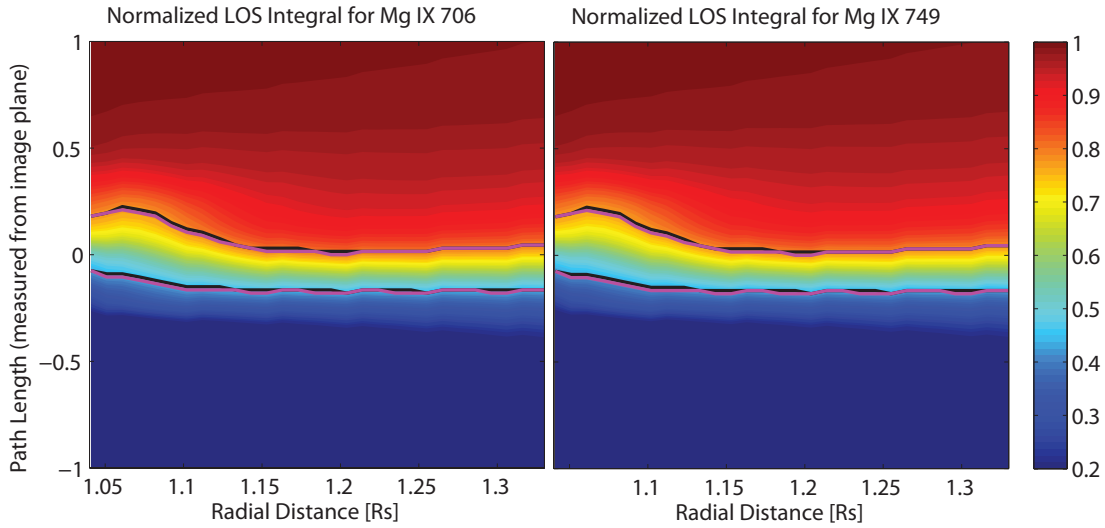

Figure 3.14: *Emissivity normalized line of sight integral for Mg IX 706Å (left) and Mg IX 749Å (right). The purple curves represent the ranges along the LOS that account for 36% of the total emission of the 706Å line, while the black curves represent the same range for the 749Å line.*

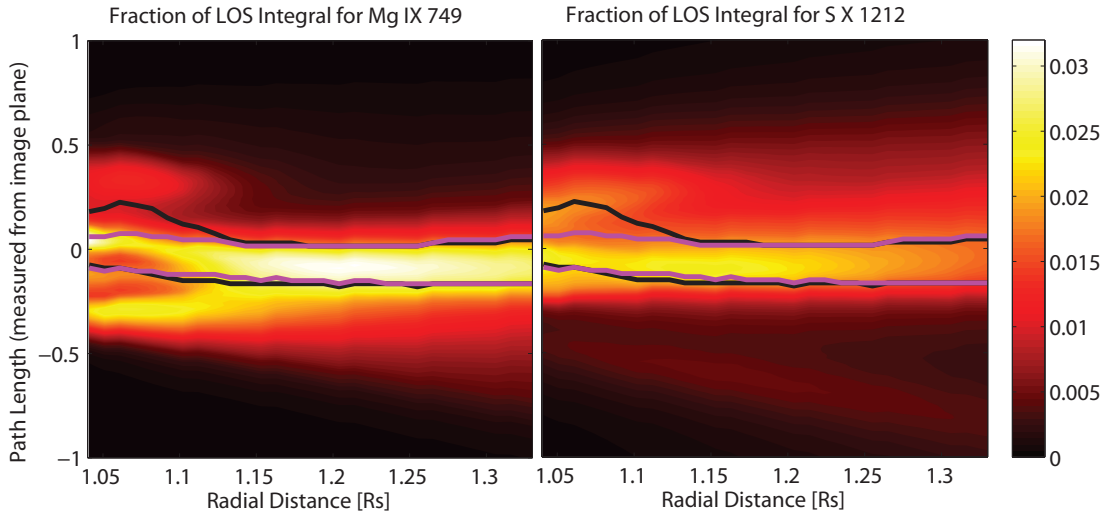

Figure 3.15: *Fractional contribution to the line of sight integral for Mg IX 749Å (left) and S X 1212Å (right). The purple curves represent the ranges along the LOS that the S X line pair has similar contribution (same region as in Figure 3.12), while the black curves represent the region where the Mg IX line pair has similar contribution (same region as in Figure 3.14).*

bars, is the same as in Figure 3.16. The comparison starts at $r = 1.15$ R_s since below that height the lines used in the temperature measurement are not emitted from the same region as the lines used for the density measurement. The shaded region corresponds to altitudes where the observed flux of the lines used for this measurement has decreased to below twice the scattered light flux, making the measurement less reliable at these heights. The measured temperature exhibits large uncertainties and variations with height, with no clear radial trend. The predicted electron temperature falls within the range of observed values, suggesting that the heating supplied by the heating mechanism is sufficient to achieve the observed coronal temperatures in the quiet corona.

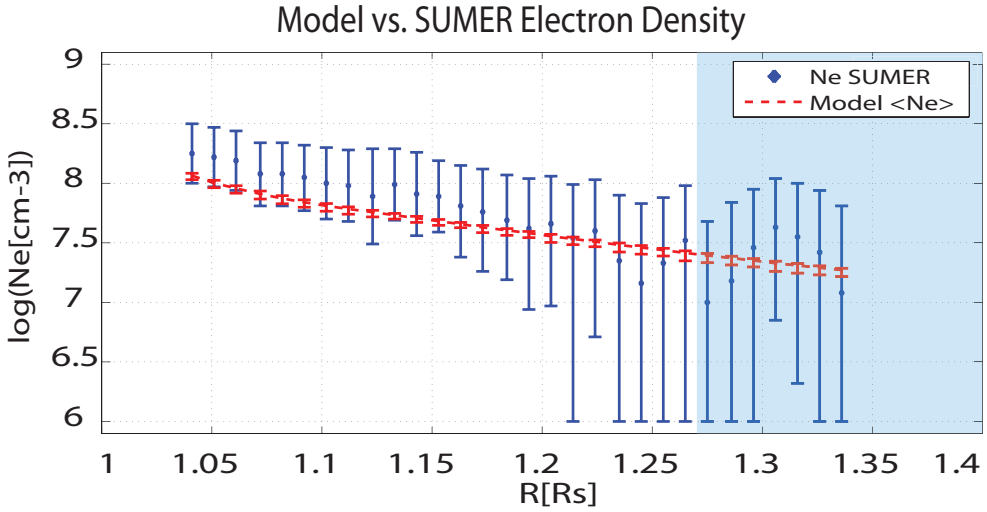

Figure 3.16: *Model / SUMER comparison of electron density. The blue curve shows the density measured using the SUMER S X 1196Å and S X 1212Å line flux ratio. The red curve shows the modeled density, averaged over the line of sight segments bounded by white squares in Figure 3.13. The model uncertainty is calculated given the minimum and maximum density along each segment. The shaded region represents the altitude above which the observed line fluxes decreased to below twice the scattered light flux (see Table 3.1).*

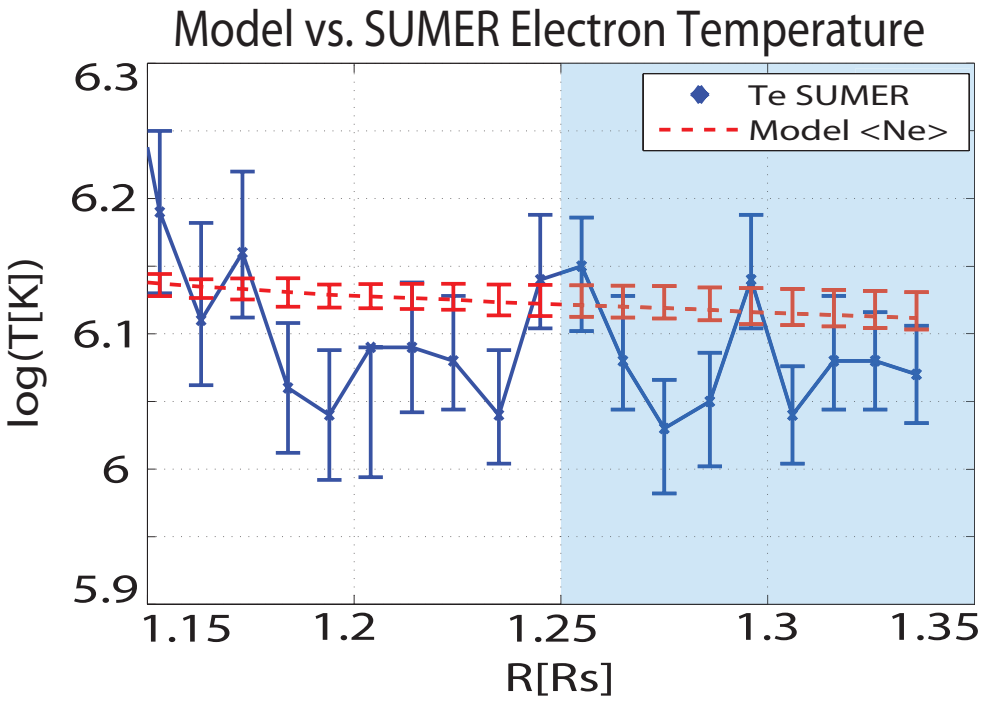

Figure 3.17: *Model / SUMER comparison of electron temperature. The blue curve shows the temperature measured using the SUMER Mg IX 706Å and Mg IX 749Å line flux ratio. The red curve shows the modeled electron temperature, averaged over the line of sight segments bounded by white squares in Figure 3.13. The model uncertainty is calculated given the minimum and maximum density along each segment. The shaded region represents the altitude above which the observed line fluxes decreased to below twice the scattered light flux (see Table 3.1).*

3.7.6 Wave Dissipation in the Pseudo-Streamer

The three-dimensional, magnetogram-driven solution allows us to study not only the synthetic line of sight line width, but also the variation of the wave amplitude along selected field lines. We recall that the line width observed from a particular direction depends on both the wave energy and the magnetic topology, as is clear from Eq. (3.2). Examining Figure 3.13, we can see that the magnetic field in the region of largest emission is composed of a closed loop structure up to a radial distance of $\sim 1.1 R_s$, above which all field lines are open. In the closed loop region, the magnetic field direction changes from approximately perpendicular to parallel to the line of

sight. Thus while the wave amplitude is expected to increase with height in this region (due to the sharp decrease in the plasma density), the fraction of it that lies along the SUMER line of sight will decrease. Above the closed loop structure the magnetic field direction is very close to perpendicular to the line of sight, and thus a larger share of the wave induced motions will contribute to the line width. This dependence on the line of sight and magnetic field geometry is illustrated in the radial variation of the line widths in Figure 3.11, where an evident change in the synthetic line widths of all ions occurs around $r = 1.1\mathrm{R}_s$.

In order to study the actual variation of the wave amplitude, we extracted the model results along three open field lines inside the region of largest emission. This will enable us to remove the effects of the line of sight geometry and directly study the wave dissipation taking place in this region. We calculate the rms of the wave velocity amplitude, $\overline{\delta u} = \sqrt{< \delta u^2 >}$, using Eq. (3.4). Hassler et al. (1990) and Moran (2001) have shown that if no wave damping is taking place, the rms wave amplitude would vary as $\overline{\delta u} \propto \rho^{-1/4}$ as a result of energy conservation along a magnetic flux tube. Thus we would expect the rms wave amplitude predicted by the model to be lower than the undamped values. The results are shown in Figure 3.18. The location of the selected field lines is shown in the inset. Line 1, colored in blue, is an open field line on the edge of the pseudo-streamer, while line 3, colored in red, in the first open field line straddling the closed loop structure. Line 2, colored in green, lies in between the other two lines. The solid curves show the rms wave amplitude as a function of the path length S along each of the field lines, while the dashed curves show hypothetical curves for undamped waves, normalized to the value of the modeled curve at $S = 0.05\mathrm{R}_s$. As expected, the rms wave amplitude sharply increases close to the inner boundary due to the sharp drop in density. Departures from the undamped curve become prominent above $S = 0.05 - 0.1\mathrm{R}_s$, although each of the field lines exhibit a different dissipation rate. It is interesting to compare the damped

and undamped curves to a similar analysis presented in *Hahn et al.* (2012) for a polar coronal hole. In Figure 5 therein, the observed effective speeds of several emission lines are compared to undamped values. Departures from the undamped curves start above heights of $0.1R_s$ and $0.2R_s$ above the limb, depending on the ion. Of the three field lines in Figure 3.18, line 1 most resembles a coronal hole field line, with minimal bending around the closed loop structure. The wave amplitude along line 1 shows very similar behavior to the one reported in *Hahn et al.* (2012). In the case of line 2 and line 3, larger departures from energy conservation occur at lower heights near the closed loop region. This is most prominent for line 3, where the wave amplitude is significantly reduced near the tip of the loop structure. In this location, higher dissipation is expected to occur due to the presence of counter-propagating waves, and the first term under the square root in Eq. (2.13) will be taken into account. Above that point, the rms wave amplitude increases at a rate similar to that of line 1, consistent with the fact that the dissipation rate is now dominated by reflections, i.e. the second term under the square root in Eq. (2.13). Line 2 also exhibits a signature of this behavior, although it is less pronounced.

3.8 Conclusions

In this work, we have examined whether the dissipation of Alfvén waves due to a turbulent cascade is a likely candidate to explain the observed large-scale distribution of coronal heating rates. By combining results from an Alfvén wave-driven MHD model with the CHIANTI atomic database, we were able to produce, for the first time, synthetic EUV spectra that include thermal and non-thermal broadening from a global model.

The ability to predict non-thermal line broadening in a wave-driven global model is an important step in testing the validity of the underlying wave heating mechanism, as this observable is directly related to wave-induced motions and is a measure of the

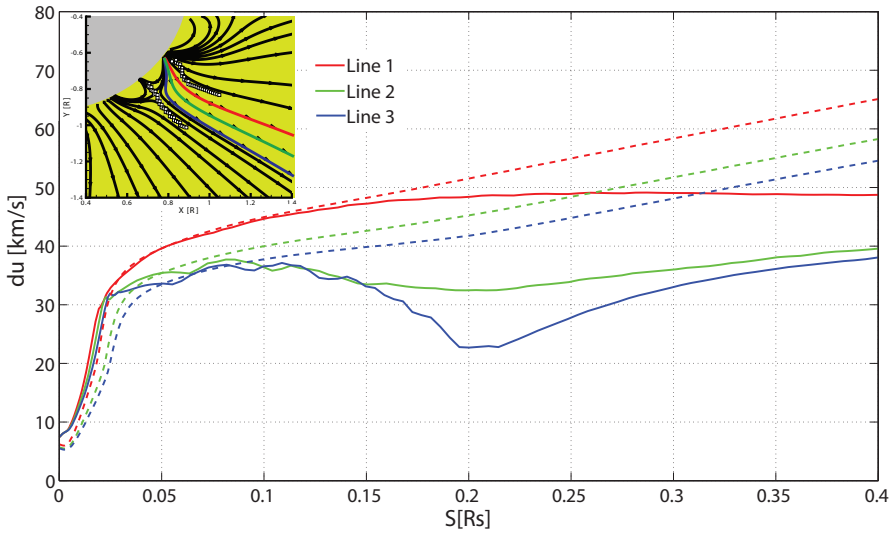

Figure 3.18: *Model results of the rms velocity amplitude of Alfén waves along selected open field lines. The inset shows the field lines in an equatorial plane. White squares denote the region of maximum emission as described in Section 3.7.5.1. The solid curves show the rms velocity amplitude extracted from the AWSoM model, while the dashed curves show hypothetical wave amplitudes for undamped waves. The hypothetical curves were normalized to the corresponding modeled value at* $S = 0.05R_s$.

modeled amplitude of the Alfvén waves. The advantage of a global model is that the predicted emission is integrated over the line of sight using the full three-dimensional solution, without invoking simplifying assumption about the geometry of the system.

Comparing the synthetic spectra to detailed SUMER observation between r=1.03 - 1.43R_s, we tested whether the AWSoM model can predict plasma properties and wave energies that are simultaneously consistent with observations. The predicted total flux in selected emission lines depends on the electron density and temperature, while the line width depends on the ion temperature and wave amplitude. We have found good agreement between predicted and observed line width, and reasonable agreement of the total flux, given the uncertainties in atomic data.

By taking advantage of the three-dimensional nature of the solution, we could calculate the relative contribution of different regions along the line of sight to the observed emission. We found that a significant fraction of the emission of several lines comes from a narrow, well defined magnetic structure: an equatorial pseudo-streamer. The electron density and temperature predicted by the model are in good agreement with the measurements performed using the emission of these lines, suggesting that this region is indeed the source of the relevant radiation detected by SUMER. This type of three-dimensional line of sight analysis is important to the interpretation of any remote observation.

In summary, we have shown that the treatment of Alfvénic energy as described in the AWSoM model simultaneously produces electron densities, temperatures, total line fluxes and line broadening that are consistent with observations. This suggests that the model correctly describes the amount of wave energy injected into the system, and the fraction of it that is deposited as heat.

Finally, we mention possible improvements and future work. First, the synthetic profiles can be calculated more accurately. The line fluxes calculations used here were based on the assumption of ionization equilibrium. This assumption may break

down, as wind-induced departures from equilibrium may occur. A more accurate calculation should be based on solving the charge state evolution in the region under question, which will be the basis of a more accurate calculation of the line fluxes. Such a calculation is presented and performed in Chapter 4. Second, as mention in the Conclusions for Chapter 2, the model's treatment of wave propagation and dissipation can be improved to describe wave reflections self-consistently, as the reflection coefficient should depend on the magnetic topology.

CHAPTER IV

Solar Wind Acceleration and Heavy-Ion Charge States

4.1 Introduction

In this Chapter, we examine whether a solar wind model in which the wind is accelerated by Alfvén waves can explain the observed charge state distributions, both in the solar corona and in the fast and slow solar wind.

As mentioned in Section 1.7.1, the fast and slow wind differ not only in their charge states, but also in the elemental abundances: the slow wind exhibits a FIP bias, while the fast wind does not. Describing elemental abundances is beyond the scope of this work, as it requires:

- 1. a multi-fluid description to describe the evolution of each element. The AWSoM model is implemented within the framework of single-fluid, two-temperature MHD.

- 2. the inclusion of an elemental fractionation mechanism responsible for the FIP bias; such a mechanism has not been clearly identified (*Laming*, 2009, 2012).

- 3. the FIP bias is most likely related to the time-dependent evolution of the plasma. This is motivated by the fact that the FIP bias observed in coronal

loops depends on the "age" of the loop , i.e. the time elapsed since its emergence from the chromosphere (e.g. *Feldman and Widing*, 2003).

We have seen in Chapter 2 that the AWSoM model is capable of reproducing the large scale structure of the fast and slow solar wind in the heliosphere, and that the resulting wind speeds at 1-2 AU are consistent with Ulysses observations. It was also shown that the thermodynamic structure of the lower corona is consistent with observed EUV emission. The wave dissipation mechanism and the heating rates in the lower corona were examined in detail in Chapter 3. Here, we wish to verify that the modeled wind acceleration rates and flow properties in the extended corona are also consistent with observations. The largest acceleration rates occur close to the Sun and below the Alfvénic point. Direct measurements of the wind speeds in this region are not available; however, by modeling the charge state evolution using the wind properties given by AWSoM, we can compare the resulting charge states distributions to observations. This then serves as an indirect test of the conditions along the wind trajectory, from its source region and up to the freeze-in height.

We adopt the diagnostic approach proposed in *Landi et al.* (2012a), where co-ordinated observations at both ends of the wind trajectory, i.e. in-situ solar wind observations and the emission from the lower corona, are used to test model predictions. In *Landi et al.* (2014, under review), this diagnostic approach was used to test predictions of three theoretical models, including the AWSoM model. That study was limited to the center of an idealized polar coronal hole. Here this work is extended to a realistic magnetic field, and covering the entire latitudinal range, so that the charge states in both the fast and slow wind are simulated.

It is important to emphasize that both the fast and the slow wind captured by the ASWoM model (see Chapter 2) originate from the open field lines region in the corona. Moreover, the steady-state simulations used in this work do not allow us to describe dynamic release of material from the closed field line region into the wind. Therefore

this work does not aim to examine which of the theories invoking dynamic release are best suited to explain the observations. However, the steady-state picture of the solar wind does not necessarily contradict the dynamic release models. *Antiochos et al.* (2012) suggested that the solar wind be classified into quasi-steady and non-steady flow types rather than into the traditional fast and slow wind; in this picture, the non-steady wind is the variable slow wind, which is formed by dynamic release of material, while the quasi-steady wind is made of both fast and slow wind flows that have similar compositional and temporal characteristics. The quasi-steady wind is not formed by dynamic release; *Antiochos et al.* (2012) associated it with low latitudes coronal holes. By modeling the wind along open field lines in the AWSoM model, we in fact describe a steady fast and slow wind, without attempting to describe the fluctuations in the non-steady slow wind properties or its causes. Instead, we explore whether the steady slow wind can carry different charge state composition compared to the fast wind, due to the different plasma conditions along the wind trajectory.

It remains to describe how one can predict the charge states using a two temperature MHD model, which does not include heavy ion species. As the abundances of elements heavier than helium are very low, they do not affect the global MHD solution. We can therefore use the electron density, temperature and speed from the AWSoM model to drive a charge state evolution model (Michigan Ionization Code (MIC), *Landi et al.*, 2012b) which calculates the ionization status of an element at any point along the wind trajectory. The modeled freeze-in distributions for O, C, and Fe are directly compared to in-situ measurements performed by the SWICS instrument on board Ulysses at 1-2AU. In the corona, on the other hand, information about the ionization state can only be gained from the observed emission associated with the different ions. As in Chapter 3, we calculate synthetic line-of-sight emission from the model and compare it to remote observations. However, the assumption of ionization equilibrium made in Chapter 3 is here relaxed, and the actual ion fractions

predicted by MIC are used instead. The synthetic line of sight emission is compared to spectral line intensities from S, Si and Fe observed in the lower corona by the EUV Imaging Spectrometer (EIS, *Culhane et al.*, 2007) instrument on board Hinode. Several spectral lines corresponding to different ionization stages are used, which allows us to examine the modeled ionization rates in detail.

This Chapter is organized as follows. The charge state evolution model is described in Section 4.2. The coupling of this model to AWSoM results is described in Section 4.3. The synthetic emission calculation using the predicted charge states is described in Section 4.4. Details on the in-situ and remote observations used in this work are described in Section 4.5. The model results and their comparison to the observations are presented in Section 4.6. Section 4.7 discusses the higher charge states modeled in the slow wind and presents a possible connection between those increases and a region of higher plasma density in the corona, located near the boundary of the coronal holes. We show that this density enhancement as predicted by the model is consistent with EUV tomographic reconstructions of the lower corona. Section 4.8 summarizes the results and discusses their possible interpretations and implications to understanding the solar wind formation.

4.2 Charge State Evolution Model

4.2.1 Evolution Along Field Lines

As heavy ions are accelerated away from the Sun, they undergo ionization and recombination due to collisions with the electrons, at rates that depend on the local electron density and temperature. The wind speed along the field lines determines how much time the ions spend at a given location; if the speed is sufficiently high, the ions do not have enough time to achieve ionization equilibrium. A model that takes into account the flow properties along the wind trajectory can fully describe

such departures from equilibrium.

The MIC code calculates the charge state evolution in the rest frame of the plasma by solving the following equation for each element (*Landi et al.*, 2012b; *Hundhausen et al.*, 1968):

$$\begin{aligned} \frac{dy_m}{dt} &= n_e \left[y_{m-1} C_{m-1}(T_e) + y_{m+1} R_{m+1}(T_e) - y_m C_m(T_e) - y_m R_m(T_e) \right] \\ \Sigma_m y_m &= 1, \end{aligned} \tag{4.1}$$

where y_m is the fraction of element y in charge state m, while R_i and C_i are recombination and ionization rate coefficients. The first two terms on the right hand side describe creation of ions with charge state m due to ionization from a lower charge state and recombination from a higher charge state, while the last two terms describe losses due to ionization and recombination of ions with charge m into higher and lower charge states, respectively. Eq. (4.1) constitutes a system of coupled continuity equations for each element. These are solved numerically using a fourth-order Runge-Kutta method with an adaptive step size which limits the change in any charge state fraction to a maximum of 10%.

The MIC model requires information about the electron density and temperature in order to solve Eq. (4.1). These are extracted from the AWSoM model along open field lines as described in Section (4.3.2). Since we are interested in the large-scale steady-state solution, the temperature and density at any point are constant in time. The wind speed parallel to the field line (in the co-rotating frame) is used to determine how much time the plasma spends at a given location in order to integrate dy_m/dt. It follows that the wind acceleration rate will impact the results, and different freeze-in distributions are generally expected for fast and slow solar wind flows. In addition, the freeze-in charge states strongly depend on the electron temperature and density up to the freeze-in height.

The temperature-dependent ionization and recombination rate coefficients are calculated using the CHIANTI 7.1 Atomic Database (*Dere et al.*, 1997; *Landi et al.*, 2013), which includes the ionization rates compiled by *Dere* (2007) and the recombination rates reviewed by *Dere et al.* (2009). Finally, we need to specify the boundary conditions for Eq. (4.1). The electron density and temperature at the base of each field line are taken directly from the AWSoM model. These quantities are also used to calculate y_m at the base by solving Eq. (4.1) assuming ionization equilibrium.

4.2.2 Role of Supra-Thermal Electrons

Due to the charge state freeze-in effect, the coronal electron temperature can in principle be estimated from the charge states observed at 1AU. This can be achieved by solving Eq. (4.1) using an assumed wind evolution profiles, and comparing the resulting frozen-in distributions to available in-situ observations. This procedure is then repeated iteratively while changing the parameters governing the wind evolution profile (e.g. *Ko et al.* (1997)) until a minimal deviation between the observations and the data is achieved simultaneously for as many ions as possible. This leads to an empirical determination of the wind parameters below the freeze-in height, from which the coronal temperature can be estimated. Previous work has shown that there is a discrepancy between the freeze-in temperature derived from in-situ charge state ratios and that derived from remote observations of the wind source region (e.g. *Ko et al.*, 1997), with the temperature required to explain the charge states in the heliosphere being generally higher than the observed coronal temperature. It has been shown that this discrepancy can be resolved if an additional population of supra-thermal electrons is assumed to be present below the freeze-in height (e.g. *Esser and Edgar*, 2000). As of yet, there is no direct observational evidence of coronal supra-thermal electrons. *Laming and Lepri* (2007) have shown that electrons obeying a kappa distribution function can explain the ionization states observed in the wind,

and that such a distribution can be created by parallel heating due to lower hybrid wave damping. *Feldman et al.* (2007) estimated the energy content of supra-thermal electrons in an active region, and found that less than 5% of the electron population can have energies above 0.91keV and less than 2% can have energies above 1.34keV in active regions.

In this work we consider the charge state evolution due to a single temperature plasma as well as a plasma with an additional hotter electron population. The additional electron population is modeled by assuming that 2% of the electrons belong to a second Maxwellian distribution at $3MK \approx 0.25keV$. The second Maxwellian produces a supra-thermal tail on top of the main electron population. This value was chosen empirically as we describe in Section (4.6), and is smaller than that estimated in *Feldman et al.* (2007). Ideally, a full parametric study of these values should be performed, guided by observations. Such a study is beyond the scope of this work. Incorporating the supra-thermal electrons in the simulation serves as a proof of concept only, to determine whether they can at the same time:

1. affect charge state composition to solve the discrepancy between remote and in-situ observations; and

2. provide observable signatures in remote observations (to our knowledge, such signatures were not found in coronal emission to date), and that their effect on the emission is consistent with observed spectra.

In order to accomplish this, two sets of ionization rate coefficients need to be calculated in order to solve Eq. (4.1): one in which only the thermal electron population is taken into account, and another where both the thermal and supra-thermal populations are considered. In addition, the presence of supra-thermal electrons will also impact the emissivity of the plasma, which will require us to modify the standard calculation of synthetic emission, as we describe in Section 4.4.

4.3 Combining AWSoM Results with the Evolution Model

4.3.1 Deriving Wind Parameters from AWSoM

The MIC code was used to solve for the charge state evolution using the ASWoM simulation for CR2063 described in Chapter 2. The charge state evolution model requires as input the electron density, temperature, and speed along the wind trajectory. Since the wind flows parallel to the magnetic field in the co-rotating frame, we trace the magnetic field lines in the 3D AWSoM solution and extract these quantities along them. The AWSoM model equations do not describe the ion motion, and it is therefore assumed that the ions move with the same speed as the electrons and protons. This assumption does not strictly hold at all locations in the solar atmosphere, and future work may take differential ion speeds into account by extending the AWSoM model to a multi-fluid MHD description.

As explained in Chapter 2, the transition region in the AWSoM model is artificially broadened and the energy equation is rescaled accordingly in order to resolve the processes in that region. This will cause the field lines extracted from the model to be longer in that region, which will introduce undesired effects as the ions will spend a longer time at a given temperature and density. It is therefore necessary to remap the field lines in order to undo this broadening, as was described in Chapter 2.

4.3.2 Field Line Selection for Coordinated Observations

Modeling the charge state evolution for all ions and all field lines in the 3D domain of the global model is computationally expensive, and therefore the number of field lines should be minimized as much as possible. On the other hand, the field lines should be chosen such that the model results can be compared to Ulysses insitu measurements covering both the fast and slow solar wind, and remote spectral observations of the lower corona.

We take advantage of high resolution observations performed by the EIS instrument on board Hinode taken during CR2063 on November 16, 2007 at 11:47:57, observing the north polar coronal hole. In the same period, Ulysses was performing its third and last polar scan, covering almost all latitudes in a period of a little over a year. This particular set of EIS observations was chosen since it includes bright and isolated emission lines from several charge states of Fe, two charge states of Si and one charge state of S. We extracted the AWSoM solution along the field lines that intersect the EIS line of sight for that date. The full latitudinal range of available Ulysses measurements (taken during a period of a year around the time of CR2063) was covered by extracting the field lines at all latitudes at 1 degree spacings. The geometry is shown schematically in Figure 4.1. The black streamlines are the selected magnetic field lines. Note that only the open field lines were used to obtain a solution from MIC, and closed field lines are shown here for clarity. The solar surface is colored by the radial magnetic field and the gray surface represents the location of the current sheet. The direction of the EIS line of sight and the general direction of Ulysses are marked by the labeled arrows.

As explained in Chapter 2, the AWSoM solution used here was obtained using a synoptic magnetogram for CR2063, thus the changes in the solar magnetic field during the year-long Ulysses polar scan are not taken into account in the simulation. The comparison of the model results to Ulysses observations should be regarded as a qualitative comparison of the large-scale structure of the solar wind charge states, and we do not attempt to track the model solution along Ulysses's trajectory. In this sense, the set of field lines shown in Figure 4.1 allow us to obtain a "snapshot" of the predicted charge states in the fast and slow solar wind during solar minimum.

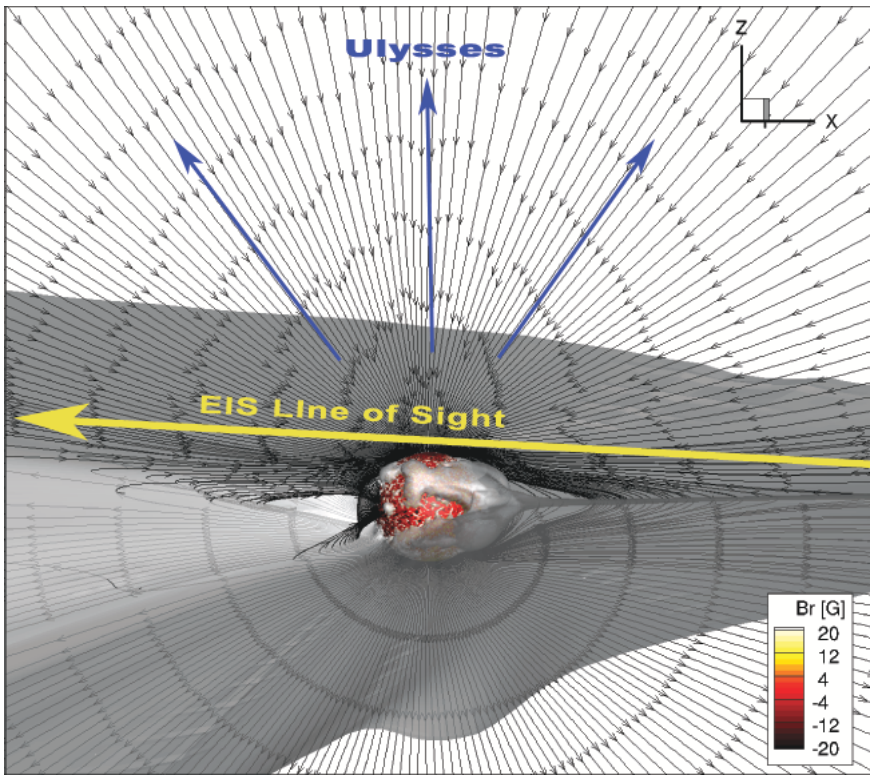

Figure 4.1: *Geometry used for comparing model results with Ulysses and EIS coordinated observations. Black stream lines show the magnetic field lines extracted from the AWSoM simulation for CR2063. Wind parameters along the open field lines were used as input to MIC. Labeled arrows mark the direction of the EIS line of sight and the general direction of Ulysses. The solar surface is colored by the radial magnetic field obtained from a synoptic GONG magnetogram. The gray surface represents the heliospheric current sheet, where the radial magnetic field is zero.*

4.4 Modified Non-Equilibrium Contribution Function for Synthetic Emission

Calculating the synthetic emission of a given spectral line requires knowledge of the contribution function, $G_{ji}(N_e, T_e)$, of the associated electronic transition from an upper level j to a lower level i. The contribution function was defined in Eq. (3.7).

4.4.1 Ion Fractions

For a spectral line emitted by an ion of element X at charge state $+m$, $G_{ji}(N_e, T_e)$ is proportional to the ratio $N(X^{+m})/N(X)$, i.e. the abundance of the ion X^{+m} relative to the total abundance of the element X. This ratio is usually found by assuming ionization equilibrium at the local electron temperature. In the case of the combined AWSoM-MIC simulation, the ions may not have sufficient time to reach ionization equilibrium due to their flow speed. These departures from equilibrium are taken into account in calculating the synthetic emission by replacing the equilibrium value of $N(X^{+m})/N(X)$ with the ion fractions predicted by MIC.

In this Chapter two cases of charge state evolution models are considered: with and without supra-thermal electrons. As discussed in Section 4.2.2, the additional electron population will change the ionization and recombination coefficients due to their higher energies, resulting in different ion fractions.

4.4.2 Level Population

The contribution function also depends on the relative level population of ions of type X^{+m} at level j, appearing as the $N_j(X^{+m})/N(X^{+m})$ term in Eq. (3.7). Supra-thermal electrons will impact the level population, since their presence will affect the collisional excitation/de-excitation rates. This effect was taken into account when calculating the emission from the MIC simulation in the case where supra-thermal electrons were included.

4.4.3 Line of Sight Emission

The AWSoM and MIC results along the field lines described in Section 4.3.2 were interpolated onto a uniform grid along the EIS line of sight and the results were used to calculate the emission at each point. The contribution function at any given point was obtained from the CHIANTI atomic database using the AWSoM electron temperature

and density, assuming elemental abundances given in *Caffau et al.* (2011), the ion fractions calculated from MIC, and the level populations predicted either with and without the additional supra-thermal electron population. The synthetic line of sight flux was obtained by integrating the emission according to Eq. (3.8).

4.5 Observations

4.5.1 Ulysses in-situ Charge States

The in-situ charge state measurements were obtained by the Solar Wind Ion Composition Spectrometer (SWICS, *Gloeckler et al.*, 1992) on board Ulysses during June 2007 to June 2008 (i.e. during a period of a year centered around the simulation time). The charge states ratios of O^{7+}/O^{6+} and C^{6+}/C^{5+} and the average charge state of Fe, $< Q >_{Fe}$ are publicly available through NASA's CDAweb. The oxygen and carbon charge state ratios are sensitive to the electron temperature in the inner corona (up to the freeze-in height of 1.5-2$R_\odot$), and they are often used to distinguish between different solar wind types and to study their source regions (e.g., *Zurbuchen et al.*, 2002; *Zhao et al.*, 2009). The average charge state of Fe is also known to vary between different solar wind regimes and was used to study the wind evolution in the outer corona (e.g., *Lepri et al.*, 2001; *Lepri and Zurbuchen*, 2004; *Gruesbeck et al.*, 2011), since it is sensitive to the electron temperature up to a freeze-in height of $\sim 4R_\odot$.

4.5.2 Emission from the Lower Corona

The observations we used in this work were taken by the EIS instrument on 16 November 2007. During this time, the EIS 2"×512" slit was oriented along the North-South direction and was pointed at 7 adjacent position along the solar E-W direction to cover a total field of view of 14"x512" whose center was located at (0",866"). The

field of view extended from 0.61 $R_\odot$ from the Sun center inside the disk and up to a height of 1.15 $R_\odot$ above the limb in the north coronal hole. At each location of the raster, the spectral range covered was $171 - 211$Å and $245 - 291$Å (with a spectral pixel size of 0.022Å per pixel) and the exposure time was 300s. From the available spectral range, we chose a set of bright and isolated spectral lines (listed in Table 4.1), which includes as wide a range of charge states belonging to the same element as possible. More details on these observations can be found in *Hahn et al.* (2010).

Ion Name	Wavelength [Å]	F_{scatt} [erg cm^{-2} s^{-1} sr^{-1}]	R_{max} [$R_\odot$]
Fe VIII	185.213	29.349	1.115
Fe IX	188.497	22.357	1.136
Fe IX	197.862	9.505	1.136
Fe X	184.537	78.007	1.136
Fe XI	188.217	101.171	1.125
Fe XI	188.299	78.057	1.125
Fe XII	195.119	121.752	1.106
Fe XIII	202.044	52.229	1.025
Si VII	275.361	14.792	1.136
Si X	261.057	15.664	1.136
S X	264.231	15.677	1.115

Table 4.1: *Selected EIS emission lines. F_{scatt} indicates the instrument-scattered light flux and $R_{\max}$ is the highest altitude at which the scattered flux is less than 20% of the observed flux (see Section 4.5.2.2).*

4.5.2.1 Data Reduction and Selection

The data were reduced using the standard EIS software made available by the EIS team through the SolarSoft IDL package (*Freeland and Handy*, 1998). Each original frame was flat-fielded, the dark current and CCD bias were subtracted, the cosmic ray hits were removed, and the defective pixels were flagged. Also, residual wavelength-dependent offsets and the tilt of the detectors were also removed. Data were calibrated in wavelength and intensity; the most recent EIS intensity calibration from Warren et al. 2014 was applied. This updated intensity calibration improves

the calibration of the long-wavelength channel (246-292 A) and also allows to account for the degradation occurred during the EIS mission. The accuracy of the calibration is ≈25%.

In order to increase the signal-to-noise ratio, the data were averaged along the E-W direction and re-binned along the slit direction (N-S) in bins of 0.01 $R_\odot$.

Only 14 bins extending from 1.025$R_\odot$ to 1.155$_\odot$ above the limb were used for comparison with the model. Pixels between 1.00 - 1.025$R_\odot$ were excluded since they might be affected by limb brightening (*Hahn et al.*, 2010). The portion of the slit pointed inside the solar disk was only used for evaluating the instrument-scattered light, as we describe in Section 4.5.2.2.

Spectral line profiles were fitted with a Gaussian curve removing a linear background. At a certain height above the limb the line emission becomes too weak, and a clear Gaussian cannot be discerned; these measurement are omitted from the analysis. The overall uncertainty in the line fluxes is obtained by taking into account the calibration error, the fitting error in the Gaussian, and the statistical error in the measurement itself.

4.5.2.2 Scattered Light Evaluation

The EIS optics causes the instrument to scatter the radiation coming from the solar disk into the detector, which can contaminate the observations even in the off-limb section of the slit. This contribution depends on the specific configuration of the instrument and on its pointing at the time of the observations and it cannot be removed a-priori. The method used for SUMER in Chapter 3 allows us to estimate the scattered light contribution in a particular set of observations, but it requires concurrent observations of chromospheric lines or continuum emission that can be used to derive the rate of decrease of the scattered light. In the case of the EIS spectrometer there is no continuum emission available. The only chromospheric line

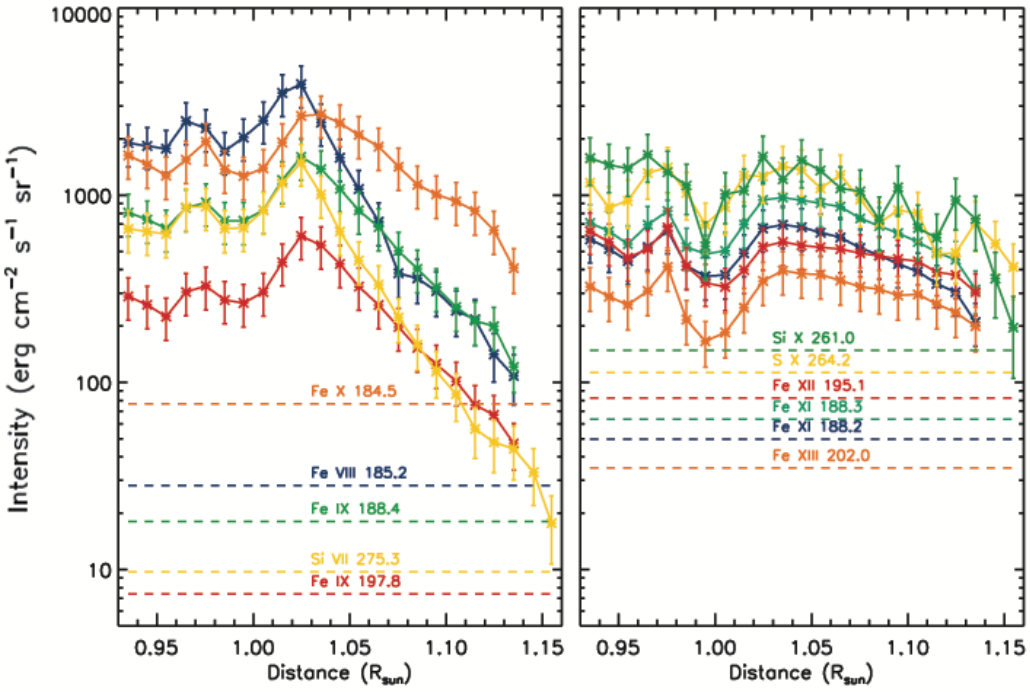

Figure 4.2: *Intensity vs. distance for the spectral lines in Table 4.1, over the EIS field of view between 0.93$R_\odot$ and the farthest end of the slit at 1.16$R_\odot$ (solid curves). The dashed lines show the estimated scattered light intensity for each line. The observed intensities and the scattered light level are color-coded in the same way. For clarity of presentation, the Si X intensity is multiplied by 10, S X by 12, and Fe XI 188.2 by 0.6.*

is from He II. *Hahn et al.* (2012) showed that the emission by this line in the off-limb section is actually real coronal emission, so this line cannot be used. EIS measured some transition region lines from O IV and O V which can potentially be used, but they are too weak. Instead, we evaluate the scattered light contribution based on EIS observations performed during a partial lunar eclipse. Using the flux ratio from the occulted and non-occulted portions of the disk, the EIS scattered light was found to be around 2% of the disk emission (Ugarte Urra 2010, EIS Software Note No. 12). We evaluate the scattered light flux for each of the lines in Table 4.1 by averaging their emission in the portion of the slit that covered the disk in the $0.61 - 0.97 R_\odot$ range. The scattered light intensity is then taken to be 2% of the

average value. The line intensities over the EIS field of view from $0.93R_\odot$ to the end of the slit are shown in Figure 4.2. For clarity of presentation, the Si X intensity is multiplied by 10, S X by 12, and Fe XI 188.2 by 0.6. It can be seen the intensity drops sharply in the off-limb portion of the slit for the lines belonging to the lower ionization stages. This is consistent with having a small contribution from scattered light: in fact, the local coronal emission decreases very rapidly as $\approx N_e^2$, while scattered light usually decreases very slowly with height above the limb. The scattered light levels for each line are shown as dashed horizontal lines, and their values are reported in the third column of Table 4.1. The actual contribution is probably lower, since the EIS configuration here is very different than the one used during the eclipse; in the present observations part of the slit pointed off the limb and therefore the telescope is less illuminated by the disk emission. To exclude any significant contamination by scattered light from this analysis, we conservatively use only observations where the scattered light level is less than 20% of the observed flux to compare the observations to model results. The maximum height at which this occurs for each line, R_{max}, is reported in the last column of Table 4.1.

4.6 Results

4.6.1 Solar Wind: Frozen-in Charge States

The frozen-in distribution predicted by AWSoM/MIC for the field lines described in Section 4.3.2 are compared to Ulysses observations taken between June 2007 and June 2008. The wind speed and density measured by Ulysses at the same period were compared to the simulation results in Figure 2.18, which demonstrated that the predicted values are in good agreement with the observations. Figures 4.3 - 4.4 show Ulysses observations (left panels) and the AWSoM / MIC results (right panels) for O^{7+}/O^{6+} and C^{6+}/C^{5+} plotted against heliographic latitude for the case of a single

temperature electron population. The first thing of note is that the charge state ratios in the region covered by the slow solar wind around the equatorial plane are higher than those outside this region, in line with observations. The overall magnitude of the modeled O^{7+}/O^{6+} and C^{6+}/C^{5+} ratios is about an order of magnitude lower than the observed values at all latitudes. However the qualitative behavior is markedly similar. Figure 4.5 shows Ulysses and model predictions of the average frozen-in charge state of Fe, $< Q >_{Fe}$, at all latitudes. The differences between the charge state distributions of Fe measured in the fast and slow solar wind are more subtle than for O and C ions (*Lepri et al.*, 2001). The predicted values of the average charge state of Fe are very close, but smaller, than the observed values, with a slight increase in the low latitude slow wind. In summary, the modeled charge states exhibit the well-known large scale behavior of higher charge states at low latitudes around the heliospheric current sheet, and lower charge states at high latitudes associated with polar coronal holes (*von Steiger et al.*, 2000).

In all the cases presented above, the observed charge states exhibit temporal variability, which is significantly higher in the slow wind. Since the AWSoM-MIC results are obtained from a steady-state model, the predicted charge states are not expected to capture this variability. In addition, the charge state evolution was only solved for selected field lines, intersecting a single meridional plane close to the Sun. Thus the latitudinal behavior of the predicted charge states constitutes a qualitative "snapshot" of the heliosphere, and the smaller-scale variations seen in the model are not to be directly compared to specific structures seen in the observations.

These results demonstrate that the wind profiles predicted by AWSoM solely along open magnetic field lines can lead to distinctly different charge states in the fast and slow solar wind, with higher ionization states occurring in the slow wind. However, the results for the charge state ratios for O and C suggests that their modeled ionization rates are insufficient for reproducing the absolute observed values in both the slow

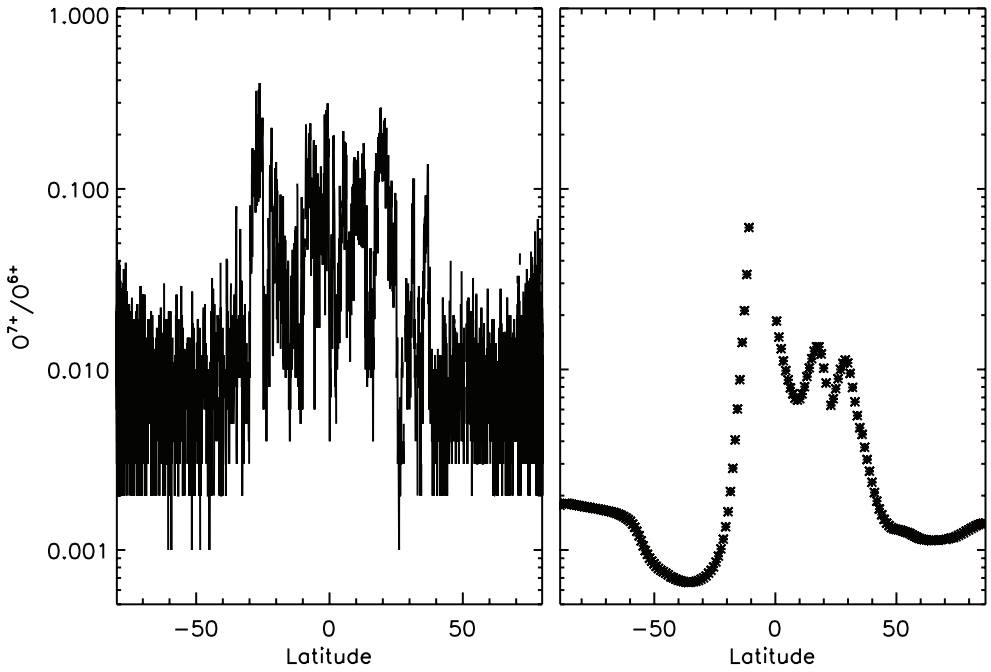

Figure 4.3: *O^{+7}/O^{+6} ratio measured by Ulysses (left) and predicted by AWSoM / MIC (right).*

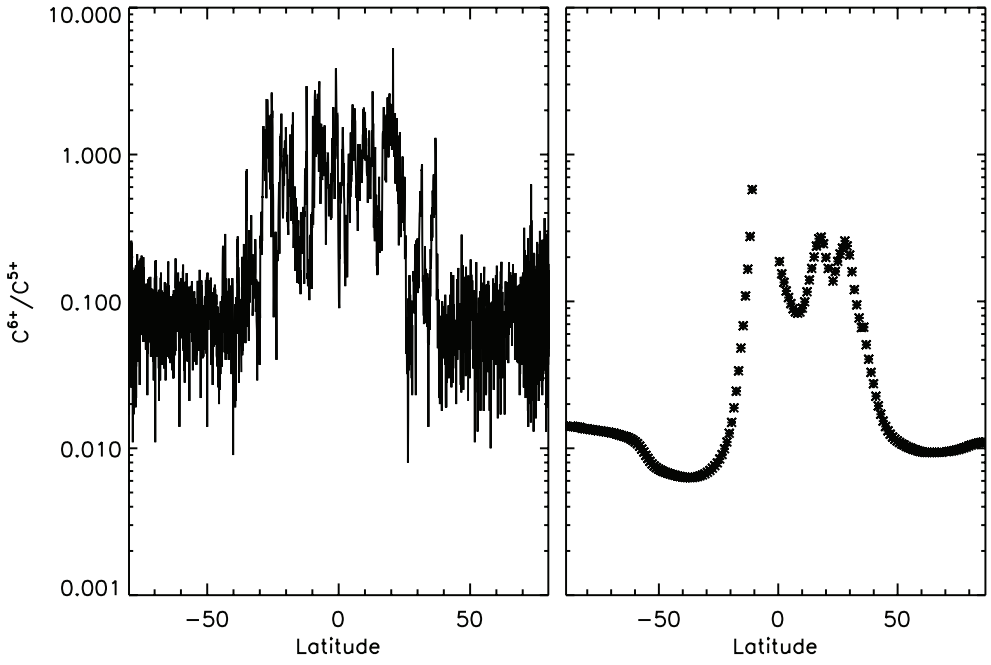

Figure 4.4: *C^{+6}/C^{+5} ratio measured by Ulysses (left) and predicted by AWSoM / MIC (right).*

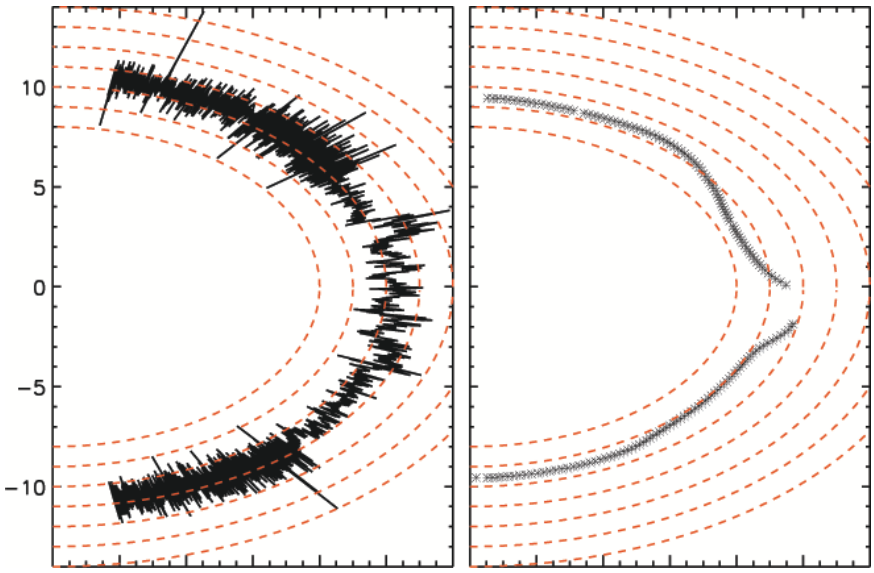

Figure 4.5: *Average charge state of Fe measured by Ulysses (left) and predicted by AWSoM / MIC (right).*

and fast wind. From Eq. (4.1), the low ionization rates can be due to several factors: 1. The AWSoM electron density is too low, inhibiting the collisions necessary for ionization to the higher charge states (C^{6+} and O^{7+}). 2. The predicted ionization rate coefficients are too small. We will explore these factors separately.

As will be shown in Section 4.7.2.1, the predicted electron density and temperature are within a factor 2 of the values predicted from independent tomographic reconstruction at most locations in the lower corona. We also showed in Chapter 2 that the 3D thermal structure predicted for CR2063 leads to synthetic EUV and soft X-ray emission that is consistent with full-disk observations of the lower corona. Even though the discrepancy between the model and these observations may be large at certain localized regions, the under-prediction of the charge state ratios occurs for field lines at all latitudes. It is therefore unlikely that the modeled wind properties along particular field lines are the cause of the low ionization; rather, the cause of the under-prediction should be present globally.

The low charge state ratios may be due to an under-prediction of the ionization

rate coefficients, which depend on the thermal energy of the electrons. This can occur even in the ideal case where the electron temperature is predicted accurately. As discussed in Section 4.2.2, it has been suggested that an additional population of supra-thermal electrons may be present in the corona and below the freeze-in height. Even a small population of supra-thermal electrons can increase the ionization rate coefficients significantly. We therefore repeat the charge state calculations using ionization and recombination coefficients based on a main electron population obeying a Maxwellian at the local electron temperature, and an additional Maxwellian at 3MK, which constitutes 2% of the entire electron population. Further details about the MIC simulation for this case are given in Section 4.2.2.

The results are shown in Figures 4.6 - 4.8. The agreement between the observed and predicted charge state ratios for O and C are significantly improved compared to the case without supra-thermal electrons, with values in both the slow and fast wind being in good agreement with the observations. This result is consistent with previous studies (e.g., *Esser and Edgar*, 2000; *Laming and Lepri*, 2007) which showed that supra-thermal electrons can resolve the apparent discrepancy between the temperature required to explain the charge states observed in the solar wind and the temperature observed in the wind source region in the corona. It is important to note that even though the supra-thermal electrons were required to obtain a good agreement with the overall magnitude of the observed charge state ratios, they play no role in determining the latitudinal structure of these observables. In fact, the increased ionization occurs at the same latitudes with and without including the supra-thermal electrons, and the factor by which the slow wind values are increased relative to the fast wind is similar in both cases. This suggests that the modeled increase in ionization in the slow wind is related to how the wind profiles along open field lines vary with latitude. This will be analyzed in detail in Section 4.7.

The results for $< Q >_{Fe}$ assuming supra-thermal electrons are shown in Figure 4.8.

They are qualitatively similar to the values predicted without taking supra-thermal electrons into account. It is possible that the average charge state is not sensitive to the presence of supra-thermal electrons, although individual ions fractions may indeed be. This will be further discussed in Section 4.6.2, where emission lines from several Fe ions are examined.

4.6.2 Lower Corona: Emission by Heavy Ions in a Polar Coronal Hole

We calculated the synthetic LOS fluxes for all the lines in Table 4.1 and compared them to their corresponding EIS observations. As explained above, the Fe XIII line had a scattered light contribution of more than 20% of the observed flux at all available heights, and was therefore removed from the analysis below. The magnitude of the synthetic emission from each point along the LOS will depend on the abundance of the ion responsible for the emission, in other words, on the ratio $N(X^{+m})/N(X)$. This ratio enters in the contribution function $G_{ji}(T_e)$ defined in Eq. (3.7). For each spectral line, four different types of ion fractions were considered:

1. ion fractions due to charge state evolution in a single-temperature electron thermal core population.

2. ion fractions due to ionization equilibrium in a single-temperature electron thermal core population.

3. ion fractions due to charge state evolution in an electron population with an additional supra-thermal electron population.

4. ion fractions due to ionization equilibrium in an electron population with an additional supra-thermal electron population.

The presence of the supra-thermal electrons impacts the ionization and recombination rate coefficients and will lead to different ion fractions. Thus two set of rate coefficients were used: one for cases 1-2 (assuming a single-temperature electron thermal core population), and a second set for cases 3-4 (including supra-thermal electrons). The

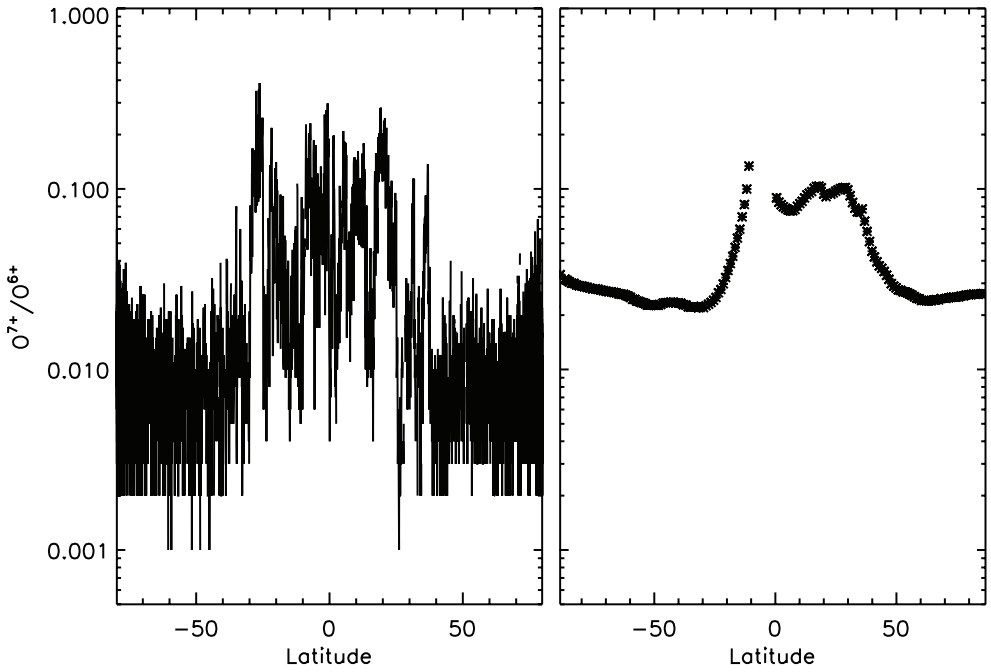

Figure 4.6: *O^{+7}/O^{+6} ratio measured by Ulysses (left) and predicted by AWSoM / MIC (right) assuming an additional population of supra-thermal electrons.*

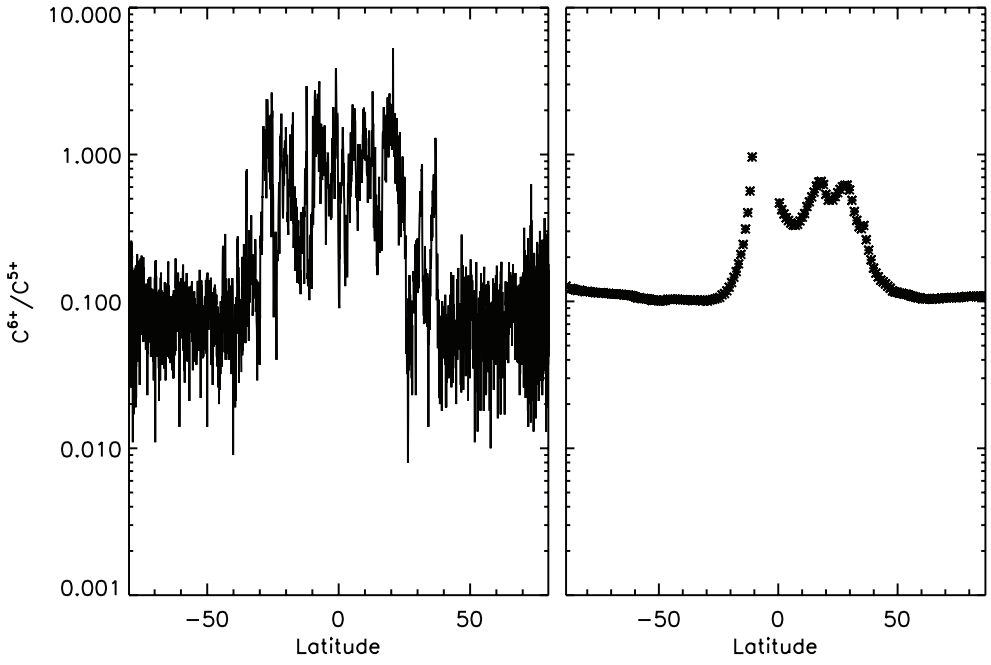

Figure 4.7: *C^{+6}/C^{+5} ratio measured by Ulysses (left) and predicted by AWSoM / MIC (right) assuming an additional population of supra-thermal electrons.*

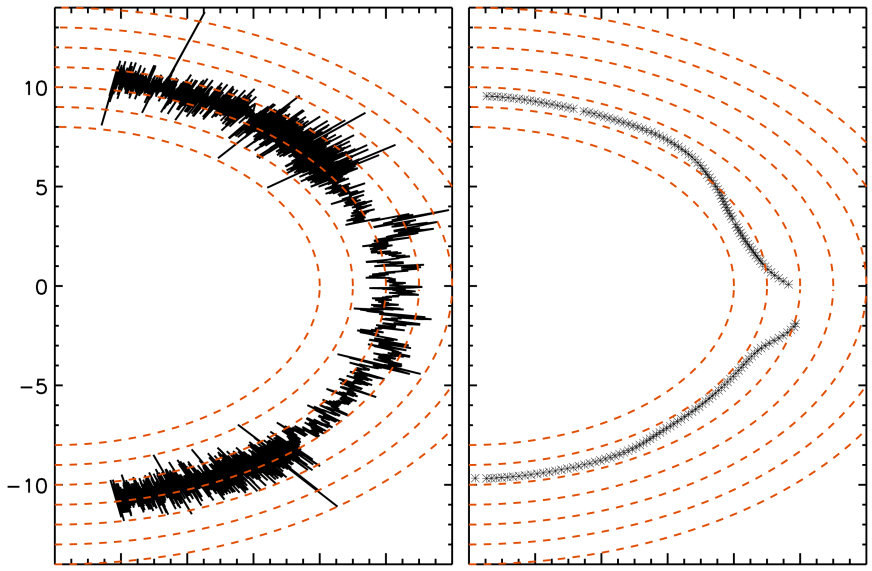

Figure 4.8: *Average charge state of Fe measured by Ulysses (left) and predicted by AWSoM / MIC (right) assuming an additional population of supra-thermal electrons.*

ion fractions in each of the cases will also depend on whether the charge state are allowed to evolve according to Eq. (4.1), as in cases 1 and 3, or whether ionization equilibrium is assumed, as in cases 2 and 4. In what follows, we refer to the evolved charge states as MIC ion fractions. Supra-thermal electrons also impact the excitation and de-excitation rates as explained in Section 4.2.2, thus their effect was also taken into account when calculating the contribution function in cases 3 and 4.

Figures 4.9 - 4.18 show the comparison of the synthetic and EIS fluxes as a function of height for each of the lines considered here. The black curve in each figure shows the EIS observations and their uncertainties. The two blue curves show the synthetic flux for a single-temperature electron population, while the red curves show the synthetic emission including the supra-thermal electron population. In each pair, the solid curve was obtained using the MIC ion fraction in the contribution function, while the dashed curves were obtained using the ionization equilibrium ion fractions. The heights at which the scattered light contribution may be higher than 20% of the observed flux are shaded in orange. These heights are reported in Table 4.1.

There are 7 lines covering different charge states of Fe, from VIII to XII. As can be seen, the synthetic emission is over-predicted for charge states 8 and 9, while it is under predicted for charge states 10-12, for all four types of predicted ion fractions. The best agreement is achieved for spectral lines belonging to Fe IX, where the synthetic emission is within the uncertainty of the measured flux at most heights.

The fact that the synthetic fluxes are either larger of smaller than the observed fluxes for different emission lines of same element, removes the possibility that these differences can be explained by uncertainties in elemental abundances, as these will shift the predicted fluxes in the same direction. Another source for the discrepancy could be contamination from streamer material that might cross the line of sight and contribute to the observed fluxes of the hotter lines, i.e. the ones emitted by the higher charge state ions. This contribution is hard to quantify from line of sight observations alone; however, the magnetic field configuration obtained by the model shows that no closed field lines cross the line of sight. The physical interpretation of these discrepancies is that in the model Fe is not ionized rapidly enough, leading to an exceedingly large population (and emission) of low charge states and an insufficient population of high charge states. This phenomena is referred to as the "delay effect" (*Landi et al.*, 2014, , under review), which found similar behavior when analyzing synthetic emission from several models. It is still possible that the model achieves the correct ionization status at altitudes higher than the EIS field of view. First, the charge states of Fe only freeze in around $4R_{\odot}$, and thus they still have sufficient time to further ionize. Second, we have seen in the previous Section that a better agreement is found when the frozen-in values of $< Q >_{Fe}$ are compared to in-situ solar wind observations.

The delay effect can also be seen in the two lines belonging to Si, where the Si VII line flux is over-predicted and that from Si X is under predicted. Unfortunately there are no publicly available data of Si charge states from Ulysses at the time of this

publication. The agreement between the predicted and observed flux for the S X line is very good. But since only a single line is used here, it cannot reveal information about the delayed ionization.

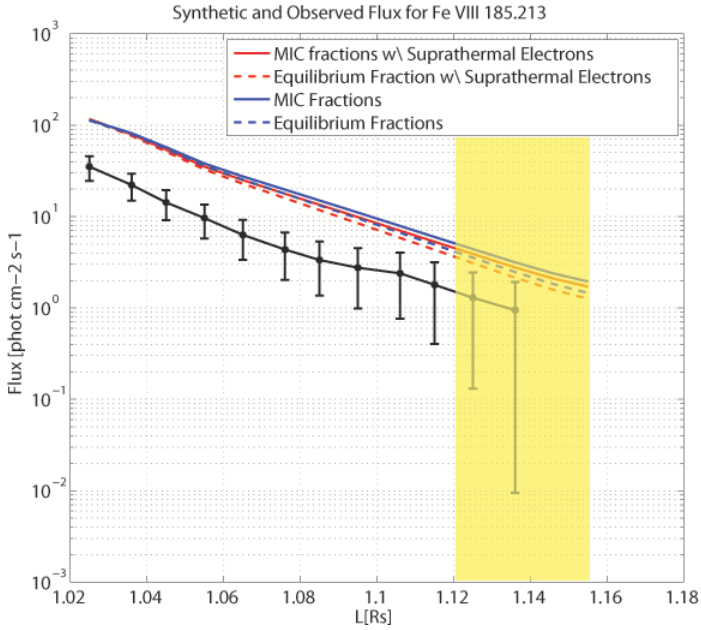

Figure 4.9: *Observed and synthetic line of sight flux vs. radial distance for Fe VIII 185Å . The black curve shows EIS observations and their uncertainties. The two blue curves show the synthetic flux for a single-temperature electron population. The two red curves show the synthetic emission including supra-thermal electrons. In each pair, the solid curve was obtained using the MIC ion fractions in the contribution function, while the dashed curves were obtained using ion fractions determined from ionization equilibrium. The shaded area represents heights at which the scattered light may contribute more than 20% to the observed flux.*

4.6.2.1 The Effect of Supra-thermal Electrons

The inclusion of supra-thermal electrons improves the agreement between predicted and observed values in all lines. For over-predicted fluxes in the lower ionization stages, the synthetic emission in the supra-thermal case is lower than in the single temperature electrons case, making it closer to the observed values. This can be explained by the fact that the supra-thermal electrons increase the ionization rate

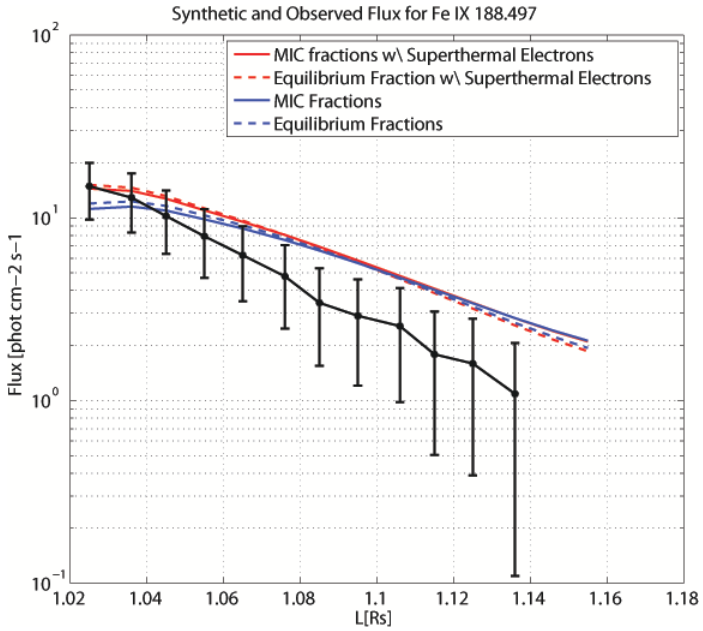

Figure 4.10: *Observed and synthetic line of sight flux vs. radial distance for Fe IX 188Å . The color coding is similar to Figure 4.9.*

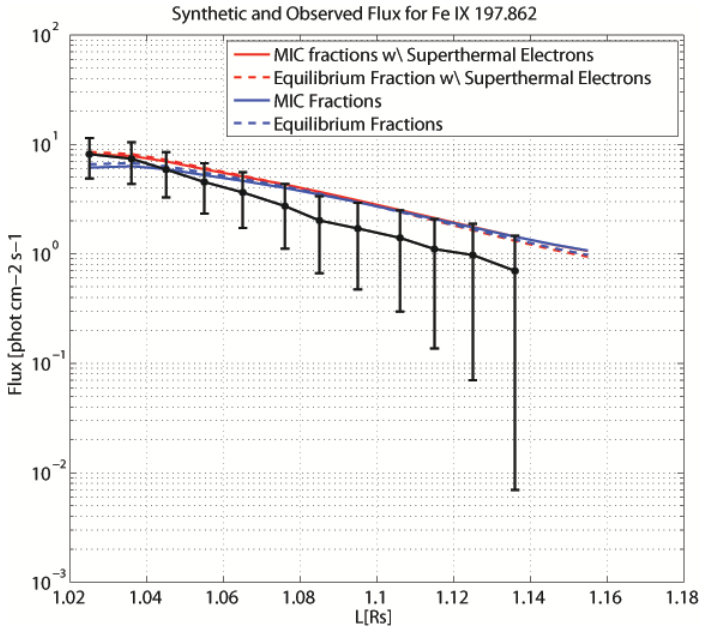

Figure 4.11: *Observed and synthetic line of sight flux vs. radial distance for Fe IX 197Å . The color coding is similar to Figure 4.9.*

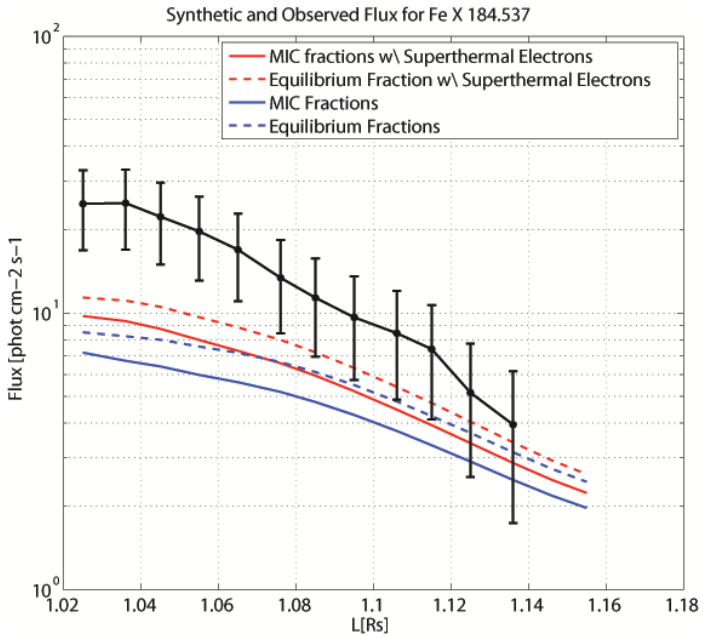

Figure 4.12: *Observed and synthetic line of sight flux vs. radial distance for Fe X 184Å . The color coding is similar to Figure 4.9.*

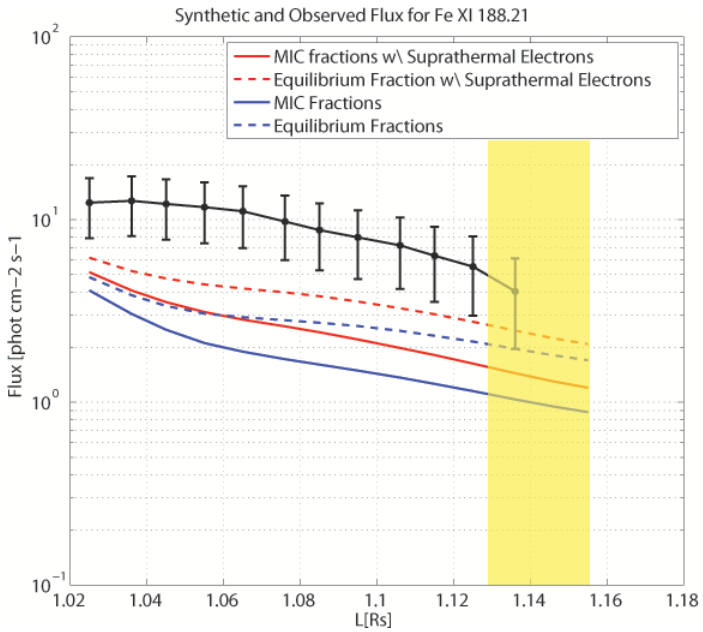

Figure 4.13: *Observed and synthetic line of sight flux vs. radial distance for Fe XI 188.21Å . The color coding is similar to Figure 4.9.*

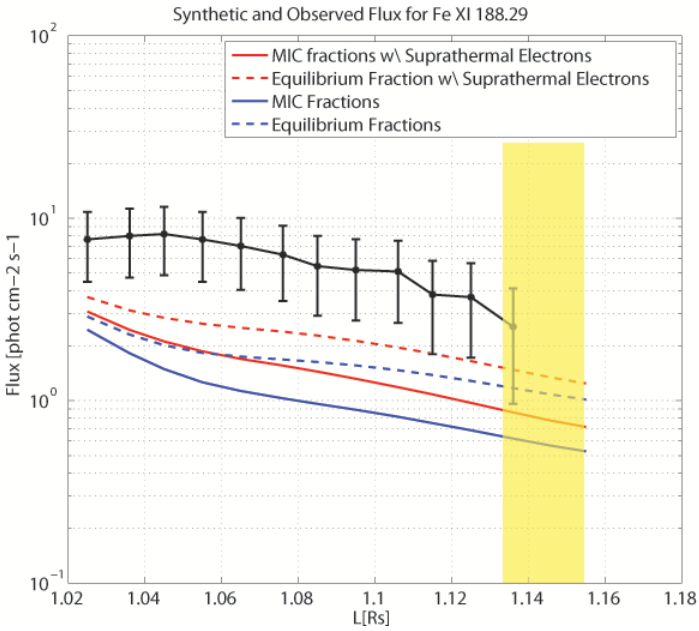

Figure 4.14: *Observed and synthetic line of sight flux vs. radial distance for Fe XI 188.299Å . The color coding is similar to Figure 4.9.*

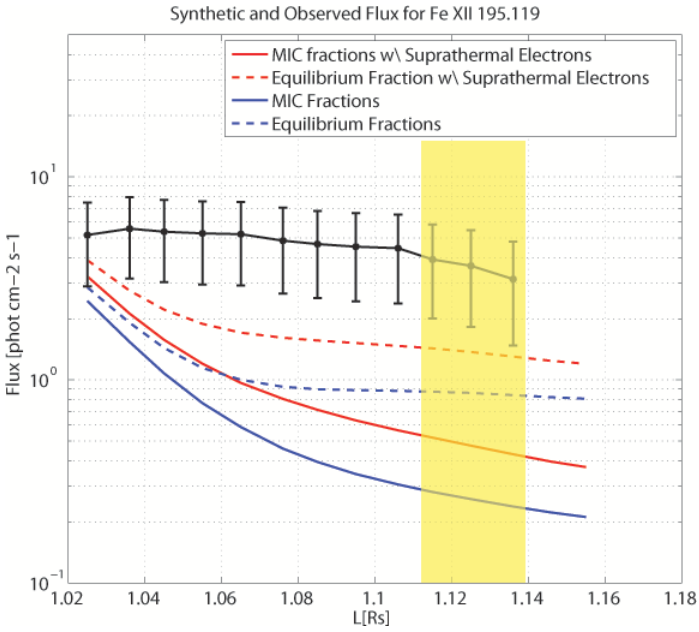

Figure 4.15: *Observed and synthetic line of sight flux vs. radial distance for Fe XII 195Å . The color coding is similar to Figure 4.9.*

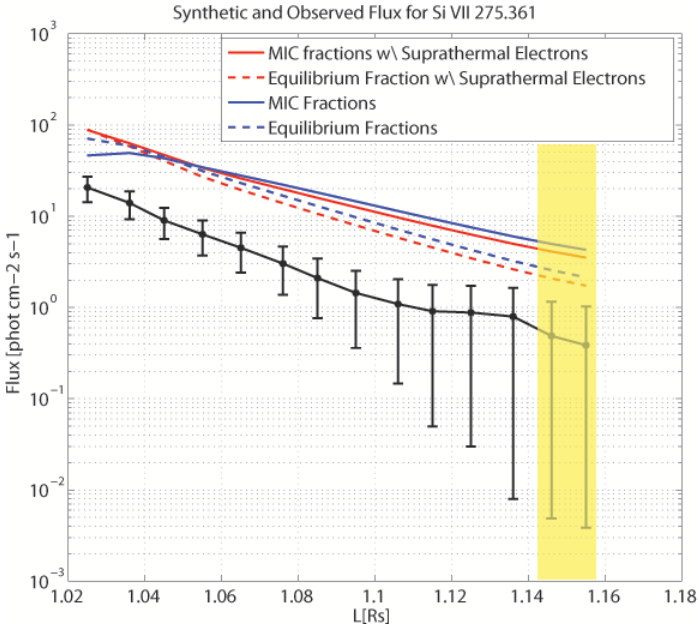

Figure 4.16: *Observed and synthetic line of sight flux vs. radial distance for Si VII 275Å . The color coding is similar to Figure 4.9.*

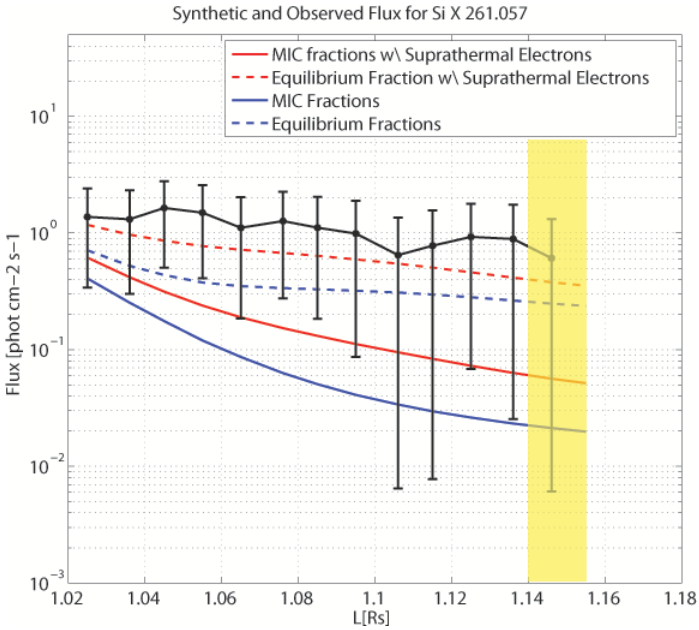

Figure 4.17: *Observed and synthetic line of sight flux vs. radial distance for Si X 261Å . The color coding is similar to Figure 4.9.*

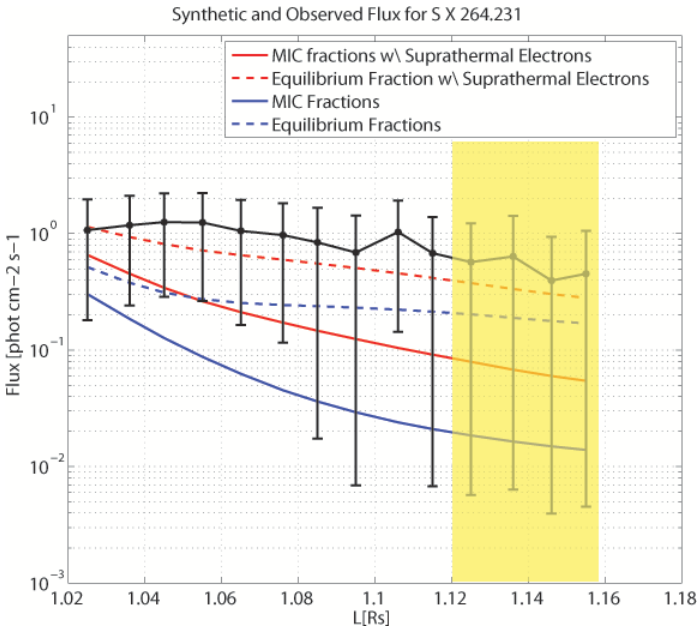

Figure 4.18: *Observed and synthetic line of sight flux vs. radial distance for S X 264Å . The color coding is similar to Figure 4.9.*

coefficients; in this case a larger portion of the element is ionized to a higher charge state, resulting in a smaller ion fraction in the lower charge states responsible for the over-predicted line emission. The reverse occurs for the under-predicted fluxes from the higher charge states: the increased ionization rates result in more ions reaching the desired charge states. This result, taken in conjunction with the comparison of modeled charge states to in-situ observations discussed in Section 4.6.1, demonstrates that the presence of supra-thermal electrons below the freeze-in height may lead to a better agreement with observations in both ends of the wind trajectory. This serves as a proof of concept that supra-thermal electrons can resolve the discrepancies between the main electron temperature observed in the corona and the frozen-in charge state values. A better agreement with the observations can be achieved by empirically adjusting the parameters of the supra-thermal electron populations, i.e. their relative portion of the entire population, and their energy. Such a procedure can help in pinning-down the properites of supra-thermal electrons and should be

performed while increasing the number of lines and ions included in the comparison, using, where possible, different instruments. However, the spatial distribution of supra-thermal electrons may not be uniform below the freeze-in height, as pointed out in *Laming and Lepri* (2007). This introduces a further degree of freedom in any parametric study aiming to determine the properties of supra-thermal electrons.

4.6.2.2 Departure from Equilibrium and Wind Acceleration

The differences between the synthetic emission calculated using equilibrium ion fraction and MIC ion fractions can be large in some of the lines. It follows that the wind profiles predicted by AWSoM may give rise to significant departures from equilibrium. The synthetic emission calculated using equilibrium ion fractions agrees better with the observations compared to the MIC ion fractions, both with and without supra-thermal electrons. In other words, the model over-estimates the departures from equilibrium. It is possible that the wind speed predicted for the coronal hole at these heights is too large, not allowing the ions sufficient time to achieve a charge state distribution that is closer to the equilibrium distribution for the local temperature. An over-estimation of the wind speed can also explain the delay effect seen at all ion charge states of Fe and Si examined here. We have seen in Chapter 2 that the wind speed at 1-2 AU is in good agreement with observations at all latitudes, especially above the coronal holes. Thus although the wind eventually reaches expected values, the acceleration rate below the freeze-in point may be too large, at least in the polar coronal hole. Thus the details of the wind acceleration process assumed in the model might need to be further refined. The wave reflection coefficient has a large impact on the wind acceleration rate, as it directly affects the wave pressure gradient which accelerates the wind. In this work, we have assumed the reflection coefficient is uniform everywhere. In reality, the reflection coefficient depends on the gradients in the Alfvén speed, and thus it will vary at different heights in the flux tube. A

self-consistent description of the reflection coefficient was introduced to the AWSoM model in *van der Holst et al.* (2014). It will therefore be instructive to explore the charge state formation rates using this more physical description.

4.7 The Open-Closed Boundary as a Source Region of the Quasi-Steady Slow Wind

The main result of Section 4.6.1 is that the well-known increase in the charge state ratios O^{7+}/O^{6+} and C^{6+}/C^{5+} in the slow wind can be reproduced by a steady-state model where the slow wind comes from open field lines rooted near the boundary with the closed field region (which we henceforth refer to as the O-C boundary). This region was invoked as the source region of the slow wind by several authors, who considered the larger expansion of flux tubes in this region as the mechanism responsible for the low wind speeds (*Suess*, 1979; *Kovalenko*, 1981; *Withbroe*, 1988; *Wang and Sheeley*, 1990; *Cranmer and van Ballegooijen*, 2005; *Cranmer et al.*, 2007). However, in this work we have directly simulated the charge state evolution in all latitudes, and verified that the observed charge state ratios can also be reproduced, at least in their large scale behavior. This is an important result, since charge state composition often serves as observational support to the idea that the non-steady slow wind must originates from closed field structures, and not from coronal holes.

The steady state model cannot describe any transient phenomena, and cannot address the high and sudden fluctuations of the charge states observed in the slow wind; these are probably caused by dynamic release due to reconnection between open and closed field lines (see a summary of several theoretical models of dynamic release appears in *Antiochos et al.*, 2012). Such a reconnection process may also explain the elemental abundances observed in the slow wind *Zurbuchen et al.* (e.g. 2002), which exhibit a FIP bias similar to that found in the closed-field regions of the

corona (*Feldman and Widing*, 2003). The AWSoM model cannot address the heavy element fractionation. Therefore the formation of high charge states slow wind in the AWSoM-MIC simulation is independent of any process responsible for the FIP-bias. Thus the theoretical picture put forth in this work does not contradict dynamic release models. Rather, it offers a complementary picture to the origin of the slow wind. It is possible that the slow wind as described by the model is actually a sub-set of the slow wind that does not come from coronal loops. If this is indeed the case, this type of wind flow will be steady, exhibit photospheric abundances, and high charge states. This picture should be tested using available data.

The Ulysses observations presented here (see, for example, Figure 4.6) show that the mean value of the charge state ratios is higher in the slow wind than in the fast wind. Furthermore, we can see that charge state ratios as low as those found in the fast wind are not found in the slow wind observations covered in this data set. This pronounced increase in charge states is consistent with a scenario where the observed slow wind is in fact a mixture of material from closed field regions and material from the open field lines rooted in the O-C boundary region, if these already carry charge state ratios that are higher than those observed in the fast wind. Thus it is possible that the slow wind simulated by the model can play a role in forming the variable charge state composition observed in the non-steady slow wind.

This result motivates us to explore the properties of the source region of the slow wind as described by the model, and to pin down the physical processes responsible for the increase in charge state ratios.

4.7.1 What Causes the Higher Charge States Ratios in the Steady Slow Wind?

The differences in charge state composition in the fast and slow wind seen in the AWSoM/MIC results suggests that the open field lines carrying these two wind types

undergo different evolution below the freeze-in height. In order to characterize these differences, we examine the maximum electron temperature occurring along each of the field lines used as input to the charge state evolution model. The result is shown in Figure 4.19, where the maximum temperature is plotted against the latitude of the end point of the field line at 2AU. As can be seen, the temperature in the latitude range ±30 corresponding to the slow wind is higher than just outside it, but similar temperatures also occur at the high latitude field lines above the coronal holes. Thus the temperature alone cannot explain the higher charge state ratios.

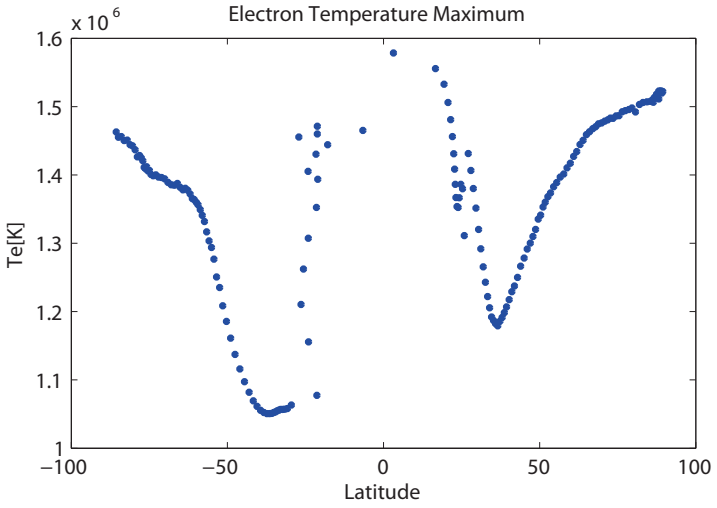

Figure 4.19: *Maximum electron temperature along each field line used in the simulation, vs. the latitude the field line reaches at 2AU.*

Figures 4.20 and 4.21 show the electron density at the location of maximum electron temperature, $N_e(T_{e,max})$, along each field line, and the height above the Sun where the maximum occurs. It can be seen that $N_e(T_{e,max})$ is higher in the slow wind/high charge state region (roughly between ±30 degrees) than just outside it, and it increases as we move closer to the equator. In the fast wind, $N_e(T_{e,max})$ is almost the same at all latitudes. Comparing Figure 4.20 to Figure 4.19, it is clear that although the maximum electron temperature of fast wind open field lines can reach values as high as those in the slow wind, this maximum occurs where the den-

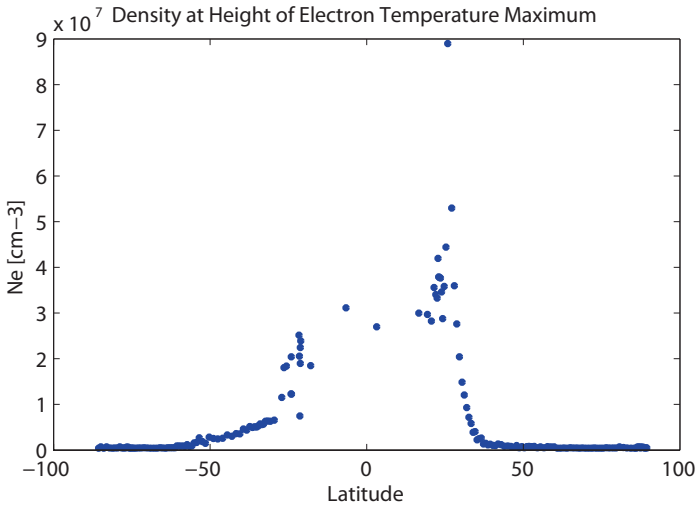

Figure 4.20: *Electron density at the height where the electron temperature reached its maximum value along the field line, vs. the field line latitude as it reaches 2AU.*

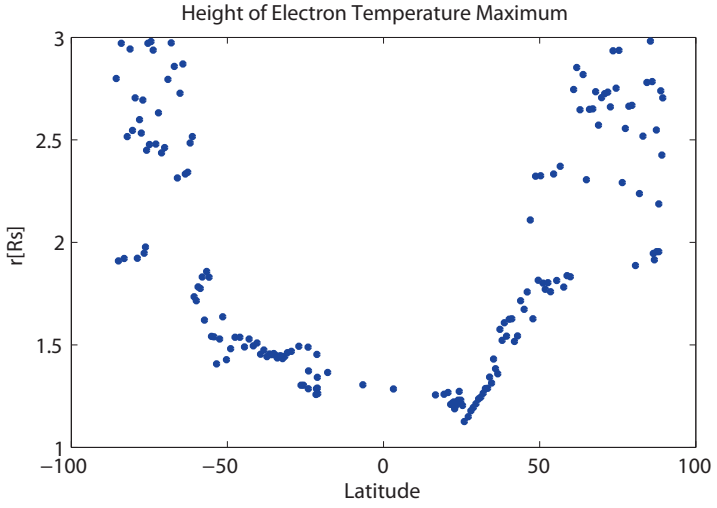

Figure 4.21: *Height where the electron temperature reached its maximum value along the field line, vs. the field line latitude as it reaches 2AU.*

sity is lower. This lower density will limit the fraction of the ions reaching higher charge states, since the ionization rate is linearly proportional to the electron density, as seen in Eq. (4.1). The height at which the maximum electron temperature occurs is larger in the high latitude field lines compared to lower latitudes, although the transition is not as sharp as the transition between low and high $N_e(T_{e,max})$ regions; in fact, the temperature maximum occurs at similar heights across the latitude range of ± 50 degrees. Thus the higher values of $N_e(T_{e,max})$ between ± 30 degrees cannot be explained by the height at which the maximum occurs. **It follows that open field lines carrying higher charge state ratios are characterized by higher electron densities at their lower edge, allowing for sufficient collisions to occur.** The magnitude of $N_e(T_{e,max})$ density increases as we get closer to edge of the coronal hole, which maps closer to the equatorial plane in the heliosphere. These slow wind/high charge state ratio field lines originate from the Open-Closed (O-C) boundary region. In order to complete this picture, we should find observational support that the O-C region exhibits higher densities, and to theoretically explain the formation of this density enhancement in the corona and in the simulations.

4.7.2 Electron Density Enhancement Near the Open-Closed Boundary

4.7.2.1 Observational Evidence using EUV Tomographic Reconstruction

Electron density and temperature in the lower corona are usually determined using remote spectral observation. This type of measurement is complicated by line of sight effects, since the emission from different regions crossing the line of sight contribute to the measured intensity. *Frazin et al.* (2005, 2009) and *Vásquez et al.* (2010) have developed a differential emission measure tomographic reconstruction method (DEMT), that can recover the 3D distributions of electron density and temperature in the corona, using multi-wavelength images taken from different points of view, which can be obtained by imaging the solar disk as the Sun rotates. The temperature

obtained from DEMT is the average electron temperature $< T_e >$ of a given volume of multi-temperature plasma. Since DEMT uses as input images from different times during a solar rotation, it can only recover steady structures; in regions where the magnetic topology or thermodynamic properties varies significantly during the rotation, the tomographic method fails, as a single structure cannot be reconstructed. These regions should be excluded from the analysis. However, the global, large scale distribution can be reliably recovered.

We use a tomographic reconstruction performed for CR2063 using STEREO/EUVI images in order to determine whether the O-C region exhibits the higher densities required to explain the charge state ratios as described in the previous section. EUV tomography allows us to determine the 3D distribution of N_e and $< T_e >$ between heliocentric distances of $1.035 - 1.135 R_\odot$. Figures 4.22 and 4.23 compare the model and tomography results at $r = 1.075 R_\odot$ for electron temperature and density, respectively. The data are plotted as a longitude-latitude map over the sphere. The black curves show the boundary of the polar coronal holes. White regions in the tomography maps correspond to regions where the tomography method fails, which occurs mostly around regions with high variability. The agreement between the model and tomography temperature maps is very good, in both magnitude and structure, although some smaller scale features are not reproduced in the model. The density comparison shows larger differences between the model and tomography, with the model over-predicting the density in the closed field region, and under predicting it in the polar coronal holes, but overall the model is within a factor of 2 of the reconstructed density. We also note that the coronal hole boundary predicted by AWSoM follows the contours of increased density and temperatures of the helmet streamer very closely, with small (up to 2-3 degrees) departures at certain regions. Other closed field regions appear as islands of higher density and temperature outside the main streamer belt. This suggests that the magnetic field topology derived from the

MHD solution at this height is realistic. The discrepancies between the boundaries may be attributed to the fact that both the synoptic magnetogram used as a boundary condition to the model, and the tomographic reconstruction, were obtained from observations taken over the entire Carrington rotation, and small scale and dynamic features will not necessarily be captured by either of these methods.

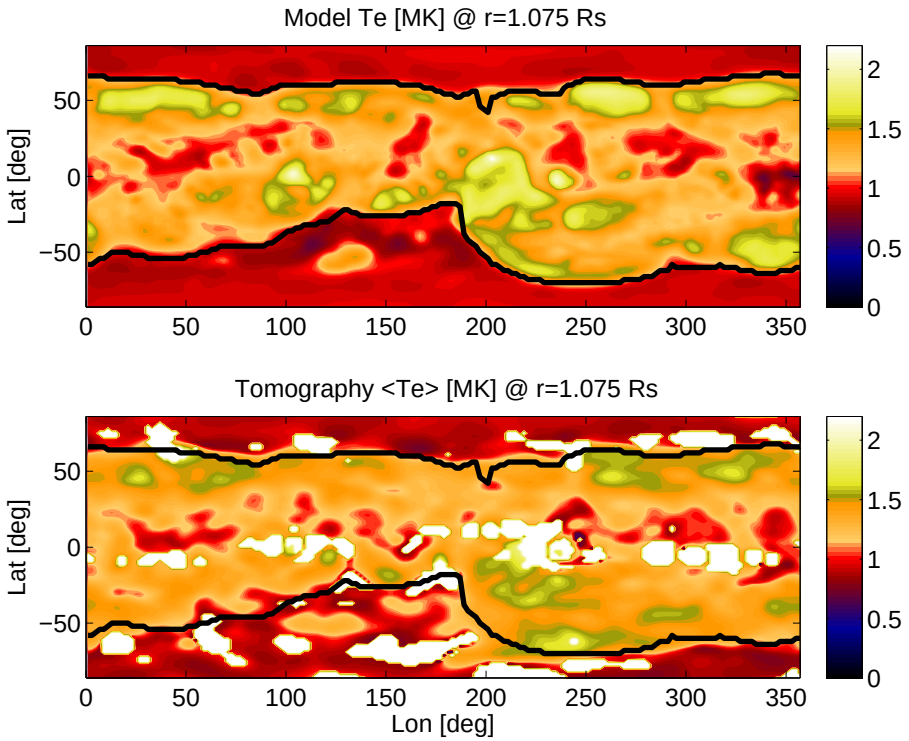

Figure 4.22: *AWSoM electron temperature T_e (top panel) and average electron temperature $< T_e >$ from DEMT (bottom panel) maps for CR2063, extracted a height of $1.075R_\odot$. Black curves show the coronal hole boundaries extracted from the AWSoM solution. The white regions in the tomography map correspond to regions which could not be reconstructed by DEMT.*

The electron density maps in both the model and the tomography show regions of higher density near the coronal hole boundaries. In order to demonstrate this clearly, we perform a statistical analysis of the electron density in the entire open field region. For each longitude, we extract from the maps the electron density as a function of angular distance (in latitude) from the streamer leg toward to pole.

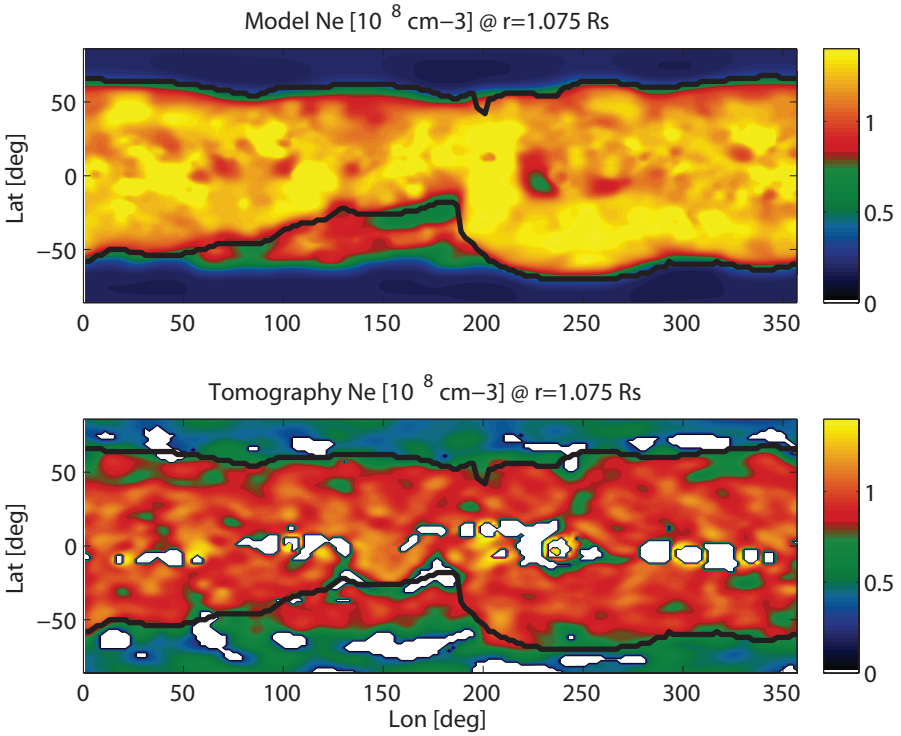

Figure 4.23: *Electron density map from AWSoM (top panel) and from DEMT (bottom panel) for CR2063, extracted a height of $1.075R_{\odot}$. Black curves show the coronal hole boundaries extracted from the AWSoM solution. The white regions in the tomography map correspond to regions which could not be reconstructed by DEMT.*

For each angular distance, the density from all longitudes are averaged together. A box in the longitude range of [50, 260] and latitude [-90,30] was excluded from the analysis, since this region exhibits a large extension of the coronal hole into lower latitudes, embedded with several islands of closed field regions. The results are shown in Figures 4.24 and 4.25 for the north and south coronal holes, respectively. The black curve in each plot shows the density profile extracted from the tomography, while the red curve shows that extracted from the modeled density map. The error bars represent the standard deviation calculated for all longitudes. The modeled density is lower than the reconstructed density, by a factor of 2-3, which is expected since this discrepancy exists in the maps. However, in both the model and the tomography the

longitude-averaged density is highest at the edge of the coronal hole, and smoothly decreases until it reaches an almost constant value by 10-15 degrees away from the outer edge. The rate of decrease vs. angular distance is similar in both the model and the tomography. It follows that the O-C boundary region has a higher density than deeper in the coronal holes, and that the density increases as we move out toward the edge of the hole. In the previous section, we showed that such a density enhancement in the lower corona can explain the increase in charge state ratios in open field lines coming from the O-C boundary region. The result from the tomography validate that such an enhancement also exist on the Sun. In the previous section, we showed that the model predicted the density enhancement for field lines lying in a single meridional plane close to the Sun. The statistical analysis performed here for all longitudes shows that this behavior is characteristic of the entire O-C boundary region, both in the model and in the tomography.

4.7.2.2 Theoretical Considerations

The increase in electron density in the O-C boundary region can be understood from a theoretical point of view if we consider the thermal energy balance along magnetic flux tubes. Field-aligned electron heat conduction will transport heat from the hotter corona toward the cooler chromosphere. This will cause the heated chromospheric plasma to advect upward, supplying the coronal portion of the flux tube with denser material. This phenomena is known as a chromospheric evaporation (c.f. *Klimchuk*, 2006), and it can explain why the foot points of flux tubes become denser due to heating events occurring at larger heights. Chromospheric evaporation can be linked to the increased density at the edges of coronal holes as follows. If we consider two flux tubes of equal cross sectional area at the chromosphere, with one tube rooted in the O-C boundary region and the other rooted closer to the pole, then the O-C tube will map to a larger cross section at a given heliocentric distance R.

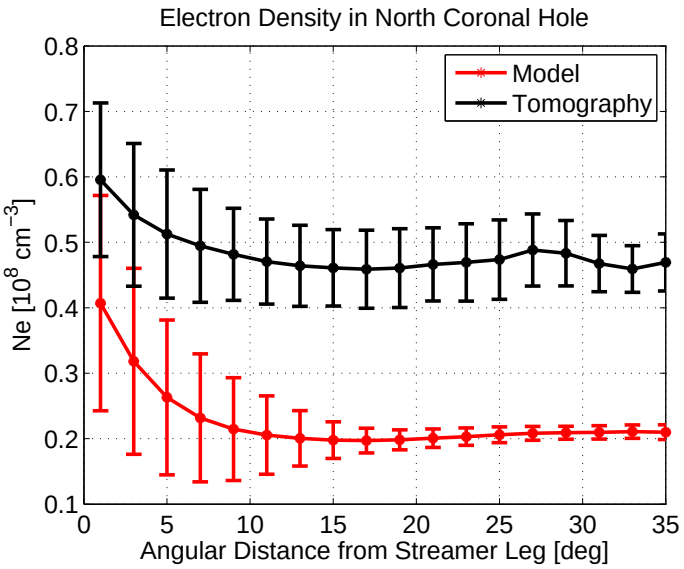

Figure 4.24: *Electron density vs. angular distance in the north coronal hole for CR2063, extracted from the model and tomography density maps at* $r = 1.075R_{\odot}$. *Angular distance is measured from the streamer leg* (0^o) *toward the pole* (30^o). *The density is averaged over all longitudes. The black and red curves shows data extracted from tomography and the model, respectively. Error bars show the standard deviation from the averaged values taken from all longitudes.*

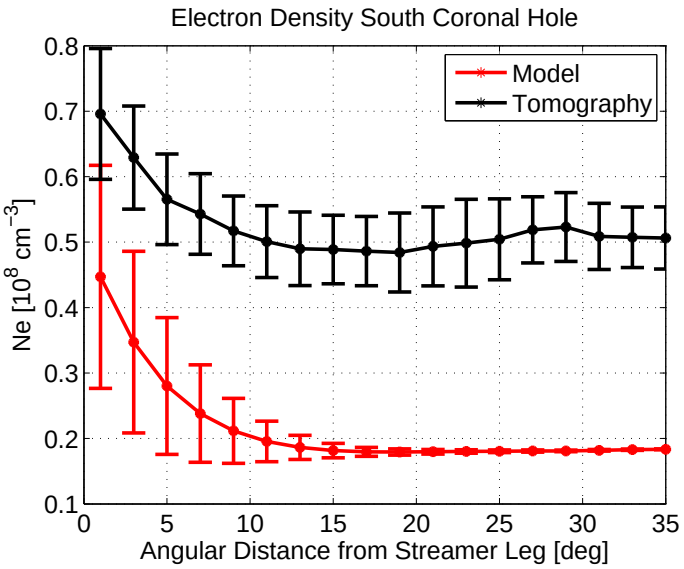

Figure 4.25: *Same as Figure 4.24, but for the south polar corona hole.*

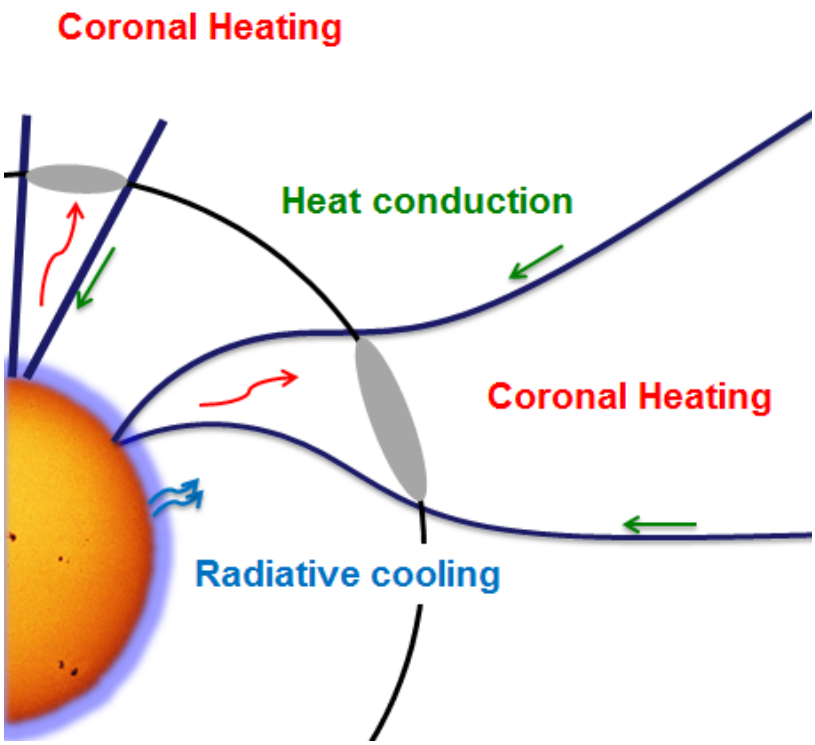

Figure 4.26: *Schematic picture of heating, radiative cooling and heat conduction in open flux tubes. Blue curves represent magnetic field lines. Grey ellipses represent the cross sectional area of the flux tubes at the height marked by the black circle. The flux tube rooted in lower latitudes maps to a larger cross section at that height, compared to the polar flux tube.*

This is depicted schematically in Figure 4.26. The O-C tube is therefore magnetically connected to a larger volume of the hot corona compared to the polar flux tube, and field-aligned electron heat conduction will then be able to transport larger amounts of thermal energy. As a result, the energy per unit area reaching the foot point of the O-C tube will be higher compared to the polar tube. This will lead to larger chromospheric evaporation per unit area, and as a consequence, to higher densities in the lower corona portion of the flux tube.

Chromospheric evaporation cannot be directly described by the AWSoM model, since the density at the top of the chromosphere is fixed, and thus the inner boundary cannot dynamically respond to the heat conducted from the corona. However, the model can mimic the effects of chromospheric evaporation as follows. In steady-state,

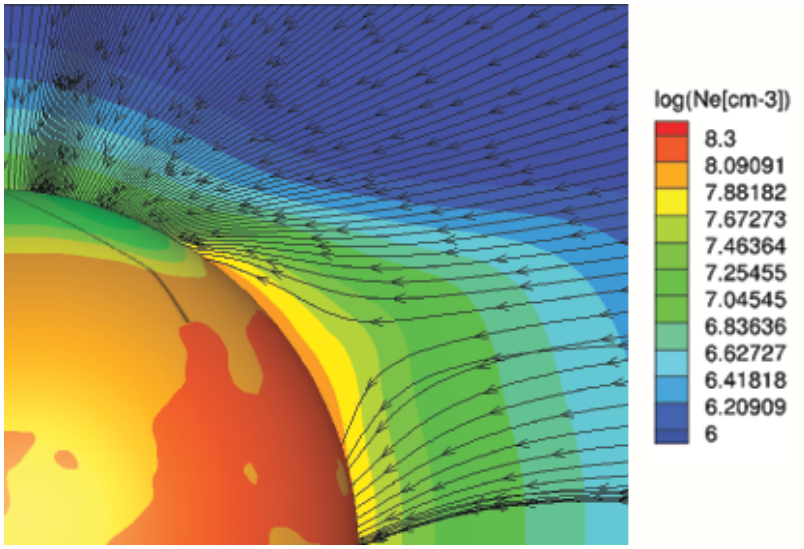

Figure 4.27: *Modeled electron density in the open field region of the corona during CR2063. The black stream lines show a selection of the field lines used in the AWSoM/MIC simulation, superimposed on the modeled electron density in the same plane. The solar surface is colored by the electron density as well.*

the energy balance near the inner boundary can be described by the electron pressure equation, Eq. (2.6), which in this case takes the form:

$$Q_{rad} + Q_{w,e} - \nabla \cdot \mathbf{q}_e = 0, \tag{4.2}$$

where Q_{rad} is the radiative cooling rate, $Q_{w,e}$ is the electron heating rate due to wave dissipation, and $\mathbf{q_e}$ is the electron heat conduction tensor. Terms related to the plasma velocity appearing in Eq. (2.6) were neglected, due to the small speeds near the inner boundary. Eq. (4.2) shows that an excess of thermal energy due to heat conduction can only be balanced by a corresponding increase in the radiative cooling rate. As Q_{rad} is proportional to the square of the electron density, the model equations will force the electron density to rise in order to achieve a steady state. With a fixed and uniform density at the inner boundary, this will result in a lower drop-off with distance of the electron density compared in regions that are more affected by heat conduction.

The conceptual picture outlined above can be verified by examining the modeled electron density along the open flux tubes. Figure 4.27 shows a selection of the open field lines used in the AWSoM/MIC simulation in the northern hemisphere, superimposed on the electron density in the same plane. The solar surface is colored by the electron density as well. The north coronal hole can be identified as the almost circular green region on the solar surface around the pole. We observe that the field lines rooted near the edge of the polar coronal hole expand super-radially, while those rooted near the hole center do not. The density drop-off with distance for the super-expanding field lines is clearly smaller than it is in the center of the coronal hole, and the density at a given height will be larger for these field lines.

4.8 Conclusions

The work presented in this Chapter has combined, for the first time, results from a global 3D model of the solar atmosphere with a heavy ion evolution model, in order to simulate the large scale latitudinal structure of charge states in the corona and solar wind. Charge states have long been a key element in theories aiming to explain the processes responsible for the formation and acceleration of the fast and slow solar wind. Any such theory should also explain the observed variations in elemental abundances between the fast and slow solar wind, namely the appearance of the FIP bias in the slow wind abundances. The AWSoM-MIC simulation presented here cannot address the FIP bias, as the AWSoM model does not describe the separate evolution of the different species, and does not incorporate any fractionation mechanism. In addition, the steady-state simulation presented here cannot capture the observed variability in the slow wind properties. However, although the work presented in this Chapter cannot solve all the open question regarding the origin of the slow wind, understanding the large scale structure of charge states in the fast and slow solar wind provides an important piece of the puzzle. The capability to predict

charge states from a global model using a realistic magnetic configuration is a major step forward in developing tools to test our understanding of solar wind formation and acceleration, and to ultimately predict space weather.

The main result of this work is that we were able to produce higher levels of the frozen-in charge state ratios O^{7+}/O^{6+} and C^{6+}/C^{5+} in the slow wind, compared to those in the fast wind. Both the slow and fast wind in this model are carried by open magnetic field lines, and thus the increase in charge states was achieved without invoking release of material from the closed field region. We have shown that open flux tubes carrying higher charge state ratios are characterized by larger electron densities in the lower corona where the electron temperature reaches its maximum. Even though open field lines carrying the fast wind may reach similar electron temperature maxima, these occur where the density is too low to allow sufficient ionization to take place. Furthermore, we found that the field lined carrying higher charge states have higher densities at a given height near their base, compared to those carrying lower charge state ratios. The slow wind/high charge state field lines are rooted in the boundary region between coronal holes and closed field line structures in the corona and are mapped to latitudes between ± 30 in the heliosphere. This means that the boundary region in the model has a higher density compared to deeper inside the coronal hole.

The formation of the density enhancement in the boundary region was explained theoretically to be due to the interplay between flux tube geometry and field aligned electron heat conduction. The density enhancement was shown to be a global feature of coronal holes in the Carrington Rotation under question. This behavior was demonstrated from the global model results, and supported by data from a tomographic reconstruction of the lower corona.

The conclusions that can be drawn from the AWSoM/MIC results are limited by the fact that they are based on a steady-state simulation, and thus cannot address any

dynamical feature in the non-steady slow wind. The fact that this model can predict the charge state increases in a steady slow wind does not contradict dynamic release models of slow wind formation, but rather complements them. A possible prediction from the work presented here is that the O-C boundary is the source region of a subset of the slow wind, which is steady and carries high charge states. The theoretical picture explaining the formation of this wind type can be unified with a dynamic release model. The O-C lines in our steady-state simulation already carry charge state ratios that are consistent with the average level observed in the non-steady slow wind; however, the charge state ratio in the slow wind fluctuates rapidly and can reach values that were not captured by the simulation. Thus these larger charge state ratios can be due to reconnection of O-C lines with closed field lines at the edges of the streamer belt (a scenario similar to the S-web model presented in *Antiochos et al.* (2011, 2012)).

The charge state distributions for Fe, Si and S below the freeze-in height were used to calculate synthetic emission that was compared to EIS observations in the lower corona, up to $1.115 R_{\odot}$ above the limb of a polar coronal hole. Comparing the results for 10 spectral lines suggests that the overall plasma ionization at this height range is too low; emission from low charge state ions was over-predicted while emission from higher charge states of the same ion was under-predicted. This "delay effect" suggest that the AWSoM wind profiles, and most probably the wind speed below the freeze-in height, need to be improved in order to reach a better agreement.

We have explored the possible role that supra-thermal electrons can play in charge state evolution. Such an electron population has been hypothesized to be present in the corona, but no direct observational evidence of their existence has been found. We have shown that supra-thermal electrons at $\sim$3MK making up 2% of the entire electron population can greatly improve the agreement between the predicted and observed charge state levels in the solar wind, consistent with previous work (*Ko*

et al., 1997; *Esser and Edgar*, 2000, e.g.).

The addition of supra-thermal electrons has reduced the discrepancies between the observed and synthetic spectral for all lines, and whether ionization equilibrium was assumed or not. To the best of our knowledge, this is the first time a possible observational signature of the presence of supra-thermal electrons was found in remote spectral observations. This serves as a proof of concept of such a procedure. Future work should include a parametric study, guided by observations at both ends of the wind trajectory, in order to pin down their properties (e.g. population size and energies).

The AWSoM/MIC predictions can be improved by using a more sophisticated description of the solar atmosphere. For example, the wind speed below the freeze-in height can be improved by including a physics-based description of wave reflections. Such a description was introduced to a newer version of the AWSoM model (*van der Holst et al.*, 2014). In addition, the effect of differential speeds of the heavy ions can be included by extending the two-temperature MHD description to a multi-fluid MHD description.

CHAPTER V

Conclusions and Future Work

5.1 Summary of This Work

This dissertation presents a comprehensive numerical and observational exploration of the scenario in which Alfvén wave turbulence is responsible for coronal heating and solar wind acceleration. The work is comprised of three major parts:

• **Global MHD model of the solar atmosphere driven by Alfvén waves.** I developed a numerical model of the solar atmosphere, in which the two-temperature MHD equations are coupled to kinetic wave equations for parallel and anti-parallel low-frequency Alfvén waves. This is the first global model that includes the entire domain from the top of the chromosphere to 2AU; as such it was the first to simultaneously predict the wind properties at 1-2AU as well as the EUV and X-ray emission from the lower corona. The model predictions were found to be in good agreement with the corresponding observations.

The model, named the Alfvén Wave Solar Model (AWSoM), constitutes a major step forward in global modeling, since: 1. Alfvén wave dissipation is the only heating mechanism; no ad-hoc geometric heating functions were included. 2. A unified approach for treating wave dissipation in both open and closed field line regions is adopted. This eliminates the need to apply empirical boundary conditions in order

to reproduce the 3D distribution of temperature and density in the corona, and wind speeds in the heliosphere. These structures emerge naturally and self-consistently with the magnetic field topology. 3. The wave dissipation mechanism is controlled by only three adjustable parameters which are constrained by observations. 4. The wave dissipation mechanism can produce a non-uniform 1-2MK corona from a uniform underlying chromosphere at 50,000 K.

• **Observational and Numerical Study of Alfvén Wave Dissipation in the Lower Corona.** The AWSoM prediction of the wave amplitude and electron temperature and density in the equatorial lower corona were tested against high-resolution spectral EUV observations. For this purpose, a new observable was developed, namely, the emission line broadening due to thermal and non-thermal (wave-induced) heavy ion motions. This is the first time this observable was synthesized from a global model. The resulting line widths, which depend on the wave amplitude, were consistent with observed line widths. The same set of observations was used to test the model prediction of electron temperature and density, which were found to be in good agreement with measured values. Thus it was shown that the wave dissipation mechanism is a viable candidate for describing both the rate at which the coronal plasma is heated, and predicting the amount of non-dissipated wave energy.

• **Solar Wind Acceleration and Charge State Distributions.** The AWSoM model was combined with a charge state evolution code, which calculates the ionization status of an element due to the local electron temperature and density, and the plasma bulk speed. The resulting charge state distributions, which depend on how these properties vary along the wind trajectory, were compared to coordinated observations at both edges of the wind flow: in-situ observations of ion composition at 1-2AU, and remote spectral observations in the lower corona. This is the first

time charge state distributions are predicted at all heliographic latitudes using wind profiles derived from a global model with a realistic magnetic field.

The results reproduced the well-known increase in charge state ratios in the slow wind compared to the fast wind. I developed a theoretical picture which explains this increase and links it to the interplay between flux tube expansion and electron heat conduction. Observational support for this theory was found in an EUV tomographic reconstruction of the lower corona.

I calculated the synthetic emission using the predicted ion fractions and compared them to observations in the lower corona. The resulting intensity profiles showed that very close to the Sun, the model does not lead to sufficient ionization, which may suggest that the wind speed profile in this region is inadequately described.

The question of whether super-thermal electrons are present in the solar corona was also explored, and a possible observational signature was found in spectral observations that paves the way for pinning down the properties of such a population.

5.2 Outcomes

The main result of this research is that heating and acceleration by turbulent Alfvén waves can explain the large scale structure of both the solar corona and the solar wind. The wave energy flux assumed in the model, which was determined based on observations, is sufficient to drive the solar wind and to create the hot corona from the much cooler chromosphere. This was verified by using a series of independent observational tests of the various properties of both the plasma and the waves. It follows that the wave dissipation mechanism proposed here is a viable candidate for a realistic description of these processes.

The development of new observables has paved the way to further investigation of these processes in the framework of global modeling. Although theoretical models

that use idealized magnetic configurations can explore the micro-physical processes in great detail, they are limited in their ability to be compared to observations without making further assumptions. A global model that is based on the observed photospheric magnetic field, and in which the magnetic topology evolves self-consistently with the plasma and the waves, can be compared in detail to observations taken concurrently with the magnetogram. This work extended the range of global data-model comparisons commonly used in the solar physics community.

5.3 Future Work

One of the limitation of the governing equations used in the AWSoM model is the empirical determination of the reflection coefficient and dissipation length, which control the wave dissipation mechanism. Furthermore, the reflection coefficient was assumed to be uniform throughout the simulation domain, an assumption that does not hold for the solar atmosphere. A natural extension of this work would be to employ a self-consistent description of these parameters based on the local properties of the plasma. This may resolve some of the discrepancies found between the model predictions and observations, especially those that are related to wind speed.

The transport of wave dissipation in the lower corona is the focus of several dedicated ground-based and space-bourne observatories currently operated or planned. This will provide the scientific community with a wealth of new measurements of the wave properties in the solar corona. The wave amplitude predictions tested in this work were limited to a very localized set of observations, both in time and in space. We can take advantage of the data supplied by these observatories to further explore the role waves play in coronal heating, and to test and refine our description of this process.

Although the large scale structure of the solar corona and the solar wind seems to be steady over periods of days or weeks, several studies have suggested that important

properties of these structures cannot be explained by a strictly steady-state description. An exciting venue for global modeling of the ambient corona and wind is the inclusion of time dependent processes such as chromospheric evaporation, open-closed field line reconnection and elemental abundance fractionation.

BIBLIOGRAPHY

BIBLIOGRAPHY

Abbett, W. P. (2007), The Magnetic Connection between the Convection Zone and Corona in the Quiet Sun, *ApJ*, *665*, 1469–1488, doi:10.1086/519788.

Abbo, L., E. Antonucci, Z. Mikić, J. A. Linker, P. Riley, and R. Lionello (2010), Characterization of the slow wind in the outer corona, *Advances in Space Research*, *46*, 1400–1408, doi:10.1016/j.asr.2010.08.008.

Alazraki, G., and P. Couturier (1971), Solar Wind Accejeration Caused by the Gradient of Alfven Wave Pressure, *A&A*, *13*, 380.

Alfvén, H. (1942), Existence of Electromagnetic-Hydrodynamic Waves, *Nature*, *150*, 405–406, doi:10.1038/150405d0.

Altschuler, M. D., and G. Newkirk (1969), Magnetic Fields and the Structure of the Solar Corona. I: Methods of Calculating Coronal Fields, *Sol. Phys.*, *9*, 131–149, doi:10.1007/BF00145734.

Antiochos, S. K., C. R. DeVore, J. T. Karpen, and Z. Mikić (2007), Structure and Dynamics of the Sun's Open Magnetic Field, *ApJ*, *671*, 936–946, doi:10.1086/522489.

Antiochos, S. K., Z. Mikić, V. S. Titov, R. Lionello, and J. A. Linker (2011), A Model for the Sources of the Slow Solar Wind, *ApJ*, *731*, 112, doi:10.1088/0004-637X/731/2/112.

Antiochos, S. K., J. A. Linker, R. Lionello, Z. Mikić, V. Titov, and T. H. Zurbuchen (2012), The Structure and Dynamics of the Corona - Heliosphere Connection, *Space Sci. Rev.*, *172*, 169–185, doi:10.1007/s11214-011-9795-7.

Antonucci, E., L. Abbo, and D. Telloni (2012), UVCS Observations of Temperature and Velocity Profiles in Coronal Holes, *Space Sci. Rev.*, *172*, 5–22, doi:10.1007/s11214-010-9739-7.

Arge, C. N., and V. J. Pizzo (2000), Improvement in the prediction of solar wind conditions using near-real time solar magnetic field updates, *J. Geophys. Res.*, *105*, 10,465–10,480, doi:10.1029/1999JA000262.

Asplund, M., N. Grevesse, A. J. Sauval, and P. Scott (2009), The Chemical Composition of the Sun, *ARA&A*, *47*, 481–522, doi:10.1146/annurev.astro.46.060407.145222.

Banerjee, D., L. Teriaca, J. G. Doyle, and K. Wilhelm (1998), Broadening of SI VIII lines observed in the solar polar coronal holes, *A&A*, *339*, 208–214.

Banerjee, D., D. Pérez-Suárez, and J. G. Doyle (2009), Signatures of Alfvén waves in the polar coronal holes as seen by EIS/Hinode, *A&A*, *501*, L15–L18, doi: 10.1051/0004-6361/200912242.

Banerjee, D., G. R. Gupta, and L. Teriaca (2011), Propagating MHD Waves in Coronal Holes, *Space Sci. Rev.*, *158*, 267–288, doi:10.1007/s11214-010-9698-z.

Belcher, J. W. (1971), ALFVÉNIC Wave Pressures and the Solar Wind, *ApJ*, *168*, 509, doi:10.1086/151105.

Binello, A. M., E. Landi, H. E. Mason, P. J. Storey, and J. W. Brosius (2001), A comparison between theoretical and solar FeXII UV line intensity ratios UV line intensity ratios, *A&A*, *370*, 1071–1087, doi:10.1051/0004-6361:20010255.

Braginskii, S. (1965), *Reviews of Plasma Physics, ed. M.A. Leontovich*, vol. 1, Consultants Bureau, New York, 205.

Breech, B., W. H. Matthaeus, S. R. Cranmer, J. C. Kasper, and S. Oughton (2009), Electron and proton heating by solar wind turbulence, *Journal of Geophysical Research (Space Physics)*, *114*, A09103, doi:10.1029/2009JA014354.

Bryans, P., N. R. Badnell, T. W. Gorczyca, J. M. Laming, W. Mitthumsiri, and D. W. Savin (2006), Collisional Ionization Equilibrium for Optically Thin Plasmas. I. Updated Recombination Rate Coefficients for Bare through Sodium-like Ions, *ApJS*, *167*, 343–356, doi:10.1086/507629.

Bryans, P., E. Landi, and D. W. Savin (2009), A New Approach to Analyzing Solar Coronal Spectra and Updated Collisional Ionization Equilibrium Calculations. II. Updated Ionization Rate Coefficients, *ApJ*, *691*, 1540–1559, doi:10.1088/0004-637X/691/2/1540.

Caffau, E., H.-G. Ludwig, M. Steffen, B. Freytag, and P. Bonifacio (2011), Solar Chemical Abundances Determined with a CO5BOLD 3D Model Atmosphere, *Sol. Phys.*, *268*, 255–269, doi:10.1007/s11207-010-9541-4.

Cargill, P., and I. de Moortel (2011), Solar physics: Waves galore, *Nature*, *475*, 463–464, doi:10.1038/475463a.

Chandran, B. D. G., and J. V. Hollweg (2009), Alfvén Wave Reflection and Turbulent Heating in the Solar Wind from 1 Solar Radius to 1 AU: An Analytical Treatment, *ApJ*, *707*, 1659–1667, doi:10.1088/0004-637X/707/2/1659.

Cohen, O., et al. (2007), A Semiempirical Magnetohydrodynamical Model of the Solar Wind, *ApJ*, *654*, L163–L166, doi:10.1086/511154.

Courant, R., K. Friedrichs, and H. Lewy (1928), Über die partiellen Differenzengleichungen der mathematischen Physik, *Mathematische Annalen*, *100*, 32–74, doi:10.1007/BF01448839.

Cranmer, S. R. (2010), An Efficient Approximation of the Coronal Heating Rate for use in Global Sun-Heliosphere Simulations, *ApJ*, *710*, 676–688, doi:10.1088/0004-637X/710/1/676.

Cranmer, S. R., and A. A. van Ballegooijen (2005), On the Generation, Propagation, and Reflection of Alfvén Waves from the Solar Photosphere to the Distant Heliosphere, *ApJS*, *156*, 265–293, doi:10.1086/426507.

Cranmer, S. R., A. A. van Ballegooijen, and R. J. Edgar (2007), Self-consistent Coronal Heating and Solar Wind Acceleration from Anisotropic Magnetohydrodynamic Turbulence, *ApJS*, *171*, 520–551, doi:10.1086/518001.

Cranmer, S. R., W. H. Matthaeus, B. A. Breech, and J. C. Kasper (2009), Empirical Constraints on Proton and Electron Heating in the Fast Solar Wind, *ApJ*, *702*, 1604–1614, doi:10.1088/0004-637X/702/2/1604.

Culhane, J. L., et al. (2007), The EUV Imaging Spectrometer for Hinode, *Sol. Phys.*, *243*, 19–61, doi:10.1007/s01007-007-0293-1.

De Pontieu, B., P. C. H. Martens, and H. S. Hudson (2001), Chromospheric Damping of Alfvén Waves, *ApJ*, *558*, 859–871, doi:10.1086/322408.

De Pontieu, B., et al. (2007), Chromospheric Alfvénic Waves Strong Enough to Power the Solar Wind, *Science*, *318*, 1574–, doi:10.1126/science.1151747.

Del Zanna, G., I. Rozum, and N. R. Badnell (2008), Electron-impact excitation of Be-like Mg, *A&A*, *487*, 1203–1208, doi:10.1051/0004-6361:200809998.

Del Zanna, G., P. J. Storey, N. R. Badnell, and H. E. Mason (2012), Atomic data for astrophysics: Fe xii soft X-ray lines, *A&A*, *543*, A139, doi:10.1051/0004-6361/201219023.

Delaboudinière, J.-P., et al. (1995), EIT: Extreme-Ultraviolet Imaging Telescope for the SOHO Mission, *Sol. Phys.*, *162*, 291–312, doi:10.1007/BF00733432.

Dere, K. P. (2007), Ionization rate coefficients for the elements hydrogen through zinc, *A&A*, *466*, 771–792, doi:10.1051/0004-6361:20066728.

Dere, K. P., E. Landi, H. E. Mason, B. C. Monsignori Fossi, and P. R. Young (1997), CHIANTI - an atomic database for emission lines, *A&AS*, *125*, 149–173, doi:10.1051/aas:1997368.

Dere, K. P., E. Landi, P. R. Young, and G. Del Zanna (2001), CHIANTI-An Atomic Database for Emission Lines. IV. Extension to X-Ray Wavelengths, *ApJS*, *134*, 331–354, doi:10.1086/320854.

Dere, K. P., E. Landi, P. R. Young, G. Del Zanna, M. Landini, and H. E. Mason (2009), CHIANTI - an atomic database for emission lines. IX. Ionization rates, recombination rates, ionization equilibria for the elements hydrogen through zinc and updated atomic data, *A&A*, *498*, 915–929, doi:10.1051/0004-6361/200911712.

Dmitruk, P., and W. H. Matthaeus (2003), Low-Frequency Waves and Turbulence in an Open Magnetic Region: Timescales and Heating Efficiency, *ApJ*, *597*, 1097–1105, doi:10.1086/378636.

Dmitruk, P., L. J. Milano, and W. H. Matthaeus (2001), Wave-driven Turbulent Coronal Heating in Open Field Line Regions: Nonlinear Phenomenological Model, *ApJ*, *548*, 482–491, doi:10.1086/318685.

Dmitruk, P., W. H. Matthaeus, L. J. Milano, S. Oughton, G. P. Zank, and D. J. Mullan (2002), Coronal Heating Distribution Due to Low-Frequency, Wave-driven Turbulence, *ApJ*, *575*, 571–577, doi:10.1086/341188.

Dong, C., and N. Singh (2013), Ion pseudoheating by low-frequency Alfvén waves revisited, *Physics of Plasmas*, *20*(1), 012,121, doi:10.1063/1.4789608.

Downs, C., I. I. Roussev, B. van der Holst, N. Lugaz, I. V. Sokolov, and T. I. Gombosi (2010), Toward a Realistic Thermodynamic Magnetohydrodynamic Model of the Global Solar Corona, *ApJ*, *712*, 1219–1231, doi:10.1088/0004-637X/712/2/1219.

Doyle, J. G., D. Banerjee, and M. E. Perez (1998), Coronal line-width variations, *Sol. Phys.*, *181*, 91–101, doi:10.1023/A:1005019931323.

Ebert, R. W., D. J. McComas, H. A. Elliott, R. J. Forsyth, and J. T. Gosling (2009), Bulk properties of the slow and fast solar wind and interplanetary coronal mass ejections measured by Ulysses: Three polar orbits of observations, *Journal of Geophysical Research (Space Physics)*, *114*, A01109, doi:10.1029/2008JA013631.

Erdélyi, R., and V. Fedun (2007), Are There Alfvén Waves in the Solar Atmosphere?, *Science*, *318*, 1572–, doi:10.1126/science.1153006.

Esser, R., and R. J. Edgar (2000), Reconciling Spectroscopic Electron Temperature Measurements in the Solar Corona with In Situ Charge State Observations, *ApJ*, *532*, L71–L74, doi:10.1086/312548.

Evans, R. M., M. Opher, R. Oran, B. van der Holst, I. V. Sokolov, R. Frazin, T. I. Gombosi, and A. Vásquez (2012), Coronal Heating by Surface Alfvén Wave Damping: Implementation in a Global Magnetohydrodynamics Model of the Solar Wind, *ApJ*, *756*, 155, doi:10.1088/0004-637X/756/2/155.

Feldman, U., and J. M. Laming (2000), Element Abundances in the Upper Atmospheres of the Sun and Stars: Update of Observational Results, *Phys. Scr*, *61*, 222, doi:10.1238/Physica.Regular.061a00222.

Feldman, U., and K. G. Widing (2003), Elemental Abundances in the Solar Upper Atmosphere Derived by Spectroscopic Means, *Space Sci. Rev.*, *107*, 665–720, doi: 10.1023/A:1026103726147.

Feldman, U., P. Mandelbaum, J. F. Seely, G. A. Doschek, and H. Gursky (1992), The potential for plasma diagnostics from stellar extreme-ultraviolet observations, *ApJS*, *81*, 387–408, doi:10.1086/191698.

Feldman, U., U. Schühle, K. G. Widing, and J. M. Laming (1998), Coronal Composition above the Solar Equator and the North Pole as Determined from Spectra Acquired by the SUMER Instrument on SOHO, *ApJ*, *505*, 999–1006, doi: 10.1086/306195.

Feldman, U., E. Landi, and G. A. Doschek (2007), Diagnostics of Suprathermal Electrons in Active-Region Plasmas Using He-like UV Lines, *ApJ*, *660*, 1674–1682, doi:10.1086/513729.

Fisk, L. A. (2003), Acceleration of the solar wind as a result of the reconnection of open magnetic flux with coronal loops, *Journal of Geophysical Research (Space Physics)*, *108*, 1157, doi:10.1029/2002JA009284.

Fisk, L. A., and L. Zhao (2009), The heliospheric magnetic field and the solar wind during the solar cycle, in *IAU Symposium*, *IAU Symposium*, vol. 257, edited by N. Gopalswamy and D. F. Webb, pp. 109–120, doi:10.1017/S1743921309029160.

Fisk, L. A., N. A. Schwadron, and T. H. Zurbuchen (1998), On the Slow Solar Wind, *Space Sci. Rev.*, *86*, 51–60, doi:10.1023/A:1005015527146.

Frazin, R. A., F. Kamalabadi, and M. A. Weber (2005), On the Combination of Differential Emission Measure Analysis and Rotational Tomography for Three-dimensional Solar EUV Imaging, *ApJ*, *628*, 1070–1080, doi:10.1086/431295.

Frazin, R. A., A. M. Vásquez, and F. Kamalabadi (2009), Quantitative, Three-dimensional Analysis of the Global Corona with Multi-spacecraft Differential Emission Measure Tomography, *ApJ*, *701*, 547–560, doi:10.1088/0004-637X/701/1/547.

Freeland, S. L., and B. N. Handy (1998), Data Analysis with the SolarSoft System, *Sol. Phys.*, *182*, 497–500, doi:10.1023/A:1005038224881.

Geiss, J. (1982), Processes affecting abundances in the solar wind, *Space Sci. Rev.*, *33*, 201–217, doi:10.1007/BF00213254.

Geiss, J., G. Gloeckler, and R. von Steiger (1995), Origin of the Solar Wind From Composition Data, *Space Sci. Rev.*, *72*, 49–60, doi:10.1007/BF00768753.

Gloeckler, G., T. H. Zurbuchen, and J. Geiss (2003), Implications of the observed anticorrelation between solar wind speed and coronal electron temperature, *Journal of Geophysical Research (Space Physics)*, *108*, 1158, doi:10.1029/2002JA009286.

Gloeckler, G., et al. (1992), The Solar Wind Ion Composition Spectrometer, *A&AS*, *92*, 267–289.

Goedbloed, J. P. H., and S. Poedts (2004), *Principles of Magnetohydrodynamics*, Cambridge University Press, UK.

Golub, L., et al. (2007), The X-Ray Telescope (XRT) for the Hinode Mission, *Sol. Phys.*, *243*, 63–86, doi:10.1007/s11207-007-0182-1.

Goossens, M., R. Erdélyi, and M. S. Ruderman (2011), Resonant MHD Waves in the Solar Atmosphere, *Space Sci. Rev.*, *158*, 289–338, doi:10.1007/s11214-010-9702-7.

Gosling, J. T. (1997), Physical nature of the low-speed solar wind, in *Robotic Exploration Close to the Sun: Scientific Basis*, *American Institute of Physics Conference Series*, vol. 385, edited by S. R. Habbal, pp. 17–24, doi:10.1063/1.51743.

Gruesbeck, J. R., S. T. Lepri, T. H. Zurbuchen, and S. K. Antiochos (2011), Constraints on Coronal Mass Ejection Evolution from in Situ Observations of Ionic Charge States, *ApJ*, *730*, 103, doi:10.1088/0004-637X/730/2/103.

Hahn, M., and D. W. Savin (2013), Observational Quantification of the Energy Dissipated by Alfvén Waves in a Polar Coronal Hole: Evidence that Waves Drive the Fast Solar Wind, *ApJ*, *776*, 78, doi:10.1088/0004-637X/776/2/78.

Hahn, M., P. Bryans, E. Landi, M. P. Miralles, and D. W. Savin (2010), Properties of a Polar Coronal Hole During the Solar Minimum in 2007, *ApJ*, *725*, 774–786, doi:10.1088/0004-637X/725/1/774.

Hahn, M., E. Landi, and D. W. Savin (2012), Evidence of Wave Damping at Low Heights in a Polar Coronal Hole, *ApJ*, *753*, 36, doi:10.1088/0004-637X/753/1/36.

Hassler, D. M., G. J. Rottman, E. C. Shoub, and T. E. Holzer (1990), Line broadening of MG X 609 and 625 A coronal emission lines observed above the solar limb, *ApJ*, *348*, L77–L80, doi:10.1086/185635.

Heyvaerts, J., and E. R. Priest (1983), Coronal heating by phase-mixed shear Alfven waves, *A&A*, *117*, 220–234.

Hollweg, J. V. (1986), Transition region, corona, and solar wind in coronal holes, *J. Geophys. Res.*, *91*, 4111–4125, doi:10.1029/JA091iA04p04111.

Hossain, M., P. C. Gray, D. H. Pontius, Jr., W. H. Matthaeus, and S. Oughton (1995), Phenomenology for the decay of energy-containing eddies in homogeneous MHD turbulence, *Physics of Fluids*, *7*, 2886–2904, doi:10.1063/1.868665.

Howard, R. A., et al. (2008), Sun Earth Connection Coronal and Heliospheric Investigation (SECCHI), *Space Sci. Rev.*, *136*, 67–115, doi:10.1007/s11214-008-9341-4.

Hundhausen, A. J., H. E. Gilbert, and S. J. Bame (1968), Ionization state of the interplanetary plasma, *J. Geophys. Res.*, *73(17)*, 54855493, doi: 10.1029/JA073i017p05485.

Iroshnikov, P. S. (1964), Turbulence of a Conducting Fluid in a Strong Magnetic Field, *Soviet Ast.*, *7*, 566.

Jacques, S. A. (1977), Momentum and energy transport by waves in the solar atmosphere and solar wind, *ApJ*, *215*, 942–951, doi:10.1086/155430.

Jin, M., W. B. Manchester, B. van der Holst, R. Oran, I. Sokolov, G. Toth, Y. Liu, X. D. Sun, and T. I. Gombosi (2013), Numerical Simulations of Coronal Mass Ejection on 2011 March 7: One-temperature and Two-temperature Model Comparison, *ApJ*, *773*, 50, doi:10.1088/0004-637X/773/1/50.

Jin, M., et al. (2012), A Global Two-temperature Corona and Inner Heliosphere Model: A Comprehensive Validation Study, *ApJ*, *745*, 6, doi:10.1088/0004-637X/745/1/6.

Judge, P. G., and M. Carlsson (2010), On the Solar Chromosphere Observed at the LIMB with Hinode, *ApJ*, *719*, 469–473, doi:10.1088/0004-637X/719/1/469.

Kano, R., et al. (2008), The Hinode X-Ray Telescope (XRT): Camera Design, Performance and Operations, *Sol. Phys.*, *249*, 263–279, doi:10.1007/s11207-007-9058-7.

Karachik, N. V., and A. A. Pevtsov (2011), Solar Wind and Coronal Bright Points inside Coronal Holes, *ApJ*, *735*, 47, doi:10.1088/0004-637X/735/1/47.

Klimchuk, J. A. (2006), On Solving the Coronal Heating Problem, *Sol. Phys.*, *234*, 41–77, doi:10.1007/s11207-006-0055-z.

Ko, Y.-K., L. A. Fisk, J. Geiss, G. Gloeckler, and M. Guhathakurta (1997), An Empirical Study of the Electron Temperature and Heavy Ion Velocities in the South Polar Coronal Hole, *Sol. Phys.*, *171*, 345–361.

Kohl, J. L., G. Noci, S. R. Cranmer, and J. C. Raymond (2006), Ultraviolet spectroscopy of the extended solar corona, *A&A Rev.*, *13*, 31–157, doi:10.1007/s00159-005-0026-7.

Kolmogorov, A. (1941), The Local Structure of Turbulence in Incompressible Viscous Fluid for Very Large Reynolds' Numbers, *Akademiia Nauk SSSR Doklady*, *30*, 301–305.

Kovalenko, V. A. (1981), Energy balance of the corona and the origin of quasi-stationary high-speed solar wind streams, *Sol. Phys.*, *73*, 383–403, doi: 10.1007/BF00151689.

Kraichnan, R. H. (1965), Inertial-Range Spectrum of Hydromagnetic Turbulence, *Physics of Fluids*, *8*, 1385–1387, doi:10.1063/1.1761412.

Laming, J. M. (2009), Non-Wkb Models of the First Ionization Potential Effect: Implications for Solar Coronal Heating and the Coronal Helium and Neon Abundances, *ApJ*, *695*, 954–969, doi:10.1088/0004-637X/695/2/954.

Laming, J. M. (2012), Non-WKB Models of the First Ionization Potential Effect: The Role of Slow Mode Waves, *ApJ*, *744*, 115, doi:10.1088/0004-637X/744/2/115.

Laming, J. M., and S. T. Lepri (2007), Ion Charge States in the Fast Solar Wind: New Data Analysis and Theoretical Refinements, *ApJ*, *660*, 1642–1652, doi:10.1086/513505.

Landi, E. (2007), Ion Temperatures in the Quiet Solar Corona, *ApJ*, *663*, 1363–1368, doi:10.1086/517910.

Landi, E. (2008), The Off-Disk Thermal Structure of a Polar Coronal Hole, *ApJ*, *685*, 1270–1276, doi:10.1086/591225.

Landi, E., U. Feldman, and K. P. Dere (2002), CHIANTI-An Atomic Database for Emission Lines. V. Comparison with an Isothermal Spectrum Observed with SUMER, *ApJS*, *139*, 281–296, doi:10.1086/337949.

Landi, E., J. R. Gruesbeck, S. T. Lepri, and T. H. Zurbuchen (2012a), New Solar Wind Diagnostic Using Both in Situ and Spectroscopic Measurements, *ApJ*, *750*, 159, doi:10.1088/0004-637X/750/2/159.

Landi, E., J. R. Gruesbeck, S. T. Lepri, T. H. Zurbuchen, and L. A. Fisk (2012b), Charge State Evolution in the Solar Wind. II. Plasma Charge State Composition in the Inner Corona and Accelerating Fast Solar Wind, *ApJ*, *761*, 48, doi:10.1088/0004-637X/761/1/48.

Landi, E., P. R. Young, K. P. Dere, G. Del Zanna, and H. E. Mason (2013), CHIANTI - An Atomic Database for Emission Lines. XIII. Soft X-Ray Improvements and Other Changes, *ApJ*, *763*, 86, doi:10.1088/0004-637X/763/2/86.

Landi, E., R. Oran, S. Lepri, T. Zurbuchen, L. Fisk, and B. van der Holst (2014), Charge state evolution in the solar wind. III. Model comparison with observations, *ApJ*.

Lepri, S. T., and T. H. Zurbuchen (2004), Iron charge state distributions as an indicator of hot ICMEs: Possible sources and temporal and spatial variations during solar maximum, *Journal of Geophysical Research (Space Physics)*, *109*, A01112, doi:10.1029/2003JA009954.

Lepri, S. T., T. H. Zurbuchen, L. A. Fisk, I. G. Richardson, H. V. Cane, and G. Gloeckler (2001), Iron charge distribution as an identifier of interplanetary coronal mass ejections, *J. Geophys. Res.*, *106*, 29,231–29,238, doi:10.1029/2001JA000014.

Linker, J. A., et al. (1999), Magnetohydrodynamic modeling of the solar corona during Whole Sun Month, *J. Geophys. Res.*, *104*, 9809–9830, doi:10.1029/1998JA900159.

Lionello, R., J. A. Linker, and Z. Mikić (2009), Multispectral Emission of the Sun During the First Whole Sun Month: Magnetohydrodynamic Simulations, *ApJ*, *690*, 902–912, doi:10.1088/0004-637X/690/1/902.

Liu, Y., et al. (2012), Comparison of Line-of-Sight Magnetograms Taken by the Solar Dynamics Observatory/Helioseismic and Magnetic Imager and Solar and Heliospheric Observatory/Michelson Doppler Imager, *Sol. Phys.*, *279*, 295–316, doi:10.1007/s11207-012-9976-x.

Marsch, E., and C.-Y. Tu (1990), On the radial evolution of MHD turbulence in the inner heliosphere, *J. Geophys. Res.*, *95*, 8211–8229, doi:10.1029/JA095iA06p08211.

Matsuzaki, K., M. Shimojo, T. D. Tarbell, L. K. Harra, and E. E. Deluca (2007), Data Archive of the Hinode Mission, *Sol. Phys.*, *243*, 87–92, doi:10.1007/s11207-006-0303-2.

Matthaeus, W. H., G. P. Zank, S. Oughton, D. J. Mullan, and P. Dmitruk (1999), Coronal Heating by Magnetohydrodynamic Turbulence Driven by Reflected Low-Frequency Waves, *ApJ*, *523*, L93–L96, doi:10.1086/312259.

Mazzotta, P., G. Mazzitelli, S. Colafrancesco, and N. Vittorio (1998), Ionization balance for optically thin plasmas: Rate coefficients for all atoms and ions of the elements H to NI, *A&AS*, *133*, 403–409, doi:10.1051/aas:1998330.

McComas, D. J., H. A. Elliott, N. A. Schwadron, J. T. Gosling, R. M. Skoug, and B. E. Goldstein (2003), The three-dimensional solar wind around solar maximum, *Geophys. Res. Lett.*, *30*, 1517, doi:10.1029/2003GL017136.

McComas, D. J., R. W. Ebert, H. A. Elliott, B. E. Goldstein, J. T. Gosling, N. A. Schwadron, and R. M. Skoug (2008), Weaker solar wind from the polar coronal holes and the whole Sun, *Geophys. Res. Lett.*, *35*, L18103, doi:10.1029/2008GL034896.

McComas, D. J., et al. (2000), Solar wind observations over Ulysses' first full polar orbit, *J. Geophys. Res.*, *105*, 10,419–10,434, doi:10.1029/1999JA000383.

McIntosh, S. W., and B. De Pontieu (2012), Estimating the "Dark" Energy Content of the Solar Corona, *ApJ*, *761*, 138, doi:10.1088/0004-637X/761/2/138.

McIntosh, S. W., B. de Pontieu, M. Carlsson, V. Hansteen, P. Boerner, and M. Goossens (2011), Alfvénic waves with sufficient energy to power the quiet solar corona and fast solar wind, *Nature*, *475*, 477–480, doi:10.1038/nature10235.

Meyer, J.-P. (1985), Solar-stellar outer atmospheres and energetic particles, and galactic cosmic rays, *ApJS*, *57*, 173–204, doi:10.1086/191001.

Mikić, Z., J. A. Linker, D. D. Schnack, R. Lionello, and A. Tarditi (1999), Magnetohydrodynamic modeling of the global solar corona, *Physics of Plasmas*, *6*, 2217–2224, doi:10.1063/1.873474.

Moran, T. G. (2001), Interpretation of coronal off-limb spectral line width measurements, *A&A*, *374*, L9–L11, doi:10.1051/0004-6361:20010643.

Ofman, L. (2004), Three-fluid model of the heating and acceleration of the fast solar wind, *Journal of Geophysical Research (Space Physics)*, *109*, A07102, doi:10.1029/2003JA010221.

Ofman, L., and J. M. Davila (1997), Do First Results from SOHO UVCS Indicate That the Solar Wind Is Accelerated by Solitary Waves?, *ApJ*, *476*, L51, doi:10.1086/310491.

Ofman, L., and J. M. Davila (2001), Three-Fluid 2.5-dimensional Magnetohydrodynamic Model of the Effective Temperature in Coronal Holes, *ApJ*, *553*, 935–940, doi:10.1086/320960.

Oran, R., B. van der Holst, E. Landi, M. Jin, I. V. Sokolov, and T. I. Gombosi (2013), A Global Wave-driven Magnetohydrodynamic Solar Model with a Unified Treatment of Open and Closed Magnetic Field Topologies, *ApJ*, *778*, 176, doi:10.1088/0004-637X/778/2/176.

Orrall, F. Q. (Ed.) (1981), *Solar active regions: A monograph from SKYLAB Solar Workshop III*.

Parker, E. N. (1958), Dynamics of the Interplanetary Gas and Magnetic Fields., *ApJ*, *128*, 664, doi:10.1086/146579.

Patsourakos, S., and J. A. Klimchuk (2006), Nonthermal Spectral Line Broadening and the Nanoflare Model, *ApJ*, *647*, 1452–1465, doi:10.1086/505517.

Phillips, K. J. H., U. Feldman, and E. Landi (2008), *Ultraviolet and X-ray Spectroscopy of the Solar Atmosphere*, Cambridge University Press.

Pietarila, A., L. Bertello, J. W. Harvey, and A. A. Pevtsov (2012), Comparison of Ground-Based and Space-Based Longitudinal Magnetograms, *Sol. Phys.*, doi:10.1007/s11207-012-0138-y.

Pneuman, G. W., and R. A. Kopp (1971), Gas-Magnetic Field Interactions in the Solar Corona, *Sol. Phys.*, *18*, 258–270, doi:10.1007/BF00145940.

Riley, P., J. A. Linker, Z. Mikić, R. Lionello, S. A. Ledvina, and J. G. Luhmann (2006), A Comparison between Global Solar Magnetohydrodynamic and Potential Field Source Surface Model Results, *ApJ*, *653*, 1510–1516, doi:10.1086/508565.

Roussev, I. I., T. I. Gombosi, I. V. Sokolov, M. Velli, W. Manchester, IV, D. L. DeZeeuw, P. Liewer, G. Tóth, and J. Luhmann (2003), A Three-dimensional Model of the Solar Wind Incorporating Solar Magnetogram Observations, *ApJ*, *595*, L57–L61, doi:10.1086/378878.

Scherrer, P. H., et al. (1995), The Solar Oscillations Investigation - Michelson Doppler Imager, *Sol. Phys.*, *162*, 129–188, doi:10.1007/BF00733429.

Schwenn, R., and E. Marsch (1990), Physics of the inner heliosphere. 1. Large-scale phenomena., *Physics and Chemistry in Space*, *20*.

Shearer, P., R. A. Frazin, A. O. Hero, III, and A. C. Gilbert (2012), The First Stray Light Corrected Extreme-ultraviolet Images of Solar Coronal Holes, *ApJ*, *749*, L8, doi:10.1088/2041-8205/749/1/L8.

Sokolov, I. V., I. I. Roussev, M. Skender, T. I. Gombosi, and A. V. Usmanov (2009), Transport Equation for MHD Turbulence: Application to Particle Acceleration at Interplanetary Shocks, *ApJ*, *696*, 261–267, doi:10.1088/0004-637X/696/1/261.

Sokolov, I. V., B. van der Holst, R. Oran, C. Downs, I. I. Roussev, M. Jin, W. B. Manchester, IV, R. M. Evans, and T. I. Gombosi (2013), Magnetohydrodynamic Waves and Coronal Heating: Unifying Empirical and MHD Turbulence Models, *ApJ*, *764*, 23, doi:10.1088/0004-637X/764/1/23.

Suess, S. T. (1979), Models of coronal hole flows, *Space Sci. Rev.*, *23*, 159–200, doi:10.1007/BF00173809.

Suess, S. T., Y.-K. Ko, R. von Steiger, and R. L. Moore (2009), Quiescent current sheets in the solar wind and origins of slow wind, *Journal of Geophysical Research (Space Physics)*, *114*, A04103, doi:10.1029/2008JA013704.

Sun, X., Y. Liu, J. T. Hoeksema, K. Hayashi, and X. Zhao (2011), A New Method for Polar Field Interpolation, *Sol. Phys.*, *270*, 9–22, doi:10.1007/s11207-011-9751-4.

Suzuki, T. K. (2006), Forecasting Solar Wind Speeds, *ApJ*, *640*, L75–L78, doi:10.1086/503102.

Tóth, G., et al. (2012), Adaptive numerical algorithms in space weather modeling, *Journal of Computational Physics*, *231*, 870–903, doi:10.1016/j.jcp.2011.02.006.

Usmanov, A. V. (1993), A global numerical 3-D MHD model of the solar wind, *Sol. Phys.*, *146*, 377–396, doi:10.1007/BF00662021.

Usmanov, A. V., and M. L. Goldstein (2003), A tilted-dipole MHD model of the solar corona and solar wind, *Journal of Geophysical Research (Space Physics)*, *108*, 1354, doi:10.1029/2002JA009777.

Usmanov, A. V., M. L. Goldstein, B. P. Besser, and J. M. Fritzer (2000), A global MHD solar wind model with WKB Alfvén waves: Comparison with Ulysses data, *J. Geophys. Res.*, *105*, 12,675–12,696, doi:10.1029/1999JA000233.

van der Holst, B., W. B. Manchester, IV, R. A. Frazin, A. M. Vásquez, G. Tóth, and T. I. Gombosi (2010), A Data-driven, Two-temperature Solar Wind Model with Alfvén Waves, *ApJ*, *725*, 1373, doi:10.1088/0004-637X/725/1/1373.

van der Holst, B., I. V. Sokolov, X. Meng, M. Jin, W. B. Manchester, IV, G. Tóth, and T. I. Gombosi (2014), Alfvén Wave Solar Model (AWSoM): Coronal Heating, *ApJ*, *782*, 81, doi:10.1088/0004-637X/782/2/81.

Vásquez, A. M., R. A. Frazin, and W. B. Manchester, IV (2010), The Solar Minimum Corona from Differential Emission Measure Tomography, *ApJ*, *715*, 1352, doi:10.1088/0004-637X/715/2/1352.

Velli, M. (1993), On the propagation of ideal, linear Alfven waves in radially stratified stellar atmospheres and winds, *A&A*, *270*, 304–314.

Verdini, A., and M. Velli (2007), Alfvén Waves and Turbulence in the Solar Atmosphere and Solar Wind, *ApJ*, *662*, 669–676, doi:10.1086/510710.

von Steiger, R., R. F. W. Schweingruber, J. Geiss, and G. Gloeckler (1995), Abundance variations in the solar wind, *Advances in Space Research*, *15*, 3–.

von Steiger, R., N. A. Schwadron, L. A. Fisk, J. Geiss, G. Gloeckler, S. Hefti, B. Wilken, R. F. Wimmer-Schweingruber, and T. H. Zurbuchen (2000), Composition of quasi-stationary solar wind flows from Ulysses/Solar Wind Ion Composition Spectrometer, *J. Geophys. Res.*, *105*, 27,217–27,238, doi:10.1029/1999JA000358.

von Steiger, R., T. H. Zurbuchen, J. Geiss, G. Gloeckler, L. A. Fisk, and N. A. Schwadron (2001), The 3-D Heliosphere from the Ulysses and ACE Solar Wind Ion Composition Experiments, *Space Sci. Rev.*, *97*, 123–127, doi:10.1023/A:1011886414964.

Wang, Y.-M., and N. R. Sheeley, Jr. (1990), Solar wind speed and coronal flux-tube expansion, *ApJ*, *355*, 726–732, doi:10.1086/168805.

Wang, Y.-M., N. R. Sheeley, D. G. Socker, R. A. Howard, and N. B. Rich (2000), The dynamical nature of coronal streamers, *J. Geophys. Res.*, *105*, 25,133–25,142, doi:10.1029/2000JA000149.

Watanabe, T., H. Hara, N. Yamamoto, D. Kato, H. A. Sakaue, I. Murakami, T. Kato, N. Nakamura, and P. R. Young (2009), Fe XIII Density Diagnostics in the EIS Observing Wavelengths, *ApJ*, *692*, 1294–1304, doi:10.1088/0004-637X/692/2/1294.

Wilhelm, K. (2006), Solar VUV measurements obtained by SOHO instruments and their radiometric calibration, *Advances in Space Research*, *37*, 225–233, doi:10.1016/j.asr.2004.12.057.

Wilhelm, K., et al. (1995), SUMER - Solar Ultraviolet Measurements of Emitted Radiation, *Sol. Phys.*, *162*, 189–231, doi:10.1007/BF00733430.

Withbroe, G. L. (1988), The temperature structure, mass, and energy flow in the corona and inner solar wind, *ApJ*, *325*, 442–467, doi:10.1086/166015.

Yeates, A. R., F. Bianchi, B. T. Welsch, and P. J. Bushby (2014), The coronal energy input from magnetic braiding, *A&A*, *564*, A131, doi:10.1051/0004-6361/201323276.

Young, P. R., T. Watanabe, H. Hara, and J. T. Mariska (2009), High-precision density measurements in the solar corona. I. Analysis methods and results for Fe XII and Fe XIII, *A&A*, *495*, 587–606, doi:10.1051/0004-6361:200810143.

Zhao, L., T. H. Zurbuchen, and L. A. Fisk (2009), Global distribution of the solar wind during solar cycle 23: ACE observations, *Geophys. Res. Lett.*, *36*, L14104, doi:10.1029/2009GL039181.

Zhou, Y., and W. H. Matthaeus (1990), Transport and turbulence modeling of solar wind fluctuations, *J. Geophys. Res.*, *95*, 10,291–10,311, doi:10.1029/JA095iA07p10291.

Zirker, J. B. (1977), Coronal holes and high-speed wind streams, *Reviews of Geophysics and Space Physics*, *15*, 257–269, doi:10.1029/RG015i003p00257.

Zurbuchen, T. H. (2007), A New View of the Coupling of the Sun and the Heliosphere, *ARA&A*, *45*, 297–338, doi:10.1146/annurev.astro.45.010807.154030.

Zurbuchen, T. H., and R. von Steiger (2006), On the Solar Wind Elemental Composition: Constraints on the Origin of the Solar Wind, in *SOHO-17. 10 Years of SOHO and Beyond*, *ESA Special Publication*, vol. 617.

Zurbuchen, T. H., S. Hefti, L. A. Fisk, G. Gloeckler, and R. von Steiger (1999), The Transition Between Fast and Slow Solar Wind from Composition Data, *Space Sci. Rev.*, *87*, 353–356, doi:10.1023/A:1005126718714.

Zurbuchen, T. H., L. A. Fisk, G. Gloeckler, and R. von Steiger (2002), The solar wind composition throughout the solar cycle: A continuum of dynamic states, *Geophys. Res. Lett.*, *29*, 1352, doi:10.1029/2001GL013946.